5-2012

Development and Experimental Analysis of Wireless High Accuracy Ultra-Wideband Localization Systems for Indoor Medical Applications

Michael Joseph Kuhn
University of Tennessee - Knoxville, mkuhn1@utk.edu

To the Graduate Council:

I am submitting herewith a dissertation written by Michael Joseph Kuhn entitled "Development and Experimental Analysis of Wireless High Accuracy Ultra-Wideband Localization Systems for Indoor Medical Applications." I have examined the final electronic copy of this dissertation for form and content and recommend that it be accepted in partial fulfillment of the requirements for the degree of Doctor of Philosophy, with a major in Biomedical Engineering.

Mohamed R. Mahfouz, Major Professor

We have read this dissertation and recommend its acceptance:

Aly E. Fathy, Richard D. Komistek, William R. Hamel

Accepted for the Council:
Dixie L. Thompson

Vice Provost and Dean of the Graduate School

(Original signatures are on file with official student records.)

Development and Experimental Analysis of Wireless High Accuracy Ultra-Wideband Localization Systems for Indoor Medical Applications

A Dissertation Presented for
the Doctor of Philosophy
Degree
The University of Tennessee, Knoxville

Michael Joseph Kuhn
May 2012

“For the Lord gives wisdom; from His mouth come knowledge and understanding.”
Proverbs 2:6

I thank the Lord for his continued provision in my life. This is dedicated to my wife, Tarah, for her love, unwavering support, and friendship. I also dedicate this to my father and mother, Michael and Trisha, for their lifelong support and for instilling in me the confidence and passion to lead a successful life.

Acknowledgements

I would like to thank my advisor and mentor through this process Dr. Mohamed Mahfouz for his continued support of my research and career goals. As a student of Dr. Mahfouz's, I have been able to gain valuable insight into how science and engineering are played out day-to-day both in academia and industry and what is required to succeed in these environments. His ambition, foresight, and willingness to take risks within the context of his research have contributed greatly to the successes and milestones that have been achieved to-date, including those outlined in this dissertation, in the pursuit to realize sub-millimeter 3-D wireless accuracy in the biomedical realm. I truly appreciate the support and friendship of Dr. Mahfouz which extends back to the Rocky Mountain Musculoskeletal Research Laboratory in Denver, Colorado starting in 2002.

I would like to thank Dr. Richard Komistek in conjunction with Dr. Mahfouz for all of the opportunities I have had stemming from the Center for Musculoskeletal Research and formerly the Rocky Mountain Musculoskeletal Research Laboratory to pursue new research avenues in biomedical engineering, work on innovative projects, present at international conferences, develop biomedical software, and work directly with biomedical companies and surgeons in orthopedics. I would like to thank Dr. Aly Fathy for his continued support and insight into this research. He has greatly impacted the development of this ultra-wideband indoor localization system which pushes the limits on achievable 3-D accuracy. During this process I have greatly benefited from Dr. Fathy's dedication to this research, attention to details, and ability to motivate students to unabashedly conduct high quality, ground breaking research and pursue excellence in their field. I would also like to thank Dr. William Hamel for his support during my time as a graduate student at the University of Tennessee.

I would like to thank my fellow graduate students who paved the way for my research including Dr. Brandon Merkl, Dr. Cemin Zhang, and Dr. Depeng Yang. Dr. Merkl and Dr. Zhang made many contributions to this system that have withstood the test of time and continue in their relevance to this research. I thank both Dr. Merkl and Dr. Zhang for their friendship and support.

I would like to thank everyone currently involved in this research including Gary To, Essam Elkhouly, Asia Wang, Nathan Rowe, Jonathan Turnmire, and Dayang Lin. Our combined efforts have been far greater than any one person, and I consider it a privilege to have been a part of this team. I would like to thank Matt Anderle, Emam Fatah, Hatem El Dakhakhni, Rimon Tadross, John Mueller, Emily Pritchard, Sumesh Zingde, Filip Leszko, Chris Carr, Joe Mitchell, Rebecca Robertson, and anyone else not mentioned for their support over the years.

Finally, I would like to thank my brother and sister, Erik and Krista, and my extended family for their friendship and support since I moved to Tennessee.

Abstract

This dissertation addresses several interesting and relevant problems in the field of wireless technologies applied to medical applications and specifically problems related to ultra-wideband high accuracy localization for use in the operating room. This research is cross disciplinary in nature and fundamentally builds upon microwave engineering, software engineering, systems engineering, and biomedical engineering. A good portion of this work has been published in peer reviewed microwave engineering and biomedical engineering conferences and journals. Wireless technologies in medicine are discussed with focus on ultra-wideband positioning in orthopedic surgical navigation. Characterization of the operating room as a medium for ultra-wideband signal transmission helps define system design requirements.

A discussion of the first generation positioning system provides a context for understanding the overall system architecture of the second generation ultra-wideband positioning system outlined in this dissertation. A system-level simulation framework provides a method for rapid prototyping of ultra-wideband positioning systems which takes into account all facets of the system (analog, digital, channel, experimental setup). This provides a robust framework for optimizing overall system design in realistic propagation environments.

A practical approach is taken to outline the development of the second generation ultra-wideband positioning system which includes an integrated tag design and real-time dynamic tracking of multiple tags. The tag and receiver designs are outlined as well as receiver-side digital signal processing, system-level design support for multi-tag tracking, and potential error

sources observed in dynamic experiments including phase center error, clock jitter and drift, and geometric position dilution of precision.

An experimental analysis of the multi-tag positioning system provides insight into overall system performance including the main sources of error. A five base station experiment shows the potential of redundant base stations in improving overall dynamic accuracy. Finally, the system performance in low signal-to-noise ratio and non-line-of-sight environments is analyzed by focusing on receiver-side digitally-implemented ranging algorithms including leading-edge detection and peak detection.

These technologies are aimed at use in next-generation medical systems with many applications including surgical navigation, wireless telemetry, medical asset tracking, and *in vivo* wireless sensors.

Table of Contents

List of Tables

List of Figures

Scientific Terminology

dB	Decibels
dBm	Decibels Referenced to One Milliwatt
°C	Degrees Celsius
cm	Centimeter
fs	Femtosecond
Gbps or Gb/s	Gigabits per Second
GHz	Gigahertz
GSPS or GS/s	Giga Samples per Second
Hz	Hertz
kbps or kb/s	Kilobits per Second
kHz	Kilohertz
Mbps or Mb/s	Megabits per Second
MHz	Megahertz
MSPS or MS/s	Mega Samples per Second
µs	Microsecond
mm	Millimeter
mVpp	Voltage Peak-to-Peak in Millivolts
ns	Nanosecond
ppm	Parts-per-Million
ps	Picosecond
sub-mm	Sub-Millimeter
Vpp	Voltage Peak-to-Peak

Acronyms

1-D	One Dimensional
2-D	Two Dimensional
3-D	Three Dimensional
AC	Alternating Current
ADC	Analog to Digital Converter
ADS	Agilent Advanced Design System
AGC	Automatic Gain Control
AOA	Angle-of-Arrival
AP	Anteroposterior

APP	Anterior Pelvic Plane
ASK	Amplitude Shift Keying
AWGN	Additive White Gaussian Noise
BA	Range Difference Base Station B – Base Station A
BAN	Body Area Network
BER	Bit Error Rate
BPF	Band Pass Filter
BPSK	Binary Phase Shift Keying
C++	C Plus Plus Software Language
CA	Range Difference Base Station C – Base Station A
CAS	Computer Aided Surgery
CCD	Charge Coupled Device
CDMA	Code Division Multiple Access
CM	Channel Model
CM1	IEEE 802.15.4a Residential LOS Channel Model
CM2	IEEE 802.15.4a Residential NLOS Channel Model
CM3	IEEE 802.15.4a Commercial LOS Channel Model
CM4	IEEE 802.15.4a Commercial NLOS Channel Model
CM7	IEEE 802.15.4a Industrial LOS Channel Model
CM8	IEEE 802.15.4a Industrial NLOS Channel Model
CMOS	Complementary Metal Oxide Semiconductor
COTS	Commercial-Off-the-Shelf
CPU	Central Processing Unit
CT	Computed Tomography
DA	Range Difference Base Station D – Base Station A
DAA	Detect and Avoid
DC	Direct Current
DDS	Direct Digital Synthesizer
DOF	Degrees-of-Freedom
DPSK	Differential Phase Shift Keying
DRO	Dielectric Resonator Oscillator
DSP	Digital Signal Processing
DSSS	Direct Sequence Spread Spectrum
EA	Range Difference Base Station E – Base Station A
ED	Energy Detection
EDA	Electronic Design Automation
ECG	Electrocardiogram
EIRP	Effective Isotropic Radiation Pattern
ELF	Extremely Low Frequency

EM	Electromagnetic
EMI	Electromagnetic Interference
FCC	Federal Communications Commission
FFT	Fast Fourier Transform
FIR	Finite Impulse Response
FMCW	Frequency Modulated Continuous Wave
FP	First Peak Detect
FPGA	Field Programmable Gate Array
FSK	Frequency Shift Keying
FWHM	Full Width Half Maximum
GDOP	Geometric Dilution of Precision
GFSK	Gaussian Frequency Shift Keying
GPS	Global Positioning System
GUI	Graphical User Interface
HDR	High Data Rate
HPF	High Pass Filter
ID	Numerical Identifier
IEEE	Institute of Electrical and Electronics Engineers
IF	Intermediate Frequency
IIR	Infinite Impulse Response
IMU	Inertial Measurement Unit
IPS	Iterative Peak Subtraction
IQ	In-Phase and Quadrature Signals
IR	Infrared
IR	Impulse Radio
ISM	Industrial, Scientific, and Medical
JTAG	Joint Test Action Group
LDR	Low Data Rate
LE	Leading Edge
LF	Low Frequency
LNA	Low Noise Amplifier
LO	Local Oscillator
LOS	Line-of-Sight
LPF	Low Pass Filter
MAC	Media Access Control
MB-OFDM	Multiband Orthogonal Frequency Division Multiplexing
MCU	Microcontroller or Microprogrammed Control Unit
MEMS	Microelectromechanical System

MF	Matched Filter
ML	Mediolateral
MIC	Microwave Integrated Circuit
MIQR	Median Interquartile Range
MIS	Minimally Invasive Surgery
MMIC	Monolithic Microwave Integrated Circuit
MoM	Method-of-Moments
MP	Multipath
MPA	Medium Power Amplifier
MRI	Magnetic Resonance Imaging
MSK	Minimum Shift Keying
NDI	Northern Digital Inc.
NLOS	Non-Line-of-Sight
OCXO	Oven Controlled Crystal Oscillator
OOK	On-Off Keying
OR	Operating Room
PAN	Personal Area Network
PD	Peak Detection
PDOP	Position Dilution of Precision
PDP	Power Delay Profile
PHY	Physical Layer
PLL	Phase Locked Loop
PPM	Pulse Position Modulation
PRF	Pulse Repetition Frequency
QNSR	Quantization Noise to Signal Ratio
QPSK	Quadrature Phase Shift Keying
RD	Range Difference
RF	Radio-frequency
RFID	Radio Frequency Identification
RMS	Root-Mean-Square
RMSE	Root-Mean-Square Error
ROM	Range of Motion
RTLS	Real-Time Location System
RSS	Received Signal Strength
RTOF	Return Time of Flight
Rx	Receiver
SI	Superoinferior
SiGe	Silicon Germanium
SMA	Sub-Miniature Version A

SNR	Signal-to-Noise Ratio
SPI	Serial Peripheral Interface
SRD	Step Recovery Diode
SS	Signal Strength
S-V	Saleh-Valenzuela
TCXO	Temperature Compensated Crystal Oscillator
TD	Time Difference (sometimes interchanged with RD)
TDMA	Time-Division-Multiple-Access
TDOA	Time-Difference-of-Arrival
TEM	Transverse Electromagnetic
THA	Total Hip Arthroplasty
TI	Texas Instruments
TKA	Total Knee Arthroplasty
TKR	Total Knee Replacement
TOA	Time-of-Arrival
Tx	Transmitter
UWB	Ultra-Wideband
UWB-IR	Ultra-Wideband Impulse Radio
UV	Ultraviolet
VCO	Voltage Controlled Oscillator
VHDL	Very High Speed Integrated Circuits Hardware Design Language
Wi-Fi	Synonymous with WLAN
WiMAX	Worldwide Interoperability for Microwave Access
WLAN	Wireless Local Area Network
WPAN	Wireless Personal Area Network
WSN	Wireless Sensor Network

1. Introduction

1.1 Motivation

The use of wireless technologies in the medical field has greatly increased both in the deployment of wireless technologies in hospital environments as well as in the research of new wireless systems and sensors designed and optimized to operate in the challenging indoor environments typical of hospitals and other medical facilities.

As the technologies utilized in businesses, hospitals, and manufacturing facilities have become more advanced, a pronounced need within the RFID market (total projected revenue in 2009 of 5.56 billion USD) has developed for high accuracy, indoor, reliable, real-time location information solutions to track people, assets, etc. [1]-[2]. Therefore, there is a great demand to develop wireless local positioning technologies as they have many diverse applications and have received considerable attention [3]. Ultra-wideband wireless signals are defined by the FCC to be any signal which occupies 500 MHz or more of bandwidth (regardless of carrier frequency, baseband included) or any wireless signal which has a 20% or higher fractional bandwidth (the bandwidth being defined by the -10 dB points on the high and low end of the occupied spectrum while the center frequency is the center of the aforementioned bandwidth) [4]. Figure 1-1 shows an example of an UWB signal where Figure 1-1a shows a baseband UWB pulse in the time domain with a width of 300 ps and Figure 1-1b shows an up-converted UWB signal in the frequency domain with a narrowband up-converted signal included for comparison. It is obvious from Figure 1-1 that an UWB signal occupies a much larger

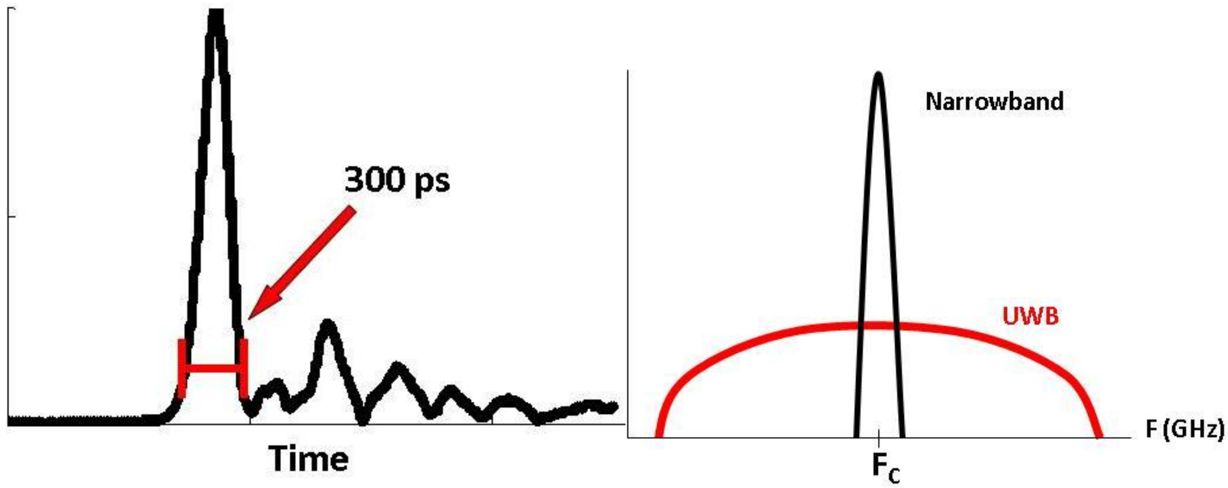

(a) (b)

Figure 1-1: Example of an ultra-wideband signal: (a) time-domain baseband 300 ps wide pulse, (b) frequency domain up-converted UWB pulse compared to typical up-converted narrowband signal.

bandwidth than the average narrowband wireless signal while at the same time having a much lower power at any given frequency (the FCC defined the upper limit of power as being -41.3 dBm/MHz [4]). The major strength of UWB signals is their ability to successfully coexist with narrowband signals as well as their short duration in the time domain, which gives UWB robust performance in multipath-ridden indoor environments and also allows for its use in high data-rate digital communication.

1.2 Background

The fundamental purpose of this research is to open up new areas of application for wireless technologies applied to medicine. This includes pushing the achievable limits in terms of high accuracy indoor 3-D localization using ultra-wideband technology and to utilize this technology in a real-time location system which tracks multiple tags simultaneously with millimeter 3-D accuracy. Additional facets of the system and of wireless technologies in general are examined including comprehensive system simulations of UWB localization systems in indoor environments, receiver-side digital signal processing, non-line-of-sight detection and mitigation, application of UWB localization systems in orthopedic surgical navigation, wireless technologies in medicine, and wireless signal propagation in hospital environments. In this work, the applications are focused mainly in the medical field, although many other potential applications exist in commercial, industrial, military, and even residential settings. UWB has only had a licensed frequency band in the United States since 2002, so much of the work being done at present is laying a foundation on which more widespread and mature technologies will be built to get UWB out into the real, usable world. The use of UWB technology in high performance localization systems requiring millimeter 3-D accuracy has not been well researched, and far fewer systems have been developed, compared to its use in cheaper but more widespread systems with lower accuracy requirements on the order of 10-15 cm 3-D accuracy.

1.2.1 Current State of Indoor Wireless Localization Systems

Wireless local positioning has many diverse applications and has been extensively studied [3],[5]. While GPS uses ultra-high precision atomic clocks to measure time-of-flight [6], a more standard method for indoor localization systems is TDOA, where all of the base stations or receivers are synchronized, and the difference in time is measured between each pair of receivers to triangulate the position of an unsynchronized tag [3]. Two main technologies have emerged as possible solutions for TDOA systems: frequency modulated continuous wave and UWB. FMCW systems can be found both in the literature [7],[8] and as commercial products [9] with various levels of accuracy. For example, Stelzer et al. achieved accuracy of greater than 10 cm for an outdoor application tracking a car around a 500 m^2 racecar track [7] while Wiebking et al. achieved accuracy around 20 cm for an indoor application covering a 15x25 m^2 2-D area [10]. Finally, Roehr et al. achieved accuracy of 1 cm in a LOS, multipath free environment using a novel chirp technique centered at 5.8 GHz [11]. Meanwhile, interest in UWB for radar applications has increased greatly following the FCC's decision to open up the bands from 3.1 - 10.6 GHz and 22 – 29 GHz for UWB use in 2002 [4]. UWB technology has inherent advantages for indoor applications in terms of robustness to multipath interference and potential for high ranging accuracy [12].

Commercial systems are already available which utilize UWB sensors for indoor asset tracking. For example, Zebra Technologies Corporation has the Sapphire DART system which can operate in indoor environments of greater than 50 m ranges while using TDOA in conjunction with UWB sensors to achieve accuracy of 10 cm [13]. Ubisense has a comparable indoor system which uses UWB in conjunction with TDOA and AOA. It has an operating range of up to 50 – 100 m and can detect sensors with accuracy of 15 cm [14]. Higher accuracy has been reported in the literature for indoor UWB positioning systems. For example, Low et al. achieved centimeter-range accuracy in a 1-D short range indoor LOS environment utilizing UWB pulse signals [15]. Zetik et al. reported sub-mm 1-D accuracy but with only extremely short displacements while accuracy decreased to 1.5 cm for 2-D localization over a 2x2 m^2 area

[16]. Meier et al. designed a 24 GHz system which uses a Kalman filter combined with correlation and phase information to reduce the uncertainty of a static point to 0.1 mm, although the uncertainty increases to 2 mm when the tag is in motion [17]. These experimental results show that UWB technology has the potential for high precision indoor localization even in harsh environments with significant multipath effects. Commercial UWB systems have localization accuracy of 10 - 15 cm. Certain short-range industrial and medical applications such as dynamic part tracking, structural testing, and 3-D tracking in computer assisted surgery require significantly higher accuracy than commercial UWB systems - accuracy in the mm or sub-mm range.

1.2.1.1 Commercial Systems

As shown in Table 1-1, current commercial UWB systems can achieve 3-D localization accuracy in the range of 10 – 15 cm. A comparison of the Sapphire DART system from Zebra Technologies Corporation and the RTLS from Ubisense is given in Table 1-1 [13],[14]. As shown in Table 1-1, the two systems share many commonalities including frequency range, operating range, compact tag size, and overall 3-D accuracy. One major difference is the method of digital communication: the Zebra Technologies Corporation system uses UWB pulse-based modulation whereas the Ubisense system uses a narrowband 2.4 GHz digital communication scheme (e.g. Bluetooth). Although Bluetooth is a more mature technology than UWB pulse-based modulation, it has a distinct disadvantage in that it is much more susceptible to multipath interference and may experience severe degradation depending on the operating

Table 1-1: Comparison of commercial UWB localization systems with specifications reported for their compact tags.

Company	Frequency Range (GHz)	Operating Range (m)	Tag Size (cm^3)	Number of Tags	Refresh Rate (Hz)	Localization Method	Accuracy (cm)
Zebra Technologies Corporation	5.94 - 7.12	> 50	1.12x 4.01x 2.11	> 100	100	TDOA	< 10
Ubisense	5.8 – 7.2	> 50	3.8x 3.9x 1.65	> 1000	20	TDOA and AOA	< 15

environment of the system. Figure 1-2 shows the two commercial systems. The Zebra Technologies system is shown in Figure 1-2a with the main controller, two base stations, and three different sized tags displayed while Figure 1-2b shows two different sized tags from the Ubisense localization system. It is obvious from Figure 1-2 that these systems are quite comparable and a few distinct trends in commercial indoor localization systems can be inferred:

- Battery operated tags with compact size
    - Low power transmitter architecture and smart power-saving circuitry
- Flexibility in network building schemes
    - Ability to build ad-hoc or self organizing networks
    - Ability to automatically combine sub-networks into an even larger framework
- 3-D accuracy of current systems still limited to cm-range or even tens of centimeters
    - Due to limited sampling rate on receiver side
    - Due also to use of square-law diode detectors at receivers
- Complicated installation with on-site help needed in setting up systems

The limitations of current commercial systems are examined when looking at state-of-the-art in research positioning systems and also the first generation UWB positioning system

(a) (b)

Figure 1-2: Commercial indoor UWB localization systems (a) Zebra Technologies Corporation, (b) Ubisense.

designed for high accuracy indoor applications (Chapter 5).

1.2.1.2 Research Systems

Competing technologies for high accuracy indoor positioning include FMCW, impulse-based (i.e. carrier-free) ultra-wideband, and carrier-based UWB. Table 1-2 provides a summary of the various research groups utilizing these three approaches for high accuracy indoor positioning. Similar accuracy levels (0.5-20 cm) have been achieved for both carrier-based [17]-[22] and impulse-based [15],[16],[23],[24] UWB positioning systems, although carrier-based systems have shown the potential for mm and sub-mm range accuracy even for 3-D indoor environments ([18],[19] and [17],[21],[22]]). FMCW has proven to be a successful competing technology for high accuracy positioning systems [7],[9],[25]-[29]. In the 5.8 GHz band for industrial, medical, and scientific applications, documented accuracy of 5-20 cm for 2-D has been achieved [7],[9],[26]-[28]. FMCW systems operating at higher frequencies including 35 GHz and 77 GHz have achieved accuracy levels of 0.1 mm [25],[29], with the system described by Feger et al. working at ranges of up to 10 m [29]. The most recent FMCW trend is a European-wide push to create low power wireless sensor networks built on 5.8 GHz FMCW technology [26]-[28]. It should be noted that in Table 1-2 many of the reported error values are standard deviation error. It is more accurate to report RMSE. RMSE is a good measure of error resulting from both the accuracy and precision, i.e., the true unbiased error when data values fluctuate above and below zero.

Ultra-wideband is a promising technology for use in short-range indoor local positioning and wireless data communications. It is well known that very high spatial resolution can be achieved using UWB due to the wide-band nature of the signals. A widely used and low complexity UWB architecture is energy detection, where the UWB signal is transmitted directly through the UWB antenna without up-conversion [24],[30]-[35]. Meanwhile, at the receiver side, the energy detection of the signal is achieved by passing the signal through a square-law device, usually a Schottky or tunnel diode, followed by an integrator and sampler. Figure 1-3 shows the typical UWB receiver architecture using energy detection. However, due to the large bandwidth of the received UWB signal, it is difficult and costly for ED-based receivers to operate at above the Nyquist rate [30]. Typically a fast comparator is used as the sampling device. For example, Buchegger et al. realized an UWB communication link with a data rate of 1.2 Mbps using the tunnel diode detector [31]. Lie et al. realized the leading-edge pulse detection method using a tunnel diode combined with an envelope detector to maintain high accuracy for UWB ranging in a multipath environment [32].

Table 1-2: Comparison of current research high accuracy positioning systems.

Research Group/ Company	System Architecture	Frequency (GHz)	Reported Error	Operating Range
University of Tennessee [18],[19]	Carrier-Based UWB	5.4-10.6	2-5 mm (3-D)	5 m/ Indoor
Waldmann et al. [20]	Carrier-Based UWB	7-8	1.7 cm (1-D)	10 m/ Indoor
Meier et al. [17],[21]	Carrier-Based UWB	22.58-25.7	0.1-2 mm (1-D)	8 m/ Indoor
McEwan [22]	Carrier-Based UWB	5.8	< 2 mm (2-D)	10 cm x 10 cm
Ossberger et al. [23]	Impulse-Based UWB	~2-7	5-10 mm (1-D)	5 m/ Indoor
Fujii et al. [24]	Impulse-Based UWB	3.7-5	20 cm (2-D)	8 m/ Indoor
Low et al. [15]	Impulse-Based UWB	3.2-5.2	1 cm (1-D)	8 m/ Indoor
Zetik et al. [16]	Impulse-Based UWB	0.01-5	1.5 cm (2-D)	2 m/ Indoor
Stelzer et al. [25]	FMCW and Interferometry	35	0.1 mm (1-D)	< 1 m/ Indoor
Stelzer et al. [7]	FMCW	5.8	10 cm (2-D)	500 m/ Outdoor
Ellinger, Mosshammer et al. [26]-[28]	FMCW	5.8	18 cm (2-D)	40 m/ Indoor
Symeo LPR [9]	FMCW	5.8	5 cm (2-D)	400 m/ Indoor
Feger et al. [29]	FMCW	77	0.1 mm (1-D)	1.5 m/ Chamber

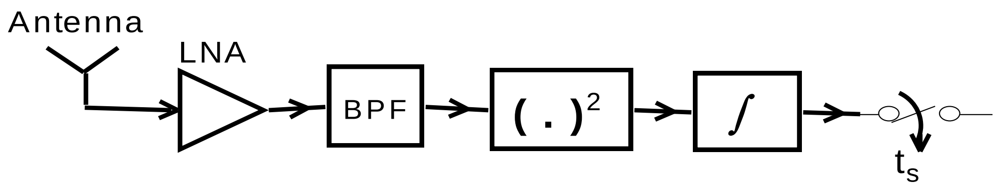

Figure 1-3: Energy detection-based UWB receiver architecture [19].

Fujii et al. achieved a 0.3 ns time resolution using the ED-based impulse detector, corresponding to 0.1 m distance resolution [24].

Another widely used UWB architecture is carrier-based impulse radio UWB, where the transmitted UWB signal is up-converted through a microwave carrier, then down-converted at the receiver side [18],[19],[36],[37]. Figure 1-4 shows the carrier-based low complexity UWB receiver architecture. In [36] the demodulator is implemented with a 2-FSK scheme, whereas in [18] the demodulator is realized through a low cost two channel sub-sampling mixer with an equivalent sampling rate of over 100 GSPS [38], followed by a digital signal processing unit implemented through a standard FPGA. However, a problem exists in the amplitude and phase differences between the I and Q channels due to hardware variation between the I and Q receiver chains, which causes distortion of the demodulated signal. Treyer et al. [39] corrected the amplitude and phase error by using the Hartley phasing-type single sideband modulator, but this method requires relatively complex circuitry and is limited to narrowband applications.

One type of non-coherent UWB receiver architecture was implemented in [22] by McEwan as shown in Figure 1-5. Upon receiving the RF bursts from the transmitter, a timing

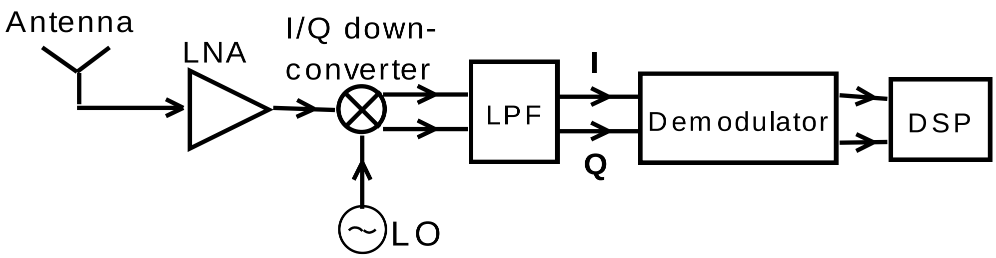

Figure 1-4: Carrier-based non-coherent UWB receiver architecture [19].

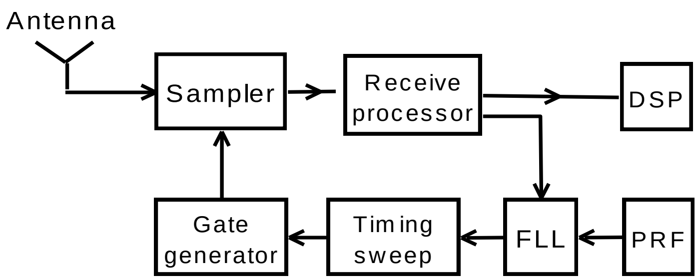

Figure 1-5: Non-coherent UWB receiver architecture using frequency locked loop [19].

circuitry with a frequency locked loop which locks the receiver PRF clock to the transmitted PRF clock so that both clocks have the same frequency and phase. However, the required receiver timing circuitry design is complex and the system is limited to operate at a relatively low carrier frequency to avoid using expensive samplers with high sampling bandwidth.

Another technique is shown in Figure 1-6, where a hybrid UWB receiver architecture combines the carrier-based and ED-based UWB receiver schemes. The down-conversion requires only one channel instead of I and Q channels as compared to Figure 1-4, which lowers system complexity and overall cost.

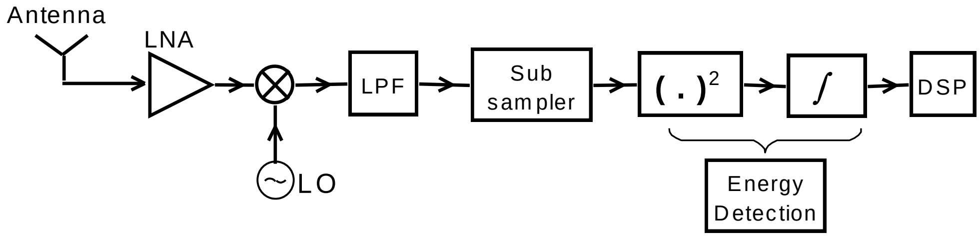

Figure 1-6: UWB receiver architecture which combines the carrier-based and energy detection-based UWB receiver schemes [19].

In Chapter 5, the 1st generation real-time localization system developed at the University of Tennessee using the receiver architecture outlined in Figure 1-6 is discussed in detail. Details on the developed system can also be found in published literature [18],[19], [37],[38]. The 2nd generation multi-tag system outlined in Chapter 7 uses a true energy detection receiver architecture to remove the need for an LO signal at the UWB receiver while also removing the overall reliance of the UWB indoor positioning system on low phase noise LOs at the wireless transmitter and receiver.

1.2.2 Wireless Systems Integrated with Medical Devices

Smart bioinstruments are broken down into various applications including diagnostics, surgical, in vivo, remote patient monitoring, and indoor positioning. Each of these applications has unique requirements and constraints related to power, sensor performance, wireless transmitter and receiver front-ends, and antenna. Table 1-3 provides an expanded list of examples divided by application. Each application has unique requirements which ultimately dictate the final system design. In vivo devices typically operate at lower frequencies (< 1 GHz) in order to avoid increased soft tissue losses [40],[41],[42], although in vivo systems are now being designed which operate at higher frequencies such as the 2.4 GHz ISM band [43],[44]. The major constraints in vivo systems continue to face include power consumption, size, and operating range. As shown in Table 1-3, typical operating ranges span from 1 cm to 10 m. Active transmitters operating around 300-400 MHz can achieve operating ranges of 5-10 m while inductive links typically operate at distances of 50 cm or less. Higher frequency in vivo links such as the 2.4 GHz ISM band can operate at 1-2 m. Most implantable devices have a form factor 1-2 cm^2, although this can be increased in certain cases such as a device integrated into an orthopedic implant [45]. Additional work done for in vivo systems includes a multi-biosignal implantable system [46] and optimizing interdigitated capacitor biosensors utilizing microwaves for biomolecular sensing [47]. [48],[49] discuss optimizing the inductive link through implantable coil design.

Diagnostic wireless bioinstruments have a much different set of requirements when compared to in vivo systems. As shown in Table 1-3, wireless 3-D gait motion systems can operate in bands such as the U.S. 900 MHz or 2.4 GHz ISM bands [50],[51]. Operating ranges of these systems need to be greater than in vivo devices and are typically 100 m or more and made for indoor/outdoor use. Power requirements can vary greatly depending on the duration for which the device is intended to operate before battery replacement. For example, the system outlined in [50] is relatively high power when compared to [51] (20 mW vs. 1-2 μW). The size of diagnostic wireless systems can be much greater than in vivo devices and includes wearable devices such as belts or shirts. The application in [51] is to monitor children over a long time frame (months or years) while [50] discusses a shorter time frame of diagnostic testing for clinical applications which could last only a few minutes to an hour. The system in [50] updates

Table 1-3: Example commercial and research medical devices broken down by application.

Biosensor	Application	Operating Range	Frequency	Size	Average Power	Data Rate/ Positioniong Accuracy
Intracranial Pressure [43]	*In Vivo*	<1 m	2.4-2.48 GHz	12 mm diamter 10 mm height	141 μW	Not Specified
None Specified [40]	*In Vivo*	2-10 m	402 – 405 MHz	3.88 mm^2 (chip only)	25 μW @ 1% duty cycle	75 kbps
Multi-Channel Neural [41]	*In Vivo*	1 cm	70-200 MHz	14 mm x 15.5 mm	14.4 mW Inductive	Up to 2 Mbps
Multi-Channel Pressure [42]	*In Vivo*	50 cm	150 MHz	Form Fitting to Implant	5 mW Inductive	1-2 Mbps
Glucose Monitoring [44]	*In Vivo*	2 m	2.4-2.48 GHz Zigbee	20 mm diameter 50 mm length	88 μW	250 kbps
3-D Gait Motion [50]	Diagnostics	>500 m	916 MHz	35.6 mm x 10 mm	10-30 mW (estimate)	115 kbps
3-D Gait Motion [51]	Diagnostics	100 m	2.4-2.48 GHz Zigbee	30 mm x 50 mm x 12 mm	1.5 μW	250 kbps
Cardiac Monitoring [53]	Remote Monitoring	50-100 m	2.4-2.48 GHz	50 mm x 50 mm (approximate)	1 mW	<2 Mbps
Cardiac, Tilt, Respiratory, Temperature [54]	Remote Monitoring	<30 m	2.4-2.48 GHz Bluetooth	Chest Belt	400 mW (estimate)	<3 Mbps
Ligament Balancing [52]	Surgical	15-20 m	315 MHz	60 mm x 20 mm x 120 mm	28 mW	100 kbps
Gamma Radiation Detector [62]	Surgical	5-10 m	2.4-2.48 GHz Bluetooth	14mm diameter 24cm length	300 mW (estimate)	<3 Mbps
Personnel & Asset Tracking [63]	Wireless Positioning	50 m	6-7 GHz Ultra-Wideband	36 mm x 33 mm x 13 mm	20 μW (estimate)	15 cm (2-D)
Personnel & Asset Tracking [13]	Wireless Positioning	50 m	6.35-6.75 GHz Ultra-Wideband	40 mm x 40 mm x 20 mm	10 μW (estimate)	<30 cm (3-D)

at 100 Hz or more while [51] does not require such a high update rate resulting in lower power consumption.

Wireless remote monitoring systems typically have similar requirements to wireless diagnostic systems. As shown in Table 1-3, the remote monitoring systems outlined in [53],[54] operate in the 2.4 GHz ISM band. In certain instances they require higher data rates than the diagnostic gait systems (1-3 Mbps versus 100-300 kbps) mainly due to the transmission of biosignals such as the electrocardiogram, electroencephalogram, temperature, respiration, etc. In some cases, remote monitoring systems will only update at long intervals (10 s to 1 minute or more), which reduces power consumption and can allow battery life to be extended to months or even years. The application in [47] is cardiac monitoring over an extended time period of up to 3 months that dictates a lower power consumption than the chest belt described in [54] (1 mW versus 400 mW) which is used for high update rate monitoring of an athlete over a shorter period of time of up to 8 hours. An excellent overview of wearable medical devices is presented in [55] while [56]-[60] provides more information on wireless sensor networks for medical applications including body area networks. [61] discusses issues related to authentication and encryption in wireless sensor networks and is a key future issue which must be addressed.

Table 1-3 provides a few examples of wireless surgical systems including a ligament balancing spacer block [50] and a gamma radiation detector [62]. Wireless surgical bioinstruments typically need to operate over a shorter operating range compared to diagnostic and remote monitoring systems (5-20 m compared to 100 m or more). Also, they only need to operate continuously during the surgery, allowing a battery lifetime of 24 hours or less. The ligament balancing spacer block [50] operates at 315 MHz since it will have to transmit signals in and around the knee during surgery, causing propagation conditions closer to in vivo. The gamma radiation detector [62] operates in the 2.4 GHz ISM band with a Bluetooth link and requires a higher bandwidth (3 Mbps versus 100 kbps) and more power (300 mW versus 28 mW) when compared to the ligament balancing system. The size constraints of surgical devices are application specific (e.g. a wireless probe for the gamma radiation detector and a wireless space block for the ligament balancing wireless pressure sensor). The wireless propagation environment of the operating room typically contains many different pieces of medical equipment and a lot of metal which creates significant scattering and multipath interference and can reduce wireless operating ranges and increase the bit error rate, especially for narrowband systems. Consequently, ultra-wideband technology has gained interest for enhanced performance of wireless surgical devices.

Two different indoor wireless positioning systems are outlined in Table 1-3 [63],[13]. These are commercial systems from Pulse Location Systems [63] and Zebra Enterprise Solutions Inc. [13]. Both of them utilize ultra-wideband wireless technology and operate in the 6-7 GHz band. The tags consume low power (10-20 μW) and can last up to 7 years depending on the update rate. They have comparable tag sizes for tracking assets (3-4 cm length and width) and can achieve wireless positioning accuracy of 15-30 cm. Both of them employ TDOA for triangulating the 2-D or 3-D position of the wireless tag. These systems have been used for industrial applications such as assembly line/automation, commercial asset tracking applications (airports), and also healthcare applications for tracking personnel and assets in a hospital. A recent push has been to develop CMOS ultra-wideband transceivers which comply with the IEEE 802.15.4a specification utilizing binary shift keying for digital modulation [64]-[66]. This reduces power consumption and size of the tag, opening up many new applications for ultra-wideband.

1.3 Contributions

Many people have contributed to this work including Drs. Cemin Zhang and Brandon Merkl who graduated in 2008, Dr. Depeng Yang who graduated in 2011, Gary To, Jonathan Turnmire, Essam Elkhouly, and Nathan Rowe. The material presented in this dissertation integrates the ingenuity, dedication, and thoughts of this team as a whole. Within this broader context, my contributions to this greater work are outlined here. My contributions cover a disparate range of topics including system-level simulations, NLOS detection and mitigation, characterizing the UWB OR channel, and multi-tag access with associated experimental analysis. These contributions are outlined as follows:

- Development of a system-level simulation framework using Matlab and ADS to analyze the performance of the UWB indoor positioning system and to characterize various sources of error including clock jitter and drift and multipath interference (Chapter 6). Simulation results are compared with experimental results. The effects of the indoor channel are quantified using the IEEE 802.15.4a channel model for both LOS and NLOS environments.

- Experimental analysis of NLOS detection and mitigation (Chapter 9 and Chapter 10) using the UWB Multi-Tag Development Platform outlined in Chapter 7. This includes FPGA-based SNR calculations and C++ software integration for LOS/NLOS detection and mitigation with discussion of the effects of NLOS and low SNR channels on the TDOA-based UWB Multi-Tag Development Platform.
- Characterizing the operating room channel for UWB signal transmission (Chapter 4). This includes frequency domain and time domain experiments with fitting of the experimental results to the IEEE 802.15.4a channel model. This includes implications of the UWB operating room channel on UWB indoor localization systems. Experimental results and analysis of electromagnetic interference in the operating room is included in the operating room channel characterization.
- Development of the UWB Multi-Tag Development Platform (Chapter 7). This includes an integrated tag design with DC power board, RF board, and 2.4 GHz digital communication link. Ten integrated tags are functional and have been tested to successfully operate in the UWB positioning system outlined in Chapter 7. The multi-tag functionality is integrated into the base station and control station FPGA digital signal processing and also the C++ real-time software application.
- Experimental analysis of the UWB Multi-Tag Development Platform (Chapter 8). This includes 3-D dynamic experiments with one and two tags. This also includes an analysis on the dynamic 3-D accuracy of four base station TDOA versus five base station TDOA.

1.4 Organization

Chapter 2 provides a broad overview of wireless technologies applied to medical applications. This includes available frequency bands, microwave interaction with biological tissues, wireless positioning systems for medical applications, and digital communication systems for medical applications including *in vivo* operation and wireless sensor networks.

Chapter 3 discusses current tracking technologies used in orthopedic surgical navigation including infrared tracking systems and low frequency electromagnetic tracking systems. The potential use of millimeter accuracy indoor UWB localization is then discussed within the context of its application to orthopedic surgical navigation. As discussed in this chapter, if the 3-D accuracy of the indoor UWB localization system can be reduced to 1-2 mm, the indoor UWB localization system can be used both intra-operatively and post-operatively in orthopedics. UWB localization technology can be applied to computer assisted surgery outside orthopedics including neurosurgery and many other surgical fields.

Chapter 4 discusses wireless signal propagation in hospital environments. The first discussion is on a Matlab simulation of an ASK 315 MHz transmitter and receiver used within the operating room with focus on multipath effects, pathloss, and operating range. Next, UWB indoor channels are examined including the indoor channel properties of the operating room measured experimentally in the frequency and time domains. This data is fit to the IEEE 802.15.4a channel model. Experimental measurements of electromagnetic interference in the operating room are also provided. Finally, a simulation is undertaken to examine the effects of IEEE 802.11a 5.8 GHz signals on the indoor UWB positioning system.

Chapter 5 discusses the 1st generation indoor UWB positioning system which was a starting point for much of the work presented in this dissertation. The architecture of the 1st generation system is presented as well as a few select experimental results. Limitations of the 1st generation system are also outlined to provide motivation for introducing the 2nd generation system in Chapter 7.

Chapter 6 discusses a system-level simulation framework for UWB localization. The simulation framework is applied within the context of the indoor UWB localization system outlined in Chapter 5. Simulation results are compared with experimental results for different types of indoor environments. Various ranging algorithms are tested for their performance in indoor environments.

Chapter 7 focuses on the development of the second generation UWB positioning system. An integrated tag which uses a 2.4 GHz MSK Zigbee-like approach is outlined and termed the UWB Multi-Tag Development Platform. Ten integrated tags are constructed, and their integration into the high accuracy indoor localization system is discussed. Challenges associated with the UWB Multi-Tag Development Platform are also outlined including system clock jitter, phase center error, system clock drift, dynamic scaling effects, and cable length offsets. Finally, the future use of MMIC integrated UWB RF front-ends for both the transmitter and receiver is discussed.

Chapter 8 presents an experimental analysis of the UWB Multi-Tag Development Platform outlined in Chapter 7. This includes dynamic experiments with one and two tags. Four base station and five base station experiments are provided to analyze the effect of having an extra base station for the TDOA calculation. An analysis of observed errors is provided. Future work is discussed including IMU integration and experiments with a four monopole UWB probe.

Chapter 9 outlines digital signal processing algorithms, the UWB receiver, and subsequent processing of data on a computer. This includes analog-to-digital conversion of the received UWB pulse as well as FPGA-implemented peak detection, leading-edge detection, noise estimation, and SNR calculation. The RS-232 link to the computer is also discussed including the need for different UWB operating modes on the computer for different system states (four base station, four base station with SNR link information, five base station, five base station with link information). An adaptive algorithm for low SNR and NLOS conditions is also outlined with associated simulation results.

Chapter 10 focuses on NLOS detection and mitigation using the SNR link information discussed in Chapter 9. The focus is on experimental setup and analysis of NLOS link conditions and techniques implemented in software to detect and mitigate the errors associated with having one or more NLOS links when performing TDOA for 3-D positioning. The next generation multi-tag system outlined in Chapter 7 and Chapter 8 is used in this NLOS detection and mitigation experimental analysis.

Chapter 11 focuses on future work and the endeavor to achieve sub-millimeter 3-D accuracy. The focus is on challenges limiting the currently achievable accuracy which include system clock jitter and drift, phase center uncertainty and variation, local oscillator phase noise, multipath interference and NLOS conditions, and sample rate limitations. A path forward is proposed which includes system-level simulations to analyze error sources combined with system enhancements such as low phase noise dielectric resonator oscillators and high stability crystals. Finally, experimental testing of the system in the operating room is needed to provide quick feedback and testing of new system enhancements.

Chapter 12 provides a high level discussion of topics covered within this dissertation and concludes with future work.

2. Wireless Technologies in Medicine

Wireless technologies have found many applications in the medical field. Varshney describes current and future uses of various wireless technologies for medical applications including intelligent mobile emergency response systems, ad hoc networks combined with WLANs for patient monitoring both inside and outside the hospital, the use of smart phones and other portable devices equipped with 802.11 WLAN technology for telemedicine applications (i.e. everyday hospital use such as downloading daily schedules, patient information, etc.), and indoor tracking of assets, personnel, and patients through Differential GPS or RFID technology [67]. Pattichis et al. gives a comprehensive overview of the wireless technologies used in telemedicine as well as an overview of systems deployed by various research groups to test the effect of telemedicine in various clinical settings for transmission of electrocardiograph, blood pressure, temperature, medical images, and other relevant signals for applications such as remote monitoring, teleradiology, and emergency care [68]. The continued advancement of modern day telecommunication systems has allowed new methods of surgical instruction, such as international telementoring, where a mature surgeon can guide and teach practicing surgeons new operative techniques through video streaming, medical robots, and high bandwidth digital communication, to be successfully used in specialized international surgical procedures [69]. Finally, the use of implantable *in vivo* sensors which utilize a telemetry system to transmit data from the body have become more common with advances in science and technology. For example, Bergmann et al. measured *in vivo* contact forces and temperatures in the proximal femoral implant of a THA using an inductive telemetry system which takes high voltage signals (e.g. 50 Vpp) at low frequencies (e.g. 3.5-4.5 kHz) and wirelessly transmits the digital information via induction coils [70],[71]. Evans and To have done extensive simulation, design, and experimental testing of MEMS capacitive pressure sensors and microcantilever technology for recording a pressure map of the knee stresses on the spacer block used in a TKA incorporating RF telemetry in the 315 MHz and 433 MHz bands [72],[73]. Reagan extended this sensor technology for *in vivo* use by embedding the sensors in a parylene coating for placement inside the polyethylene insert of a TKA and optimizing sensor performance for *in vivo* loading, which allows pressure mapping of the knee stresses on the femoral condyles [74].

2.1 Medical Frequency Bands

Wireless medical devices, for both positioning and communication, have stringent requirements on the frequency bands in which they can operate. Table 2-1 highlights the different bands both in the United States and Europe which can be used for indoor medical applications for both narrowband and UWB applications. UWB has available frequency bands from 3.1 – 10.6 GHz and 22 – 29 GHz in the U.S. Only portions of that 3.1 – 10.6 GHz band are currently available in Europe. A number of telemetry bands exist in the U.S., and both the U.S. and Europe have instrumentation, scientific, and medical bands available, mainly in the 300 MHz to 3 GHz range. As shown in Table 2-1, *in vivo* telemetry applications typically use bands in the RF and lower microwave frequency range for operation (i.e. 315 MHz, 402 – 405 MHz, and up to 1427 – 1432 MHz in the United States while Europe uses 433.05 – 434.79 MHz and 868

– 870 MHz). In order to understand why telemetry bands are not allocated above 1.43 GHz, it is necessary to look at the complex permittivity of human tissues as done in Section 2.2. The UWB positioning system operates from 5.4 – 10.6 GHz in the upper region of the 3.1–10.6

Table 2-1: Summary of licensed medical wireless frequency bands.

Location	Frequency Band	Frequency (MHz)
U.S.	Medical Implant Communications Service	402 - 405
U.S.	Wireless Medical Telemetry Service	608 – 614 1395 – 1400 1427 - 1432
U.S.	ISM	315 902 – 928 2400 – 2483.5 5150 - 5875
Europe	ISM	433.05 - 434.79 868 - 870 (short-range) 2400 - 2483.5
U.S.	UWB	3.1 – 10.6 GHz 22 – 29 GHz, center freq > 24.075 GHz
Europe	UWB	4.2 – 4.8 GHz 6 – 8.5 GHz 3.4 - 4.2 GHz **Pending**

GHz band while most wireless telemetry systems for *in vivo* use operate at 433.92 MHz in the 433.05 - 434.79 European ISM band and at 315 MHz for the U.S. ISM band. As shown in Figure 2-1, the allocated band in the United States goes from 3-10.6 GHz at a power level of -41.3 dBm/MHz. Compared to Europe, where the power level is required to be at -71.3 dBm/MHz from 4.8-6 GHz, -65 dBm/MHz from 8.5-10.6 GHz, and can only be at -41.3 dBm/MHz from 3.4-4.8 GHz if detect and avoid circuitry is implemented to minimize interference with other wireless systems operating in this band. Figure 2-2 compares the UWB bands in Japan versus

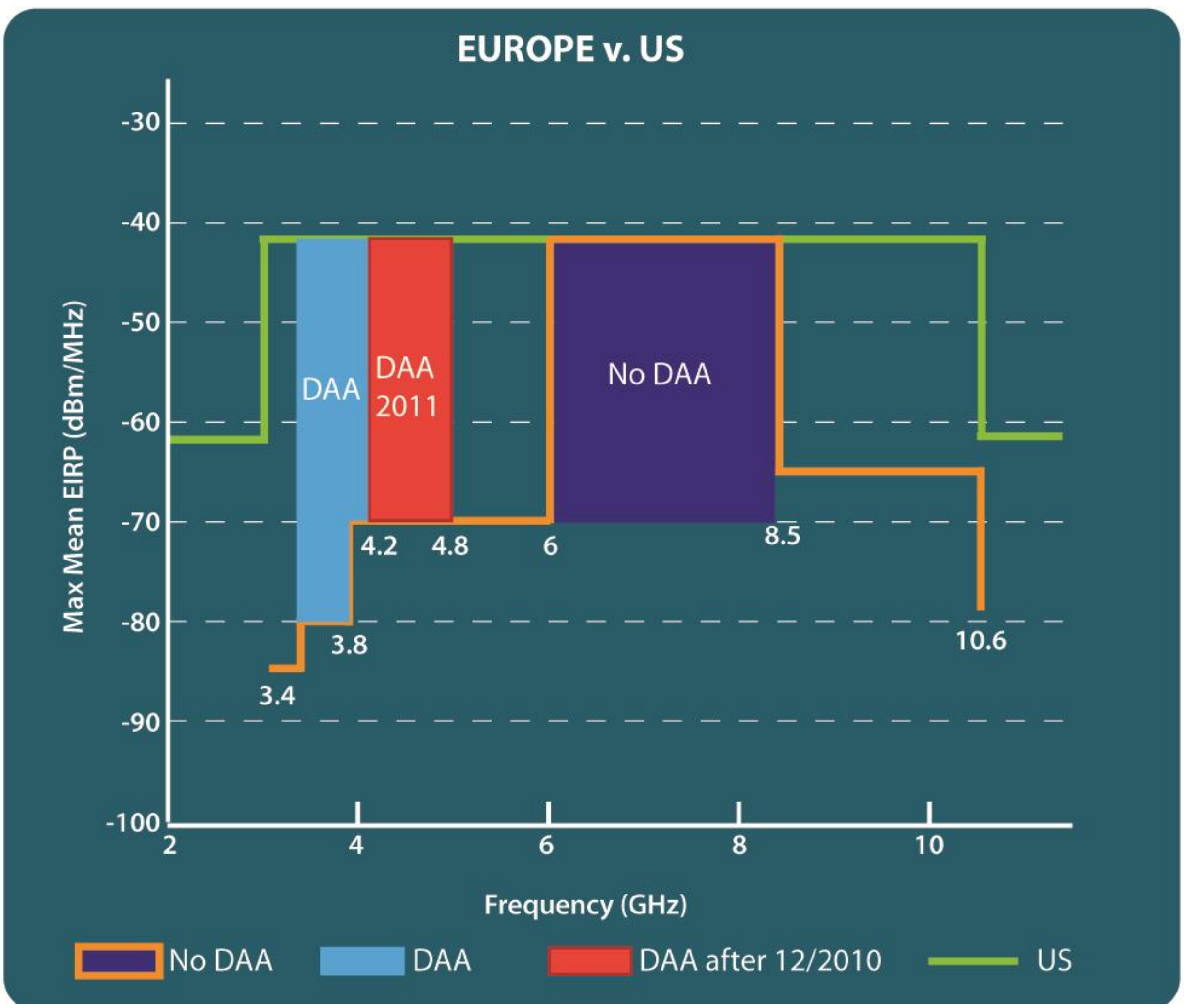

Figure 2-1: Comparison of allocated UWB bands between 3-11 GHz in the U.S. versus Europe.

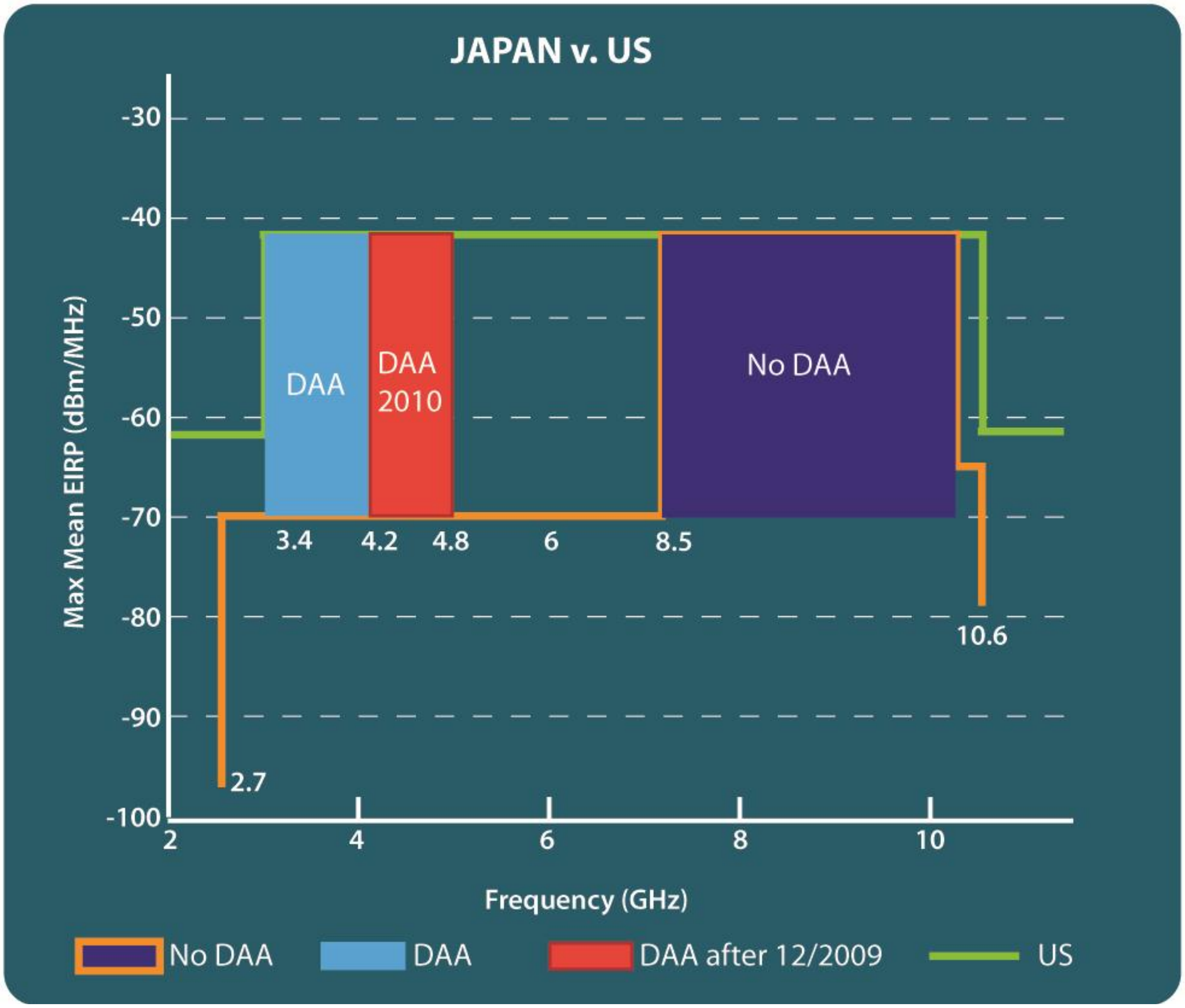

Figure 2-2: Comparison of allocated UWB bands between 3-11 GHz in the U.S. versus Japan.

the United States. Similar to Europe, the Japanese regulations also require DAA in the 3.4-4.8 GHz band. The main difference between the European band and the Japanese band is in the no DAA band: in Europe, this exists from 6-8.5 GHz while in Japan, this band goes from 8.5-10.6 GHz. From looking at Figure 2-1 and Figure 2-2, it is clear that the various restrictions imposed around the world make designing one system for worldwide operation difficult to impossible. Multiple variations of a system may be needed to meet the various worldwide regulations.

2.2 Microwave Interaction with Biological Tissues

The electrical characteristics of biological tissues change dramatically from DC through higher frequencies such as X-ray and gamma radiation. At very low frequencies (the kHz range), the primary means through which electrical current travels through the body is conduction via the extracellular matrix. At the visible frequency range and even higher in ultraviolet and X-ray frequency ranges, most electromagnetic waves are able to pass through biological tissues, with differing amounts of energy being absorbed by different tissues. Between these two extremes lie the RF/Microwave frequency bands. Electrical properties of biological tissues change dramatically over this frequency range. There are specific techniques, such as coaxial probe dielectric measurements, which can be followed to apply a uniform method for electrical characterization of biological tissues (or other lossy media) over this frequency range.

RF/Microwave radiation is considered from 100 kHz – 30 GHz [75]. Although the interaction of radiation with biological tissues changes significantly over this range, there are some similar properties that provide coherence for grouping RF/Microwave frequencies together. First, over this whole frequency range radiation can be considered non-ionizing. Ionizing radiation includes UV and X-ray, and these frequency ranges are characterized by disruption of atomic structures. Second, it is convenient and useful to use RF/Microwave frequencies for the purpose of radiating electromagnetic energy. At low frequencies and extremely low frequencies, the wavelength of the transmitting signal is much larger than the structures used in transporting it. Radiation at LF and ELF is not typically seen. Conversely, the wavelengths in the RF/microwave range are comparable to their corresponding transmission lines (millimeter to meter in size), which makes them ideal for radiation applications.

The RF/microwave frequency range has already been well researched and has many current uses in the medical field. Current successful applications include benign prostatic hyperplasia, endometrial ablation, cardiac ablation, microwave assisted balloon angioplasty, and localized hyperthermia [75]. One of the more recent applications is in radiometry (a device used to measure low power EM radiation). The radiometer can be used both to measure the temperature distribution of biological tissues as well as to monitor hyperthermia systems [76]. Central to designing any of these systems is a thorough understanding of the electrical properties of the tissues that will be exposed to the EM energy. An enormous amount of research has been done in this area. This has included use of a wide range of measurement techniques, testing on many different types of animals as well as humans, and testing of biological tissues in different environments (e.g. *in vivo*, *in vitro*, over a range of temperatures, etc.).

2.2.1 Complex Permittivity

The complex permittivity is a common method used to characterize the electrical properties of an arbitrary medium. Combined with other electrical parameters, such as conductivity and skin depth, it can be used to provide complete electrical characterization. (2-1) shows the basic definition of complex permittivity

$$\varepsilon^* = \varepsilon' - j\varepsilon'' \quad (2\text{-}1)$$

where the first term, ε′, represents the capacitive nature of the tissue (i.e. amount of charge stored in it) while ε″ characterizes the lossy nature of the medium. Using these two terms, it is possible to calculate α and β, which can then be used to characterize how an EM wave behaves inside the medium [77]. (2-2) and (2-3) show this process.

$$\alpha = \frac{2\pi}{\lambda_o}\sqrt{\frac{\varepsilon^{'}}{2}(\sqrt{1+tan^2\delta}-1}$$
$$\beta = \frac{2\pi}{\lambda_o}\sqrt{\frac{\varepsilon^{'}}{2}(\sqrt{1+tan^2\delta}+1} \tag{2-2}$$

$$E(z) = E_0 e^{j\omega t-(\alpha+j\beta)z} \tag{2-3}$$

Finally, once the electrical field is known, the power dissipated through the region is

$$P = E(z)^2\sigma \tag{2-4}$$

assuming the conductivity σ of the medium is known combined with (2-3). This shows the usefulness in knowing the complex permittivity and how it can be used to characterize radiation in an arbitrary medium. The electrical losses can be attributed to both ionic conduction and dipole rotation [78].

$$\varepsilon" = \varepsilon"_d + \varepsilon"_c \tag{2-5}$$

The standard technique to model the complex permittivity for an arbitrary material is through the Cole-Cole equation

$$\varepsilon(w) = \varepsilon_\infty + \frac{\Delta\varepsilon}{1+(j\omega\tau)^{1-\alpha}} \tag{2-6}$$

where there is a dispersion peak in the loss factor whose size and place depends on the relaxation time, τ, and dispersion factor α. Figure 2-3 shows typical curves for the complex permittivity of human tissues as modeled through the Cole-Cole equation (2-6) [79]. A multi-

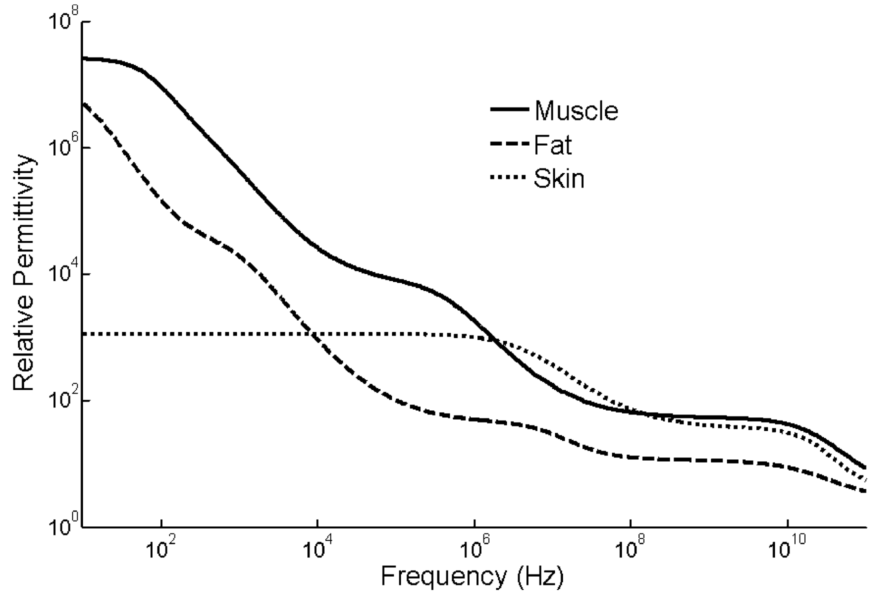

(a)

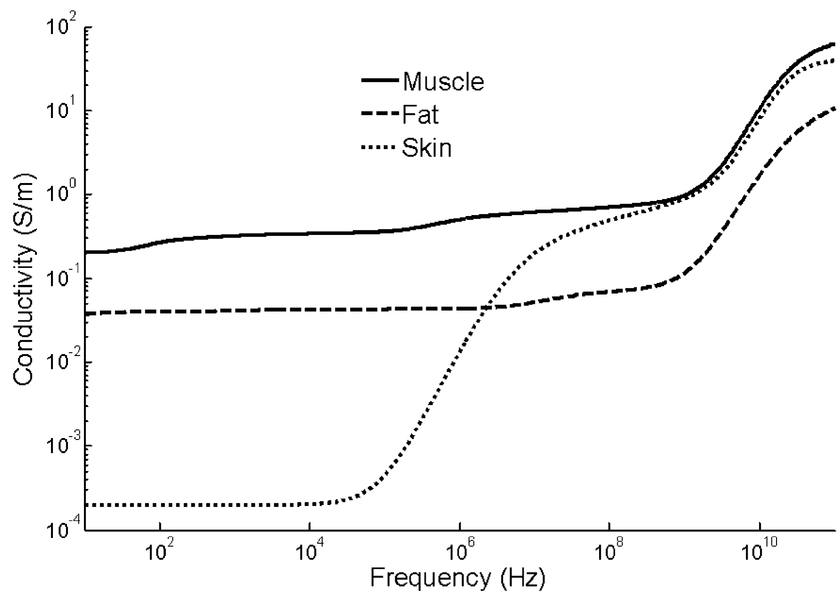

(b)

Figure 2-3: Electrical properties of human muscle, fat, and skin at 37°C. (a) relative permittivity, (b) conductivity.

peak Cole-Cole equation (2-7) is used by Gabriel et al. and allows a parametric model for complex permittivity to be established where multiple dispersion peaks and relaxation times are taken into account [79].

$$\varepsilon(w) = \varepsilon_{\infty} + \sum_{i=1}^{4} \frac{\Delta \varepsilon_i}{1 + (j\omega\tau_i)^{1-\alpha_i}} + \frac{\sigma_{ionic}}{j\omega\varepsilon_0} \tag{2-7}$$

The loss factor in an arbitrary medium (i.e. ε″) is due to both ionic conductivity and dipole rotation, and dipole rotation is the primary means through which losses occur over the RF and microwave frequency range. The various losses experienced through the microwave frequency range are shown in Figure 2-4. The temperature increases the ionic conductivity, which is the main reason the loss factor tends to increase with increases in temperature over the lower microwave frequency range (DC – 1 GHz) [78]. Above 1 GHz, the effects due to ionic

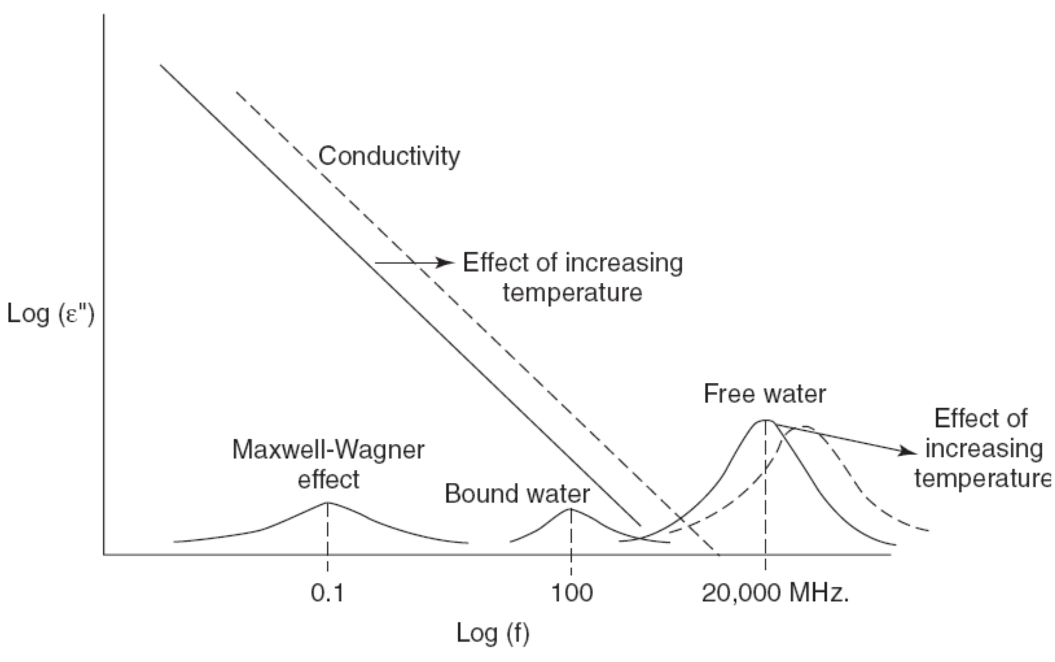

Figure 2-4: Water and temperature effects on the loss factor [78].

conductivity lessen, and the loss factor is primarily due to dipole rotation (or free-water dispersion). This has the effect of decreasing the loss factor of water-based tissues, at least over the range of 3 – 17 GHz, with increase in temperature. Figure 2-5 shows how changes in temperature affect both ε′ and ε″ for water over a range of frequencies and temperatures [78]. As Figure 2-5 shows in a qualitative sense, over the microwave frequency range of interest (3-17 GHz), increases in temperature tend to decrease ε′ by an almost consistent amount (decrease of ~8 for an increase in temperature of 25°C) and also tend to decrease ε″. Since most biological

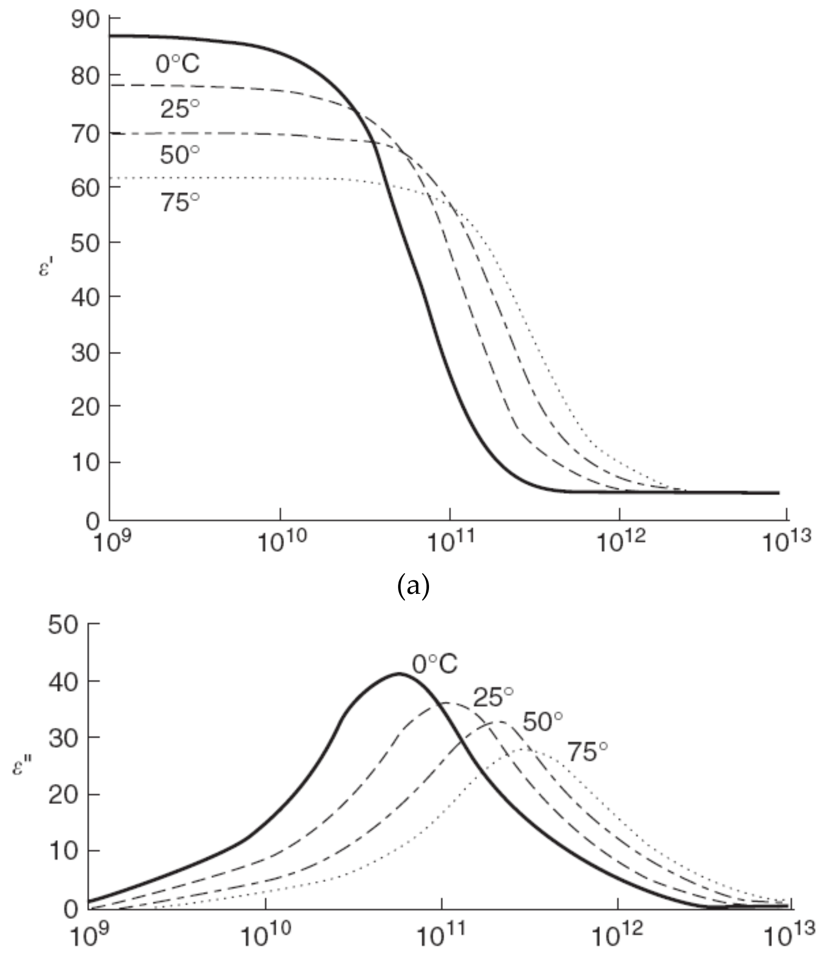

(b)

Figure 2-5: Effects of temperature on complex permittivity of water: (a) ε′, (b) ε″ [78].

tissues, especially muscle and liver, are highly water-based, they tend to follow similar trends for variation of complex permittivity over a range of temperatures. The change in complex permittivity of water is mostly due to the change in viscosity that occurs in water for varying temperatures. For example, a 32.4% decrease in viscosity of water is observed when going from 20°C to 37°C. This causes a decrease in the relaxation time τ of approximately 38.2%.

2.2.2 Coaxial Probe

Although there are a number of methods for measuring the complex permittivity of different materials, only a few of these techniques work for biological tissues. This is due to the relatively high ε′ and ε″ seen in most biological tissues. Because the complex permittivity of most tissues is several factors larger than that of air, higher order modes of propagation exist within the tissue when using transmission measurement techniques such as waveguides or free space antennas. The measurement technique best suited for measuring the complex permittivity of high loss materials is the coaxial probe. This is a technique that has been widely researched in literature. Throughout the 1970s many studies were undertaken to measure the complex permittivity of different biological tissues with a coaxial probe. Athey et al. did extensive testing on a live feline [80]. They used a complex capacitance model for the probe and obtained good results for skeletal muscle, smooth muscle, liver, kidney, and spleen. Pethig provided an excellent review of what had been done in literature on various types of tissues for both animals and humans [81]. Finally, Gabriel et al. did an exhaustive review on previous work done in literature over the whole spectrum of biological tissues which included work done on animals

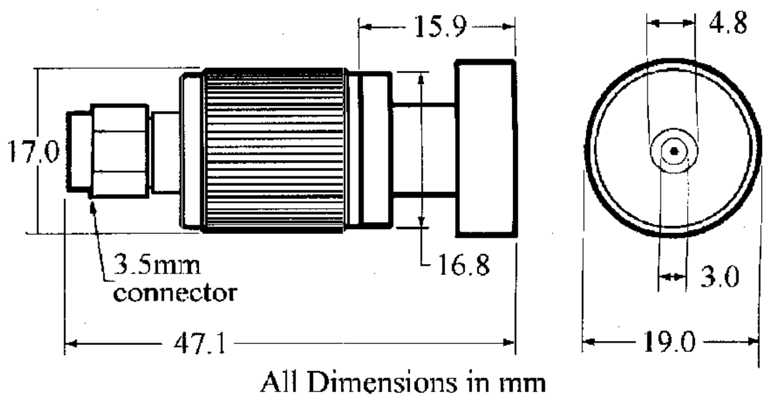

Figure 2-6: Agilent 85070D coaxial probe [84].

and humans [82]. Most of the initial work went from radio frequencies to 10 or 20 GHz, although more recently, with the advent of vector network analyzers with higher frequency ranges, people have been able to extend measurements up to 110GHz [83]. A dielectric probe is depicted in Figure 2-6 [84]. It can operate over a frequency range of 200 kHz–20 GHz and a temperature range of -40 °C to 200 °C. It maintains an error of ε_r' ±5% and tanδ ±0.05 over these ranges. Coaxial probe measurements of biological tissues are discussed in [85].

2.3 Positioning Systems

In terms of current technologies used for indoor localization in hospital environments, commercial systems are available which use Wi-Fi, received signal strength, RFID, ultrasound, and UWB. Clarke et al. ran an experiment where these five systems were tested in multiple locations inside an operating room and compared for their performance in 3-D indoor localization [86]. As shown in Figure 2-7, UWB performed orders of magnitude better than the other technologies with RF localization being the only other one to consistently localize points with even sub-meter accuracy [86]. Signal strength, Wi-Fi, and RFID systems all suffered from multipath effects given their narrowband nature while the ultrasound system only reported the nearest distance from the transmitting tag to the nearest receiver, so it was not able to report 3-D position values at all. This experiment shows in a quantitative manner how UWB localization systems can obtain better 3-D localization results than other wireless technologies in medical indoor environments using LOS signals. Time Domain Corp. offers the PLUS® RTLS for indoor asset tracking solutions, utilizing UWB operating at a center frequency of 6.6 GHz with around 1 GHz bandwidth and an operating range near 50 m [63]. Figure 2-8 shows the use of the PLUS® RTLS for asset tracking in a hospital environment [87]. This allows tracking of patients, staff, and medical equipment which can be used to optimize workflow processes and provide better management of these different assets.

The development of the IEEE 802.15.4a standard for LDR WSNs has resulted in a substantial amount of research and development on UWB CMOS transceivers [65],[66] which comply to the standard. Startup companies have also begun to appear (DecaWave), integrating an IEEE 802.15.4a transceiver with RTLS, giving LDR communication (110 kbps to 6.8 Mbps), high location accuracy (10 cm), and large operating ranges (up to 500 m indoor LOS and up to 45 m indoor NLOS) [64]. The use of these WSNs for sensing, LDR communication, and positioning make them an excellent candidate for a wide variety of applications including telemetry of bodily vital signs in BANs, which can be extended into PANs, process optimization in logistics and manufacturing, emergency services, military, and high security (assuming proper measures are taken on the network layers above the UWB physical layer).

The push taken by DecaWave in utilizing CMOS technology for ultra-low power UWB transceivers which comply to the IEEE 802.15.4a standard, are compact in size (a 4.5 mm x 4.5 mm ball grid array), work in NLOS conditions, and can be used for high accuracy localization, is a good summary of the current momentum in research for UWB positioning integrated with WSNs.

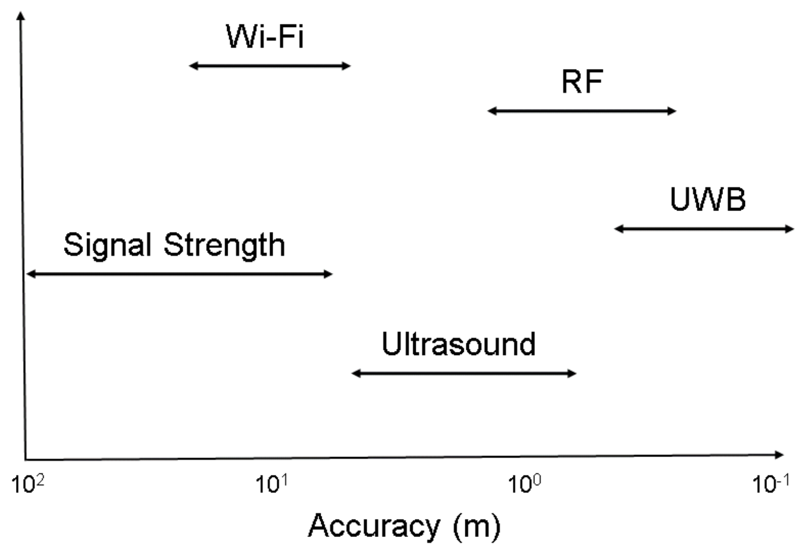

Figure 2-7: Accuracy of indoor localization systems in OR [86].

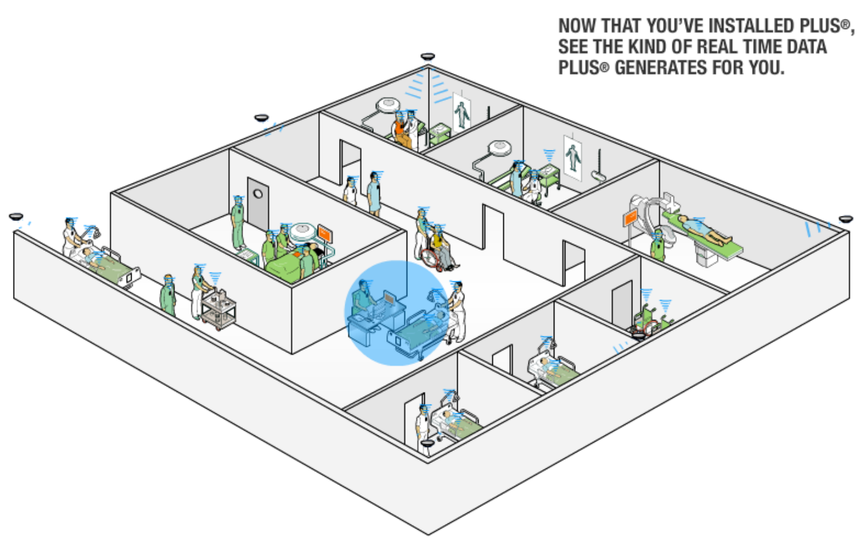

Figure 2-8: PLUS® RTLS from Time Domain Corp. for asset tracking in a hospital [87].

2.4 Communication Systems

The prevalence of wireless communications systems in medicine has increased significantly in recent years with the pervasive nature of mobile devices, satellites, and computers. There are many wireless technologies that are currently employed in medical facilities including WLAN, cellular telephone technologies (e.g. CDMA-2000, IS-95, etc.), Bluetooth, Zigbee, WiMAX, and various telemetry digital communication frameworks (e.g. frequency shift keying, amplitude shift keying, etc.). As shown in Figure 2-9, the concept of telemedicine is now a reality where video, audio, and even vital signals can be transmitted wirelessly from remote health centers, ambulances, homes, ships, and even intensive care units to relay up-to-date patient information instantaneously for immediate medical assistance [88]. One major push in the area of telemedicine is the concept of personal telehealth, where the patient can take a proactive and autonomous approach in monitoring their health. As shown in Figure 2-10, the Continua Health Alliance is a non-profit, open industry coalition of over 200 healthcare and technology companies promoting an interoperable personal healthcare ecosystem where multiple sensors integrated with various wireless technologies and a network infrastructure allow remote monitoring of the patient's home to monitor various activities including medication tracking, blood sugar levels, blood pressure and heart rate [89]. Given the vast number of applications in medicine for telehealth, wireless sensor networks, and wireless telemetry, the various wireless technologies enabling this communication need to be examined to understand their strengths and weakness. Section 2.4.1 introduces *in vivo* wireless telemetry, Section 2.4.2 looks at the use of Bluetooth in medical sensor and *ex vivo* wireless telemetry, and

Section 2.4.3 introduces UWB digital communication including its integration into wireless sensor networks.

2.4.1 In Vivo Wireless Telemetry

As discussed in Section 2.2, the losses seen when transmitting microwave signals through biological tissues above 1.98 GHz increase dramatically. Therefore, when transmitting wireless signals through tissues, frequencies much less than 1.98 GHz should typically be used. As shown in Table 2-1, ISM bands are available in the United States and Europe which operate at 315 MHz and 433 MHz. These are the ideal frequency bands for *in vivo* wireless telemetry. Figure 2-11 shows a standard ASK transmitter where a baseband digital signal modulates a RF signal operating at either 315 MHz or 433 MHz to transmit digital information. Figure 2-12 shows a MAX1472 (Maxim IC) transmitter connected to a 433 MHz chip antenna (Tricome)

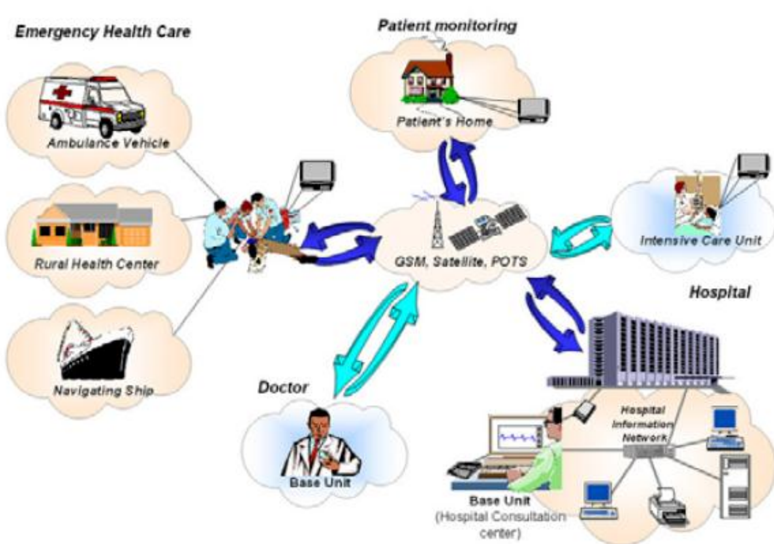

Figure 2-9: Overview of comprehensive telemedicine architecture where wireless technologies enable faster diagnosis and detection inside hospitals, at rural health centers, and from mobile ambulance vehicles [88].

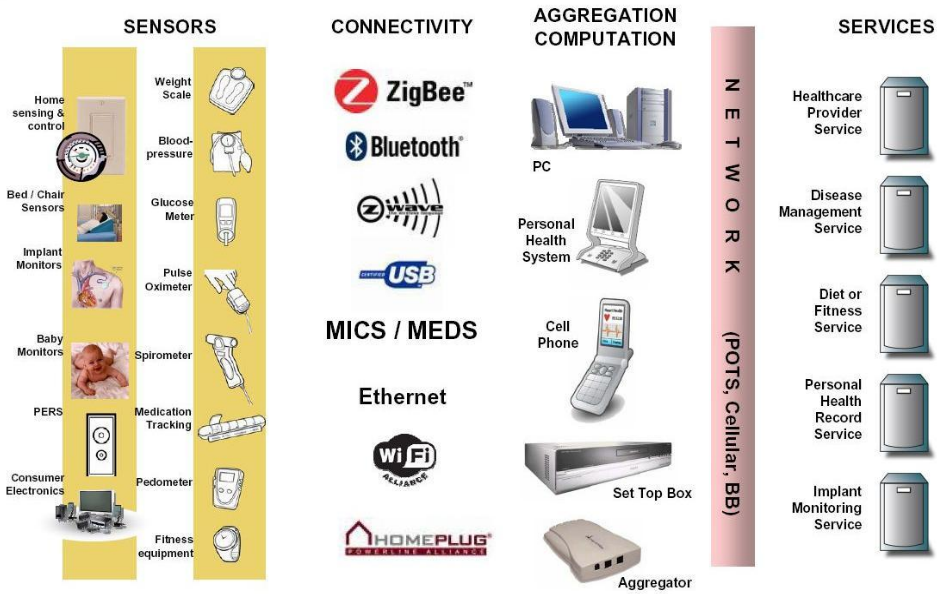

Figure 2-10: Continua Health Alliance personal healthcare ecosystem where various sensors are used to wirelessly and remotely monitor the patient's health including blood pressure, heart rate, etc. [89].

(Tricome) used to transmit pressure data from an *in vivo* sensor in the knee joint in the 433 MHz ISM band. Wireless telemetry from *in vivo* sensors is a promising field which has many applications including embedding sensing systems into orthopedic implants to help monitor for infection as well as overall operation of the joint. Also, 1.4 GHz can be used for short range wireless telemetry applications including knee pressure sensing.

2.4.2 Bluetooth

Bluetooth represents another up and coming technology for *ex vivo* wireless telemetry of digital information in medical sensors. It is one of the wireless technology standards supported by the Continua Health Alliance [89] and is currently integrated into most computers and smart phones. Bluetooth fits into the IEEE 802.15.1 standard for WPANs. The specifications for Bluetooth operation are shown in Table 2-2 where a targeted operating range is 10-100 m with

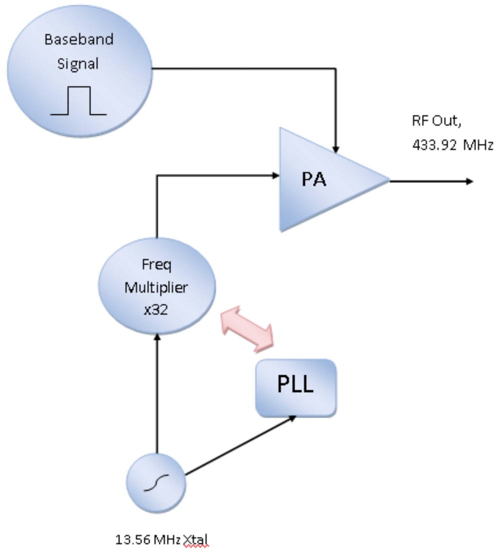

Figure 2-11: Standard ASK transmitter architecture where a digital signal modulates the RF carrier operating at 315 MHz or 433 MHz.

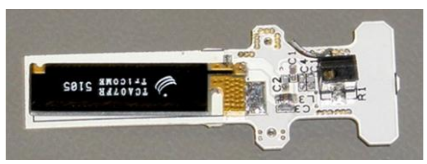

Figure 2-12: Transmitter for *in vivo* wireless telemetry which uses a MAX1472 ASK transmitter operating at 433 MHz connected to a chip antenna to transmit digital information.

data rates of up to 1 Mbps. Compared to the IEEE 802.15.4a standard, which is for ultra-low data rate WPANs, Bluetooth costs more, has added complexity, consumes more power, has a farther operating range (100 m versus 10 m), and can transmit at faster data rates (1 Mbps versus 0.25 Mbps). Bluetooth employs FSK or GFSK. Figure 2-13a shows an example of a WPAN for wireless fitness monitoring while Figure 2-13b shows a WPAN for wireless monitoring of bodily vital signals [90]. Figure 2-14 shows the Avant® 4000 Oximeter from Nonin Medical, Inc. (Plymouth, MN) which is used for wireless monitoring of the oxygen saturation level of a patient's blood for continuous and remote monitoring [91]. Chapter 7 discusses a multi-tag access scheme for UWB localization with a protocol similar to Bluetooth.

2.4.3 Ultra-Wideband and Wireless Sensor Networks

The use of UWB in digital communications has skyrocketed since the Federal Communications Commission's decision to open up the 3.1-10.6 GHz band in the United States in 2002 [4]. The IEEE 802.15.3a task force examined the use of both direct sequence spread

Table 2-2: Bluetooth specifications.

Frequency	Data Rate	Operating Range	Modulation Type
2.4-2.483 GHz	Up to 1 Mbps	10-100 m	FSK,GFSK,MSK

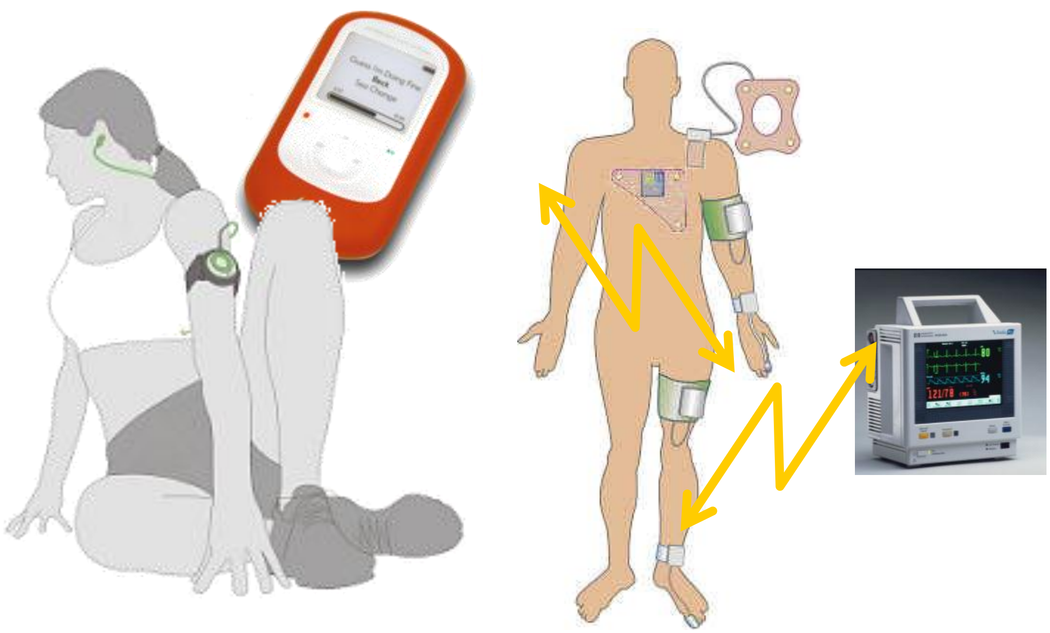

(a) (b)

Figure 2-13: WPANs for a) wireless fitness monitoring, b) wireless monitoring of vital data [90].

Figure 2-14: Avant® 4000 Oximeter from Nonin Medical, Inc. (Plymouth, MN) for wireless, remote, continuous monitoring of oxygen saturation level in blood utilizing Bluetooth technology [91].

spectrum and MB-OFDM for high data rate (e.g. 480-1100 Mbps), short range wireless communication. MB-OFDM utilizes frequency division multiplexing by allocating 500 MHz bands through the 3.1-10.6 GHz UWB spectrum. With up to 14 separate bands, the symbols are transmitted by utilizing multiple frequency bands where quadrature phase shift keying is the underlying modulation technique in conjunction with frequency division multiplexing. Table 2-3 shows the specification for high data rate UWB digital communication with an operating range of 10 m and data rates as high 1100 Mbps. Figure 2-15 shows the chipset from Wisair which utilizes MB-OFDM in the 3.1-4.8 GHz band for high data rate UWB digital communication up to 1100 Mbps for applications including transmitting video signals [92]. Low data rate UWB applications also exist mostly in the area of wireless sensor networks which comply to the IEEE 802.15.4a standard. These devices are especially appealing since they can be compact in size, offer data rates of greater than 1 Mbps, and provide a method for high accuracy localization. DecaWave has a new RTLS which utilizes a UWB CMOS transceiver in an ad-hoc network approach which adheres to the IEEE 802.15.4a standard, giving low data rate

Table 2-3: UWB specification for high data rate digital communication.

Frequency	Data Rate	Operating Range	Modulation Type
3-10.6 GHz	480-1100 Mbps	3-10 m	MB-OFDM

Figure 2-15: Wireless USB is now a certified technology which utilizes UWB MB-OFDM for high data rate digital communication. Commercial chipsets and products are available, including the CMOS chipset from Wisair which is commercially available in a range of products [92].

communication (110 kbps to 6.8 Mbps), high location accuracy (10 cm), and large operating ranges (up to 500 m indoor LOS and up to 45 m indoor NLOS) [64].

3. Ultra-Wideband Positioning and Orthopedic Surgical Navigation

In modern day health care, orthopedics is defined as the branch of medicine which deals with diseases and injuries to the musculoskeletal system of the human body. Central to the musculoskeletal system are the joints in the human body including the knee, hip, ankle, spine, elbow, shoulder, jaw, etc. As mentioned in [93], the advent of the orthopedics industry happened late in the 19th century in Warsaw, Indiana when Revra DePuy replaced traditional wooden splints with a new and improved metal counterpart. Shortly after, one of his apprentices, Justin Zimmer, formed his own orthopedics company which has grown to become Zimmer, Inc. In 1977, yet another orthopedics company, Biomet, Inc., was formed in Warsaw, Indiana by another group of entrepreneurs, two of which were former Zimmer employees [94]. The orthopedics industry still revolves around Warsaw, Indiana with these three major companies headquartered there. The use of plastics in the orthopedics industry now rivals its need for metals. With full mechanical replacements available for nearly all human joints, the focus of surgery in orthopedics has come to the forefront of the industry. It is estimated that 500,000 knee replacement surgeries will be performed in the United States in 2008 alone with that number projected to increase to as high as 3.2 million total knee surgeries in 2018 [93].

Since a large portion of the money in orthopedics goes to replacement surgeries, it should come as no surprise that a correspondingly large push has been made to utilize technology in improving the outcomes of orthopedic surgeries. CAS has many direct applications in orthopedics due to a combination of factors including the rigidity of bones, the direct biomechanics aspect of the human musculoskeletal system which must be considered when reconstructing a joint, and the obvious potential to include various medical imaging modalities into the mix of technologies utilized in performing an orthopedic surgery. Expanding on the above advantages for incorporation of CAS in orthopedic surgeries, since bones are inherently rigid, tracking systems can be used to intraoperatively track bones with a much greater ease and accuracy than soft tissues (e.g. neurosurgery or abdominal surgery) [95]. Reconstruction of the proper biomechanics of the musculoskeletal system has implications in that certain biomechanical axes and angles must be considered when implanting artificial components in a human joint such as the knee. For example, in the knee, the mechanical axis, which goes from the femoral head through the center of the ankle, must be properly aligned relative to the artificial knee joint to ensure proper functioning of the implanted joint. With the use of intraoperative medical imaging and intraoperative 3-D tracking of the relevant bones, it is possible for computer assistance to be provided to the surgeon to ensure accurate reconstruction of the relevant biomechanical axes and angles. As far as medical imaging modalities are concerned, X-rays, CT, MRI, and fluoroscopy have all been used either preoperatively or intraoperatively in orthopedic surgeries. Fluoroscopy is the most common intraoperative tool while X-rays and CT scans are typically done preoperatively. Next, MRI is much less common in orthopedic surgeries since it is better suited for analyzing soft tissue, although it is commonly used when examining problems related to muscles or cartilage. Finally, ultrasound is not commonly used intraoperatively during orthopedic surgeries due to its inherent noisiness compared to X-rays, CT, and fluoroscopy, but it has certain advantages such as being radiation-free, relatively inexpensive, and able to provide real-time 3-D imaging, which make its application to orthopedic surgery the focus of some current research groups [95].

3.1 Current Tracking Technologies

The fundamental 3-D tracking technologies currently used in CAS for orthopedic applications are optical and electromagnetic tracking systems. Figure 3-1 shows the Polaris Spectra® 3-D optical tracking system from Northern Digital Inc. This optical tracking system is an industry standard which has found wide use in CAS for orthopedics applications including the current push in joint replacement surgeries for small incisions, i.e. minimally invasive surgeries [96]. This optical tracking system works by infrared light being reflected off of the passive markers on the probe (Figure 3-1b) and then being received by two infrared cameras on the receiver shown in Figure 3-1a (essentially two charge-coupled devices which work in the infrared light range instead of the visible light range like a standard digital camera). As discussed by researchers at Northern Digital Inc. in [97], optical tracking systems with passive or wireless probes can obtain comparable 3-D accuracy to active or wired optical probes, although misconceptions are commonly held by users of the 3-D trackers where

(a) (b)

Figure 3-1: Polaris Spectra optical tracking system from Northern Digital Inc. (a) optical receiver, (b) passive optical probe with four reflective markers.

it is thought the use of a passive optical probe reduces the 3-D accuracy of the optical tracking system compared to that of an active optical probe. The rated 3-D accuracy of the Polaris Spectra system is 0.25 mm RMSE for a single marker [97],[98] with 0.233 mm RMSE for 3-D position of a rigid body with active markers and 0.231 mm RMSE for 3-D position of a rigid body with passive markers [97]. The results from [97] prove that with correct usage of the optical tracking system, comparable performance can be achieved with both passive and active markers. The operating range of the Polaris Spectra is 0.950 to 3.000 m out-of-plane distance from the optical probe to the receiver with an in-plane size of 1.856 x 1.470 m^2 at a z-distance of 3.000 m.

The main limitation of the Polaris Spectra is its limited view volume when compared to other optical tracking systems offered by NDI. For example, Figure 3-2 shows the view volume for the NDI Optotrak Certus while Figure 3-3 shows the view volume for the NDI Polaris Spectra. The Optotrak Certus extends 3.8 m in the z-direction and has a large in-plane volume of 2.6 x 3.5 m^2 at its maximum while the Polaris Spectra extends 2.050 m in the z-direction and has an in-plane volume of 1.856 x 1.470 m^2 at its maximum [98],[99]. Consequently, the Optotrak 3020 (precursor to the Optotrak Certus with a comparable view volume) was used in most experimental setups since the UWB receivers needed to be spread out in order to ensure a low PDOP, which is critical in obtaining high 3-D positioning accuracy.

The main advantage electromagnetic tracking systems have over optical tracking systems is their ability to operate in NLOS conditions, whereas optical tracking systems require a LOS signal with the optical receiver. The main disadvantage of electromagnetic tracking systems is their elevated susceptibility to metallic interference. One of the de facto standard systems for electromagnetic tracking in orthopedic-related CAS is the Flock of Birds® system

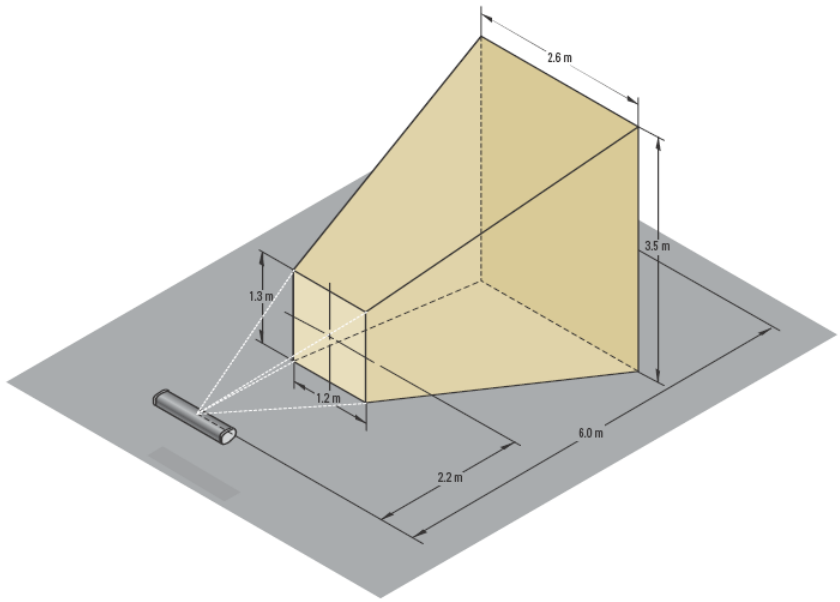

Figure 3-2: NDI Optotrak Certus view volume with 3.8 m in the z-direction and an in-plane area of 2.6 x 3.5 m² at a z distance of 6 m [99].

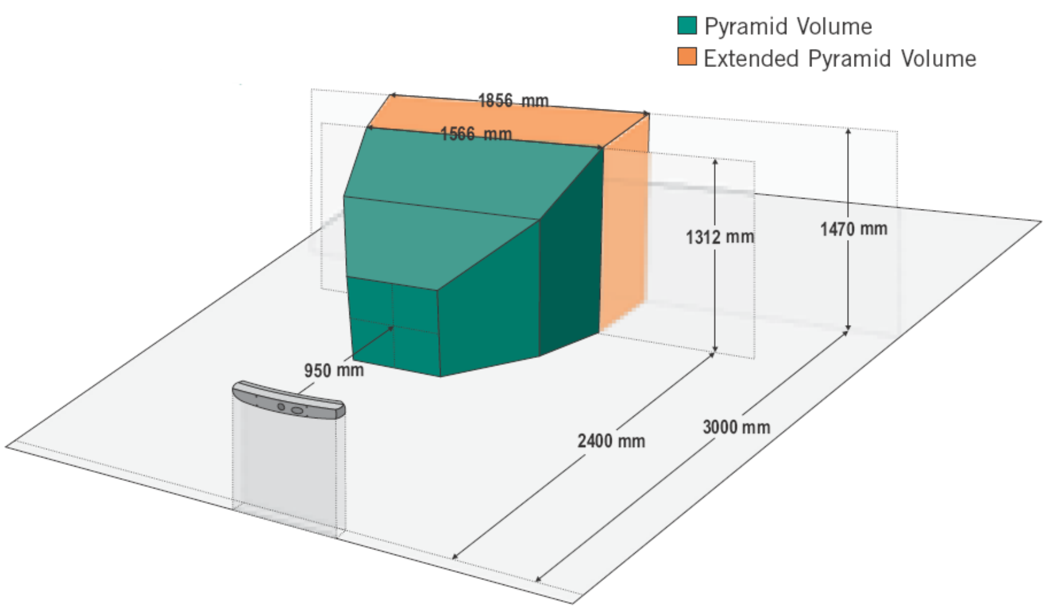

Figure 3-3: NDI Polaris Spectra view volume with 2.050 m in the z-direction and an in-plane area of 1.856 x 1.470 m² at a z distance of 3.000 m [98].

Figure 3-4: Flock of Birds electromagnetic tracking system from Ascension Technology Corporation [100].

from Ascension Technology Corporation. Figure 3-4 shows the Flock of Birds system with the main controller, transmitting coils, and electromagnetic sensors displayed [100]. The 3-D static position accuracy of the system is reported to be 1.8 mm RMSE using the mid-range transmitter over an operating range of 0.203 to 0.762 m from the transmitting coil to the sensor [100]. The system is able to take data at a rate of 144 Hz. The maximum operating range of the system with 1.8 mm RMSE is 0.75 m from transmitting coil to magnetic sensor, noticeably smaller than the operating range of the Polaris Spectra and Optotrak Certus optical tracking systems. Ascension Technology Corporation has another system known as the 3-D Guidance medSAFE tracking system. As shown in Figure 3-5, it uses miniaturized magnetic sensors, with the newest generation of sensors being 0.90 mm in diameter. This small size allows the sensor to be embedded into the tip of a hollow 19-gauge needle [101]. For example, a sensor similar to the one shown in Figure 3-5 is currently embedded into the working channel of a bronchoscope which highlights how these sensors can be used to track catheters and scopes into organs and vessels internal to the human body. These miniaturized sensors have a static 3-D RMSE of 1.4 mm. The medSAFE electromagnetic system is an approved medical device by the Food and Drug Administration for use in the United States and is specified as Class 1, Type CF, Defib Proof [101]. The 3-D tracking systems currently used in CAS for orthopedic applications have certain limitations (e.g. LOS requirement for optical trackers and susceptibility to metal for electromagnetic trackers) but nonetheless have been successfully integrated into commercial orthopedic surgical navigation systems. The UWB indoor positioning system has neither of the shortcomings experienced by these two systems (i.e. LOS limitations or susceptibility to metallic interference). The main challenge with UWB localization technology is consistently achieving accuracy comparable to optical and electromagnetic trackers.

3.2 Overview of Orthopedic Surgical Navigation Systems

With the outgrowth of orthopedic surgery and total joint replacements to so many joints

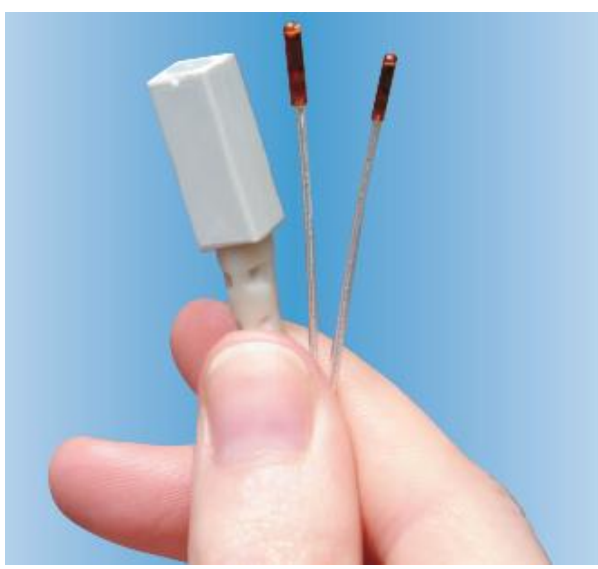

Figure 3-5: Miniaturized magnetic sensors for use with 3-D Guidance medSAFE electromagnetic tracking system from Ascension Technology Corporation [100].

in the human body (e.g. ankle, knee, hip, spine, elbow, wrist, shoulder, jaw, etc.) and with multiple surgical approaches for a single joint, it comes as no surprise that the CAS systems designed to assist in these procedures are themselves a diverse bunch. It is first worth making a few distinctions in how to classify orthopedic surgical navigation systems: passive navigation systems refer to navigation systems which use a 3-D tracking system, e.g. optical or electromagnetic as described in Section 3.1, to track the spatial positions and orientations of bones and surgical tools in real-time during the surgery. A surgeon has complete control of a passive surgical navigation system. An active navigation system has a robot which can make decisions based on sensor (e.g. position or force) feedback and perform autonomous surgical tasks without the assistance of the surgeon. Active systems are not commercially available due to the hesitancy of doctors, hospitals, and engineers to adopt navigation systems which remove the surgeon from wielding control over how the orthopedic surgery is performed [102]. A newer development is a class of navigation systems known as semi-active. In this type of system, a robot is still incorporated into the navigation system, but now the robot is still under the control of the surgeon, and the surgeon is able to utilize the robot in making the surgical cuts needed for the orthopedic surgery. An example of this is the Tactile Guidance System™ from MAKO Surgical Corp., shown in Figure 3-6. This system uses the robotic arm in Figure 3-6 combined with tactile feedback sensing to provide robotic assisted unicompartmental knee resurfacing [103].

A standard orthopedic surgical navigation system can be seen in Figure 3-7. In this CAS system, optical tracking is employed to track both the bones of the patient (by drilling holes and

Figure 3-6: Tactile Guidance System™ from MAKO Surgical Corp. [103].

rigidly attaching optical markers) as well as the surgical tools. The optical trackers must have LOS visibility with the optical receivers in order to be tracked. The final 3-D scene is displayed on the user interface to provide feedback to the surgeon. Multiple tools are tracked simultaneously in order to provide real-time feedback on the tools' positions and orientations relative to the anatomy of the patient. The surgery in Figure 3-7 is a Total Knee Replacement, so the relevant anatomy includes the distal portion of the femur and the proximal portion of the tibia as well as the patella. Figure 3-8 shows a portion of the tools needed in performing a TKR. This includes tibial and femoral cutting guides, spacer blocks for ligament balancing, etc. These tools are used in TKRs whether or not the surgery is done with CAS assistance. Figure 3-9 shows the final goal of orthopedic CAS systems where the patient anatomy, in this case the femur and tibia, are tracked relative to surgical tools such as cutting guides for the femur and tibia. Since the 3-D positions and orientations of all of these rigid bodies are known, it is then possible to automatically calculate relevant surgical axes and angles, such as the mechanical axis of the femur (displayed along with the anatomical axis of the femur and transepicondylar axis). Figure 3-10 shows the Stryker Knee Trac System being used on a cadaver. Optical trackers are rigidly attached to the femoral cutting guide and also to the femur itself. More information on this system can be found in [104].

3.3 Commercial Navigation Systems

In Section 3.2, an overview of the components used in an orthopedic surgical navigation system was presented, including the widespread use of optical tracking, how bones are also optically tracked, and a brief introduction to how custom software is then used to calculate relevant surgical axes and angles and provide real-time feedback to the surgeon on implant placement, where to place the cutting guides, ligament balancing, etc. In this section, different

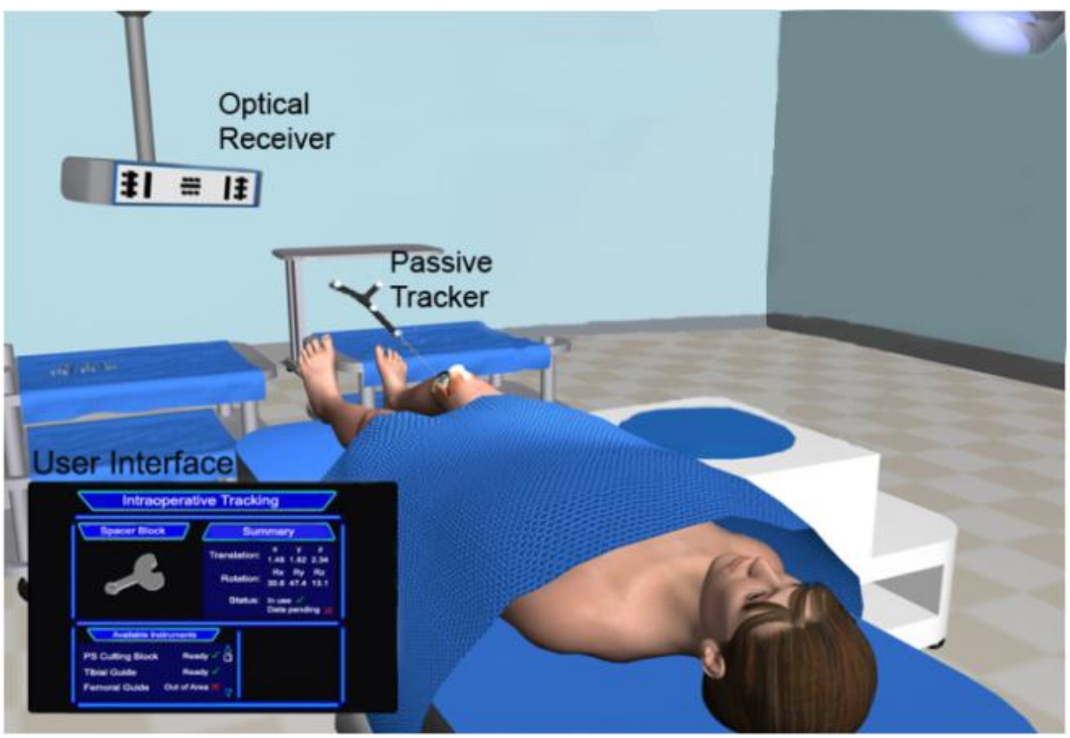

Figure 3-7: CAS system where optical tracking is utilized to assist in a TKR.

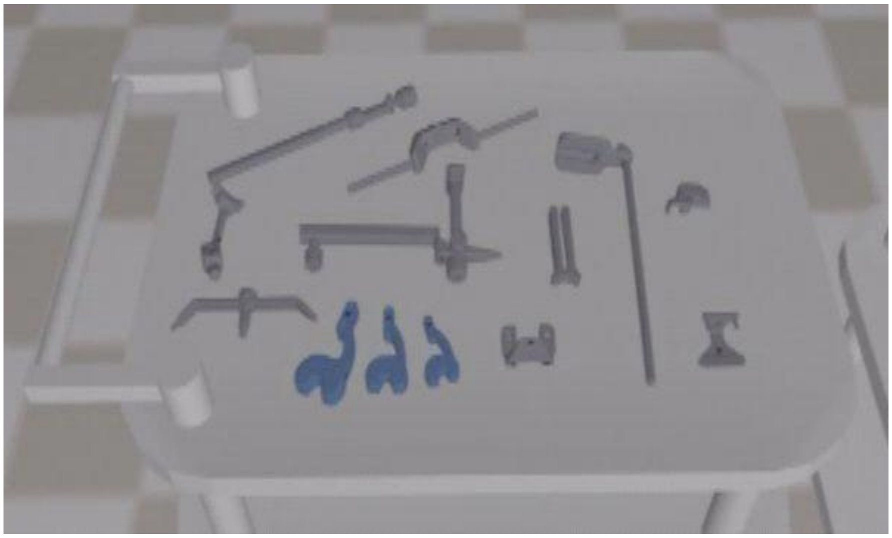

Figure 3-8: Surgical tools used in a TKR including spacer blocks for ligament balancing.

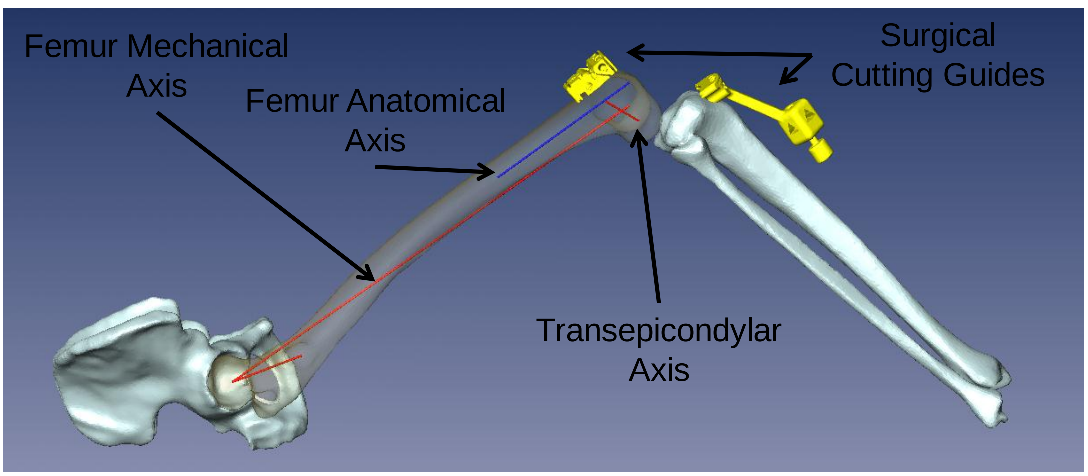

Figure 3-9: Illustration of final goal of intra-operative CAS system where the patient anatomy is tracked (in this case the femur and tibia) as well as the surgical tools. This provides real-time feedback on tool positions relative to surgical axes such as the mechanical axis of the femur.

state-of-the-art orthopedic navigation systems are discussed with the primary goal being to highlight novel technologies, point out inherent strengths and weaknesses in the different systems, and to provide a comprehensive overview of the commercial systems currently deployed in hospitals around the world.

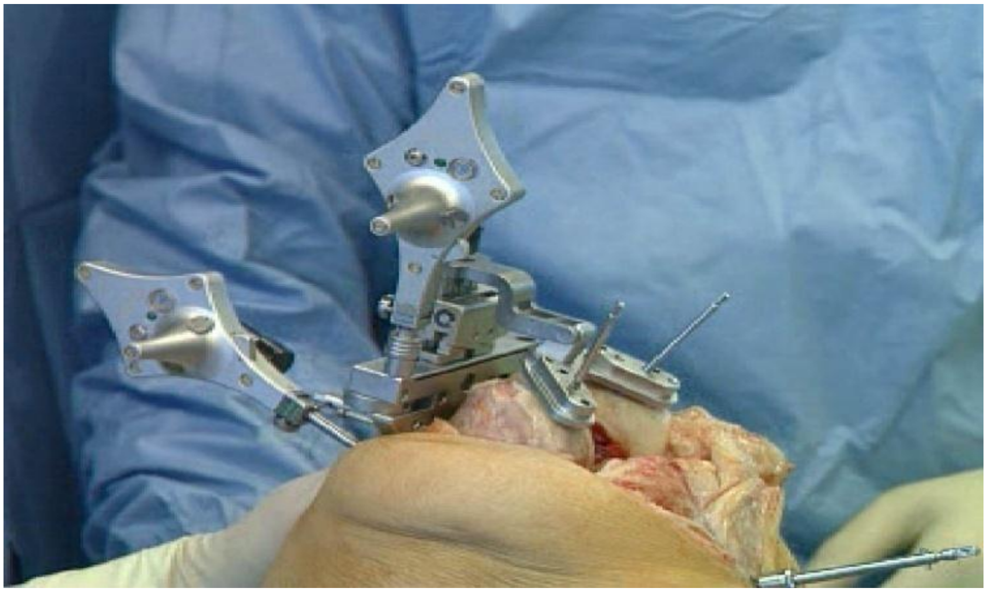
Figure 3-10: Example of a CAS system used in a TKR where optical trackers are attached to the femoral cutting guide and also to the femur itself. Stryker Knee Trac System (imageless).

Although CAS systems in orthopedics have become more widespread over the last few years, there is still controversy over their effectiveness and overall necessity when weighing the costs and benefits of these systems. As discussed in [95], it is still unclear whether the use of CAS in orthopedic surgeries presents clear benefits in terms of overall success of the surgery. For example, a 2003 US NIH Consensus Development Report geared towards TKA concluded that there was some evidence of increased accuracy, but with higher costs and longer surgical times, the overall benefits remained unclear [105]. Also, studies have been done by the Ontario Health Technology Advisory Committee as well as the California Blue Cross. The Ontario committee concluded that navigation and robotic technologies for use in orthopedic surgeries were still in an investigational phase. The California Blue Cross investigated whether or not the increased costs associated with CAS merited reimbursement on the state level. The lack of randomized control trials for the major surgical operations for which CAS systems are targeted, including THA, TKA, and pelvic fracture repairs, caused the California Blue Cross to reach the same conclusion as the Ontario committee and label the use of navigation systems in orthopedic surgical procedures as investigational and not necessary for completing the medical procedures [95]. Therefore, even though orthopedic navigation systems exist and are in use at hospitals today, inherent limitations such as increased surgical time, cost of the navigation systems, lack of substantial evidence in terms of how they help surgical outcomes, etc. continue to place pressure on their usefulness and current design. These limitations are pushing the development of disruptive technologies to bring out a new generation of orthopedic navigation systems which are less invasive, easier to use, more accurate, and provide the surgeon with a greater suite of high technology tools which can be utilized to enhance orthopedic surgical procedures and improve patient outcomes. When looking at commercial navigation systems, the most intuitive approach is to focus on certain orthopedic surgical procedures and then compare the available navigation systems in terms of underlying technologies and overall usefulness to the surgeon. Therefore, TKA and THA procedures are examined and the available navigation systems compared. It should be noted that surgical navigation systems are available for a variety of other surgeries not touched upon here (both orthopedic and beyond) including spine, trauma, and neurosurgery. TKA and THA are focused on because they are the most common orthopedic surgeries. Also, the integration of UWB would first be applied to TKA followed by THA.

3.3.1 Knee Arthroplasty

The available CAS systems for unicompartmental and total knee arthroplasty can be divided into distinct categories including imageless or image-free, CT-based, and more recently intraoperative fluoro-based. The most prevalent type of navigation systems are imageless, where a sequence of steps is needed to identify relevant landmarks across the lower limb including the hip center, ankle center, and medial and lateral epicondyles. Figure 3-11 shows the Medtronic imageless knee navigation system including their patented AXIEM™ electromagnetic sensors for bone tracking and the overall software user interface [106]. The Stryker Knee Trac System, which uses optical tracking and an imageless framework, is shown in Figure 3-12a while the software interface for the BrainLAB VectorVision® System, which can be used both in an imageless framework and also in a CT-based framework, is shown in Figure 3-12b [104,107]. More knee navigation systems exist, including the Navitrak® System from

Figure 3-11: Medtronic knee navigation system highlighting AXIEM™ electromagnetic tracking sensors and software interface for selecting where to make the anterior femoral cut [106].

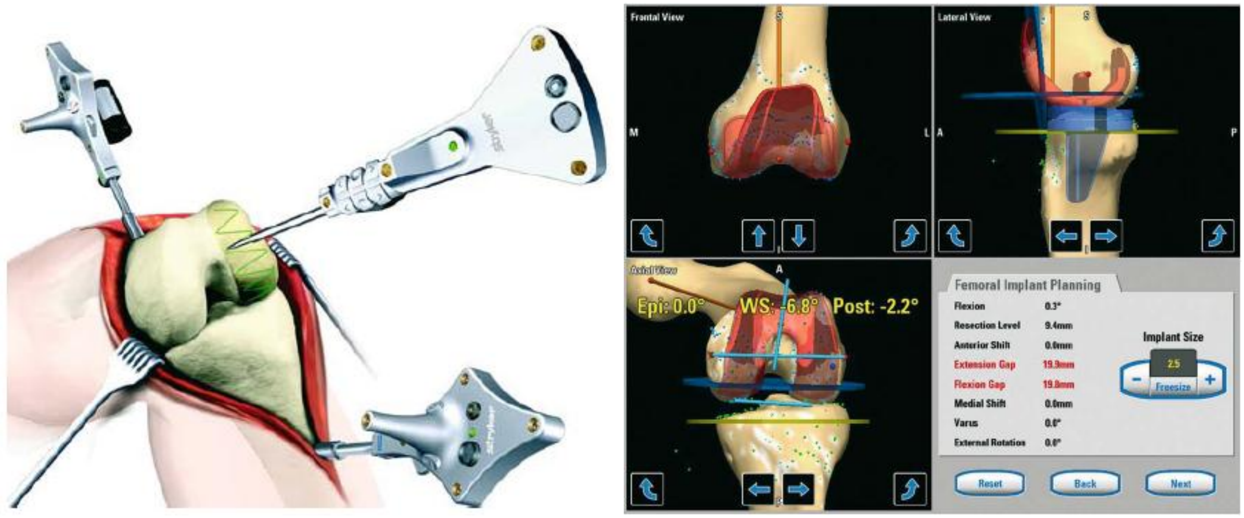

(a) (b)

Figure 3-12: (a) Stryker Knee Trac System employing imageless navigation with optical tracking [104]; (b) BrainLAB VectorVision® System utilizing the software interface for rotation of the femoral component [107].

Orthosoft, Inc., the PI-Galileo System for ligament balancing from Plus Orthopedics Aarau, the Surgitecs Bone-Morphing System from Praxim, and the OrthoPilot® KneeSuite™ from Aesculap AG [108]-[111].

With the initial design of knee navigation systems, such as the OrthoPilot® system [111], the main concern in correct implant alignment concentrated on the varus/valgus condition of the implanted knee since studies showed its importance in the 10-year survival rate of the implant [112]. After locating the mechanical axis of the lower leg and aligning the implanted knee with this axis, it is possible to greatly minimize varus/valgus conditions in the implanted knee. Jenny et al. performed a multi-center study with the OrthoPilot® system which found statistically significant differences in the mechanical axis alignment when comparing manual techniques to navigation with the OrthoPilot® system [113]. The three-month postoperative radiographs of a total of 570 TKA patients (235 implanted with the OrthoPilot® system and 235 implanted without a navigation system) were examined and it was found that 92% of patients implanted with the navigation system had optimal mechanical axis alignment compared to only 72% of the patients implanted without a navigation system [113]. Next, the internal/external rotation of the normal knee must be determined so that the implanted knee can be rotated likewise. This is currently done by having the surgeons pick landmarks or point clouds on the medial and lateral epicondyles. The transepicondylar axis can then be determined and used in determining the external/internal rotation. Also, Whiteside's line can be determined and used to find an AP axis, providing information on the external/internal rotation of the femur. Figure 3-12b shows the BrainLAB user interface for calculating external/internal rotation. Note that the Whiteside line, transepicondylar axis, and posterior condylar axis can all be seen. All major commercial imageless systems incorporate this process in their surgical approach, including the Stryker Knee Trac System, the OrthoPilot® system, and the BrainLAB VectorVision® System [104],[107],[111].

Stability of the implanted knee is also of prime importance to ensure a positive surgical outcome. The collateral ligaments and posterior cruciate ligament play key roles in maintaining knee stability throughout flexion. This can be examined by measuring the gaps between the implanted femur and tibia at both flexion and extension and ensuring a rectangular shape at both positions (if the gap on the medial or lateral side is significantly different, e.g. 2-5 mm, the knee may buckle under loading conditions). Also, if the gap spacing is not equal at flexion and extension, this can cause areas of tightening or loosening as the knee goes from extension to flexion [95]. The OrthoPilot® system, along with the BrainLAB VectorVision® System and PI-Galileo System, uses a special gap measuring tool so that medial and lateral gaps can be measured at flexion and extension, displaying feedback information via the software interface for the surgeon [111]. Conversely, the Knee Trac System from Stryker uses the transepicondylar axis as well as the proximal resection of the tibia to determine a curve for both the medial and lateral condyles that can be rotated through the complete range of motion, although this technique is susceptible to the accuracy in measuring the transepicondylar axis [111]. Another point of consideration is instability of the patellofemoral joint after TKA. If the line-of-action of the quadriceps tendon pulls the patella laterally, which is most prone with the leg in extension, subluxation of the patella can result along with general knee pain [114]. Given the susceptibility of the patellofemoral joint to instability, it should come as no surprise that navigation systems are now used to resurface, replace, or in some way reposition the patella during TKA. For example, the OrthoPilot® system can be used to implant a patellar endoprosthesis as needed. More commonly, the system can be used to help orient the patella after resurfacing. Post-operative, three month radiographs showed reduction in lateralization and tilt of the patella compared to preoperative radiographs [111]. The Surgitecs Bone-Morphing System places even greater emphasis on the patella by placing an intra-operative optical tracking device to it and tracking its 3-D position and orientation during the surgery [110]. The placement of the femoral implant is optimized in terms of its position with both the tibia and patella. Also, the patella is factored into the soft tissue ligament balancing procedure [110]. Many other additions and variants to the technologies and procedures described here exist when performing knee arthroplasties. For example, the Surgitecs system uses deformable shape models to create 3-D patient-specific models from painted points which can then be used to provide more accurate model-specific information to the surgeon [110]. The PI-Galileo navigation system uses a device to measure actual ligament tension during flexion and extension. This information is then used along with external/internal rotation of the femur and the AP joint line to optimize the rectangular gap at flexion and extension [109].

Imageless knee navigation systems are much more widespread than CT-based navigation systems. Lüring et al. examined both the imageless and CT-based navigation systems from BrainLAB in use at the University of Regensburg, Germany from 2002-2006. It was observed that by 2006, 1300/yr knee surgeries were being performed with the imageless system while only 180/yr or so were performed with the CT-based navigation system, with the CT-based navigation system reserved for more difficult surgeries involving significant bone deformities [107]. The CT scan of the knee is taken preoperatively. 3-D models of the bones, including the femur, tibia, and patella, are created and used in a preoperative step to plan the surgical procedure. Next, the 3-D patient-specific models are tracked intra-operatively by having the surgeon register 20 or so points which are used in 3-D fitting of the bone surfaces. This works well in extreme cases where normal knee anatomy cannot be assumed due to gross deformities of the patient's bones [107].

A new type of knee navigation system is currently available since the development of portable, fluoroscopic systems. Victor describes testing of the Medtronic fluoroscopic navigation system on 100 patients where 50 surgeries were performed with the fluoroscopic navigation system and 50 surgeries were performed without it. A significant difference in correct mechanical axis alignment was achieved for the group using fluoroscopic navigation versus the group without it (100% versus 73.5%) [115]. This preliminary study shows the potential for incorporation of an intra-operative imaging modality such as fluoroscopy for use during a knee surgery. With the current push towards MIS in orthopedics, an imaging modality such as fluoroscopy is well suited for incorporation given the added difficulty in ensuring proper implant alignment with the limited visibility of smaller incisions. Also, the use of magnetic sensors for 3-D tracking, specifically the AXIEM™ sensors from Medtronic described in Figure 3-11, have been incorporated in a pilot study where the quadriceps sparing MIS TKA surgical approach was performed in 75 patients and EM sensors were used to track the femur and tibia. Preliminary post-operative results show that the EM system performed well (a 100% success rate using post-operative radiographs), although two instances occurred where the EM system was abandoned during the surgery because of gross inaccuracies in tracking the 3-D position and orientation of the femur and tibia [116].

3.3.2 Hip Arthroplasty

Total hip arthroplasties comprise the second most common total joint replacement surgery behind knee replacements with 230,000 THAs performed in the United States in 2004 [95]. Outcomes of THAs have shown excellent long term survival rates in some cases exceeding 90% at 15-20 years post-operative [117]. Due to increased life span and younger patients becoming candidates for hip replacements, the ideal target life span for an implanted hip is 30-

50 years. Revisions bring added complications, so it would be ideal to have the average life span of a hip replacement extend to 50 years. Premature failure of hip implants occurs mainly because of infection, instability, and wear [95]. Of these causes, instability and wear can be targeted by CAS systems whereas infection is mainly linked to aseptic techniques, laminar airflow in the operating room, and the use of antibiotic bone cement.

There are a number of factors to consider when looking at the stability of the implanted joint. For example, the surgical approach has an effect in the joint's stability. Masonis et al. examined over 14 clinical studies spanning a 30 year period which included 13,000 primary total hip replacement surgeries [118]. They concluded that lower dislocation rates, around 0.55% to 3.95%, were achievable with the right surgical approach. The posterior approach consistently had the highest dislocation rates (up to 20%), although a more recent study by Kwon et al. found that dislocation rates decreased for the posterior approach when soft tissue repair was performed [119]. One of the main causes of premature joint dislocation is inaccurate orientation of the acetabular cup. Parratte et al. reported that manual techniques for orienting the acetabular component resulted in large ranges of variation including 27° in abduction and 37° in anteversion [120]. This large variation in cup orientation can cause femoroacetabular impingement, reduce the range-of-motion, and increase the chance for dislocation and wear. However, dislocation rates are still relatively low, so no study currently exists which shows a statistically significant reduction in hip dislocation rates when CAS systems are used to perform the surgery.

Wear in the hip joint has been identified as the main long term complication in implanted hip joints [121]. Wear can cause small particles to be released which then induce osteolysis around the implant, resulting in loosening and failure. Next, it is necessary to look at femoral head resurfacing, which has emerged as an alternative to total hip arthroplasty for younger and more active patients [95]. Early failures of resurfaced hips have been studied and can be linked to varus placement of the implant. Next, Back et al. report that it takes somewhere around 60 hip surgeries for a surgeon to consistently be able to place the acetabular cup implant within 5° of the desired orientation [122]. This indicates a steep learning curve in becoming consistent and proficient in performing optimal hip replacement surgeries. Minimally invasive techniques for hip surgeries have been introduced and short-term benefits such as shorter hospital stays and reduced blood loss have been documented [123]-[124], but substantial long term benefits are still lacking [125]. Reininga et al. are currently performing a study which will determine whether or not computer-navigated MIS in hip arthroplasty will result in a quicker recovery time at three months post-operative and at least an equivalent outcome relative to manual techniques at six months post-operative [126].

Although the long-term benefits of CAS in hip replacement surgeries is still lacking, there are several factors, including more accurate placement of the acetabular component, integration of CAS systems with MIS surgical approaches, reduction or elimination of the learning curve for new surgeons consistently being able to achieve accurate acetabular placement, and the ability to measure and correct leg length discrepancies intra-operatively (leg length discrepancies are a common problem after hip replacement surgeries and can cause premature implant failure [127] and have been the cause for numerous law suits against hospitals and surgeons [128],[129]) that provide ample motivation for the introduction of CAS systems and techniques into hip arthroplasty surgeries. Three main types of CAS systems are available for hip replacement surgeries, similar to knee arthroplasty as outlined in Section 3.3.1, including imageless, CT-based, and fluoroscopy-based.

All commercial hip navigation systems track the tools used in determining correct cup and stem placement intraoperatively. As shown in Figure 3-13, the main goal of hip navigation systems in terms of correct cup placement is to correctly determine the acetabulum orientation relative to the Anterior Pelvic Plane and provide feedback to the surgeon on the orientation in terms of abduction, anteversion, and flexion angles intraoperatively. The abduction angle is defined as the rotation of the acetabulum relative to the axis normal to the

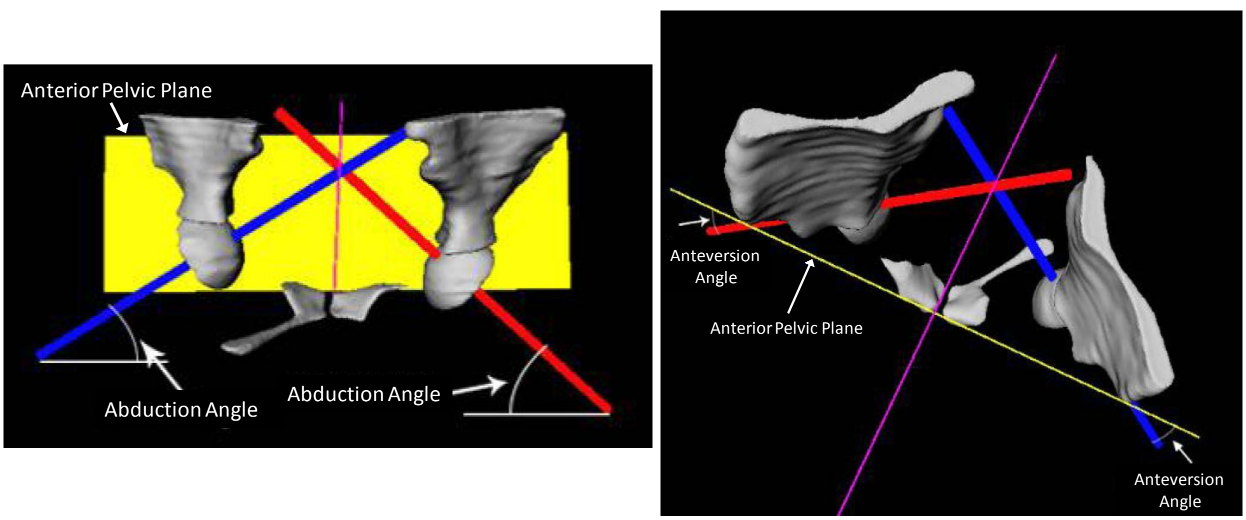

(a) (b)

Figure 3-13: 3-D scene showing the pelvis aligned with the Anterior Pelvic Plane as well as an axis for each acetabulum (a) posterior view highlighting the abduction angle of the acetabulum, (b) superior view highlighting the anteversion angle of the acetabulum.

APP, visible in the sagittal plane, as shown in Figure 3-13a. The anteversion angle is defined as the rotation of the acetabulum relative to the superior/inferior axis defined by the APP, producing a rotation visible in the coronal plane, shown in Figure 3-13b. Although CT-based and fluoro-based hip navigation systems exist, imageless systems are the de facto standard. For example, Medtronic has an imageless hip procedure which utilizes tracking of the cup to track the acetabular orientation relative to the APP. Leg length and offsets can be calculated as well as pelvic tilt. Similar to other commercial systems, bone morphing is included through the use of deformable shape models for accurate estimation of the patient anatomy [130]. Figure 3-14a shows the software interface for the Stryker iNstride Hip Navigation system [131]. The Stryker system has many similar features to the Medtronic hip navigation system including leg length, offset, the ability to only track the pelvis, etc. Additional features include using either the anatomical or functional pelvic plane, simulated kinematic analysis across the ROM to analyze lift off and impingement, support of multiple surgical approaches including new MIS approaches, and the ability to track the femur intraoperatively. Next, the OrthoPilot® HipSuite™ is shown in Figure 3-14b. The OrthoPilot® system tracks both the femur and pelvis intraoperatively. Similar to the Medtronic and Stryker systems, it calculates leg length, offset, and performs a kinematic analysis through the ROM to simulate impingement (which causes post-operative joint dislocation) [132]. Finally, the OrthoPilot® system takes into account pelvic tilt (or flexion), which needs to be considered when performing a hip replacement surgery to ensure accurate measurement of inclination and anteversion of the acetabulum. The OrthoPilot® system was tested on 80 patients. Anteversion, inclination, and leg length were

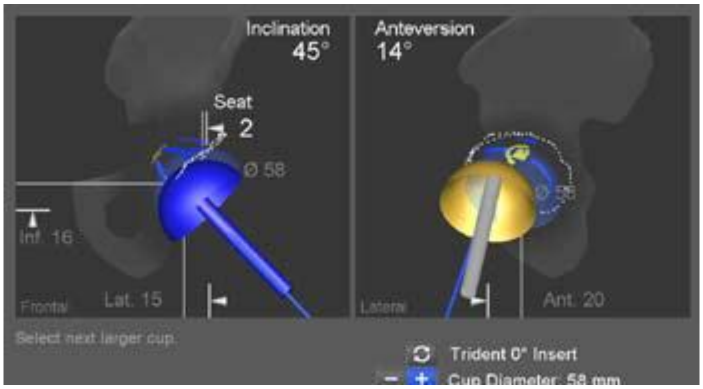

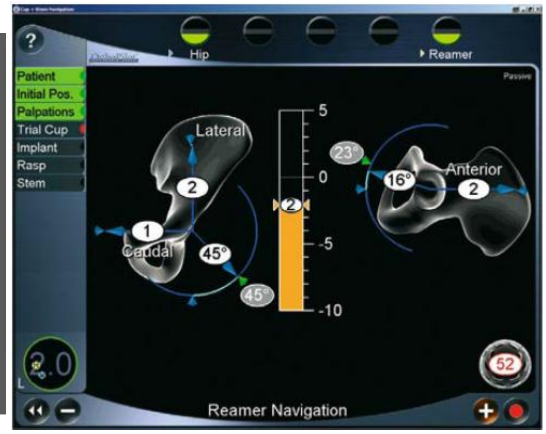

(a) (b)

Figure 3-14: (a) Stryker iNstride Hip Navigation software interface for acetabular alignment [131], (b) OrthoPilot® HipSuite™ software interface for reamer navigation of the acetabulum [132].

measured post-operatively with full leg radiographs and compared with the data obtained intraoperatively with the OrthoPilot® system. The average error in inclination angle was 3.66°, average error in anteversion angle was 6.86°, and average leg length error was 4.58 mm. All of these values are substantially lower than the variation observed with manual techniques (see [120]). The post-operative X-rays concluded that 96% of the acetabular cups were positioned inside the safe-zone, defined as the Lewinnek safe-zone that spans 40° ± 10° inclination and 15° ± 10° anteversion [133].

Other studies have been done with similar imageless hip navigation systems including the BrainLAB VectorVision® Hip Essential system and the Aesculap Orthosoft® Navitrak® system [134]. Similar to the previous imageless systems, these navigation systems use kinematic techniques to locate landmarks such as the APP, acetabulum, and femoral head. The BrainLAB system uses statistical models whereas the Orthosoft® system displays 3-D models of the implants along with picked points, axes, and other geometrical structures useful for orienting components during the surgery. In order to study the effects of the CAS systems in hip replacement surgeries, two groups were defined each with 37 patients: the first group had either the BrainLAB or Orthosoft® navigation incorporated in their surgery while the second group had a manual technique with no computer assistance [134]. The post-operative results from the group incorporating CAS were significantly better including higher average Harris Hip Score (95 versus 84), lower inclination and anteversion standard deviation (±2° versus ±5° and ±2° versus ±4°), and lower leg length discrepancy (±3 mm versus ±1 cm) [134]. Even more imageless hip navigation systems have been built and tested including an adaptation of the Praxim Total Knee Solution incorporating bone morphing to work for hip navigation [135].

CAS is also used in hip resurfacing procedures. Figure 3-15a shows the BrainLAB VectorVision® Navigation System where a cloud of points have been painted on the proximal femoral head. These points are used in a bone morphing algorithm to get a patient-specific model which allows a more accurate CAS approach than conventional techniques for hip resurfacing [136]. Figure 3-15b shows the software interface for the Smith and Nephew Birmingham Hip Resurfacing system which, similar to the BrainLAB system, digitizes a point cloud on the proximal femur (150 points on the head, 40 points on the neck, and 20 points on the impingement area near the lesser trochanter) to create a patient-specific model [137]. The Birmingham Hip Resurfacing system is an imageless system, although preoperative, intra-operative, and post-operative X-rays can be incorporated for planning and validation of the hip resurfacing procedure. The initial results in hip resurfacing navigation look promising. 28

(a) (b)

Figure 3-15: (a) BrainLAB VectorVision® Navigation System software interface for picking points on the neck and head of the femur [136], (b) Smith and Nephew Birmingham Hip Resurfacing system software interface post-operative validation [137].

patients were tested with the BrainLAB system and post-operative radiographs confirmed a slightly valgus mean shaft-neck angle of 137° ± 2.1° in the frontal plane with an average deviation of 2.9° in the axial plane [136]. Hess obtained similar results where 67 patients had navigated hip resurfacing procedures. The mean shaft-neck angle was 7.0° valgus from its normal position with a standard deviation of 2.8° [137]. These results are similar to those reported by Bäthis et al. for the BrainLAB system [136]. The preliminary results of these two studies show the potential CAS systems have in hip resurfacing procedures.

The commercial trend in hip navigation has been away from the use of a preoperative CT scan due to cost and in a great majority of CAS-based hip arthroplasty and hip resurfacing surgeries, the imageless systems described previously provide excellent results compared to manual techniques, negating the need to incorporate an imaging modality either preoperatively (CT) or post-operatively (fluoroscopy). The HipNav system designed by Jaramaz et al. was one of the first hip navigation systems built and incorporated 3-D models obtained from a preoperative CT-scan for intraoperative use [138]. No major existing commercial system incorporates a preoperative CT scan in their hip navigation system, whether the system is used for hip arthroplasty, hip resurfacing, or MIS. Fluoroscopy is much more widely adapted in commercial systems mainly because it can provide valuable information to the surgeon during MIS hip surgeries. Haaker et al. tested the Orthosoft® cup and stem navigation system from Aesculap incorporating intraoperative fluoroscopy [139]. Both lateral and ventral surgical approaches were used and, although quantitative results on orientations, etc. are not provided, although after six months post-operative, excellent results were seen with the lateral approach while more work on integrating the navigation system into the ventral approach needs to be done to ensure its success. Next, the Medtronic image guided system (incorporating O-Arm technology) was used in testing the two-incision MIS approach [140]. As shown in Figure 3-16, a navigated surgical pointer is registered to the fluoroscopy images and used to determine the location for the anterior incision. Both the femur and pelvis are tracked intra-operatively with trackers. A similar procedure to that shown in Figure 3-16 is used to accurately determine the location for the femoral incision. Results show that an average of 21 seconds of fluoroscopy is needed in the procedure. The surgery is lengthened by an average of 20 minutes, and the initial qualitative post-operative results show no dislocations and leg-length discrepancies of less 2 mm. The use of image guided navigation systems in MIS hip surgeries provides a promising platform for a more widespread use of CAS in hip arthroplasty.

Figure 3-16: Intra-operative fluoroscopy image overlayed with surgical pointer to determine location of anterior incision using the Medtronic image guided system [140].

3.4 UWB and Future Navigation Systems

The main purpose of surgical navigation systems is to provide real-time feedback and quantitative assessment to the surgeon regarding the quality of the surgical process. The overall surgical process can be divided into three distinct steps: pre-operative, intra-operative, and post-operative [141]. [142] provides an excellent overview of the operating room of the future from the orthopedic perspective. Figure 3-17 outlines how novel technologies can be used in each of these steps to help provide more information with better accuracy for surgeons, implant designers, and patients. In the pre-operative step, technologies such as automatic 3-D segmentation of CT datasets and biplanar X-ray reconstruction are used in creating patient-specific 3-D models of the patient's bones, which are then tracked on a computer in the intra-operative phase [143],[144]. Once an accurate model of the patient's anatomy is created, advanced analysis of the joint anatomy can be used to provide feedback to the surgeon on implant sizing and other relevant specifications [145]. In the intra-operative phase, 3-D real-time tracking of the patient's bones as well as surgical tools can be done through registering a bone tracking system with a high accuracy UWB positioning system and using the UWB positioning system for tool tracking, tracking of the capacitive sensor ligament balancing system into the surgical scene, and finally incorporation of the UWB technology into smart surgical tools. The ligament balancing system uses microcantilever pressure sensors. The smart provisional, used to determine patient implant size intra-operatively, uses MEMS-based pressure sensors. The final phase is post-operative analysis. A novel 3-D to 2-D registration algorithm is already in use for extracting 6 degree-of-freedom (3-D translation and 3-D rotation) information from fluoroscopic images [146]. This can be combined with a gait analysis lab. Current gait analysis is done by either tracking with one or more video cameras or by using passive or active optical markers which reflect or emit signals to a multiple (e.g. 8) of infrared cameras. Figure 3-17 provides an overview of the complete navigation system. More details are provided on the intra-operative step including smart surgical tools in Section 3.4.1, the post-operative step including gait analysis in Section 3.4.2.

3.4.1 Intra-Operative Phase

As shown in Figure 3-17, the intra-operative phase consists of real-time tracking of smart tools or instruments, bones, and the capacitive ligament balancing system. The smart provisional provides intra-operative feedback to optimize soft tissue interaction with orthopedic joint replacements. The smart provisional system utilizes the 315 MHz and 433.92 MHz frequency bands for data transmission.

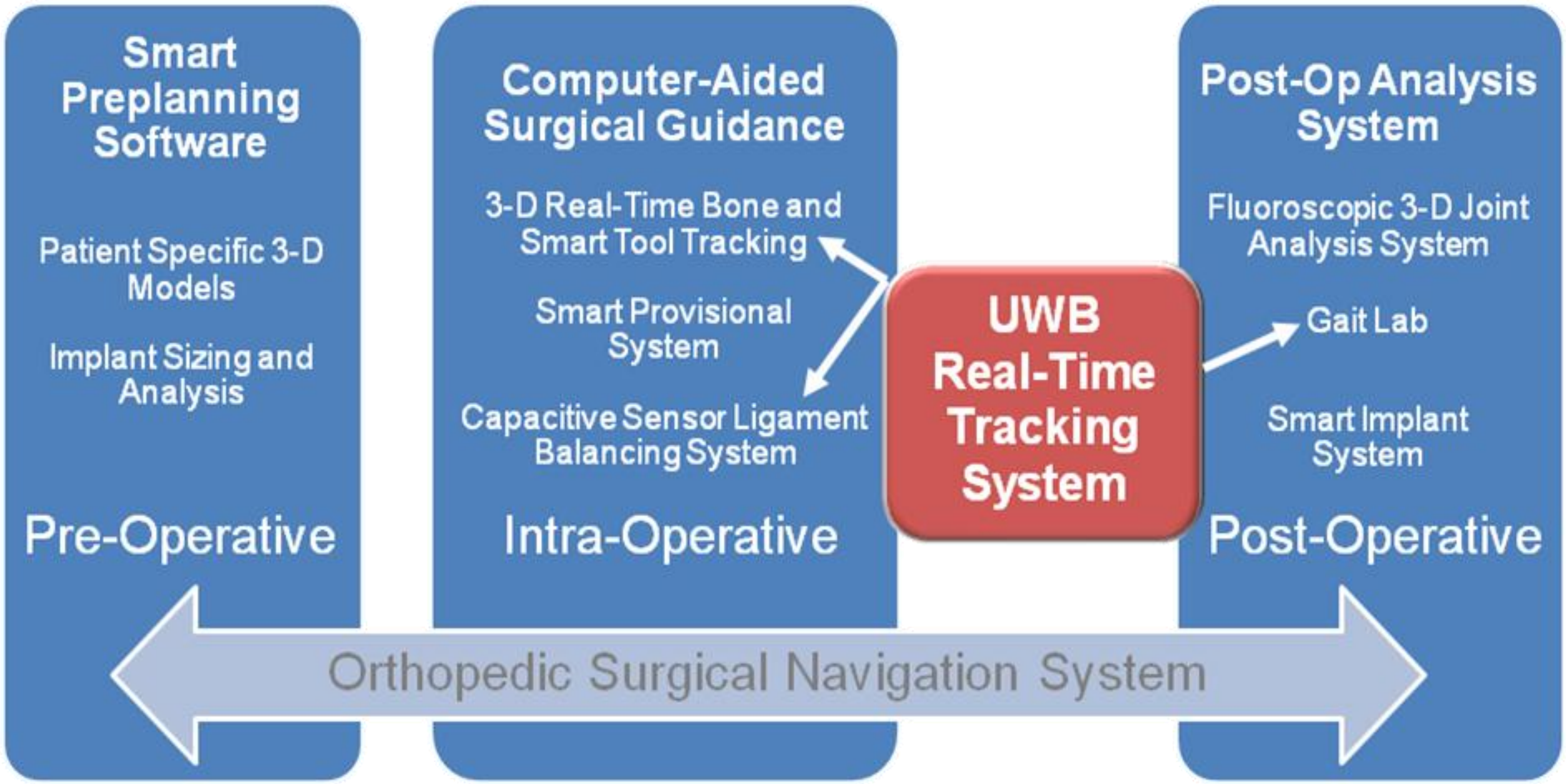

Figure 3-17: Overview of orthopedic surgical navigation system including pre-operative, intra-operative, and post-operative phases [141].

The incorporation of the intra-operative pressure sensing system inside the spacer block combined with an UWB localization probe that tracks its location in real-time, as illustrated in Figure 3-18, is an example of the future technology in surgical navigation: smart surgical tools. Figure 3-19 further illustrates the integration of the UWB tracking system and microcantilever pressure sensing spacer block system. A UWB probe containing a 3-6 element UWB monopole array is used to obtain the 3-D position and 3-D orientation of a rigid body. The femur, tibia, and spacer block have UWB probes rigidly attached to them, as shown in Figure 3-19. The UWB positioning system outlined in Chapters 7 and 8 has dynamic 3-D accuracy of 3-7 mm. This can cause 4-6 mm of translation error and 1-3° of x,y,z rotation error for each rigid body. This is still too high for surgical navigation applications where 1-2 mm of 3-D translation accuracy and <1° of x,y,z rotation is needed to ensure proper implant alignment to the patient anatomy. Conversely, this accuracy is acceptable for ligament balancing applications since the system can still use the pressure mapping of the medial and lateral condyles to monitor the compartmental pressures. The UWB positioning system provides quantitative data on the varus/valgus condition of the knee. It also provides an accurate measure of the quality of the distal and posterior cuts on the femur to the proximal cut on the tibia. This quickly alerts the surgeon to any problems in the surgical resection intra-operatively.

3.4.2 Post-Operative Phase

A post-operative analysis system uses a hybrid system combines tracking data, from either an optical or UWB-based tracking system, with image data [93]. The data is fused to provide highly accurate gait analysis. UWB tracking has the potential to integrate with sensor-based systems and even medical imaging modalities to create advanced intra-operative and post-operative guidance systems with the potential to revolutionize the technology used in surgical navigation. Figure 3-20 shows a conceptual drawing of a RF UWB probe used for

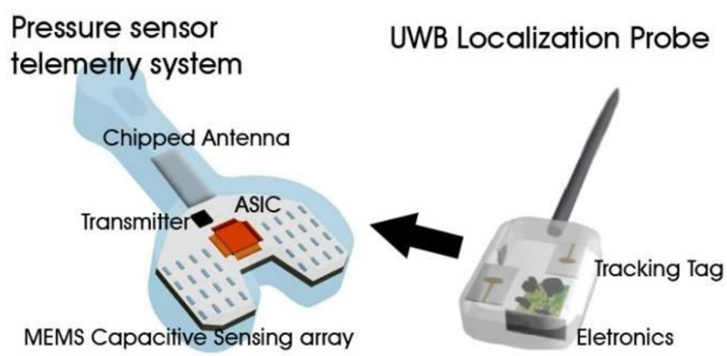

Figure 3-18: Illustration of a smart surgical tool. The spacer block, with embedded pressure sensing-telemetry system, is tracked in 3-D by an UWB localization probe.

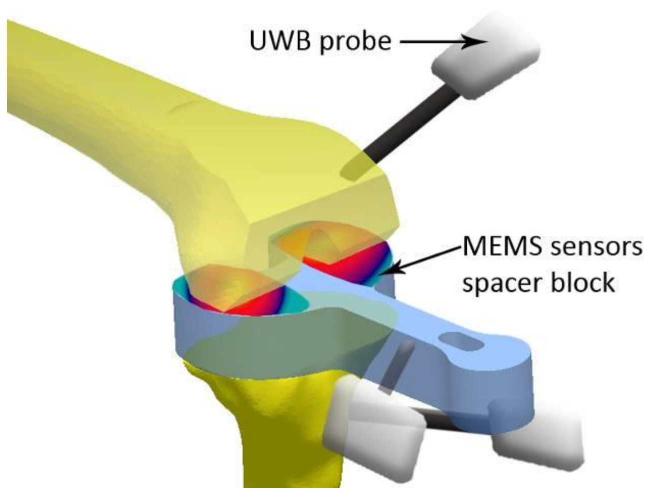

Figure 3-19: Illustration of the MEMS spacer block integrated with the UWB positioning system for 3-D real-time tracking. UWB probes are rigidly fixed to the femur and tibia to track the bones in real-time. A UWB probe is also rigidly attached to the spacer block to track it in real-time.

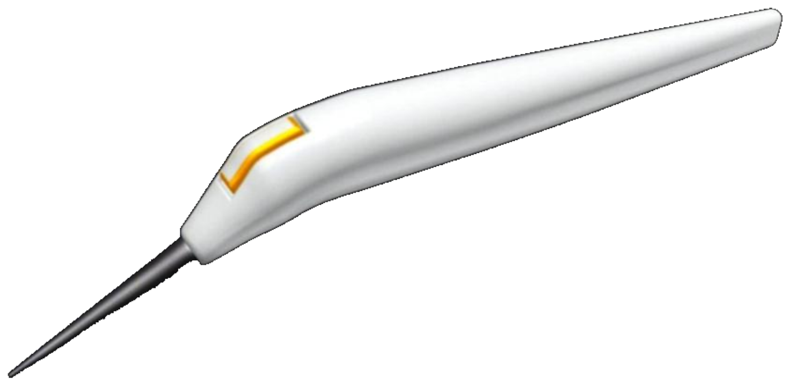

Figure 3-20: Conceptual drawing of UWB RF surgical navigation probe for painting points in computer assisted orthopedic surgery.

painting points in orthopedic surgical navigation. The points could then be used for bone morphing, intra-operative tracking, or landmark detection.

4. Wireless Signal Propagation in Hospital Environments

The main concern with using wireless tracking and communication technology in the OR and other hospital environments is the high level of scatterers and corresponding multipath interference experienced when transmitting wireless signals. While the experiment from Clarke et al. [86] provides quantitative data on how wireless real-time positioning systems perform in the OR, it is also useful to look into narrowband and UWB channels and their effect on narrowband and UWB signals for communication and positioning applications. There are two typical approaches used when modeling wireless channels: the first is statistical models used to model generic environments (e.g. industrial, residential, commercial, etc.), which incorporate LOS or NLOS measurements taken in the time and frequency domains, which are then used in setting the parameters of these statistical models. The second method uses ray tracing techniques to model specific geometrical layouts (e.g. buildings, cities) and can provide a more accurate depiction of which obstacles and structures will have the greatest effect on wireless propagation [93]. The drawback with ray tracing is the static nature of the results (i.e. results are only valid for a certain scenario of objects placed in the scene). Even if the wireless systems in the operating room are static, other objects will not be including people, patients, the operating table, and medical equipment.

The effects of hospital environments on both narrowband telemetry systems (e.g. 315 MHz or 433 MHz systems) as well as UWB positioning and communication systems operating in the 3.1-10.6 GHz band are discussed in Sections 4.1 and 4.2. This includes time and frequency domain experiments outlined in Section 4.2 which were used in obtaining parameters for a

UWB channel model for the operating room environment fit to the IEEE 802.15.4a channel model. Section 4.3 outlines an experiment to quantify which types of wireless signals are found in the operating room which have the potential to cause electromagnetic interference with narrowband and UWB wireless systems. Finally, Section 4.4 discusses the susceptibility of our UWB positioning system to WLAN interference in the 5.8 GHz ISM band and includes specifications for a multi-stage bandpass filter which is needed to ensure the UWB receivers are not jammed by high power WLAN interferers.

4.1 Narrowband Telemetry Systems

Attenuation of wireless signals due to soft tissue is one of the major obstacles in designing *in vivo* wireless systems, including systems which operate in the 315 MHz and 433 MHz ISM bands (Table 2-1). The lossy nature of soft tissue to signals in the RF and microwave frequency range has been extensively researched (Section 2.2). The electrical properties of an arbitrary medium (e.g. muscle, fat) can be completely characterized by the relative permittivity ε' and conductivity σ

$$\varepsilon^{*} = \varepsilon' - j\varepsilon'' \qquad \sigma = \varepsilon''\varepsilon_0\,\omega \tag{4-1}$$

where ε^{*} is the complex permittivity, ε'' is the imaginary portion of the complex permittivity signifying loss, and ω is the radial frequency. As outlined in Section 2.2, human tissues have been characterized in terms of their complex permittivity and conductivity which allows the study of propagation of wireless signals through human tissues. As mentioned in Section 2.2, the losses observed in human tissues rise sharply above 1.43 GHz.

Figure 4-1 outlines a simulation conducted using the tissue properties in Section 2.2. The electric field and tissue interfaces were simulated following the procedure outlined in [75] where a recursive process is used to solve for the equivalent impedances of each tissue and reflection coefficients for each tissue interface (e.g. muscle-fat, fat-skin, and skin-air). The signal first travels through 10 mm of muscle and then through the muscle-fat interface, then through 5 mm of fat and through the fat-skin interface. Part of the signal is reflected at the fat-skin interface, which then travels back to the fat-muscle interface. Solving for the equivalent impedances and reflection coefficients for each tissue and interface in the same order as the emitted signal takes into account this phenomenon where electric field waves can effectively bounce around between two interfaces [75]. For the simulation, a modulated ASK signal is transmitted at 10 dBm power at 315 MHz, 433 MHz, 915 MHz, and 2.4 GHz. As shown in Table 4-1, all signals will experience some loss due to the tissues. The losses incurred at 315 MHz and 433 MHz are 12.5-22.5 dB lower than the losses incurred at 915 MHz and 2.4 GHz. Operating at 315 MHz and 433 MHz successfully meets the operating range of in vivo systems while

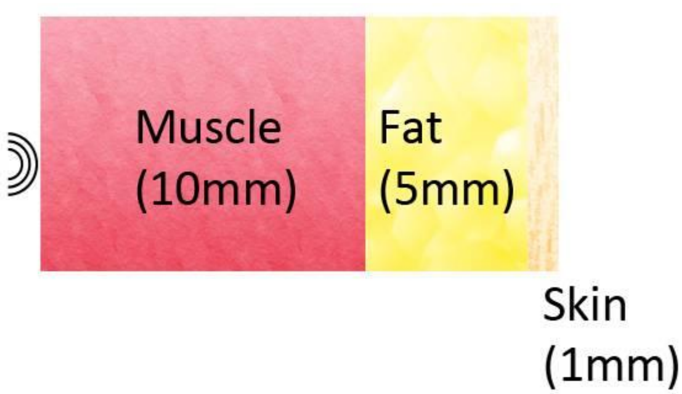

Figure 4-1: Overview of simulation setup where the soft tissues of the knee are simulated using a 10 mm layer of muscle, 5 mm layer of fat, and 1 mm layer of skin followed by air.

operating at 915 MHz and above results in losses through the medium too high to obtain an operating range of even 5 m.

It is worth noting that RFID systems are commercially available for hospital use which operate in the 433 MHz band [147]. Also, ECG telemetry systems have been designed which operate in the 433 MHz band using FSK at ranges up to 40 m [148]. 30-40 dB more pathloss is noticed indoors versus outdoors for a 433 MHz ASK link. This significantly reduces the operating range of systems using the 315 MHz and 433 MHz bands inside a hospital. For example, given a receiver sensitivity of -115.6 dBm, a transmitter power of -10 dBm after the chip antenna, the tissue losses outlined in Table 4-1, and the indoor pathloss specified by the manufacturer [149], the maximum operating range of the telemetry system is 20 m in the 315 MHz band and 15 m in the 433 MHz band, both satisfying a standard operating range requirement of 5 m for being able to transmit inside a standard hospital room.

The block diagram of an ASK receiver is shown in Figure 4-2. The RF signal is down

Table 4-1: Simulated losses for transmitted ASK signals at various frequencies.

Frequency	Loss (dB)
315 MHz	28.5
433 MHz	32.5
915 MHz	45
2.4 GHz	51

converted via an image rejection fully differential mixer. The mixer is coherent in that a PLL is used to lock onto the phase of the incoming RF signal. Using a coherent receiver provides a lower BER compared to a non-coherent receiver. As shown in Figure 4-2, the I and Q channels are extracted from the incoming RF signal and then summed to get the down converted IF signal. The 10.7 MHz IF signal is then sent through a bandpass filter. This is followed by an IF limiting amplifier. The IF limiting amplifier acts as both an amplifier and a low pass filter. After going through the IF limiting amplifier, the signal is sent to the data slicer. The data slicer acts like a comparator (with a couple extra op amp stages) to output the final, recovered, coherent baseband signal. Once again this system is fabricated and packaged into a CMOS chip. The sensitivity of the receiver is -114 dBm [150]. It also includes an on-chip AGC stage. This increases the dynamic range of the receiver by an extra 37dB.

4.1.1 Matlab System Simulation of ASK Transmitter and Receiver

A simplified version of the ASK transmitter/receiver system was simulated to analyze how the BER changes relative to the SNR. Figure 4-3 shows the input signal at 100 kb/s where the amplitude has been normalized from zero to one. For this simulation, a sampling frequency of 100 MS/s was used to ensure that that the IF signal (10.7 MHz) was recovered correctly. Next, the input baseband data was used to modulate the 10.7 MHz IF signal. The data must be downconverted at the receiver into the 10.7 MHz IF signal. Figure 4-4 shows the same ASK signal with AWGN. Specifying the noise amplitude relative to the signal amplitude allows the SNR of the resulting signal to be controlled. Varying the noise amplitude is used

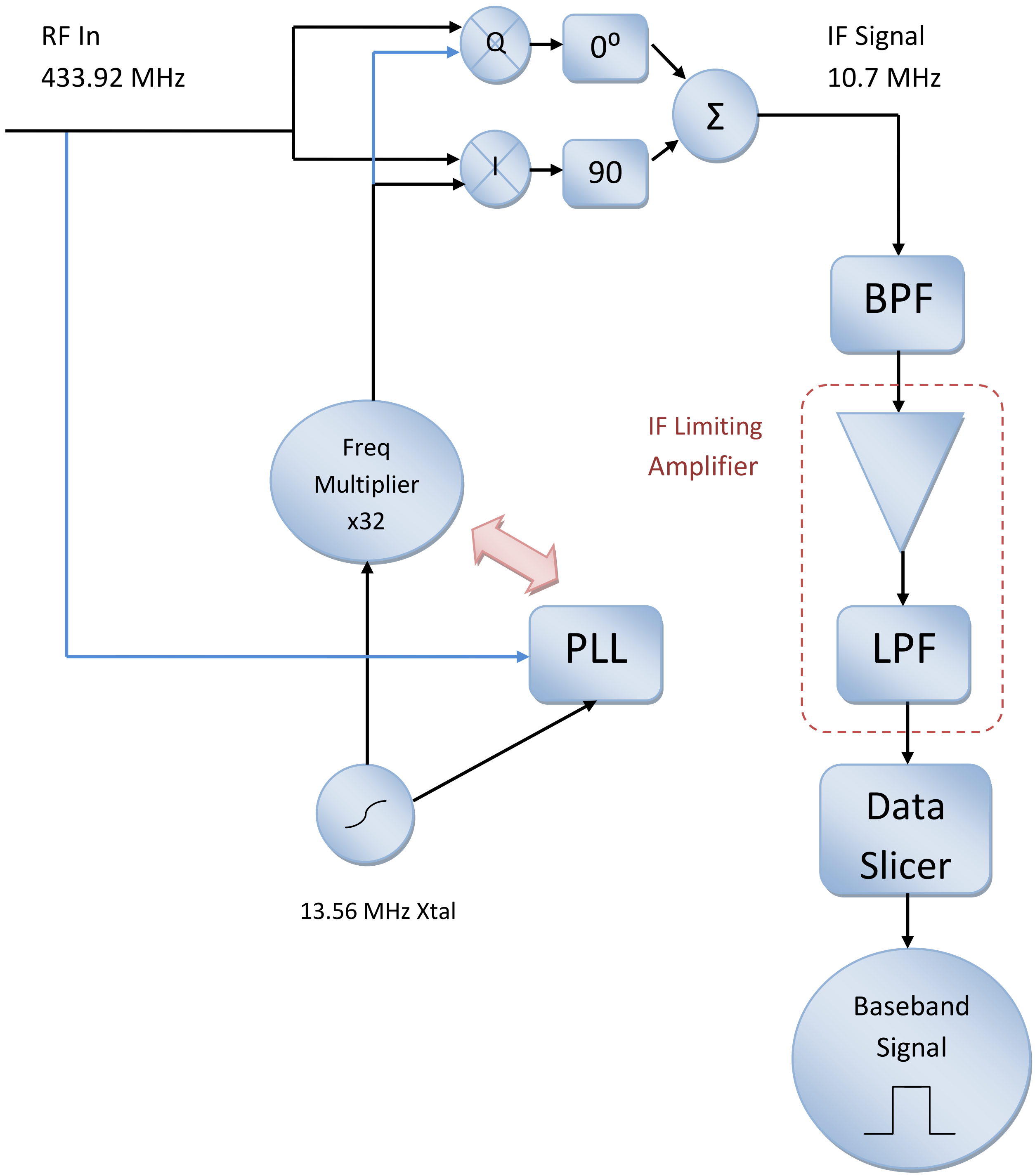

Figure 4-2: Block diagram of the MAX1473 ASK receiver.

to generate the BER versus SNR plots. Figure 4-5 shows the frequency response of the bandpass filter. From the specs in the datasheet [150], the bandpass filter was designed to be centered at 10.7 MHz, have a passband from 7-13 MHz with 3dB ripple or less, and to have a stopband

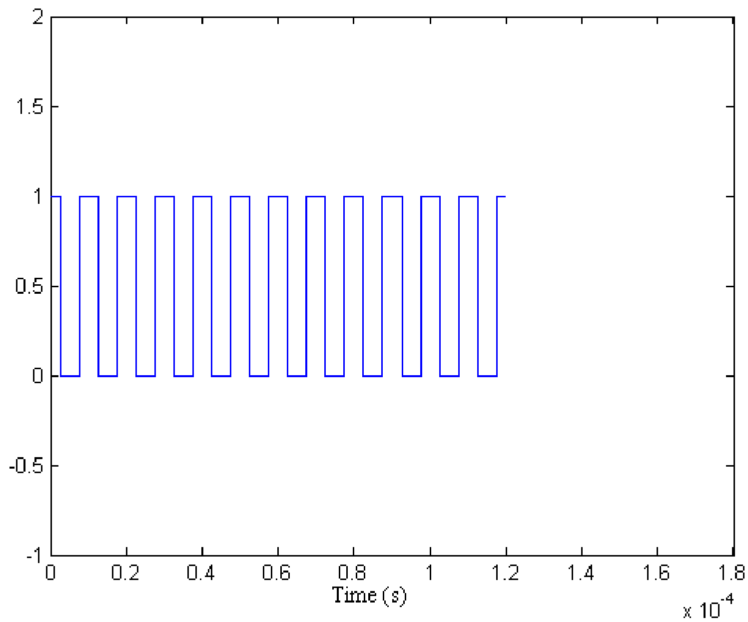

Figure 4-3: Normalized binary input data stream.

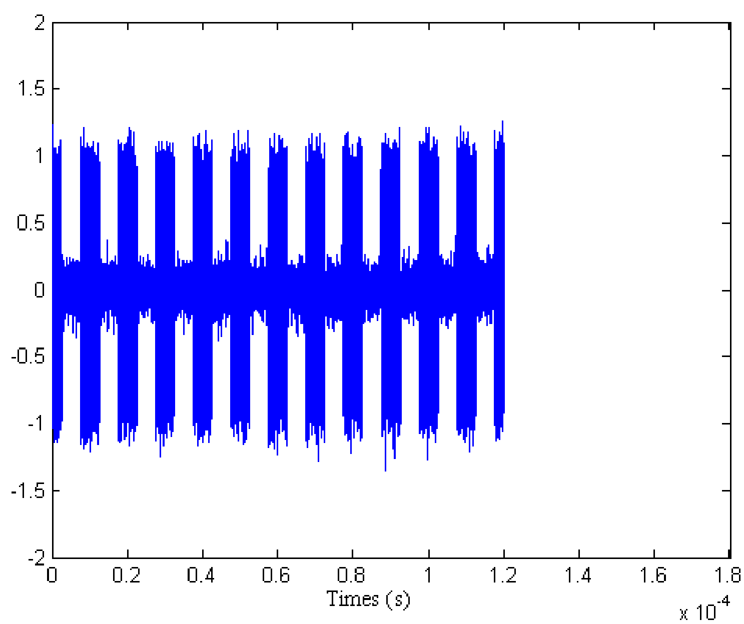

Figure 4-4: ASK signal at transmitter with the addition of AWGN.

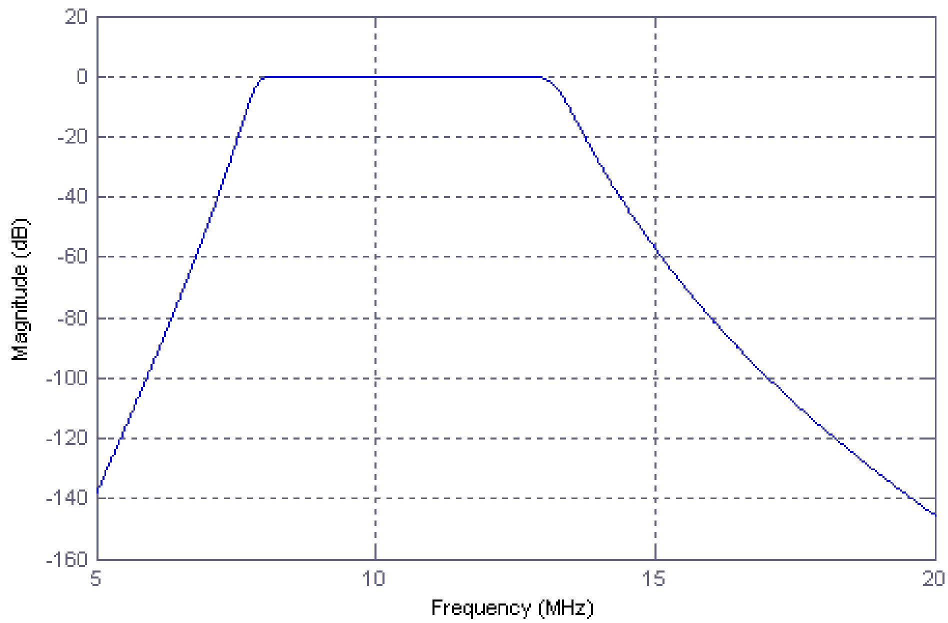

Figure 4-5: Frequency response of bandpass filter.

below 5 MHz and above 16 MHz with at least 80 dB attenuation. This was realized with a 6 order Butterworth bandpass filter. It is difficult to realize a filter of this order when designing the bandpass filter in CMOS. Figure 4-6 shows the resultant signal in both frequency and time after passing through the bandpass filter. As shown in Figure 4-6a, after passing through the bandpass filter, and with the addition of the noise, the signal contains many harmonics, although they are 60-100 dB below the main signal. The next block in the receiver chain is the IF limiting amplifier. It can be assumed that this amplifier is linear. The cutoff frequency of the low pass filter is 700 kHz, which will completely eliminate the 10.7 MHz IF signal. The last step is to send the signal through the data slicer. For all practical purposes, this is just a comparator, although in designing a real system, the data slicer is typically more complex. The data slicer in the MAX1473 receiver includes the basic op amp comparator configuration as well as two other

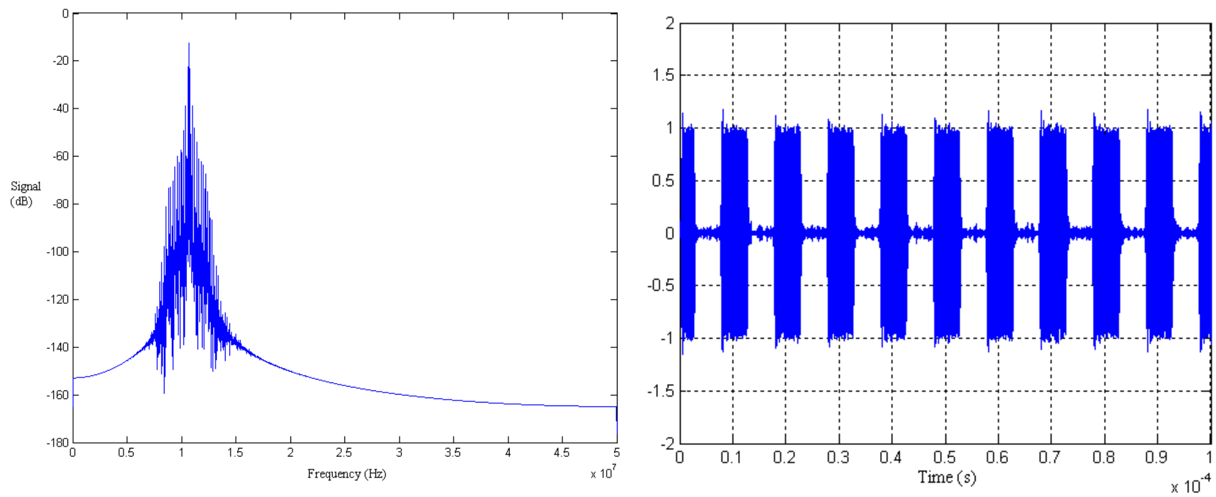

(a) (b)

Figure 4-6: (a) Frequency spectrum in dB of ASK signal after BPF, (b) Corresponding signal in time domain.

op amps for peak detection which are needed to detect bits before the capacitor in the LPF of the circuit has gotten sufficiently saturated. Figure 4-7 shows the received data stream juxtaposed with the transmitted data stream. The receiver is coherent, which means the phase of the signals will be locked, as seen in Figure 4-7. A small discrepancy exists at the beginning of the Rx data stream. This is caused by the slow temporal response of the low pass filter. In the MAX1473 this will not occur since the data slicer is able to compensate for these effects.

Figure 4-8 shows the theoretical and simulated BER versus SNR for the ASK system. As expected, the BER of the actual system is worse than the theoretical limit using ASK. In [150], a BER of 0.2% is given. They do not specify the SNR of the signal. If a standard SNR of 10dB is assumed, then the theoretical limit of ASK is 7E-4 while the simulated system produces a BER of 0.3%, which is closer to the BER given in the specifications of the MAX1473 receiver. Finally, it is worth noting the divergence of the two curves in Figure 4-8, especially for larger SNR values (10 or 12 dB). Simulations of the ASK system were performed in Matlab using the Matlab BERTool. This allows a theoretical BER to be calculated alongside a semi-analytic solution, and finally a solution obtained using a Monte Carlo simulation. As shown in Figure 4-9, the semi-analytic and Monte Carlo simulations are more realistic when compared to the actual performance of an ASK system. The theoretical BER is much lower than actual performance seen because it assumes no noise or interference or fading due to scatterers. It should be noted that the theoretical BER in Figure 4-9 is lower than that in Figure 4-8. This is because convolutional encoding is used in the simulations in Figure 4-9 to reduce the error further (and also is more realistic to an actual system). The Monte Carlo simulation gives a BER of

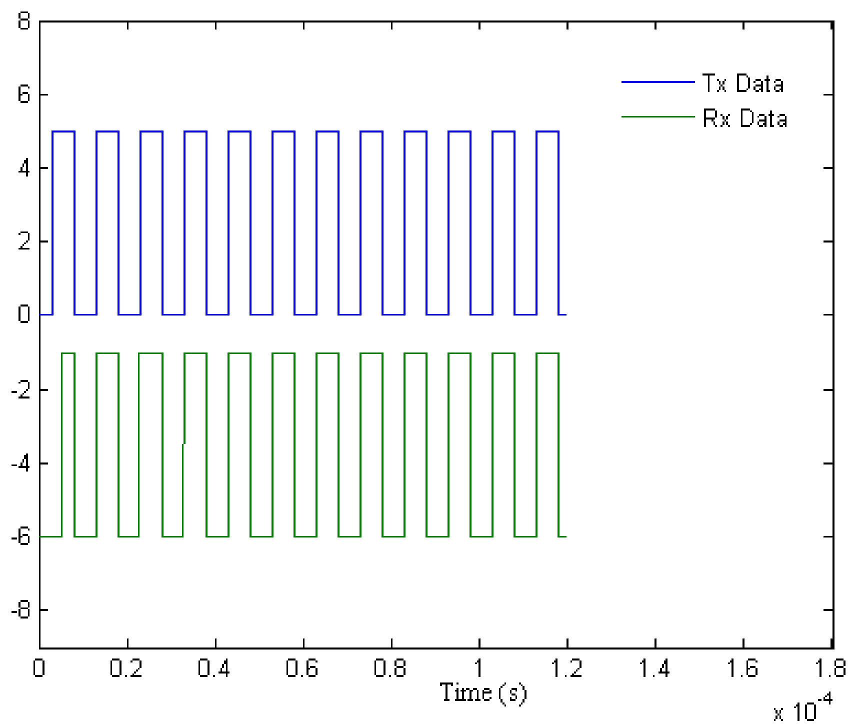

Figure 4-7: Original data stream and recovered data stream after passing through Tx/Rx.

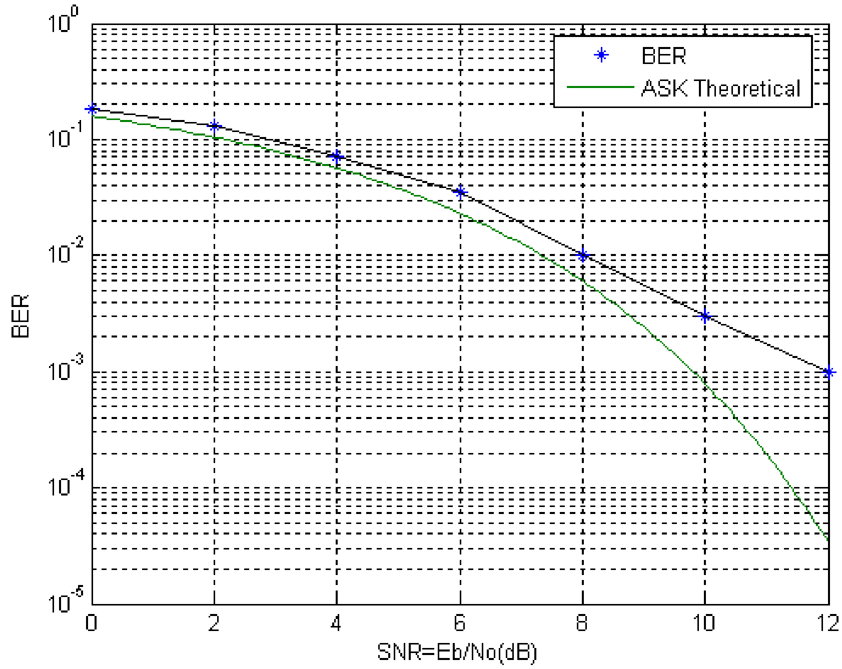

Figure 4-8: Theoretical and simulated BER of the ASK system.

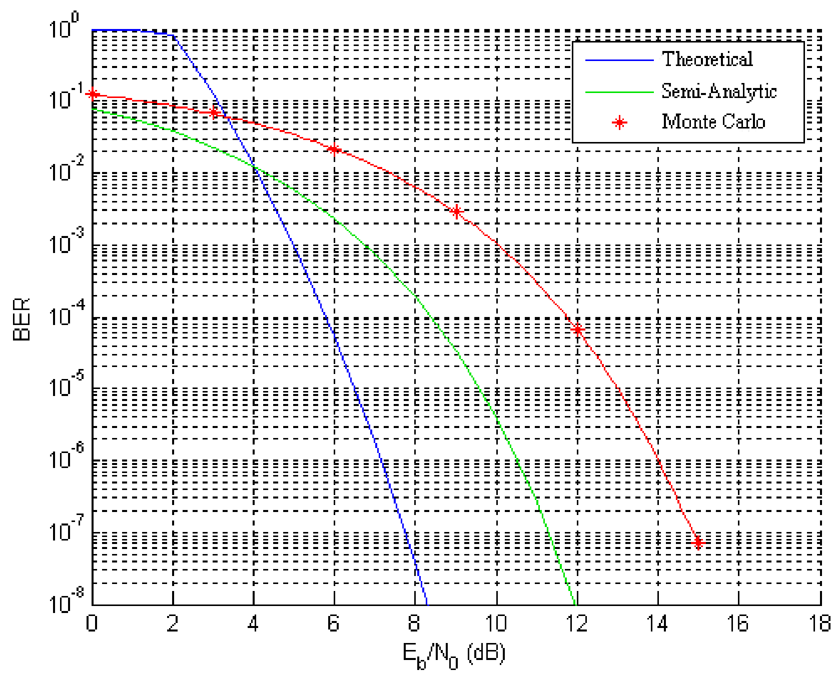

Figure 4-9: Comparison of theoretical, semi-analytic, and Monte Carlo methods for computing the BER of the 433 MHz ASK system.

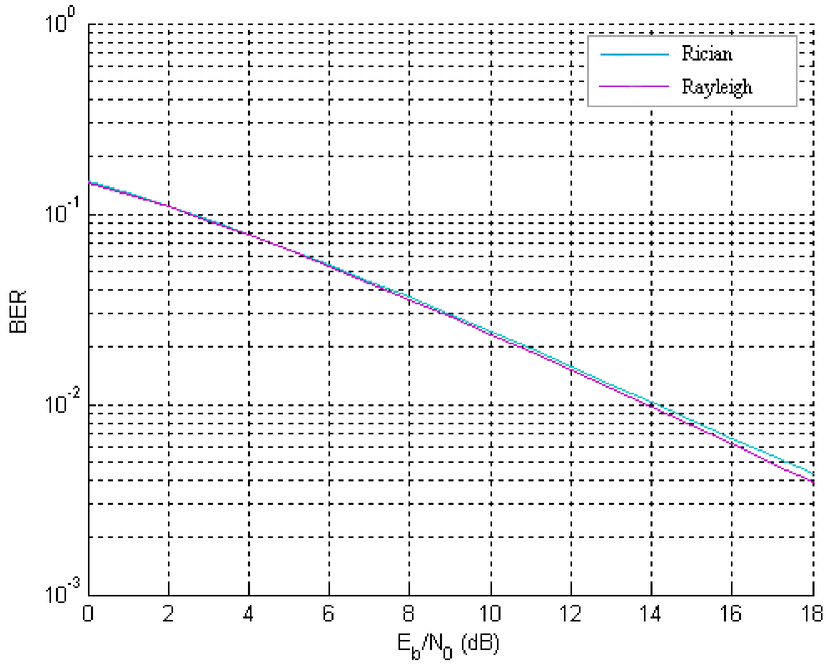

Figure 4-10: Theoretical performance of the ASK in fading Rayleigh and Rician channels.

0.1% at SNR=10dB. This almost identical to the manufacturer specification of 0.2% and also to the calculated BER from the Matlab simulation (0.3%). Finally, as shown in Figure 4-10, the performance of ASK is drastically reduced in fading multipath channels, such as Rayleigh and Rician channels. The theoretical lower bounds of the BER of an ASK system is 10^6 higher at SNR=10dB than that of a system in an AWGN channel. This explains the reason ASK systems are not used in dense, multipath environments.

4.2 UWB Operating Room Channel

UWB systems have been designed and targeted for various medical applications given their robustness to dense multipath interference found in hospital environments as shown in Figure 4-11. Given the large amount of metallic interference, an accurate characterization of this environment is needed to design and simulate its effects on system performance. In developing the UWB positioning system outlined in Chapter 5, the IEEE 802.15.4a channel model has been used in the back-end DSP, which uses a large number of parameters and random variables in modeling a wide variety of environments (e.g. indoor industrial LOS/NLOS, indoor commercial LOS/NLOS, indoor residential LOS/NLOS, outdoor, body-area-networks) [151],[152]. The

$$h(t) = \sum_{l=0}^{L} \sum_{k=0}^{K} a_{k,l} \exp\left(j\varphi_{k,l}\right) \delta(t - T_l - \tau_{k,l}) \tag{4-2}$$

$$PL(d) = PL_0 + 10n\, log_{10}\left(\frac{d}{d_0}\right) \tag{4-3}$$

impulse response of the UWB channel in the time domain is shown in (4-2) while the pathloss model used in the corresponding UWB channel is shown in (4-3). These models have been used both in simulating the behavior of the UWB positioning system (Chapter 6) and in designing and implementing receiver-side pulse detection algorithms for highly accurate 1-D distance measurements between the transmitter and receiver, integral to the high performance of the system (Chapter 9).

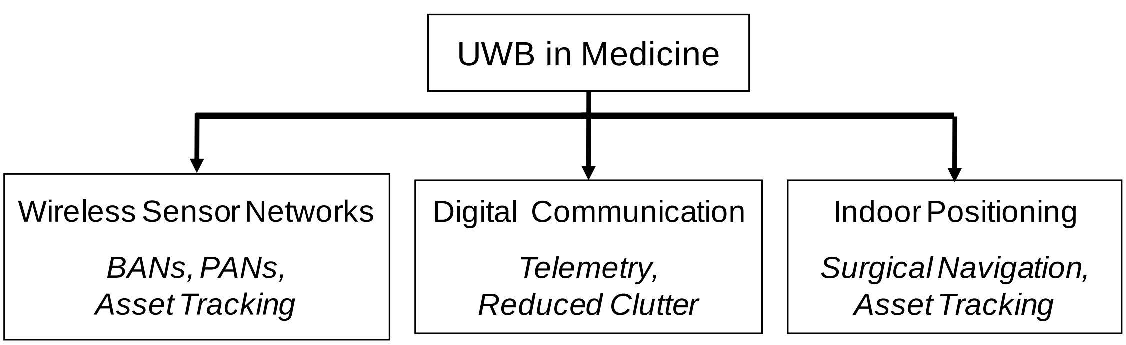

Figure 4-11: Various facets of UWB in medicine including wireless sensor networks, high data rate digital communication, and indoor positioning.

Although the IEEE 802.15.4a UWB channel model has been fit to many environments, the OR is one place where measurement data is lacking and modeling information is still non-conclusive. The most comprehensive analysis was done by Hentila et al. who used time domain and frequency domain measurement techniques in analyzing UWB channels in different hospital environments including the operating room, X-ray examination room, and intensive care unit [153]. The data best fit to a Nakagami-m distribution using a modified Saleh-Valenzuela model, similar to (4-2). Many techniques exist for performing indoor channel measurements of an UWB signal. For example, Irahhauten et al. discusses both frequency domain and time domain techniques [154] which can be used in conjunction with one another for an accurate description of channel fading versus frequency, root-mean-square delay spread, path loss, power delay profile, and many other measurements.

4.2.1 Experimental Setup

Extensive time domain and frequency domain measurements in the operating room both during surgery (live) and not during surgery (non-live) for Tx-Rx distances of 0.5 m to 4 m. Figure 4-12 and Figure 4-13 show the time domain and frequency domain setups to collect data in the OR. Figure 4-14 and Figure 4-15 show the live and non-live setups where the layout of the dual OR is shown to highlight the Tx and Rx locations for both the live and non-live experiments. Note that both monopole and single element Vivaldi antennas are used for transmission and reception. The basic strategy in the time domain is to send out a narrow UWB pulse, either baseband or modulated by a carrier signal, in the 3.1-10.6 GHz band approved by the FCC [4]. Indoor measurements can also be measured at bands higher than the standard 3.1-10.6 GHz (e.g. 22-29 GHz) with the understanding that the effective isotropic radiated power is limited to -51.3 dBm/MHz rather than the -41.3 dBm/MHz available in the lower band [4]. Figure 4-16 shows the experimental setup during the non-live case (Figure 4-15) for obtaining both time and frequency domain data while Figure 4-17 shows the experimental

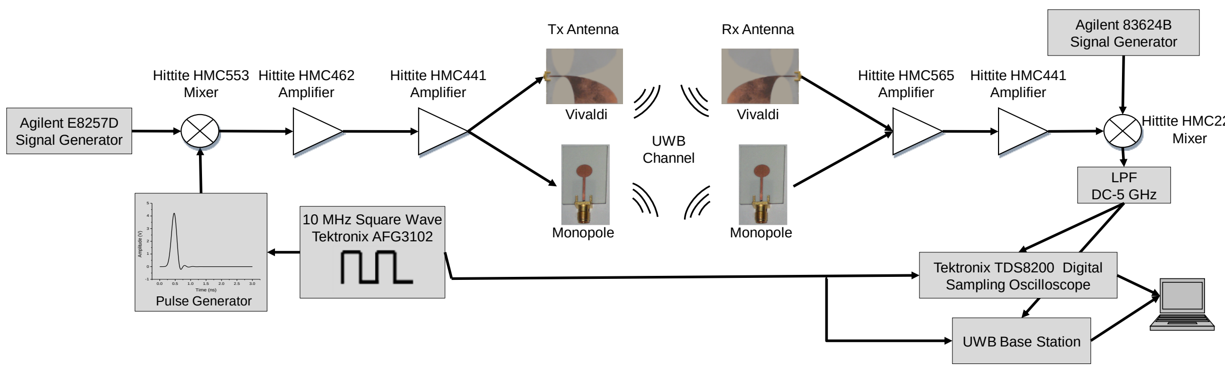

Figure 4-12: Experimental setup to collect time domain data in the operating room with the UWB localization system.

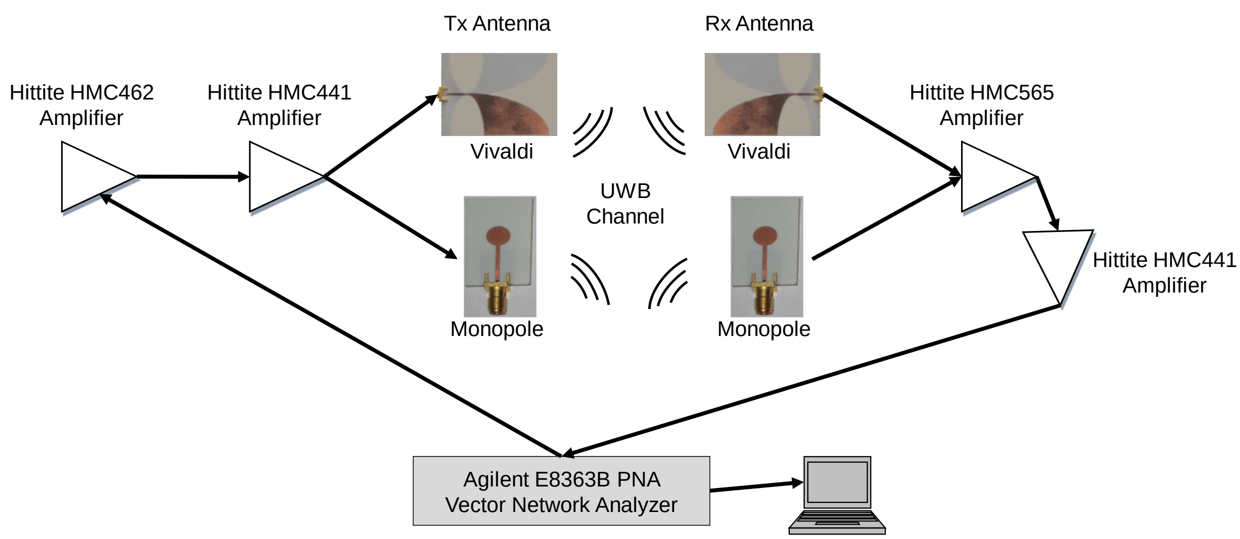

Figure 4-13: Experimental setup to collect frequency domain data in the operating room for characterization of the 3.1-10.6 GHz UWB band.

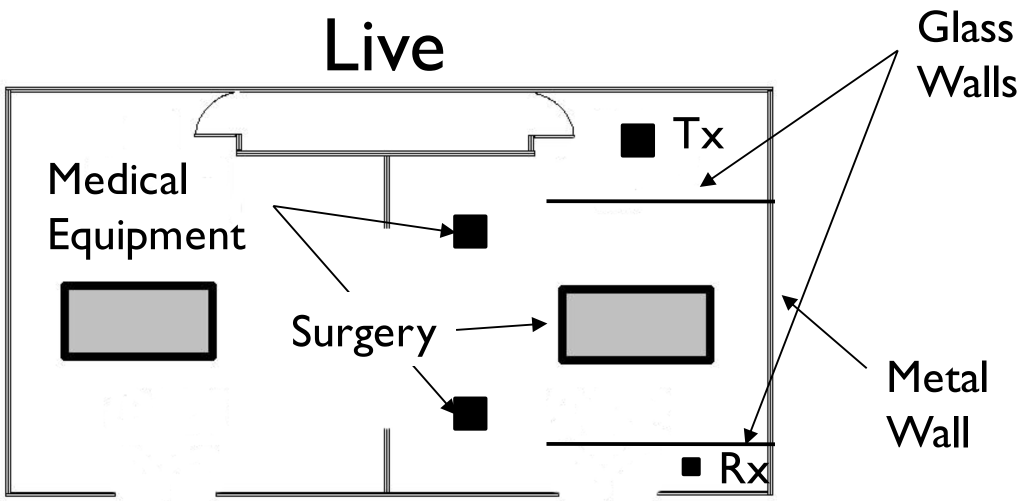

Figure 4-14: Layout of dual operating room during surgery outlining the patient table, glass walls, medical equipment, doors, and walls. The Tx and Rx were positioned 4 m apart across the surgery.

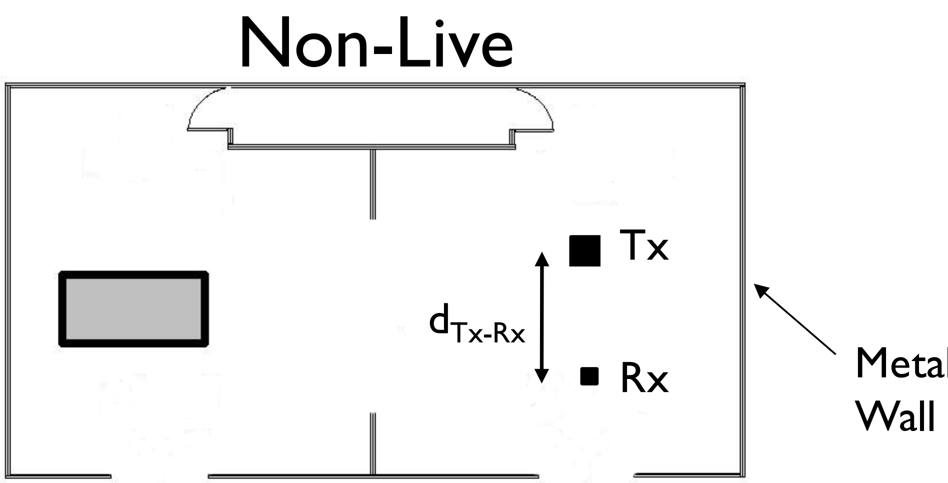

Figure 4-15: Layout of dual operating room without surgery taking place where medical equipment, glass walls, and the patient table have been removed. The Tx and Rx were placed in the surgical area and moved from 0.5-4 m apart.

setup during an orthopedic surgery (the live case in Figure 4-14). In Figure 4-12, the 10 MHz triggering signal is synchronized between the transmitter and receiver, and the received signal is processed both by a UWB base station and also with a Tektronix TDS8200 equivalent time oscilloscope. When performing measurements in the frequency domain, the typical approach is to use a vector network analyzer to sweep across the UWB frequency range (e.g. 3.1 – 10.6 GHz) and measure the S-parameter response of the channel where a UWB signal is passed between a transmitting and receiving antenna. The inverse Fourier transform can then be used to convert the signal from a frequency response into an impulse response in the time domain. This allows frequency dependent fading and path loss as well as the RMS delay spread and power delay profile measurements to be obtained. In Figure 4-13, an Agilent E8363B vector network analyzer is used to collect data. Also, once again both monopole and single element Vivaldi antennas are used in transmission and reception both for comparison and factoring out antenna effects from the channel measurements.

4.2.2 Experimental Results

Table 4-2 shows a truncated list of parameters for the LOS operating room environment fit to the IEEE 802.15.4a channel model which were obtained with time domain and frequency domain experimental data. Figure 4-18 shows the pathloss for the OR environment obtained by fitting experimental data to (4-3) and compared to residential LOS, commercial LOS, and industrial LOS. The pathloss in the OR is most similar to residential LOS, although this can change depending on which instruments are placed near the transmitter and receiver or the locations of the UWB tags and base stations in the room. Figure 4-19 shows pathloss obtained for a Tx-Rx distance of 0.49 m where the transmitting (monopole) and receiving (Vivaldi) antenna effects have been removed. Small scale fading effects can be seen as well as frequency dependent pathloss, which is captured in the parameter κ in Table 4-2. Figure 4-20 shows an

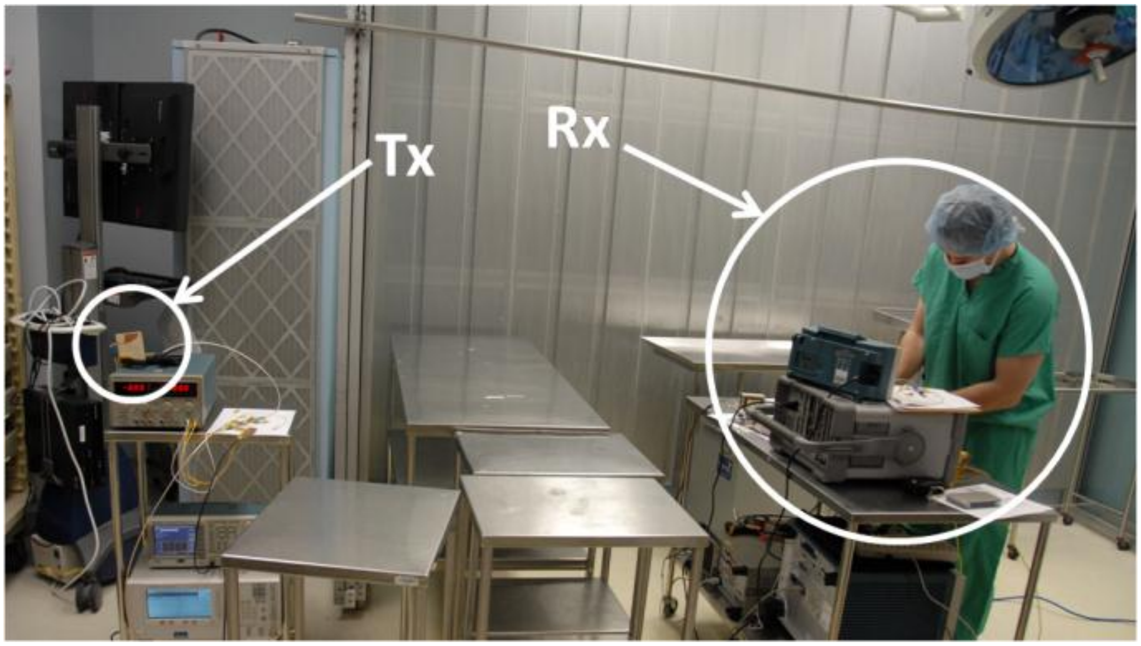

Figure 4-16: Experimental setup in the operating room during non-live scenario.


Figure 4-17: Experimental setup in the operating room during an orthopedic surgery.

example time domain signal where significant multipath interference is caused by reflections from metal tables and walls. Figure 4-21 shows an example time domain received signal for a Tx-Rx distance of 1.49 m using the monopole antenna for transmitting and single element Vivaldi antenna for receiving. A decaying exponential is overlayed on the received signal to highlight the intra-cluster decay, defined by γ_0 = 1.33 in Table 4-2. The pathloss of the LOS OR channel is most like a residential LOS environment whereas the power delay profile is closer to an industrial LOS environment (γ_0 = 0.651) where dense clusters of multipath quickly decay (rather than the residential LOS environment where γ_0 = 12.53). The mean number of clusters ($\bar{L} = 4$) is in between the residential and industrial LOS environments ($\bar{L} = 3$ and $\bar{L} = 4.75$). The inter-cluster decay constant and inter-cluster arrival rate (Λ and Γ) for the operating room channel are more similar to the industrial LOS channel rather than the commercial or residential LOS channels. The operating room LOS channel is similar to the industrial LOS channel in its time domain characteristics (i.e. multipath interference and decay) while it is similar to the residential LOS channel in its frequency domain characteristics.

4.3 Electromagnetic Interference in the Operating Room

EMI in the OR was measured across a wide frequency range in the context of comparing the interference present in useable frequency bands for narrowband and UWB communication and localization systems (for available bands see Table 2-1). These experiments were conducted inside an OR while orthopedic surgeries were being conducted including hip and knee replacements. A wide frequency range of 200 MHz – 26.5 GHz was examined.

Table 4-2: Summary of parameters fit to the IEEE 802.15.4a channel model with experimental UWB data taken in the operating room.

Operating Room	LOS
PL_0 [dB]	-47.5
n	1.33
κ	0.95
$\bar{L}$	4
Λ [1/ns]	0.095
λ [1/ns]	n/a
γ_0 [ns]	1.33
k_γ	0.217
Γ [ns]	10.8

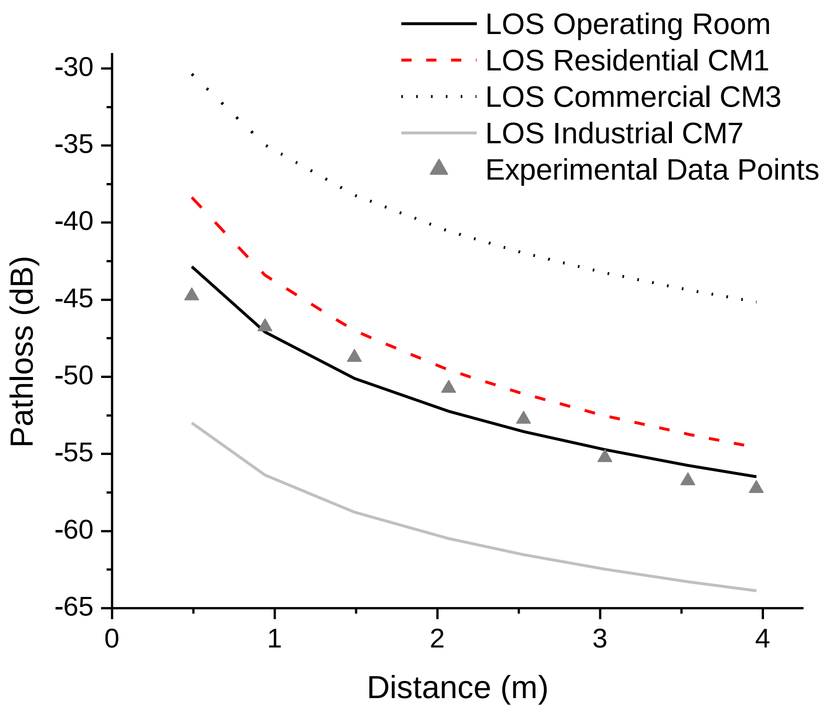

Figure 4-18: Comparison of pathloss for IEEE 802.15.4a LOS channels. The pathloss for the OR environment is most similar to residential LOS [141].

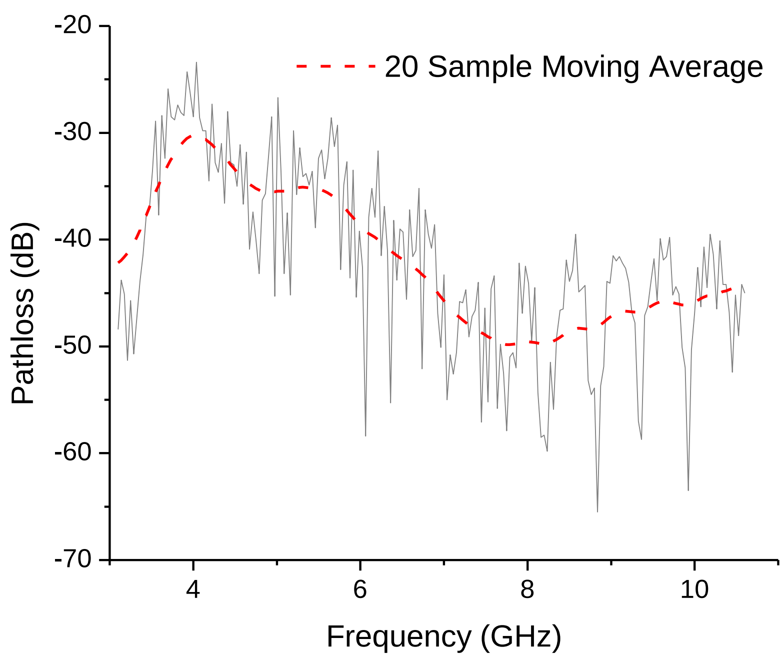

Figure 4-19: Pathloss obtained with the Tx and Rx placed 0.49 m apart where effects from the transmitting (monopole) and receiving (Vivaldi) antennas have been removed. The frequency dependence, κ in Table 4-2, can clearly be seen as well as small scale fading effects.

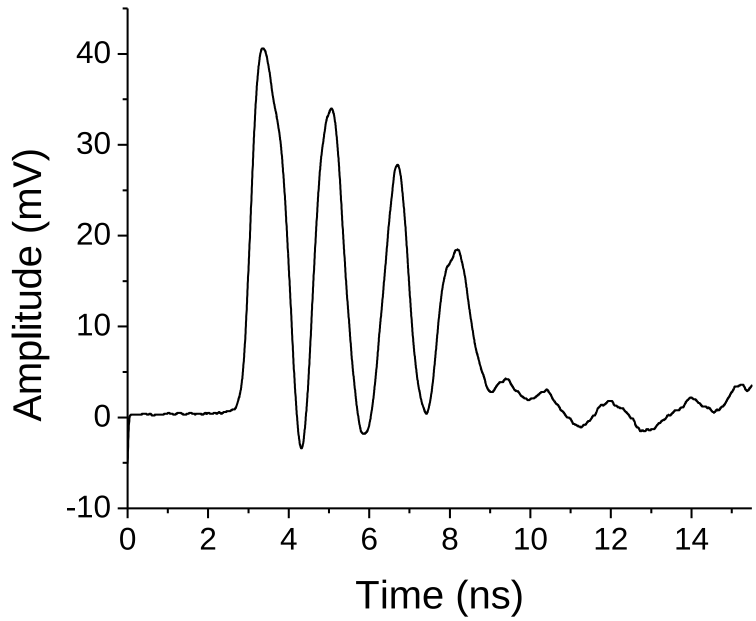

Figure 4-20: Experimental received time domain signal with noticeable multipath interference caused by metal tables and walls in the operating room.

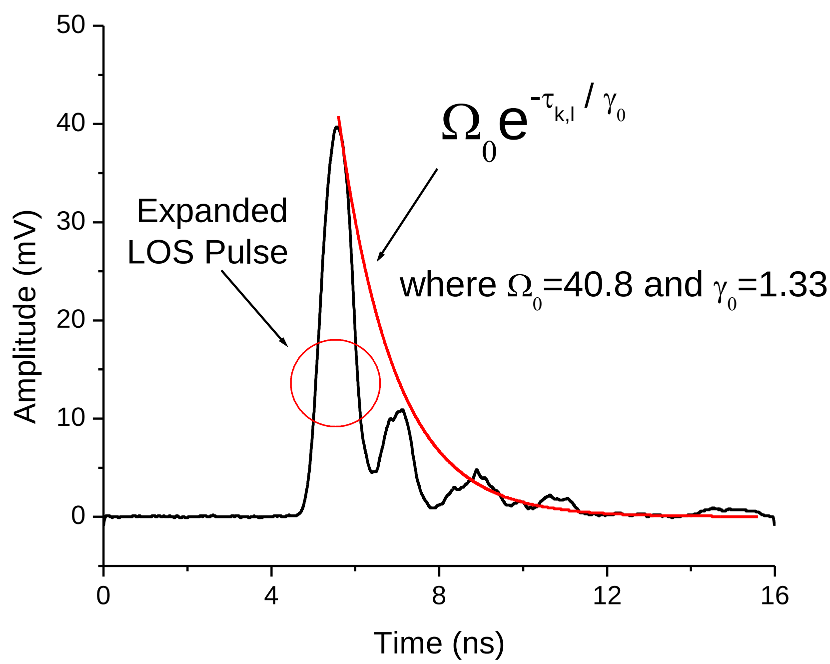

Figure 4-21: Example received signal in the time domain for a Tx-Rx distance of 1.49 m highlighting the distortion (seen as expansion) in the LOS pulse due to a dense cluster of multipath rays. The overlayed exponential is fit using γ_0 as outlined in Table 4-2 to show the intra-cluster decay of the LOS cluster.

4.3.1 Operating Room Indoor Environment

EMI was measured over a large frequency band (200 MHz – 26 GHz) in the OR during four separate orthopedic surgeries. Figure 4-22 shows a layout of the dual OR. Two ORs allow a faster turn-around time in completing the four surgeries. Figure 4-23 shows the experimental setup in the OR. Besides the operating table, numerous other pieces of medical equipment were present during the surgery including an anesthesia machine, ventilator, surgical lamps, various monitoring equipment, visualization screens, carts containing necessary orthopedic surgical tools, drills, etc. Also, numerous people were present including the surgical team, orthopedic company representatives, and spectators observing the surgery. The combination of people and medical equipment closely packed into the OR creates a dense multipath indoor environment that can greatly disrupt standard RFID tracking systems. UWB systems have inherent advantages that make them a strong candidate for use in dense multipath environments such as the OR.

4.3.2 Experimental Setup

Various hardware was needed to get accurate measurements across the wide band of 200 MHz – 26 GHz. Table 4-3 summarizes all of the equipment needed in running this experiment. It should be noted that all reported gain and noise figure values are averages across the frequency range of operation. Figure 4-24 shows the four antennas used to cover the entire frequency range. The standard setup for each of the frequency bands measured included an antenna, two stages of amplification, and a spectrum analyzer for visualization. Commercial off-the-shelf components were used whenever possible.

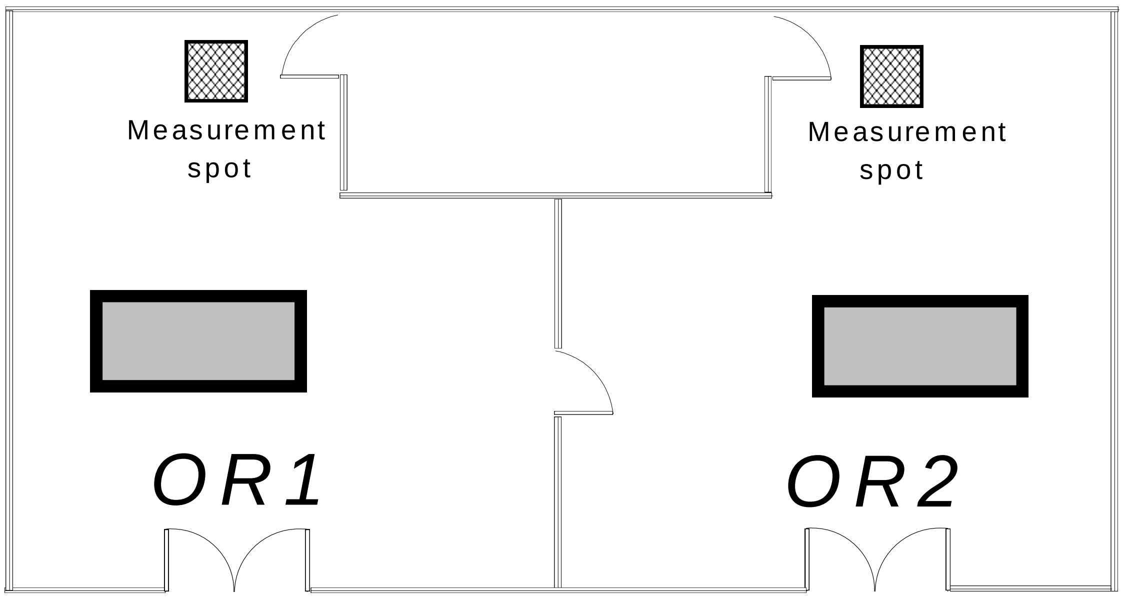

Figure 4-22: Layout of dual operating room including operating tables and measurement locations.

Using the hardware summarized in Table 4-3, four setups were needed to cover the entire frequency range. From 200 MHz – 800 MHz, the biconical antenna (Figure 4-24a) and two Hittite HMC465 LNAs were used. From 800 MHz – 3 GHz, both disc and horn antennas (Figure 4-24b and Figure 4-24c), a Mini-circuits ZX60-3011 LNA, and a Hittite HMC465 LNA were used. From 3 GHz – 18 GHz, the broadband horn (Figure 4-24c) and two Hittite HMC465 LNAs were used. Finally, from 18 GHz – 26 GHz, the Vivaldi 4-element array (Figure 4-24d) and two HMC517 LNAs were used. Before conducting the experiment, it was assumed that most of the EMI detected would be in the range of 200 MHz – 3 GHz. This conclusion was made because WLAN and Bluetooth transceivers (operating at 2.4 – 2.48 GHz) were already present in the OR. Also, this frequency range covers GPS (1.575 GHz), US cellular phone frequencies, and a number of medical bands. Table 2-1 lists the major medical, scientific, and UWB frequency

Figure 4-23: Experimental setup in the OR.

bands in the US and Europe [4],[155],[156]. A majority of the scientific and medical bands in both Europe and the US fall between the frequencies of 200 MHz – 3 GHz. Also, most RFID systems operate in the MHz range up to 3 GHz. Even though RFID systems can operate at 5.8 GHz or 24.125 GHz, limitations still exist on how well a system with small bandwidth can handle the dense multipath environment of the OR at these high frequencies. When looking at different wireless bands currently in use, whether WLAN, cellular phones, GPS, or medical, the advantages of operating in the higher frequency bands of 3.1 – 10.6 GHz and 22 – 29 GHz

Table 4-3: Hardware used in broadband OR measurements.

Device	Model # / Type	Frequency (GHz)	Gain (dB)	Noise Fig. / Pattern
LNA	Mini-circuits ZX60-3011	0.4 – 3	10	1.6 dB
LNA	Hittite HMC465	DC - 20	15	3.5 dB
LNA	Hittite HMC517	17 – 26	19	2.7 dB
Antenna - A	TDK MBA-2501 Biconical	0.25 – 1	23	Omni-directional
Antenna - B	Kathrein Scala 800-10249 Disc	0.824 – 0.960, 1.425 – 3.6, 5.15 – 6	2	Omni-directional
Antenna – C	Double ridged TEM horn	1 – 18	8	Directive
Antenna - D	Vivaldi array – 4 element	18 – 26	10	Directive
Spectrum Analyzer	Agilent E4407B ESA-E	9 kHz – 26.5	n/a	n/a

useable for UWB become clear.

4.3.3 Experimental Results

Using the equipment setup described in Section 4.3.2, EMI was measured over the frequency range of 200 MHz – 26 GHz. The results from these measurements can be seen in Figure 4-25, Figure 4-26, Figure 4-27. A number of signals were detected in the lower frequency

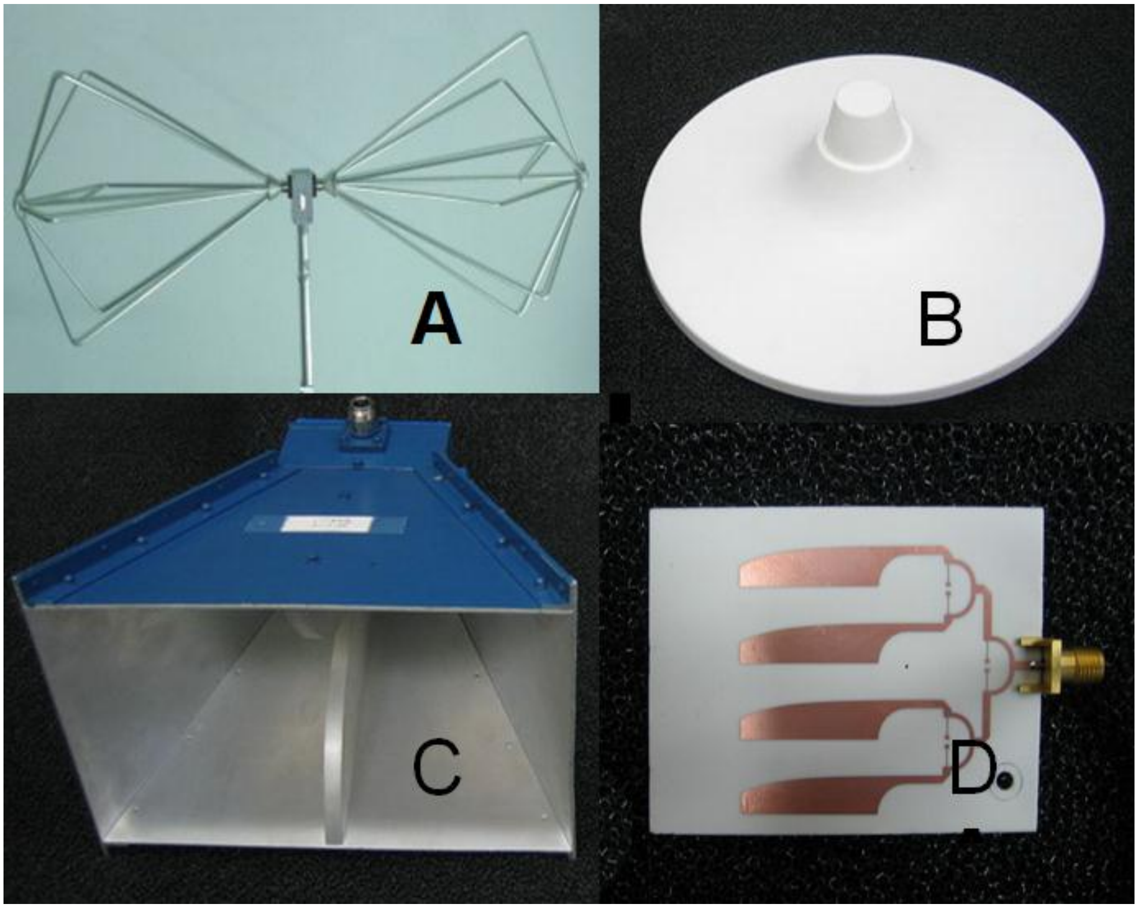

Figure 4-24: Antennas used in OR measurements: a) biconical, b) multiband disc, c) broadband TEM horn, d) 4-element Vivaldi array.

range of 400 MHz – 2.5 GHz. As shown in Figure 4-25, no appreciable signals were picked up between 200 – 800 MHz. Although there is a small spike near 470 MHz, it is only 6dB above the noise floor and is considered noise. Also, there are no licensed frequency bands in the US that could correspond to the 470 MHz peak. Figure 4-26 shows the frequency band from 800 MHz – 3 GHz. A number of different signals were found in this frequency range. The two strongest signals, which were found at 872 MHz and 928 MHz, correspond to CDMA2000 uplinks and downlinks (US cellular bands). The peak at 1.95 GHz also corresponds to a US

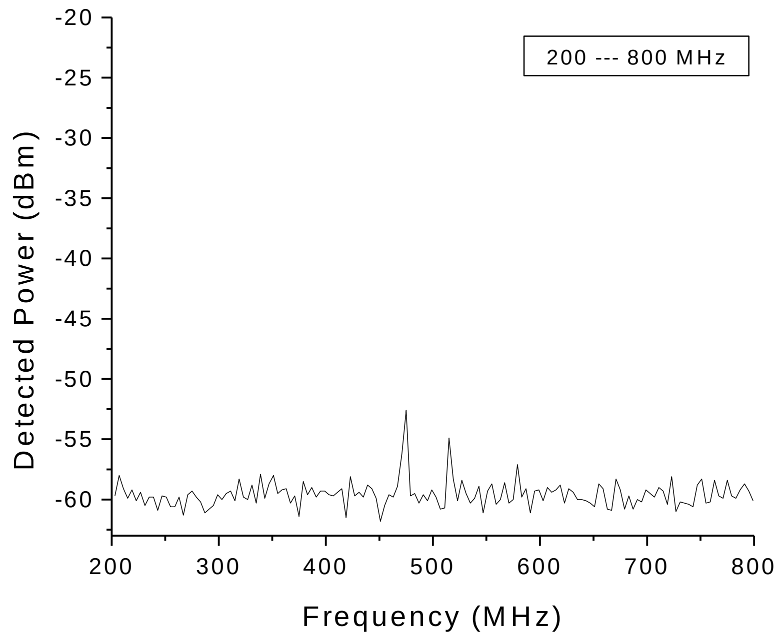

Figure 4-25: Measured EMI over frequency range of 200 – 800 MHz.

cellular band. Finally, the peak at 2.4 GHz is caused by WLAN and Bluetooth components. Figure 4-27 shows the frequency band from 3 – 26 GHz. No noticeable signals were picked up across this entire band. This is somewhat unexpected since there are ISM and WLAN bands between 5 – 6 GHz, which could be the major culprit causing interference that could affect the UWB system. The UWB positioning system operates over a frequency band of 5.4 – 10.6 GHz as shown in Figure 4-28, effectively bypassing all potential EMI except for the U.S. ISM band at 5150 – 5875 MHz, which is where IEEE 802.11a WLAN systems currently operate (802.11n systems also operate in this band). Since interference from this band is a concern for UWB systems operating in the OR, a comprehensive simulation of potential WLAN interference is outlined in Section 4.4.

The frequency bands containing noticeable EMI correspond to widespread technologies

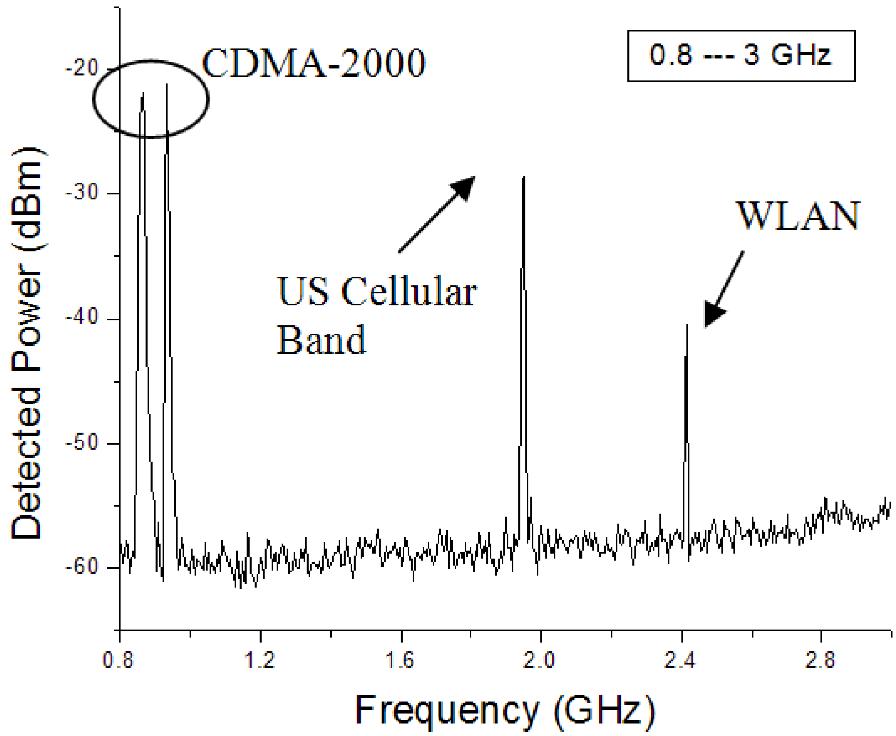

Figure 4-26: Measured EMI over frequency range of 800 MHz – 3 GHz.

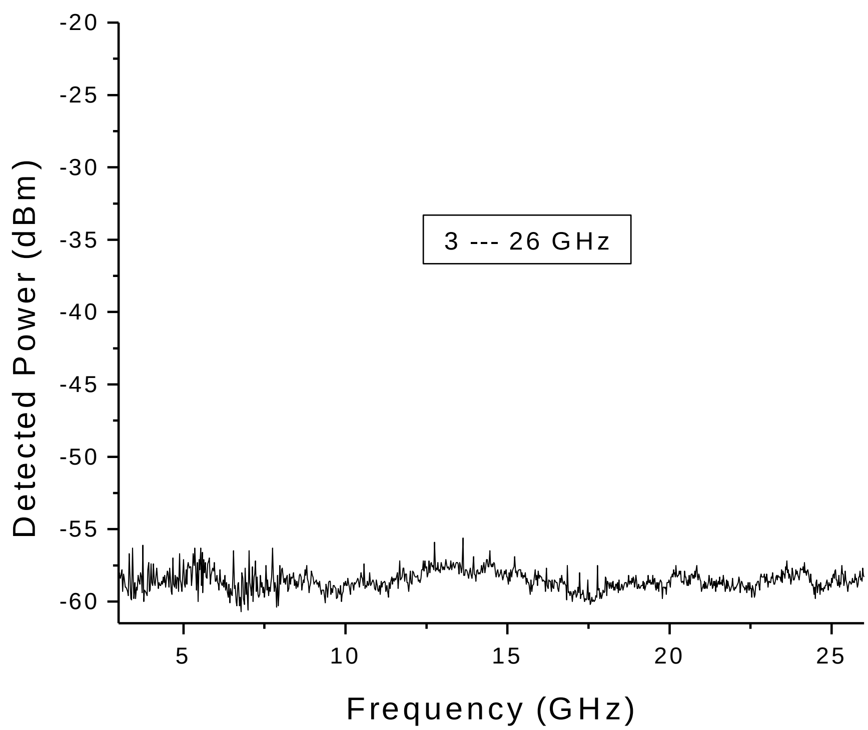

Figure 4-27: Measured EMI over frequency range of 3 – 26 GHz.

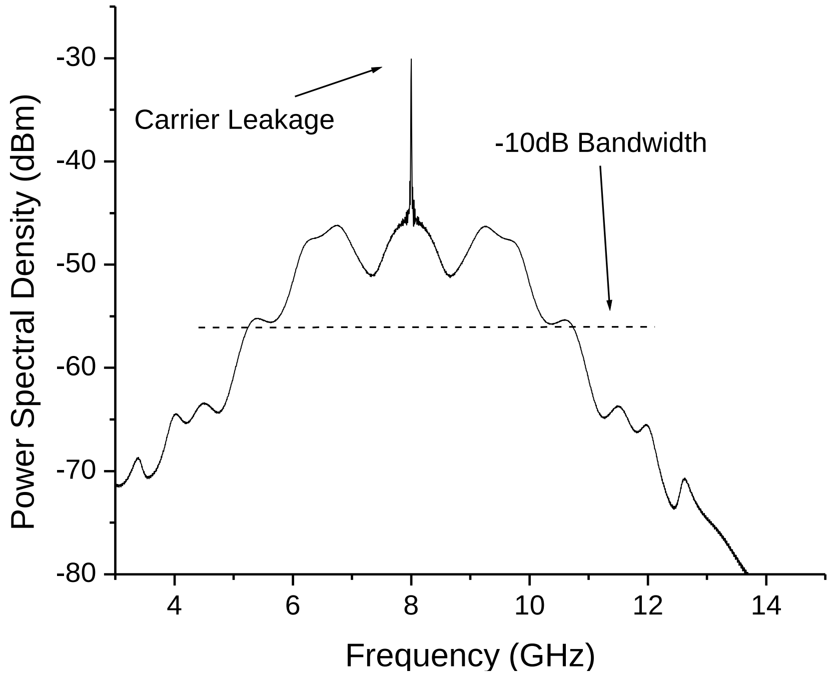

Figure 4-28: Power spectral density of simulated UWB signal showing -10 dB bandwidth from 5.4-10.6 GHz which bypasses interfering signals observed below 3 GHz. This spectrum contains the IEEE 802.11a WLAN band (5.15-5.875 GHz) as outlined in Section 4.4.

that will likely be seen in the average OR. One surprise was the almost complete absence of US scientific and medical bands. Many medical devices do conduct wireless operations at the frequency bands summarized in Table 2-1, but besides the WLAN signal at 2.4 GHz seen in Figure 4-26, no significant EMI corresponding to these frequency bands was detected in the OR.

As outlined in Table 2-1, there is another UWB frequency band from 22 – 29 GHz that can be used for localization systems. As seen from Figure 4-27, there is no EMI in the band from 22 – 26 GHz. One reason for having no EMI is that very few licensed bands exist between 22 – 29 GHz that would affect an OR (most are used for astronomy). Also, signals in this frequency band tend to be attenuated more by the atmosphere and are typically used for short range applications. Using UWB for localization in the OR holds a distinct advantage over other technologies because of both the large bandwidth used as well as the higher frequencies available for operation.

4.4 WLAN Interference at 5 GHz

Technologies exist which operate in frequency bands in the lower UWB spectrum (3.1 – 10.6 GHz), including ISM at 5.15 – 5.875 GHz, WiMAX at 3.3 – 3.8 GHz, 5.15 – 5.35 GHz, and 5.75 – 5.825 GHz, and WLAN at 5.47 – 5.825 GHz. These technologies will directly interfere with an RFID or UWB system operating at or below 5.8 GHz. Some fixes to block WLAN and WiMAX signals from UWB systems include integrating a notch filter into the UWB antenna design [157]. Although this could provide a viable solution, another notch filter would need to be used to block licensed frequencies in the 3 – 4 GHz range (e.g. WiMAX). Zhang et al. examined incorporating notch filters into UWB antennas for LO leakage cancellation [158]. The feasibility of using notch filters to block all possible frequency bands while still being able to correctly transmit an UWB pulse waveform is low. A more feasible solution for an UWB system is to operate in the higher part of the 3.1 – 10.6 GHz band.

The UWB localization system described in Chapter 5 operates from 5.4-10.6 GHz, as shown in Figure 4-28. Since the ISM band extends from 5.15-5.875 GHz and the UWB monopole and Vivaldi antennas operate over this range, the susceptibility of the UWB localization system to interference from IEEE 802.11a/n systems needs to be addressed. A simulation has been performed of the UWB localization system in the presence of a 5 GHz interferer utilizing the simulation framework described in Chapter 6. Agilent ADS was used to generate an IEEE

802.11a WLAN signal. The approach for adding channel effects to the IEEE 802.11a signal is similar to that followed by Bellorado et al. [159]. The pathloss model for the operating room shown in Figure 4-18 was used for modeling the pathloss of both the UWB and IEEE 802.11a signals. LOS between the IEEE 802.11a source and the UWB base stations was assumed. Multipath fading was modeled by a Rician fading channel with a K-factor of 6 dB for the WLAN system. Interference from the IEEE 802.11a source was examined at distances of 1, 2, 5, and 10 m from the UWB base stations. The distance from the UWB transmitter to each UWB base station was kept between 1-2 m LOS and the time domain indoor channel for the OR described in Section 4.2 was used to model multipath interference for the UWB system.

Figure 4-29a shows the power spectral density for an input signal seen at the UWB receiver where both the UWB pulse and IEEE 802.11a signals are present. The WLAN signal is 2 m LOS from the UWB base station. The time extended signal obtained by the UWB receiver for the received signal in Figure 4-29a is shown in Figure 4-30b. No visible UWB pulse is detected because of the high power WLAN interfering signal. Figure 4-29b shows the received signal after passing through two stages of amplification and a three-stage stub-based bandpass filter where a -35 dB stopping amplitude is seen at 5.5 GHz and the passband begins at 6.8 GHz. Zhu et al. achieved comparable experimental performance with multi-stage bandpass filters using ground plane aperture techniques [160]. The added distortion of the UWB pulse from the bandpass filter does not affect the overall system accuracy since the leading-edge detection algorithm (Section 5.2.6) only looks for the initial leading edge rather than attempting to reconstruct the correct pulse shape. Figure 4-30c shows the time extended received signal for the power spectrum shown in Figure 4-29b. The UWB pulse is once again clearly seen, although, as shown in Table 4-4, with the addition of a bandpass filter to remove the WLAN interference, the SNR of the received pulse drops 6.2 dB for a WLAN interferer placed 2 m from the UWB base station. Similar results for the received SNR are seen for WLAN transmitting distances of 1, 5, and 10 m with the SNR increasing as the WLAN interferer moves farther away (9.74 dB with a 10 m distance). The use of automatic gain control, as discussed in Section 6.5, is needed in the UWB localization system both to extend the operating range and also to ensure correct operation in the presence of IEEE 802.11a interference to compensate for the loss in SNR due to the addition of a bandpass filter in the receiver chain.

Table 4-4: SNR of received time extended UWB signals with and without IEEE 802.11a interference.

Received Signal	SNR (dB)
No WLAN Interference	14.4
WLAN Interference	0.165
WLAN Interference with Front-End Filter	8.20

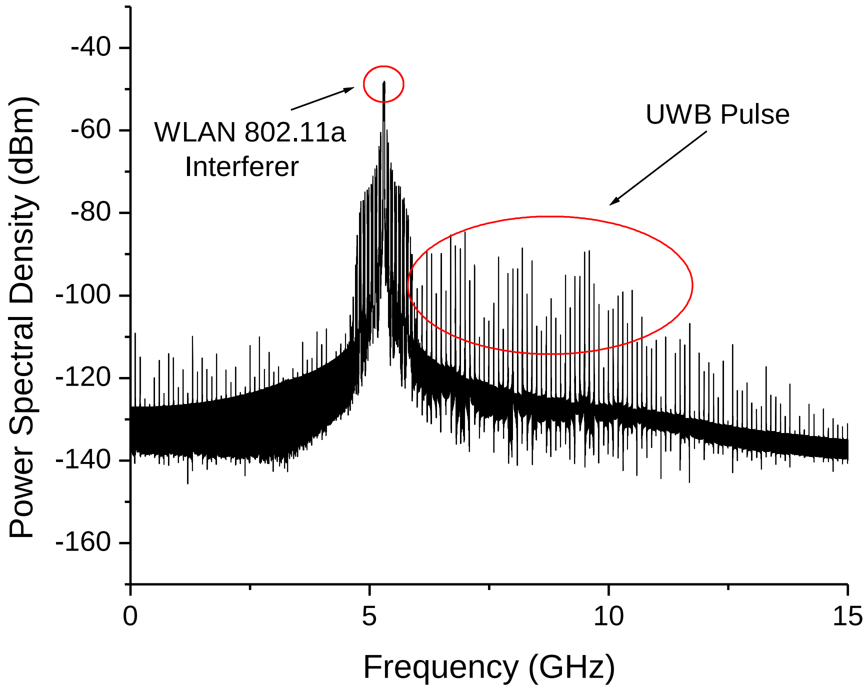

(a)

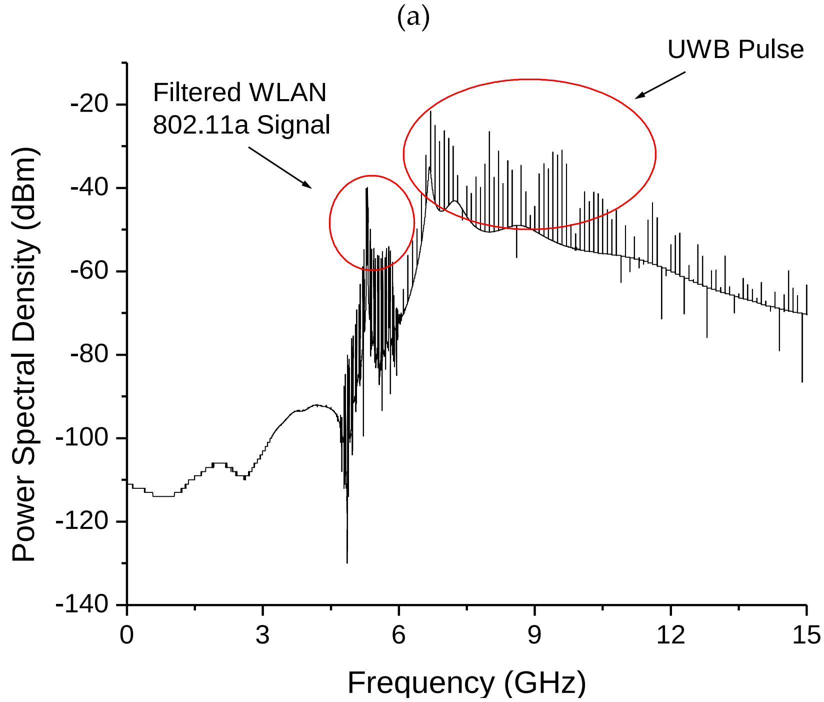

(b)

Figure 4-29: Power spectral density showing the UWB spectrum where (a) the UWB pulse from the positioning system can be seen as well as interference from an IEEE 802.11a source placed 2 m from the UWB base station, (b) the IEEE 802.11a signal is filtered out by the UWB base station.

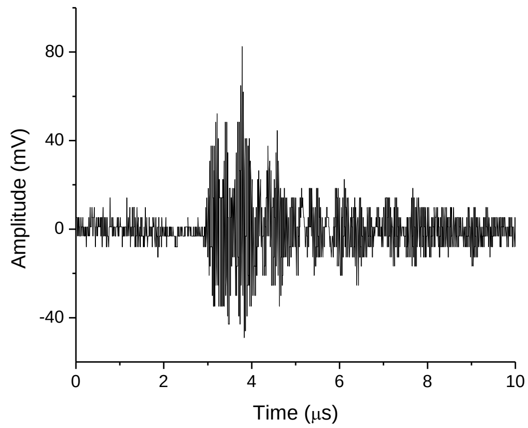

(a)

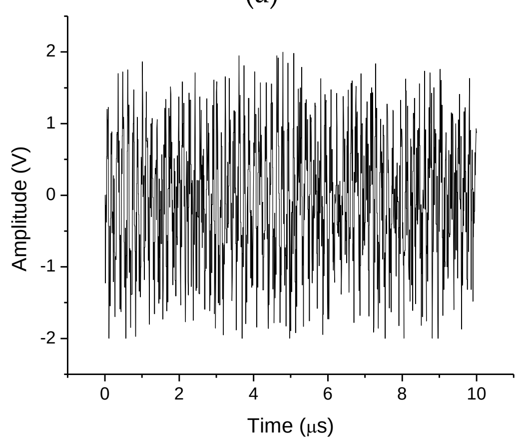

(b)

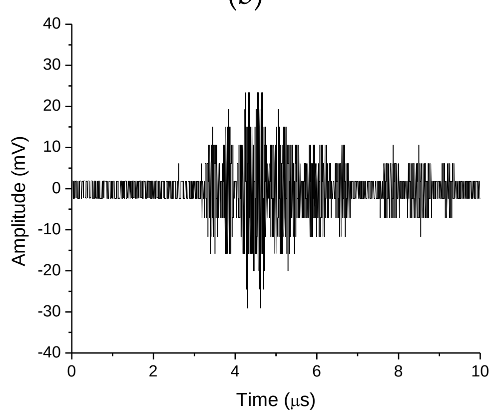

(c)

Figure 4-30: Received time domain signals after passing through the UWB receiver architecture including two stages of amplification, downconversion, LPF, sampling mixer, and ADC conversion. (a) Time extended UWB pulse with no 5 GHz interference, (b) time extended UWB pulse with 5 GHz interference where receiver saturation occurs, (c) time extended UWB pulse with 5 GHz interference and a bandpass filter to mitigate the effects of the IEEE 802.11a interferer.

5. Development of the 1st Generation Real-Time Indoor UWB Positioning System

The challenges in developing the 1st generation millimeter range accuracy real-time UWB positioning system include: generating ultra-wideband pulses, pulse dispersion due to antennas, modeling of complex propagation channels with severe multipath effects, need for extremely high sampling rates for digital processing, synchronization between the tag and receivers' clocks, clock jitter, LO phase noise, frequency offset between the tag and receivers' LOs, and antenna phase center variation. For such a high precision system with mm or even sub-mm accuracy, all these effects should be accounted for and minimized. A comprehensive simulation framework has also been utilized in quantifying the accuracy of the system in realistic multipath, indoor environments in terms of the overall sensitivity to the mentioned challenges in achieving high accuracy (see Chapter 6). In this chapter, the 1st generation UWB positioning system architecture is presented along with methods to mitigate and account for the aforementioned challenges in achieving 3-D real-time millimeter range accuracy. A selected set of experimental results using the first generation UWB positioning system are also included.

5.1 System Architecture

The complete setup of the first generation UWB positioning system is shown in Figure 5-1. The source of the UWB transmitter is an SRD based pulse generator with a pulse width of 300 ps and bandwidth of greater than 3 GHz. A detailed discussion of the pulse generator design can be found in [161]. The Gaussian pulse is up-converted with an 8 GHz carrier and then transmitted through an omni-directional monopole UWB antenna. Multiple base stations are located at distinct positions to receive the modulated pulse signal. The received modulated Gaussian pulse at each base station first goes through a directional Vivaldi receiving antenna and then is amplified through an LNA and demodulated to obtain the I signal. Only one channel rather than I/Q is required since carrier offsets are also applied at the UWB receiver. After going through a LPF, the I channel is sub-sampled using an UWB sub-sampling mixer, extending the signal to a larger time scale (i.e. μs range) while maintaining the same pulse shape [38]. The PRF clocks are set to be 10 MHz with an offset frequency of 1-2 kHz between the tag and base stations which corresponds to an equivalent sampling rate of 50-100 GS/s. Finally, the extended I channel is processed by a conventional ADC and standard FPGA

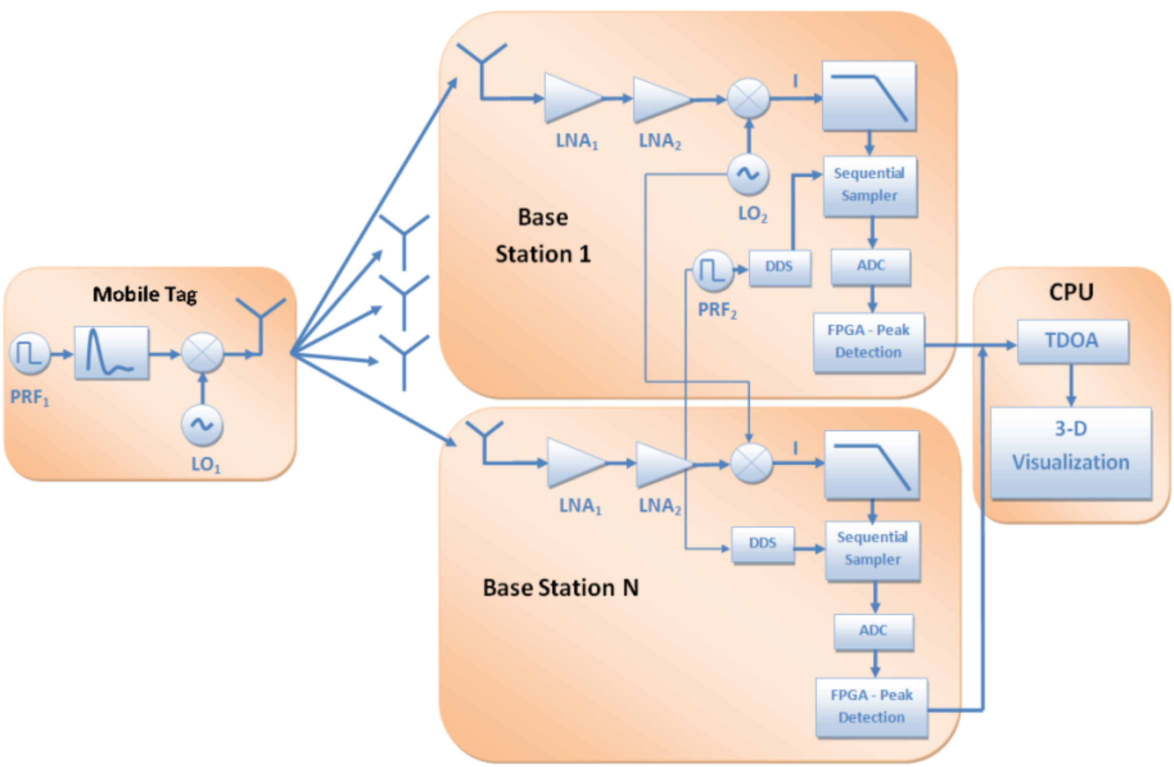

Figure 5-1: System architecture of UWB positioning system which includes a carrier-based transmitted signal at the tag and LO down-conversion and leading-edge detection at the UWB receiver.

unit. Leading-edge detection is performed on the FPGA. The time sample indices are sent to a computer where additional filtering and the final TDOA steps are performed to localize the 3-D position of the UWB tag.

5.1.1 Low Phase Noise Local Oscillators

The impact of phase noise from the LOs at the transmitter and receiver has large effects on the resulting performance of the first generation UWB positioning system. Carriers with high and low phase noise performance have been studied at the UWB transmitter and receiver, and the impact of carrier sources with different phase noise performance on the resulting localization system jitter has been analyzed through experimental analysis. As shown in Figure 5-2, there is an order of magnitude difference in 3-D error when a non-coherent LO base station signal is used compared to having the LO signal coherent at all four base stations when examining the experimental results from the first generation UWB positioning system.

5.1.2 Sub-Sampling Mixer at the UWB Receiver

To detect narrow pulses on the order of a few hundred picoseconds (i.e. 300 ps or 3 GHz bandwidth in our system), analog to digital converters with at least 6 GS/s are needed to satisfy the Nyquist criterion. However, such high performance ADC units are currently either not commercially available or too expensive for most applications. A realistic alternative approach to real-time sampling is to sub-sample the UWB pulses while maintaining the initial pulse shape through extended time techniques. The extended UWB signals can then be handled by readily available commercial ADCs, reducing overall system cost [162],[163]. Both the first

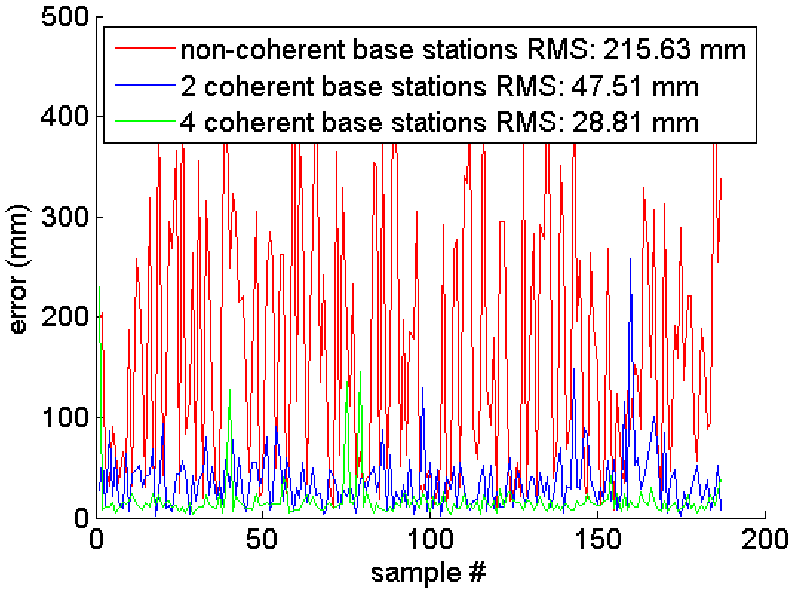

Figure 5-2: Raw data captured using wired transmitter and receiver clocks while changing between coherent and non-coherent LOs at each of the four base stations [93].

generation and second generation systems use a compact UWB sub-sampling mixer integrated with a fast strobe generator for this purpose [38]. The sampler utilizes a simple broadband balun structure [164] and a balanced topology. Figure 5-3 shows the schematic of the designed sampler.

The designed sampler based on the sub-sampling method uses the same technique as the COTS high speed sampling modules, such as the Tektronix 80E01 [165] and Picosecond 7040 [166]. In the actual system, a DDS circuit is used to trigger the strobe-step generator with a PRF of $PRF_2 = f_0 \pm \Delta f$. The original transmitted Gaussian pulse has a repetition frequency of $PRF_1 = f_0$ =10 MHz. If the added offset frequency (Δf) is set to be 100 Hz, the corresponding extending ratio is $\alpha = f_0 / \Delta f$ =100,000. Noticeable ranging errors can occur during the time extension process due to the stability of PRF_1 and PRF_2. This is due to drifting between the two clocks during the

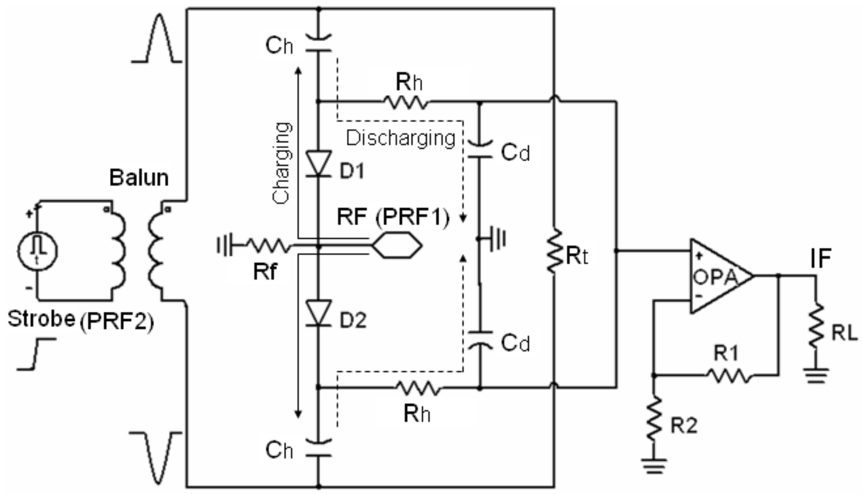

Figure 5-3: Schematic of the sampling mixer highlighting the broadband balun and balanced topology [38].

10 ms interval needed to time extend the signal.

5.1.3 System Clock Jitter and Scaling Effects

The PRF_1 and PRF_2 clock signals (see Figure 5-1) between the tag and receiver in this system are not synchronized. This results in synchronization problems when incorporating the sub-sampling mixer (discussed in Section 5.2.3) since 100,000 pulses are needed to extend the pulse from 300 ps to 30 μs, which corresponds to a 1000 GS/s sampling rate. In the 1st generation system, the extended time signal can then be adequately sampled with a 20 MS/s ADC, given the bandwidth of the sub-sampled signal is 0.03 MHz, although in the actual system the 20 MS/s ADC can be replaced by a higher performance ADC (e.g. 24 bit, 250 MS/s). This can potentially increase system performance by reducing quantization error through extending the dynamic range and increasing the sampling rate with little difference in chip and manufacturing costs.

Techniques exist to calculate clock jitter in the time domain given the phase noise of the crystal [167], and crystal manufacturers provide crystal stability specs in terms of parts-per-million. On the surface, the stability factor would appear to have less of an effect than actual clock jitter. For instance, the stability factor of ±0.5 ppm for the 10.0 MHz Vectron VTC4-A0AA10M000 crystal yields clock jitter of 50 fs [168]. However, the effects of the stability factor are amplified during the sub-sampling process and cause time-scaling to occur.

Any frequency offset occurring between PRF_1 and PRF_2 would cause apparent time-scaling in the sub-sampled signal. The ±0.5 ppm stability of the crystal equates to 5 Hz of variation in the clock signal. This causes the nominal frequency of PRF_1 to be 10.000000 MHz ± 5 Hz and the nominal frequency of PRF_2 to be 9.999900 MHz ± 5 Hz, with the worst case scenario being a difference of 10 Hz between the two signals. If the offset frequency (Δf) is set to be 100 Hz, the corresponding extending ratio is $\alpha = f_0 / \Delta f$ =100,000. However, with a potential offset of ± 10 Hz, Δf has the potential to be 100 ± 10 Hz, thus α = 100,000 ± 11,111. This time scaling may be time-varying depending on the thermal stability of the clocks, although this is a slow variation with a drift rate of less than 10 Hz, which allows the TDOA algorithm to calibrate such systematic error. Since all the base stations acquire synchronous samples clocked by PRF_2, the time-scaling effect will be unknown, but consistent across receivers. Consequently, the 1-D ranging errors will be roughly ±11%. The TDOA algorithm using time differences will likewise be affected. This problem has been examined in the field of geolocation [169], and has been likened to multidimensional scaling [170].

Besides stability, the jitter of these 10 MHz clocks must be examined. When the phase noise is integrated from 1 Hz – 5 MHz using an Agilent E5052A Signal Source Analyzer, RMS jitter for the crystal is found to be between 1 – 1.5 ps [168],[171]. This technique is the most accurate way to measure clock jitter of highly stable crystals. If 1.5 ps of RMS jitter is assumed for both 10 MHz crystals, total system RMS jitter σ_{sys} due to the two unsynchronized clocks of 2.12 ps is obtained

$$\sigma_{sys} = \sqrt{\sigma_{clk\,1}^{2} + \sigma_{clk\,2}^{2}} \tag{5-1}$$

where σ_{clk1} and σ_{clk2} are assumed to be uncorrelated normal random variables [167],[172] of mean $\mu = 0$ and standard deviation $\sigma = 1.5$ ps. The jitter described in (5-1) will cause normally distributed noise of $\mu = 0$, $\sigma = 2.12$ ps (corresponds to 0.64 mm error) to be added to each sampled point. A simulation using Agilent ADS2006A has been carried out to study how such jitter affects the sampler performance during the sub-sampling process. Figure 5-4 shows the measured time variation of the pulse peak position at consecutive measurement cycles. The peak to peak variation is below 10 ps while the RMS jitter is 3.48 ps. The measured RMS jitter is 1.36 ps larger than the theoretical result of 2.12 ps, which can be interpreted as the added jitter from the sub- sampling mixer, DDS, and ADC circuitry. The measured system clock jitter of 3.48 ps corresponds to 1.05 mm of error.

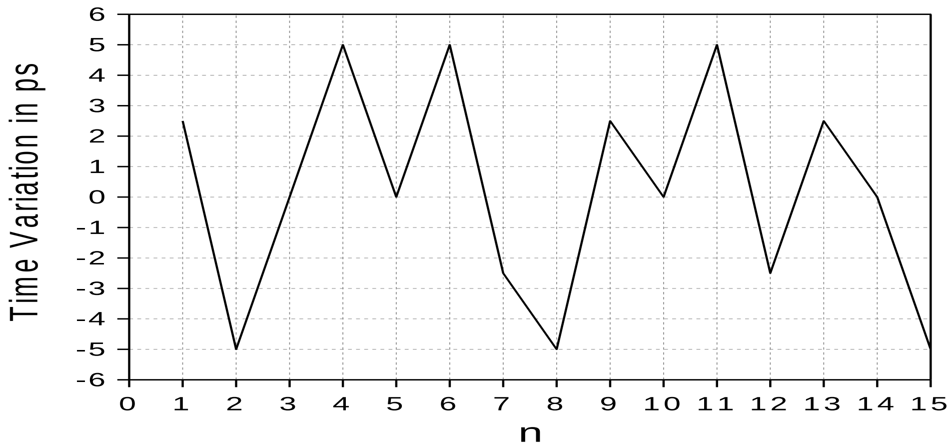

Figure 5-4: Time variation of the pulse peak position acquired over *n* sample points [18].

5.1.4 Energy Detection after the Sub-Sampling Mixer

An important problem of the first generation UWB positioning system using the single channel approach is the carrier-leakage present in the received signals and its effects on the 1-D ranging of the UWB positioning system. Figure 5-5 shows the single channel output after the sub-sampling process when the tag is put at a static position. The "shoulders" come from the equivalent offset carrier frequency $\Delta\omega_{eq}$, which modulates the time extended pulse signal $P_{ex}(t)$. The impact of phase noise from the carrier source has been translated not only as the timing jitter, but also as the "shoulder" amplitude variation of the modulated signal. When the SS method with a fixed voltage triggering threshold is used, the random "shoulder" amplitude variation produces another source of error. When the tag is moving, the peak amplitude may vary, causing 1-D ranging errors in accurately detecting the received signal.

To further understand the impact of the "shoulder" effect, the dynamic scenario has been investigated. Under this situation the tag is considered moving continuously away from

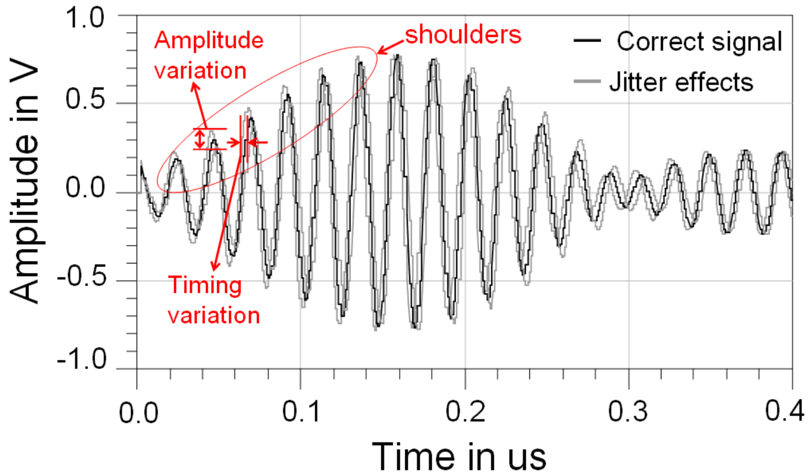

Figure 5-5: The "shoulder effect" in static scenario: the received single channel sub-sampled signal modulated by the equivalent offset carrier frequency [19].

the base station up to one wavelength at the carrier frequency. In the simulation model, in order to study how the "shoulder" effect responds only to the tag dynamic movement, no phase noise was included in the carriers. Table 5-1 compares energy detection versus no energy detection using the system architecture described in Figure 1-6. The simulated time position errors have been recorded as the tag moves a distance of one wavelength, and the standard deviation errors have been calculated. It shows that the energy detection minimizes the "shoulder" effect and substantially reduces the standard deviation error. No carrier phase noise effects are included in the simulated results.

Table 5-1: Simulated standard deviation error for dynamic scenario.

No Energy detection		Energy Detection	
18.0 ps	5.40 mm	2.87 ps	0.86 mm

5.1.5 Leading-Edge Detection

The leading-edge detection scheme used in the 1st generation UWB system described in this chapter is Merkl's max-ratio leading-edge detection algorithm [93] outlined in Algorithm 1.

Algorithm 1: Max Ratio Leading-Edge Detection [93]

---

1. Let $h(t)$ be the received UWB multipath signal as defined by the IEEE 802.15.4a channel model.

$$h(t) = \sum_{l=0}^{L}\sum_{k=0}^{K} a_{k,l}\exp\left(j\varphi_{k,l}\right)\delta(t - T_l - \tau_{k,l}) \tag{5-2}$$

2. $h(t)$ is converted to digital by a 105 MSPS, 10 bit ADC providing 1024 discrete values and denoted $h[t]$.

3. $h[t]$ is passed through a 16-element averaging window

$$y[t] = avewindow(abs(h[t]),16) \tag{5-3}$$

where $avewindow(x, n)$ denotes the function which averages the signal for a window size n and $abs()$ takes the absolute value of the original signal $h[t]$ [93].

4. The averaged signal $y[t]$ then goes through two maximum window filters of sizes n_1 and n_2 samples

$$\text{max\_}n_1[t] = maxwindow(y[t], n_1) \tag{5-4}$$

$$\text{max\_}n_2[t] = maxwindow(y[t], n_2) \tag{5-5}$$

where $maxwindow(x, n)$ denotes the function which returns the maximum for a given window size n. For the original algorithm $n_1 = 16$ and $n_2 = 272$.

5. A binary ratio is obtained

$$\begin{aligned} \mathrm{r}[t] = (&\text{max\_}n_1[t] * \alpha > \text{max\_}n_2[t]\ \&\& \\ &\text{max\_}n_2[t]\ > thresh) \end{aligned} \tag{5-6}$$

where α is a fixed threshold (currently set to two), $thresh$ is an estimate of the noise defined in (5-7), and r$[t]$ is the final binary value indicating whether or not a leading-edge has been detected [93].

6. $$thresh = n_{noise} + t_{switch} \tag{5-7}$$

where n_{noise} is an estimate of the current noise level and t_{switch} is a manually set threshold which can be set to 2^n for n=0,1,2,..,8, typically set to n=0.

5.1.6 Antenna Phase Center Error

Accounting for antenna phase center variation at the transmitters and receivers is critical for performance in high accuracy localization systems. Ideally all frequencies contained in the pulse are radiated from the same point of the UWB antenna and thus would have a fixed phase center [173]. In this case, all frequencies travel the same distance within the same time, and the pulse can be received undistorted.

In practice, however, the phase center varies with both frequency and direction. For localization systems that require high accuracy, this can result in significant localization errors. For example, to compensate for phase center variation in GPS antennas, automated high precision robots are used in a calibration procedure to move a GPS antenna into 6000 – 8000 distinct orientations [174]. In the case of our transmitting antenna, which is an UWB monopole, phase center variation is less than 1 mm and is considered negligible (both across the frequency band from 6 – 10 GHz and as the azimuth angle is varied). Phase center variation along the broadside direction was simulated to estimate the axial position of the Vivaldi phase center.

Figure 5-6 shows the simulated phase center variation over the desired frequency band at broadside using CST software, with the original point set at the input of the Vivaldi antenna, as shown in Figure 5-7. The variation in phase center over frequency can be further reduced by placing a dielectric rod over the end-fire portion of the Vivaldi antenna [175]. The average phase center position across the frequency band of 6 – 10 GHz is obtained at 39.5 mm which is later used as the "apparent phase center" in directivity-dependent phase center measurements.

Since the UWB pulse contains broadband frequency information, a more accurate method for defining the phase center variation of the Vivaldi antenna is to employ time domain techniques. As shown in Figure 5-7, an experiment was setup in an anechoic chamber to quantify how the phase center is affected by the directivity based on time domain measurement. Both transmitting and receiving Vivaldi antennas were put face to face and separated by a distance of 1.5 m. The receiving antenna was rotated around the calculated "apparent phase center" (at 39.5 mm, shown in Fig. 17) from -45° to $+45^{\circ}$ at 5° per step. The apparent phase center was tracked on the receiving Vivaldi antenna as it was rotated from -45° to $+45^{\circ}$ with an optically tracked probe. These reference points from the optical system were used to calculate the actual center of rotation during the experiment. This allowed changes in the actual phase center as the receiving antenna was rotated to be separated from physical movement of the apparent phase center, shown in Figure 5-7.

Figure 5-8 shows the measured phase center displacement for both the E and H cuts. As shown in Figure 5-8, the measured phase center variation versus rotating angle indicates a

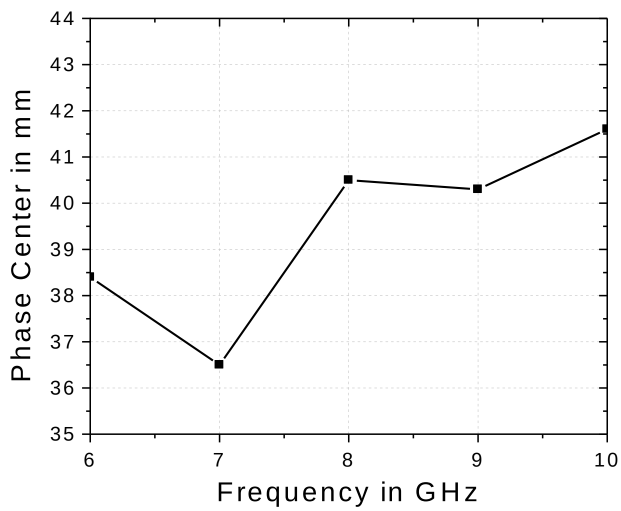

Figure 5-6: Simulation of broadside Vivaldi phase center location versus frequency [18].

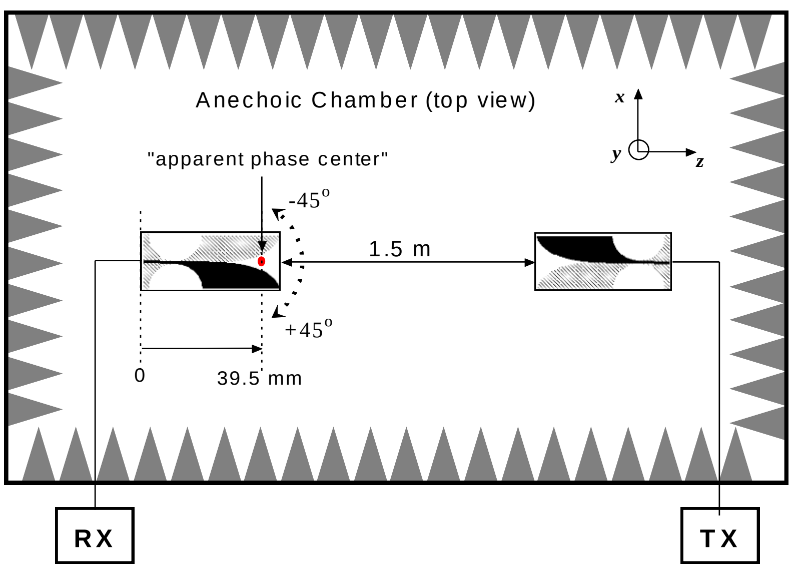

Figure 5-7: Experimental setup of Vivaldi antennas in an anechoic chamber used to measure Vivaldi antenna directivity-dependent phase center variation [18].

small phase center variation of less than 2 mm within $\pm 20^{\circ}$ while the variation degrades dramatically with an angle greater than 30°. TDOA-related error due to this phase center error can be minimized by varying the number of base stations and their orientation in a standard size room. Additionally, other techniques to calibrate out the phase center error in a practical

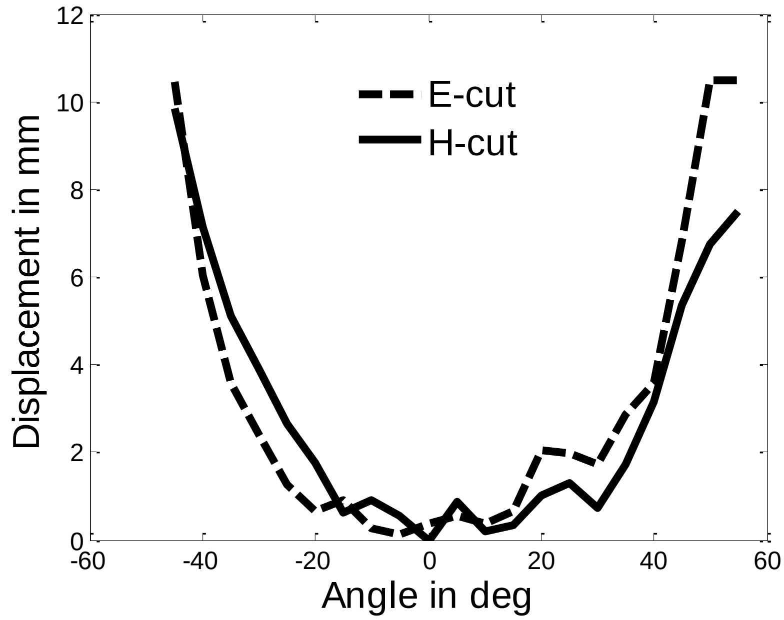

Figure 5-8: Measured Vivaldi phase center error versus angle for E-cut and H-cut.

system by either assuming or measuring orientation for each base station is required to achieve sub-mm accuracy.

5.1.7 Time Difference of Arrival

Algorithm 2: TDOA Algorithm

There are four receivers at known positions R_{x1} or (x_1, y_1, z_1), R_{x2} or (x_2, y_2, z_2), R_{x3} or (x_3, y_3, z_3), and R_{x4} or (x_4, y_4, z_4), and a tag at unknown position (x_u, y_u, z_u) (Figure 5-9). The measured distance between four known receivers to the unknown tag can be represented as ρ_1, ρ_2, ρ_3, and ρ_4, which is given by

$$\begin{aligned}\rho_i &= \sqrt{(x_i - x_u)^2 + (y_i - y_u)^2 + (z_i - z_u)^2} + ct_u \\ &= f(x_u, y_u, z_u, t_u)\end{aligned} \tag{5-8}$$

where i = 1, 2, 3, and 4, c is speed of light, and t_u is the unknown time delay in hardware. The differential distances between four receivers and the tag can be written as

$$\begin{aligned}\Delta\rho_{1k} &= \rho_1 - \rho_k \\ &= \sqrt{(x_1 - x_u)^2 + (y_1 - y_u)^2 + (z_1 - z_u)^2} \\ &- \sqrt{(x_k - x_u)^2 + (y_k - y_u)^2 + (z_k - z_u)^2}\end{aligned} \tag{5-9}$$

where k = 2, 3, and 4, and the time delay t_u in hardware has been cancelled. Differentiating this equation will give

$$\begin{aligned}d\Delta\rho_{1k} &= \frac{(x_1 - x_u)dx_u + (y_1 - y_u)dy_u + (z_1 - z_u)dz_u}{\sqrt{(x_1 - x_u)^2 + (y_1 - y_u)^2 + (z_1 - z_u)^2}} \\ &+ \frac{(x_k - x_u)dx_u + (y_k - y_u)dy_u + (z_k - z_u)dz_u}{\sqrt{(x_k - x_u)^2 + (y_k - y_u)^2 + (z_k - z_u)^2}} \\ &= \left(\frac{x_1 - x_u}{\rho_1 - c\tau_u} + \frac{x_k - x_u}{\rho_k - c\tau_u}\right)dx_u \\ &+ \left(\frac{y_1 - y_u}{\rho_1 - c\tau_u} + \frac{y_k - y_u}{\rho_k - c\tau_u}\right)dy_u \\ &+ \left(\frac{z_1 - z_u}{\rho_1 - c\tau_u} + \frac{z_k - z_u}{\rho_k - c\tau_u}\right)dz_u\end{aligned} \tag{5-10}$$

In (5-10(5-12), x_u, y_u, and z_u are treated as known values by assuming some initial values for the tag position. dx_u, dy_u, and dz_u are considered as the only unknowns. From the initial tag position the first set of dx_u, dy_u, and dz_u can be calculated.

These values are used to modify the tag position x_u, y_u, and z_u. The updated tag position x_u, y_u, and z_u can be considered again as known quantities. The iterative process

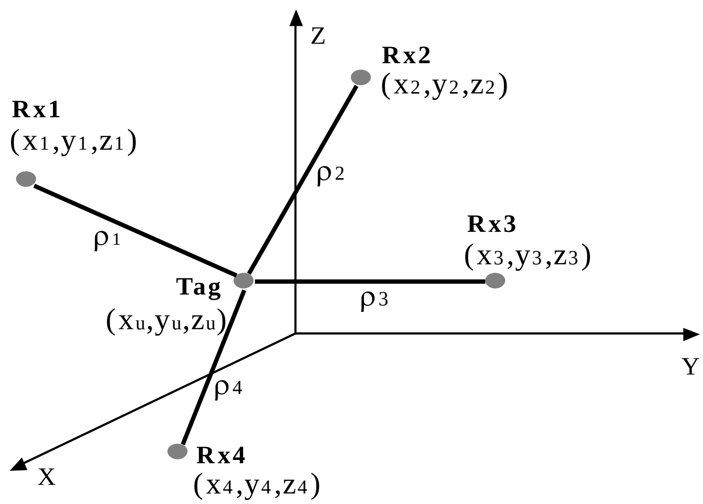

Figure 5-9: Calculation of tag position based on TDOA approach.

continues until the absolute values of dx_u, dy_u, and dz_u are below a certain predetermined threshold given by

$$\varepsilon = \sqrt{dx_u^2 + dy_u^2 + dz_u^2} \tag{5-11}$$

The final values of x_u, y_u, and z_u are the desired tag position. The matrix form expression of (5-10) is

$$\begin{bmatrix} d\Delta\rho_{12} \\ d\Delta\rho_{13} \\ d\Delta\rho_{14} \end{bmatrix} = \begin{bmatrix} \alpha_{11} & \alpha_{12} & \alpha_{13} \\ \alpha_{21} & \alpha_{22} & \alpha_{23} \\ \alpha_{31} & \alpha_{32} & \alpha_{33} \end{bmatrix} \begin{bmatrix} dx_u \\ dy_u \\ dz_u \end{bmatrix} \tag{5-12}$$

where

$$\begin{aligned} \alpha_{k-1,1} &= \frac{x_1 - x_u}{\rho_1 - c\tau_u} + \frac{x_k - x_u}{\rho_k - c\tau_u} \\ \alpha_{k-1,2} &= \frac{y_1 - y_u}{\rho_1 - c\tau_u} + \frac{y_k - y_u}{\rho_k - c\tau_u} \end{aligned} \tag{5-13}$$

$$\alpha_{k-1,3} = \frac{z_1 - z_u}{\rho_1 - c\tau_u} + \frac{z_k - z_u}{\rho_k - c\tau_u}$$

The solution of (5-13) is given by

$$\begin{bmatrix} dx_u \\ dy_u \\ dz_u \end{bmatrix} = \begin{bmatrix} \alpha_{11} & \alpha_{12} & \alpha_{13} \\ \alpha_{21} & \alpha_{22} & \alpha_{23} \\ \alpha_{31} & \alpha_{32} & \alpha_{33} \end{bmatrix}^{-1} \begin{bmatrix} d\Delta\rho_{12} \\ d\Delta\rho_{13} \\ d\Delta\rho_{14} \end{bmatrix} \tag{5-14}$$

where *[ ]*$^{-1}$ represents the inverse of the α matrix. If there are more than four receivers, the least-squares approach can be applied to find the tag position.

5.2 Real-Time Experiments

Two 3-D experiments with unsynchronized LOs and PRF clock sources were carried out, where four base stations are used for the 3-D TDOA measurements.

5.2.1 3-D Dynamic Free Motion

The 3-D positions were measured for each base station utilizing the Optotrak 3020 system, which also serves as a reference for comparing the 3-D real-time accuracy of the 1st generation UWB localization system. The Optotrak 3020 has 3-D real-time accuracy of better than 0.3 mm. The basic experimental setup is shown in Figure 5-10. It should be noted that the spatial spread of the base stations along the z-axis is the largest (2498 mm), while the x-axis is the smallest (1375 mm). In the dynamic mode, the tag is moving randomly inside the 3-D space. The 3-D motion of the tag is then plotted and UWB measurements are compared with Optotrak measurements. RMSE is used to report the error since it is the true unbiased error when data values fluctuate above and below zero. Figure 5-11 plots the UWB trace and Optotrak trace in the 3-D dynamic mode for freeform motion. The overall 3-D RMSE is 6.37 mm. The error along the *x-axis* contributed most to the overall distance error, which can be explained by the limited spread of base stations along the *x-axis* and can be calculated using the PDOP definitions in [18].

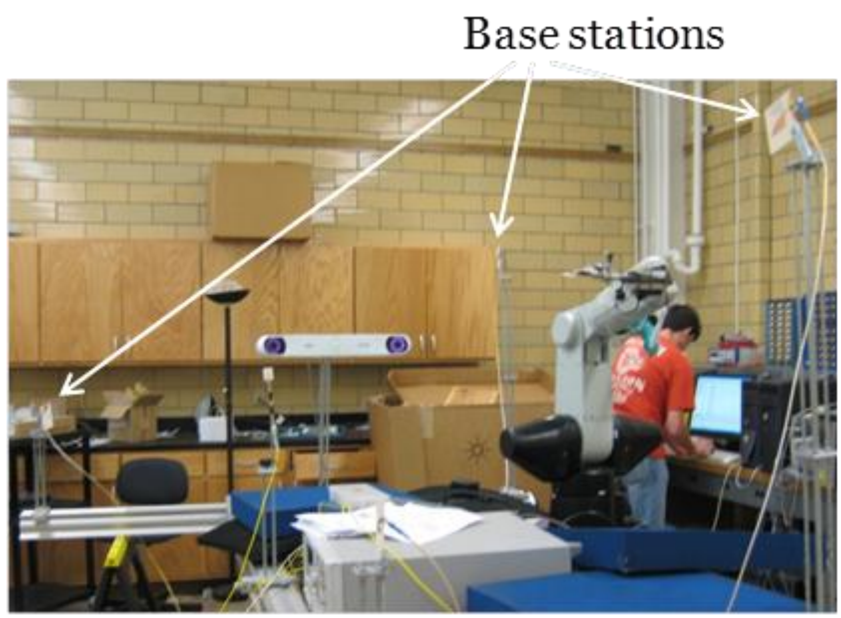

Figure 5-10: 3-D localization experiments with four base stations deployed.

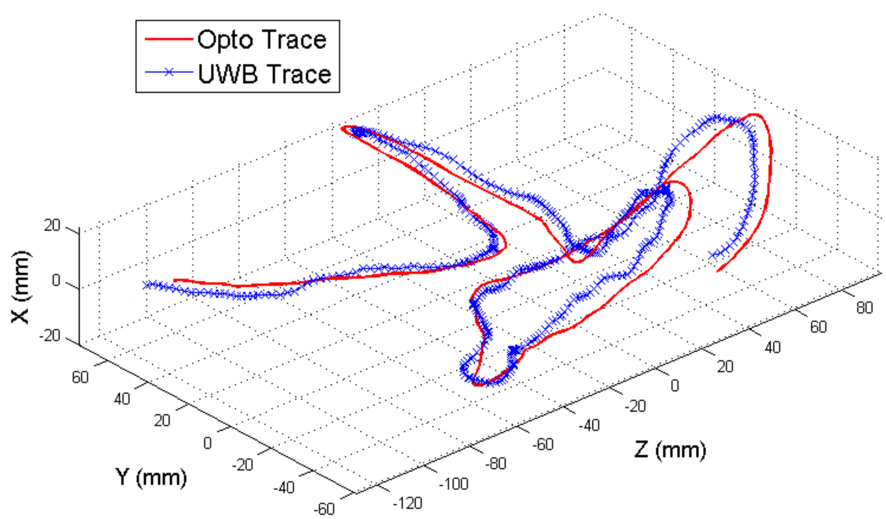

Figure 5-11: 3-D dynamic random mode with energy detection. UWB trace is compared to Optotrak trace [19].

5.2.2 3-D Robot Tracking

The next 3-D experiment is dynamic tracking of a robot position. The experimental setup is shown in Figure 5-12. The monopole antenna and the reference Optotrak probe are tied together and then fixed to the arm of the CRS A465 robot. The robot was pre-programmed to specifically cover 20 distinct static positions in a 3-D volume, stopping for three seconds at each position and then moving to the next position and so on. The measured traces by the UWB system are compared to the Optotrak reference system as shown in Figure 5-13. The overall dynamic 3-D robot tracking RMSE is 5.24 mm. In Table 5-2 the real-time 3-D experimental results are summarized under various scenarios for the first generation UWB positioning system. The reported RMSE are based on 1000 continuous data points recorded and compared to the Optotrak 3020 system.

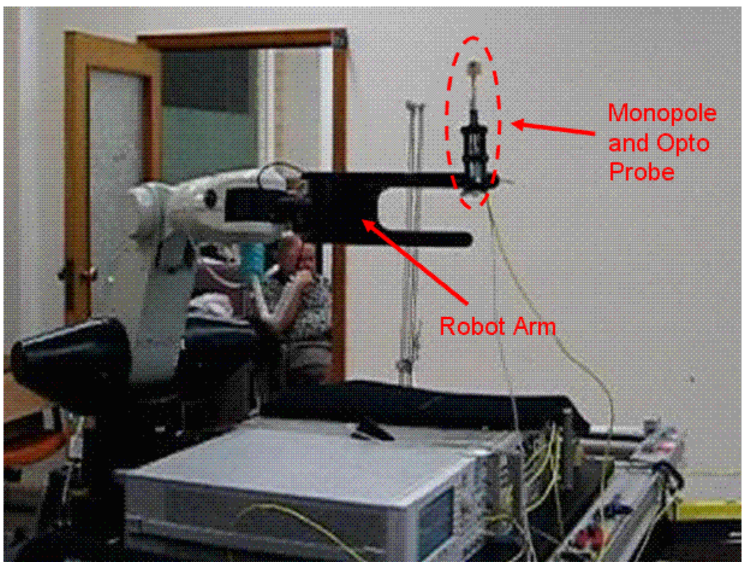

Figure 5-12: Experimental setup of robot tracking using the first generation UWB positioning system.

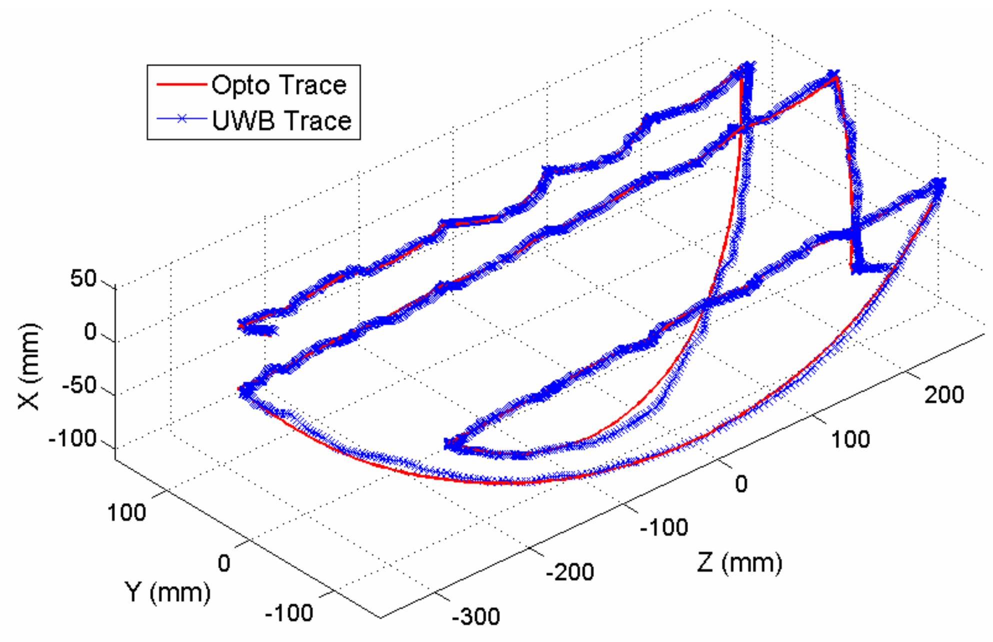

Figure 5-13: 3-D dynamic robot tracking. UWB trace compared to Optotrak trace [19].

Table 5-2: Error Summary – 3-D unsynchronized localization experiments.

3-D Experiments	RMSE (mm)
Tag free random motion	6.37
Robot dynamic tracking	5.24
Robot static positions (20 distinct locations)	4.67
Static position w/ 106 times of average	1.98

5.3 Limitations of the 1st Generation UWB Positioning System

The first generation UWB positioning system overcame many challenges and resulted in achievable accuracy levels of 5-6 mm 3-D real-time accuracy. This accuracy is considered ground breaking for a wireless positioning system of this type in real-time dynamic 3-D experiments. Conversely, the first generation UWB positioning system has key limitations which limit its application and use as a viable real-time location system moving forward. These limitations include:

- Low phase noise local oscillators required at both the tag and receiver (bench-top instruments)
    - Not practical for real system implementation
    - Requires tag and receiver redesign
- System has been tested with only one tag
    - Design tradeoffs and other practical issues arise when adding multi-tag tracking
- System has been tested with only four base stations
    - More base stations can improve accuracy by reducing geometric dilution of precision
- System has not been tested in non-light-of-sight conditions
- The ultra-wideband operating room channel has not been characterized to facilitate UWB systems designed for the OR

These limitations are addressed in the second generation UWB RTLS. The second generation system is outlined in Chapters 7-10 and discusses solutions to these limitations including a true energy detection receiver to remove the low phase noise LO dependency, a complete multi-tag system, five base station experiments compared to four base station experiments, system performance in NLOS conditions, and the UWB operating room channel.

6. A System-Level Simulation Framework for UWB Localization

This chapter is largely derived from the journal article published in the IEEE Transactions on Microwave Theory and Techniques in December 2010 titled "A system-level simulation framework for UWB localization" [179]. I would like to thank my coauthors Mohamed Mahfouz, Cemin Zhang, Brandon Merkl, and Aly Fathy for their contributions to this work.

UWB positioning systems have inherent advantages when applied to indoor environments, most notably their robustness to multipath interference. A need exists within the RFID market (total projected revenue in 2009 of 5.56 billion USD) for high accuracy, indoor, real-time 3-D location information [2]. Clark et al. ran an experiment where five indoor positioning systems (narrowband signal strength, Wi-Fi, ultrasound, RF, and UWB) were tested in multiple locations inside an operating room at a hospital and compared for their performance in 3-D indoor localization [86]. The UWB system (Ubisense [14]) was the only system of the five to consistently achieve 3-D positioning accuracy of less than a meter. The most notable commercial UWB indoor localization systems are the Sapphire DART system from Zebra Technologies Corporation, the RTLS from Ubisense, the PLUS system from Time Domain Corp., and the DecaWave RTLS, shown in Table 6-1 [13],[14],[63],[64]. The Symeo LPR-2D is a positioning system based on FMCW technology with performance comparable to commercial UWB positioning systems [9]. As shown in Table 6-1, many different positioning techniques are used in these systems including TDOA, AOA, TOA, and RTOF [3].

Wireless positioning systems have also received a large amount of attention among research groups. This includes systems built using impulse-based (i.e. carrier-free) UWB,

Table 6-1: Comparison of commercial wireless indoor positioning systems.

Company	Freq (GHz)	Range (m)	Tags	Localization Method	Accuracy (cm)
Ubisense [14]	5.8 – 7.2	50	>1000	TDOA and AOA	< 15
Zebra [13]	5.9– 7.1	50	>100	TDOA	< 10
Time Domain [63]	6.1 – 7.1	30-58	8000	TDOA	30-90
DecaWave [64]	3.5-7	70-500	11,000	TOA and TDOA	< 10
Symeo [9]	5.7-5.9	400	n/a	RTOF	5

carrier-based UWB, and FMCW. An excellent comparison of various systems designed by research groups using these approaches can be found in [19]. The first generation system outlined in Chapter 5 is a carrier-based UWB indoor positioning system which outperforms current commercial systems by an order of magnitude (i.e. mm-range 3-D accuracy) [18],[19],[141],[176]. This system uses a unique approach where only one channel is downconverted instead of an I/Q downconversion process [19]. This is combined with a sub-sampling mixer [38] to time extend the UWB signal and make it easier to sample with a conventional ADC (e.g. 105 MSPS, 10 bit). The final step is a novel leading-edge detection algorithm which locates the rising edge of the incoming UWB pulse and is extremely robust to multipath interference [93],[177],[178]. The experimental results from this system show its mm-range accuracy to be intact even in a dynamic experiment where the transmitter is allowed to freely move about in 3-D [19].

A novel simulation framework is utilized to simulate the complete UWB positioning system in realistic indoor channel environments [179]. This includes the analog and digital portions of the UWB transmitter and receiver, the UWB antennas, the UWB indoor channels, and the final index filtering and TDOA calculations done on a computer. This simulation framework utilizes ADS from Agilent [180] which combines RF/transient simulations with Ptolemy for discrete time or digital simulations. Finally, ADS also includes Matlab and Verilog cosimulation tools which are utilized in adding realistic UWB channel effects (from the IEEE 802.15.4a channel model), postprocessing the data, and running realistic DSP algorithms at the UWB receiver. Table 6-2 provides a summary of research groups and different methodologies for system-level simulations of wireless communication and radar systems. The novel aspects of this work compared to the others outlined in Table 6-2 related to radar and positioning systems includes the addition of realistic UWB channel effects from the IEEE 802.15.4a channel model, incorporation of antenna effects including radiation patterns and phase center variation, and simulation of actual experimental setups which allows direct comparison to experimental results. More discussion on the methodologies shown in Table 6-2 is presented in Section 6.1.

6.1 Simulation Framework

Many challenges exist in performing a comprehensive system-level simulation of a UWB positioning system. As shown in Figure 6-1, in order to simulate the entire system, both the analog and digital portions must be taken into account. As mentioned by Eberle [181], varying

Table 6-2: Comparison of wireless system-level simulation methodologies.

Research Group	Type of System	Simulation Framework	Portions of System Simulated
This Work [179]	UWB Indoor Positioning	ADS Ptolemy/ ADS Transient/ Matlab/Verilog	Analog, Digital, UWB Channel
Eberle [181]	Wireless Communication (non-UWB)	FAST/OCAPI/ Matlab	Analog, Digital, Channel
Kürner et al. [182]	THz Communication System	ADS Ptolemy/ ADS Transient/ Matlab	Analog, Digital, Channel
Tüchler et al. [172]	CMOS UWB Positioning System	CMOS Simulator/ Matlab	Digital, UWB Channel
Lecointre et al. [183]	Digital UWB Communication Rx	VHDL Simulator/ Matlab	Digital, UWB Channel
Zhai et al. [184]	UWB Communication/Radar	ADS Ptolemy/ ADS Transient/ FDTD/MOM	Analog, Digital, Channel
Manzi et al. [185]	UWB Communication/WLAN	Simulink	Analog, Digital, Channel
Jue et al. [186]	Chirped Radar/ SatCom Interferer	ADS Ptolemy/ ADS Transient/ Matlab/HDL	Analog, Digital, Channel

levels of complexity exist when accurately simulating a mixed signal system from the ground up. As shown in Figure 6-1, these varying levels of complexity (e.g. transistor/device level, component level, and overall system level) must be considered when designing a system-level simulation framework. Besides the analog and digital portions of the system, other disparate effects must be considered including the UWB antennas. This includes polarization effects, phase center variation, and radiation pattern effects. The UWB channel is exceedingly important in indoor environments because of the dense number of scatterers which causes non-trivial multipath interference and even NLOS conditions. The tag and base station positions must also be considered since geometric position dilution of precision degrades overall 3-D positioning accuracy. The final TDOA or TOA calculation must also be performed in order to simulate actual system performance.

No simulation tools exist which have the capability to simulate all of these disparate components. One approach outlined by Eberle is the use of FAST (an optimized system-level front-end simulation C++ API for digital telecom applications) combined with an extensive OCAPI library which takes high level C++ code, representing the design of a certain digital architecture, and translates it through a multi-step process from floating point to fixed point to VHDL [181].

Incorporating OCAPI in this process maximizes the potential for code re-use, essential in the design of digital systems. The complete framework wraps FAST and OCAPI with a Java middle layer and a Matlab GUI and provides a robust and complete simulation tool that has

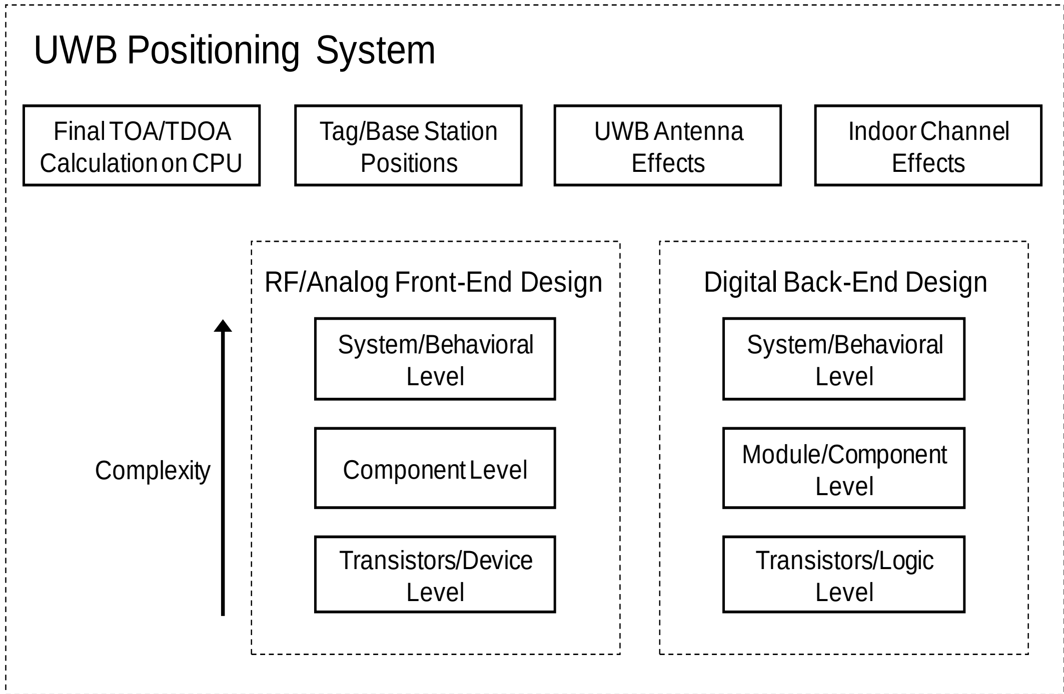

Figure 6-1: Overview of components which need to be taken into account when performing a system-level comprehensive simulation of the UWB positioning system.

been successfully used in transceiver simulation and design [181],[187],[188]. Unfortunately, this simulation framework is not commercially available and requires a large team of scientists and computer programmers to implement.

A more feasible solution for a research or design group with a limited number of RF/microwave engineers is to utilize an existing electronic design automation suite such as Advanced Design System from Agilent Technologies [180]. ADS offers an extensive RF/analog simulation framework for simulating RF front-ends which includes tools for transient, envelope, harmonic balance, frequency, and intermodulation distortion simulations. ADS also has an integrated Ptolemy simulator for discrete time digital simulations with extensive DSP libraries. Transient simulations can be embedded within discrete time Ptolemy simulations. Finally, co-simulation of the Ptolemy framework with Matlab and Verilog simulators provides a comprehensive simulation framework where analog, digital, and advanced signal processing with Matlab and Verilog can be integrated together for complete system solutions. Although the co-simulation functionality is relatively new, it has already started to see use both in industry and academia. Examples include modeling of high speed serial links [186], modeling of an X-band satellite uplink signal, and a chirped radar system with interference from a satellite uplink [189]. Kürner et al. utilized a comprehensive simulation framework for THz communication systems constructed in a similar fashion to the framework outlined in this work [182]. Zhai et al. used ADS for mixed signal simulation of a time-reversal UWB system with potential use in radar and communications applications [184].

Figure 6-2 shows the proposed simulation framework utilized in comprehensively simulating the UWB positioning system. The initial UWB transmitter and receiver positions and orientations are defined in Matlab. ADS is then used for simulating the UWB transmitter outlined in Figure 6-3. After obtaining a pulse train from the UWB transmitter, the signal is sent back to Matlab where effects from the Tx and Rx UWB antennas as well as the indoor UWB channel are added using the IEEE 802.15.4a channel model for channel effects. More information on this process is given in Section 6.2. The pulse train is sent back into ADS where the signal is processed by the UWB receiver. This includes all of the RF/analog components outlined in Figure 6-3 as well as the sampling mixer, where the train of pulses is sub-sampled to produce a time-extended signal. After passing through the ADC, the signal is sent back into either the Verilog or Matlab co-simulator for FPGA leading-edge or peak detection (the different receiver algorithms are compared in Section 6.2.2). Next, a new pulse train with time-extended pulses is created and system jitter and AWGN are added. A 21-sample MIQR filter is applied to the pulse train. The final TOA or TDOA calculation is performed in Matlab with 5x averaging using the specified transmitter and receiver positions and orientations to complete the simulation.

6.2 System Architecture

The designed system is inherently a mixed signal system. Therefore, the analog portion of the transmitter and receiver is presented first, followed by an overview of the digital

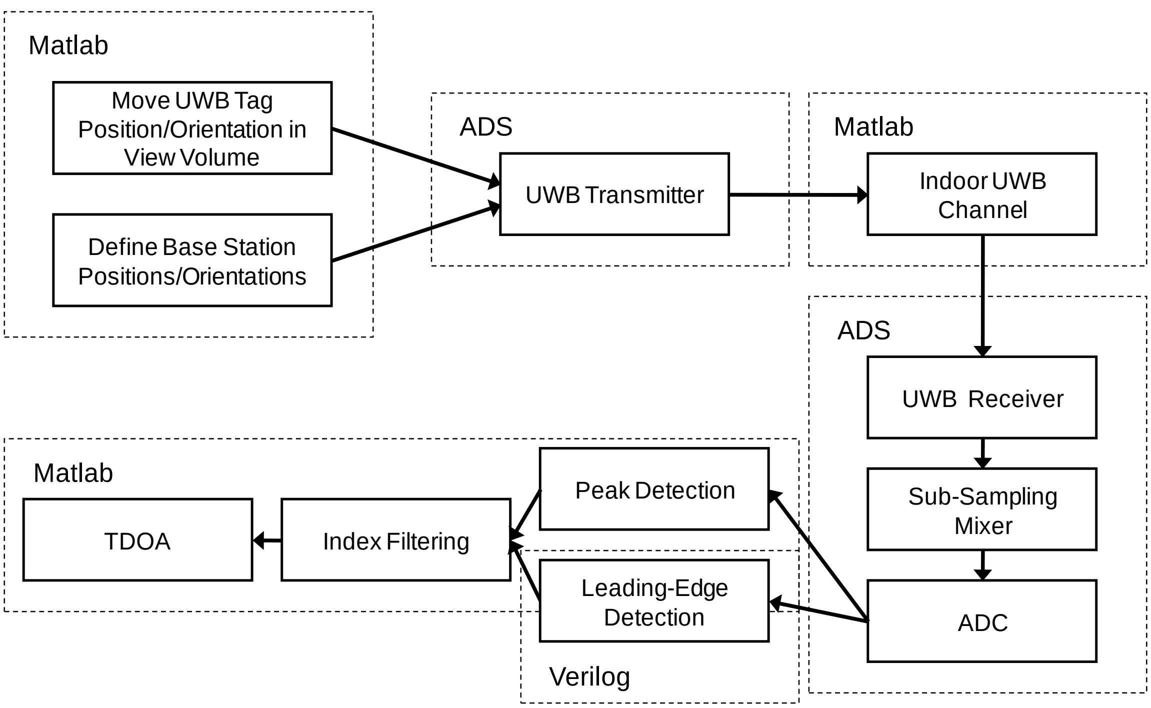

Figure 6-2: Block diagram of overall system simulation outlining the different portions of the system simulated in Matlab, Agilent ADS, and Verilog.

processing carried out on the receiver-side which includes real-time DSP on a FPGA and further post-processing, including the final TDOA calculation done on a computer.

6.2.1 Tx and Rx Analog Front-Ends

The transmitter and receiver architectures for the UWB positioning system are shown in Figure 6-3. A 10 MHz clock signal is generated from a Vectron VTC4 temperature controlled oscillator and triggers a SRD to generate a 300 ps Gaussian pulse [19]. Next, the UWB pulse is upconverted by a low phase noise LO (Agilent E8257D signal generator, LO_1) using a double balanced Hittite HMC553 mixer. After passing through two stages of amplification using a Hittite HMC565 LNA and a Hittite HMC441 MPA, the signal is transmitted via a broadband, omni-directional monopole antenna [190]. Figure 6-4a shows the baseband Gaussian pulse while Figure 6-4b shows the modulated pulse after going through the transmitter chain including the UWB monopole antenna, with the final transmitted signal denoted $x(t)$.

Next, the signal goes through the UWB channel, which can be described in various ways depending on the application. For instance, an ideal channel where no pulse distortion and only frequency independent pathloss is incurred is used in Section 6.3.2 so that other system-related effects such as the LO frequency offset, phase shifts between I and Q channels, and the performance of various peak detection algorithms can be examined. One standard technique for modeling noise in an UWB channel is the addition of AWGN [191], although Ricean and Rayleigh fading channels are more widely accepted since they can model multipath interference

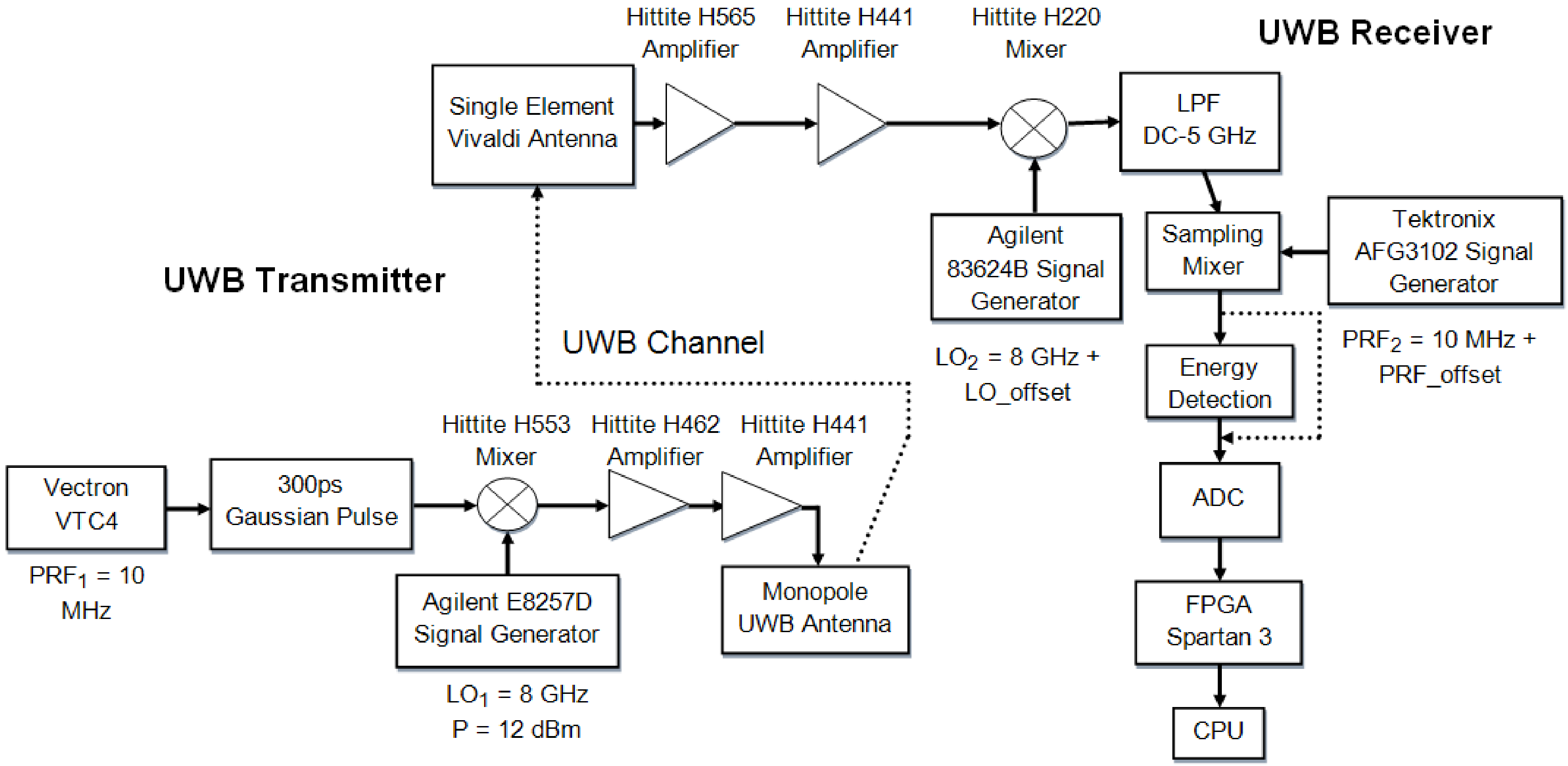

Figure 6-3: Block diagram of UWB transmitter and receiver architectures including the UWB channel.

with and without a LOS signal [192]. The most widely accepted indoor UWB channel model was devised by the IEEE 802.15.4a task force and models multipath interference by groups of clusters which are composed of individual rays [151],[152] for different environments including industrial, residential, etc. In order to add channel multipath effects, the transmitted signal $x(t)$ is convolved with the channel impulse response

$$y(t) = x(t) \otimes h(t) \tag{6-1}$$

where $y(t)$ is the transmitted signal with the addition of channel-dependent multipath. $h(t)$ is the complex baseband impulse response of a received UWB signal as defined by

$$h(t) = \sum_{l=0}^{L} \sum_{k=0}^{K} a_{k,l} \exp\left(j\varphi_{k,l}\right) \delta\left(t - T_l - \tau_{k,l}\right) \tag{6-2}$$

where $a_{k,l}$ represent the cluster and ray peak amplitudes, and the Dirac function marks the times when multipath peaks arrive [151],[152]. Two summations are needed: first ($k = 0\ to\ K$)

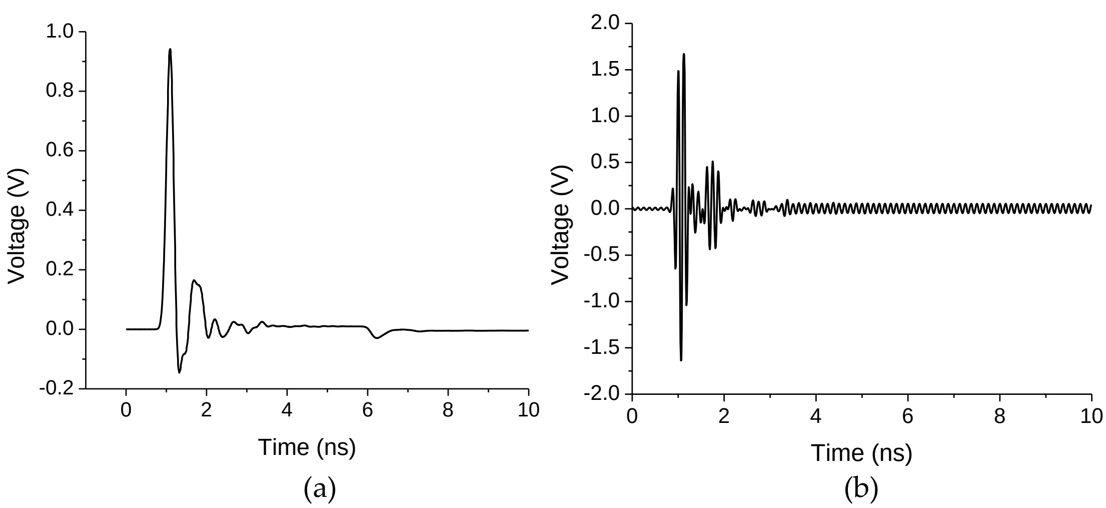

Figure 6-4: Simulated (a) baseband Gaussian pulse generated from a SRD, (b) modulated UWB pulse after passing through the transmitter chain outlined in Figure 6-3 including the monopole UWB antenna, denoted $x(t)$.

represents individual rays in the multipath cluster whereas the second ($l = 0\ to\ L$) represents the number of clusters, which are visible on the macro-scale when examining the received signal in the time domain. $\tau_{k,l}$ is defined as the intra cluster decay constant and dictates the duration of each cluster. Separate Poisson random variables are used to model the inter-cluster and inter-ray arrival times. The channel model used by the IEEE 802.15.4a task force is an extension of the Saleh-Valenzuela channel model [193] where the number of occurring clusters is modeled as a random variable with a small mean value rather than an infinite number of clusters of decaying intensity as done in the original SV model. A simpler model which has found widespread use in place of (6-2) is

$$h_1(t) = \sum_n a_n(t) s\big(t - \tau_n(t)\big) \tag{6-3}$$

where a_n represent the peak amplitudes and τ_n represent the arrival times of the received pulses [18],[194],[195]. (6-3) is much simpler than (6-2) and only models the received UWB signal as a summation of pulses with certain amplitudes and delays, neglecting phase variation caused by the channel as well as the cluster and ray phenomena observed experimentally. The channel model used in designing a UWB positioning system (e.g. (6-2) versus (6-3)) has strong implications in overall positioning performance since it dictates the peak or leading-edge detection method used at the base stations. More discussion on the implications of using (6-2) versus (6-3) is given in Section 6.2.2 in discussing the various peak and leading-edge detection algorithms tested in this simulation framework. Finally, pathloss effects are added to $y(t)$

$$PL(d) = PL_0 + 10n\, log_{10}\left(\frac{d}{d_0}\right) \tag{6-4}$$

where PL is dependent on the Tx-Rx distance, values for PL_0 and n are obtained from the IEEE 802.15.4a channel model for different environments (e.g. industrial LOS, residential NLOS, etc.), and $d_0 = 1m$ [151],[152]. Figure 6-5a shows an example of a complex impulse response obtained from the IEEE 802.15.4a industrial LOS channel model while Figure 6-5b shows the signal $y(t)$ after convolving the transmitted pulse $x(t)$ with the channel impulse response $h(t)$.

The simulation of antenna effects including Vivaldi antennas is discussed in [196]. The signal then enters the UWB receiver by passing through a single element Vivaldi antenna followed by two stages of amplification with the Hittite HMC565 LNA and Hittite HMC441 MPA. The signal is then downconverted by LO_2, which is offset in frequency from LO_1. *LO_offset* is needed to ensure signal detection since only one channel rather than I and Q combined is used for non-coherent positioning [19]. Next, the signal is time extended through an equivalent

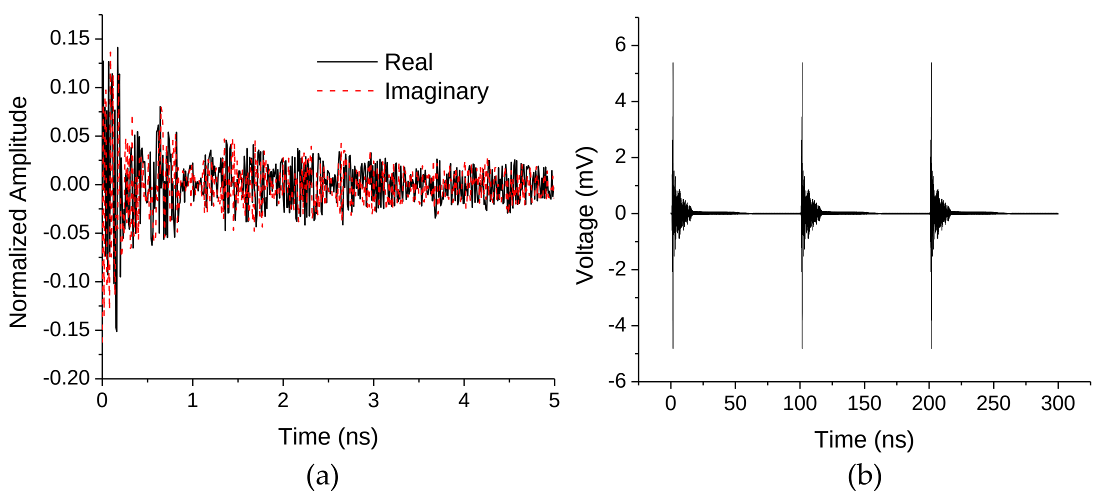

Figure 6-5: Simulated (a) complex impulse response using the IEEE 802.15.4a industrial LOS channel model, (b) pulse train with $PRF_1 = 10\, MHz$ where the transmitted signal $x(t)$ is convolved with the channel impulse response $h(t)$ and pathloss effects are incorporated for Tx-Rx distance of 2.5 m [178].

time sampling process as outlined in [38] which requires PRF_2 to be offset by *PRF_offset* from PRF_1. The use of an energy detection circuit to remove carrier leakage from the time extended signal is then investigated which is implemented with a Schottky diode circuit [19]. The signal is then converted to digital with a conventional ADC of 105 MSPS, 10 bit followed by leading-edge detection on a FPGA and the final TDOA calculation on a computer. Figure 6-6a shows a simulated UWB signal after time extension by the sampling mixer including effects from the indoor channel and transmitter while Figure 6-6b shows a corresponding signal obtained experimentally for a Tx-Rx distance of 1m. The experimental and simulated signals show good agreement in terms of the characteristics of the time domain signals, which provides the first step in validating the overall simulation framework.

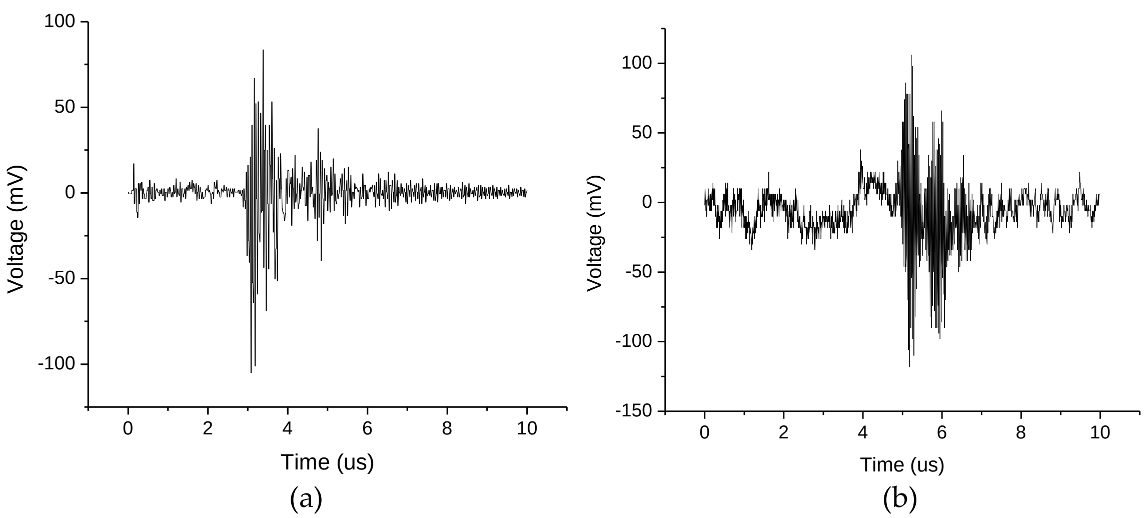

Figure 6-6: Time extended UWB pulse obtained at the UWB receiver after passing through the sampling mixer including indoor channel effects and non-linearities from the UWB transmitter: (a) simulated, (b) experimental.

6.2.2 Rx Digital Back-End

Figure 6-7 provides an overview of the receiver digital backend where a 105 MSPS, 10 bit ADC converts the signal to digital. This is followed by real-time peak or leading-edge detection on a FPGA, additional filtering of the time indices, and the final TDOA calculation done on a computer. Figure 6-8 shows the fast Fourier transform of a simulated UWB time extended pulse before the ADC including multipath effects and receiver non-linearities. A majority of the pulse power is contained from 0-30 MHz, justifying the use of a 105 MSPS, 10 bit ADC.

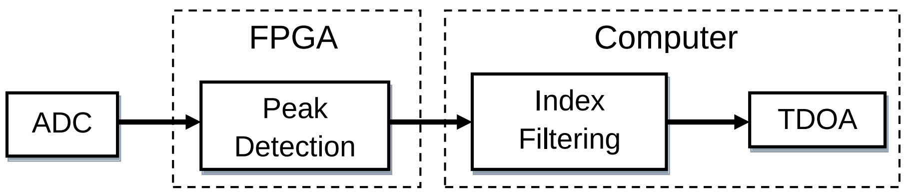

Figure 6-7: Block diagram of digital backend at the UWB receiver.

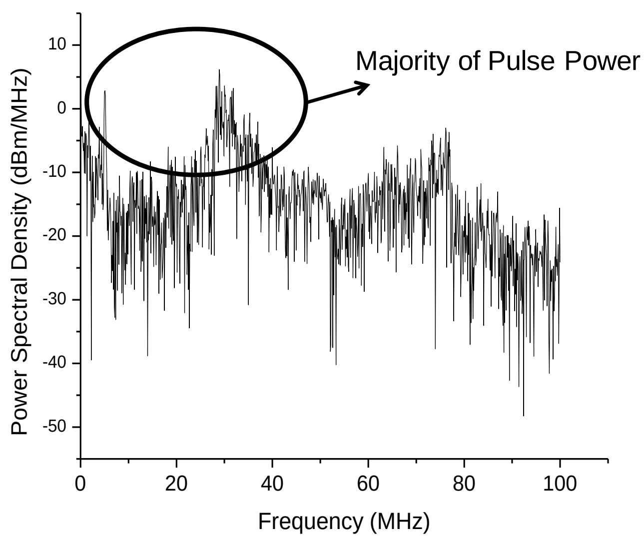

Figure 6-8: Frequency content of simulated time extended UWB pulse including receiver and multipath effects. The majority of the pulse power is contained from 0-30 MHz.

After passing through the ADC, the signal is sent through the FPGA where the leading edge or peak of the received signal is detected to give an accurate estimate of the time-of-arrival for the received UWB pulse. Accurate detection of the incoming UWB signal is critical for high accuracy localization. As mentioned in [93], the current method used in the first generation system consists of detecting the leading-edge of the incoming UWB signal versus detection of the first peak of the incoming UWB signal. This builds off of the work of Fontana et al. [12],[197],[198]. As discussed in [198], the leading-edge detection scheme employed by Fontana et al. is currently utilized in UWB communication and localization systems produced by Zebra Technologies [13]. The leading-edge detection algorithm utilized in the experimental system is denoted $LE[t]$ and is outlined in [93] where the ratio between two moving average signals, one with 16 samples and the other with 256 samples, is tracked and used to find the pulse leading-edge (currently set at a fixed threshold of ¼ the max pulse amplitude). It should be noted that the moving average signals are obtained from a 16-sample averaged version of the initial received signal.

In order to understand the robustness of leading-edge detection in localization systems where dense multipath interference occurs, it is necessary to compare the leading-edge detection algorithm to other standard peak detection algorithms currently employed in UWB localization both in theory and actual experimental systems. One peak detection method built directly from (6-3) is the peak search and subtract or iterative peak subtraction method as described in [18],[194],[195] which uses an estimate of the multipath-free impulse response

$$h_f[t] = h_0[t] - \sum_{j=0}^{L} MP_a^j s[t - MP_\tau^j] \tag{6-5}$$

where h_f[t] is the multipath-free impulse response obtained by subtracting out L scaled and time delayed versions of a template of the transmitted baseband signal s[t] from the original impulse response $h_0[t]$. After obtaining the cleaned impulse response h_f[t], the main LOS peak can be found with a conventional method such as a matched filter, as done in [18], or a threshold-based method (signal strength). As mentioned in [199],[200], search and subtract techniques can successfully be used to remove narrowband interference from received UWB signals, but, as illustrated in Figure 6-9 and Figure 6-10, this only works for either narrowband interferers or when the multipath UWB peaks have a noticeable spread (e.g. at least half a pulse width [18]) between them. As shown in Figure 6-10, when a dense multipath environment such as the IEEE 802.15.4a industrial LOS channel model is used, search and subtract algorithms produce large errors since the inherent channel model on which they are constructed, (6-3), is no longer a valid approximation of the received signal. Although subtraction techniques have limitations in multipath intensive environments, they have been successfully used in the frequency domain to remove ground surface reflections in ground penetrating UWB radar [201]. The final received signal is

$$r[t] = ADC\big(y(t - j(\tau)) + n(t)\big) \tag{6-6}$$

where $r[t]$ includes $n(t)$, AWGN from the amplifiers and other active components in the transmitter and receiver chains outlined in Figure 6-3, $j(\tau)$, jitter from the PRF clocks, local oscillators, thermal effects, and other active sources measured experimentally and modeled as a Gaussian random variable, and the final ADC conversion by a 105 MSPS, 10 bit ADC.

Other standard peak detection algorithms include a matched filter, signal strength, and first peak detection. The first step in a matched filter is

$$\hat{y}[t] = r[t] \otimes s[t] \tag{6-7}$$

where $r[t]$ is the received signal at the FPGA outlined in (6-6), $s[t]$ is a baseband template of the original transmitted pulse, and $\hat{y}[t]$ is the resultant signal. Additional steps such as a low pass filter or envelope detection can be used on the output signal $\hat{y}[t]$. The final detected peak is then defined as

$$MF[t] = \max\big(filt(\hat{y}[t])\big) \tag{6-8}$$

where the maximum of the filtered output $\hat{y}[t]$ is considered the peak of the received UWB pulse. Examples of matched filters used in UWB positioning and communication systems are given in [15],[202]. It should be noted that in [15] extra steps are taken to ensure detection of the first peak while in [202] a bank of correlators are used in performing the final peak detection. As discussed in [12], matched filters can successfully filter out narrowband interference, but, similar to the search and subtract technique, exhibit noticeable errors in dense indoor environments similar to the received signal presented in Figure 6-10.

Signal strength is another standard algorithm used in both narrowband and wideband indoor positioning. In order to properly determine the highest signal strength, the envelope of the received pulse is taken by first removing any DC offset, squaring the received signal $r[t]$, and averaging the signal, First the signal is averaged

$$a[t] = env(\,(r[t] - DC\_offset)^2) \tag{6-9}$$

where $a[t]$ is the final signal after taking a 15-sample envelope of the squared received signal with no DC offset. The final SS peak is then located

$$SS[t] = \max(a[t]) \tag{6-10}$$

where $SS[t]$ is the maximum of the envelope signal. As discussed in [203], this is a standard UWB localization approach, similar to TOA or TDOA, although the overall accuracy is typically much less than time-based approaches. For example, even with the use of a Kalman filter, Guvenc et al. were only able to achieve overall 3-D accuracy of 2.48 m [204] with the Ekahau RTLS [205]. It should be noted that a nearest neighbors approach was used in [204] rather than a triangulation technique. The Ekahau RTLS is a narrowband system which operates over WLAN [205].

The final ranging algorithm tested is first peak detection. Similar to [206], the first peak in the time domain is obtained from the envelope of the received signal $a[t]$

$$FP[t] = \max(first\_peak(a[t])) \tag{6-11}$$

where $first\_peak()$ finds the first contiguous portion of the received signal $a[t]$ when the amplitude is 6dB above the noise floor. The maximum of this portion of the received signal is considered the correct time index for the UWB pulse and is denoted $FP[t]$. Variations of this peak detection method have been proposed which include combining a first peak detection scheme with the total received signal power using a linear unbiased estimator for low-complexity UWB positioning systems [207] while Chehri et al. use the first peak for TOA ranging in a mine after application of a subspace method with LOS accuracy around 1m, making it a cross between first peak detection and the search and subtract methods [208].

Figure 6-9 and Figure 6-10 show two simulated time extended signals obtained after the ADC in the receiver chain shown in Figure 6-3 where $LO\_offset = 3MHz$ and $PRF_2 = 10MHz + 10kHz$, resulting in a time expansion factor $\alpha = 1000$ [19]. Jitter effects, AWGN, and time scaling effects are not included in the simulations. The difference between Figure 6-9 and Figure 6-10 is that no channel effects or pathloss were added to Figure 6-9 while industrial LOS multipath interference from (6-2) and pathloss from (6-4) were added to the received signal in Figure 6-10. Overlaid on both figures is the ideal received pulse where the LOs and PRF clocks are coherent at the transmitter and receiver and no channel effects were added. This is considered the ideal received signal and provides a reference signal with which to compare non-ideal signals. As shown in Figure 6-9, the peak detection algorithms successfully locate the correct peak of the signal envelope even though carrier leakage, noise from non-coherent LOs and PRF clocks, and distortion effects from the sub-sampling mixer are included in the received signal. As shown in Figure 6-10, when multipath interference and pathloss are introduced, the signal envelope no longer shows a clear peak. This causes gross 1-D ranging errors from the peak detection algorithms of up to 30 cm for SS. Conversely, the leading-edge algorithm correctly finds the leading-edge in both cases with 1-D ranging error of 1-3 mm. Similar trends are found in the simulation results reported in Sections 6.3 and 6.4 when comparing leading-edge detection to these other four ranging algorithms.

As outlined in Figure 6-7, after peak or leading-edge detection on the FPGA, the final time index values from the N base stations are sent to a computer. Before the final TDOA calculation, additional filtering of the time indices is performed. This includes both averaging of multiple index values to remove Gaussian noise caused by LO and PRF jitter as well as a special type of filter, termed the MIQR filter [93]. It is similar to a median filter in that a histogram of data values is obtained from a moving window of n samples. The MIQR filter returns the average value of the 25th and 75th percentiles from the corresponding histogram [93]. The need

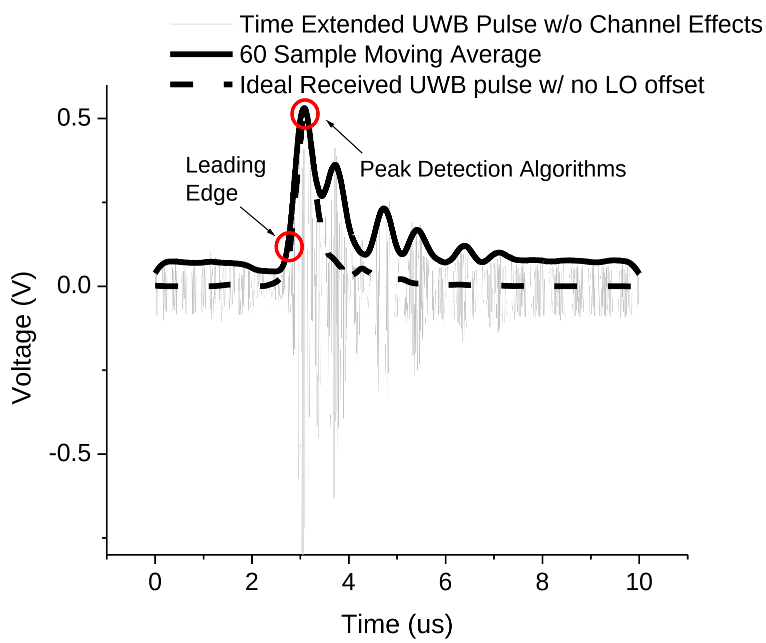

Figure 6-9: Simulated UWB time extended pulse for ideal case with $LO_offset = 3$MHz. Channel effects (e.g. pathloss, multipath interference) are not included to provide an ideal received signal. The system architecture in Figure 6-3 is used to capture the non-ideal performance of various system components. In the ideal case, both the use of peak detection and leading-edge detection algorithms at the FPGA result in accurately detecting the UWB pulse. The ideal case includes use of an ideal channel. PRF_1 and PRF_2 are not coherent.

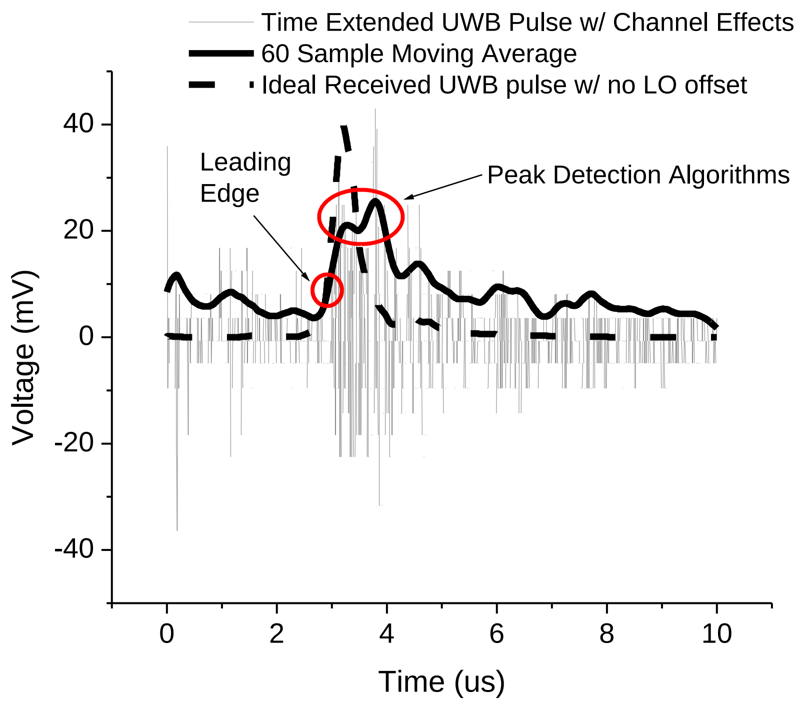

Figure 6-10: Simulated UWB time extended pulse with $LO_offset = 3$MHz. IEEE 802.15.4a industrial LOS channel (CM7) effects (e.g. pathloss, multipath interference) are included to provide a realistic received signal. The system architecture in Figure 6-3 is used to capture the non-ideal performance of various system components. PRF_1 and PRF_2 are not coherent. With a smaller SNR and the addition of multipath interference and significant pathloss, a large variation in the detected peak is observed which results in gross 1-D ranging errors of up to 30 cm. The leading edge still provides accurate 1-D ranging even in this harsh environment.

for this filter is outlined in Figure 6-11 where a zoomed-in portion of the digital time extended received signal in Figure 6-9 is shown as well as a moving average window of four samples obtained from the squared signal to get the envelope. Ripples or shoulders are noticeable in the envelope signal. The existing shoulders combined with jitter from the PRF clocks and LOs causes a bimodal distribution in the time index values which can be subsequently filtered out by the MIQR filter. It should be noted that this shoulder effect is mitigated by the addition of the energy detection circuit in the receiver chain after the sampling mixer, as shown in

Figure 6-3 and outlined in detail in [19]. With the addition of energy detection in the receiver chain, a bimodal distribution is no longer seen but rather a Gaussian distribution. This allows simple averaging of the index values to be used to increase overall 3-D accuracy, although combining the energy detection circuit with the MIQR filter provides the most robust and accurate system architecture for mitigating the shoulder effect. The TDOA algorithm utilized here is outlined in [93] where a guess at the correct 3-D position is made and an iterative approach is used to converge to the true 3-D position. When more than four base stations are used, a least squares approach is taken to find the correct 3-D position. More information on TDOA algorithms can be found in [6].

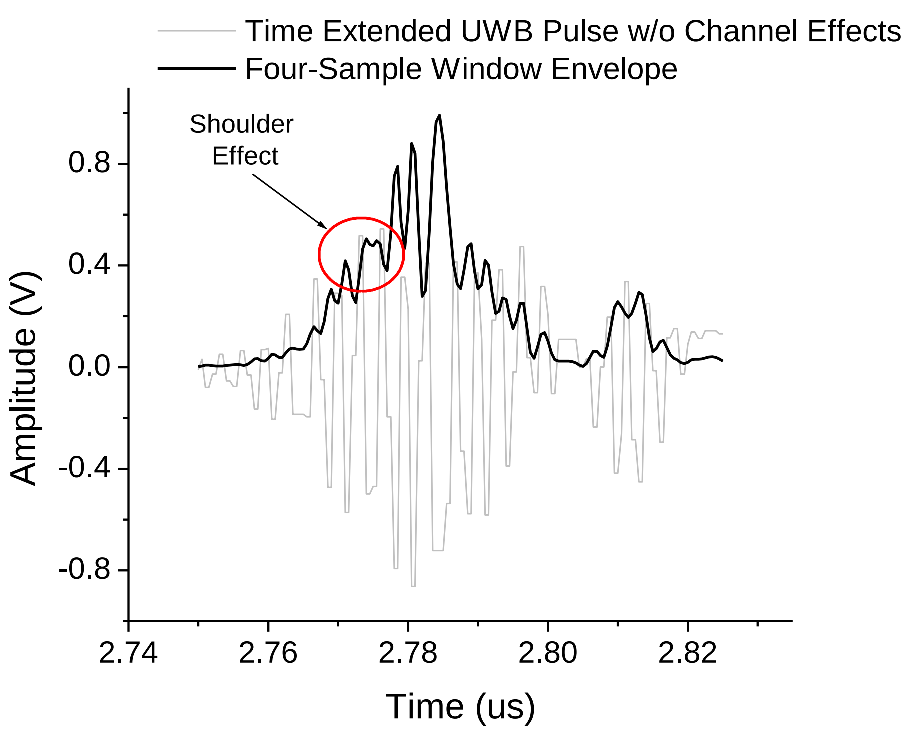

Figure 6-11: Simulated UWB time extended pulse with $LO_offset = 3$MHz. A zoomed-in portion of Figure 6-9 is shown to highlight the shoulder effects caused by carrier leakage in the time extended received signal.

6.3 Simulations Along an Optical Rail

All of the simulations performed in Sections 6.3 and 6.4 are based off of actual experimental setups utilizing the UWB positioning system described in [18],[19]. The experimental setup for the optical rail experiment is outlined in Section 6.3.1 while the simulation results for the ideal situation with no multipath interference are presented in Section 6.3.2. Section 6.3.3 examines the optical rail experiment with the addition of LOS and NLOS multipath interference. Finally, Section 6.3.4 compares experimental results with simulation results which include LOS multipath interference.

6.3.1 Optical Rail Experimental Setup

The experimental setup for the optical rail experiment is shown in Figure 6-12. Four UWB base stations are placed at distinct 3-D locations. Similar to the experimental setups in [18],[19], an optical tracking system is used to measure the 3-D location of each Vivaldi antenna phase center for all four base stations. An optical probe is attached to the UWB tag and the data from the optical and UWB positioning systems is synchronously processed on a computer. At the computer, a 21 sample MIQR filter is applied to the time indices returned by the peak or leading-edge detection algorithm, and the final 3-D position returned by the TDOA algorithm is averaged five times. It should be noted that the stability of the Vectron VTC4 temperature compensated crystal oscillators ($PRF_1$and PRF_2) is ±0.5ppm. This produces time scaling effects, as outlined in [18], which are nontrivial and worsen as the expansion factor α is increased. The effects from time scaling are observed experimentally and included in this simulation framework. As outlined in [93], static and dynamic calibration procedures are used to calibrate the UWB positioning system to the optical tracking system and can help compensate for time scaling effects caused by the different time offsets observed at each base station. After calibration of the optical and UWB systems, real-time experiments can be run where mm-range 3-D accuracy of the UWB positioning system has been verified. The simulation results presented in this section are run on this experimental setup. This provides the ability to compare simulation versus experimental results and ensures simulation results can be relevantly used in designing and understanding our experimental system.

6.3.2 Ideal Case - Excluding Channel Effects

In order to understand the system behavior and illustrate the reasoning behind using the final system architecture, it is necessary to first simulate the UWB system without channel effects. All of the non-ideal components shown in Figure 6-3 are included in these simulations

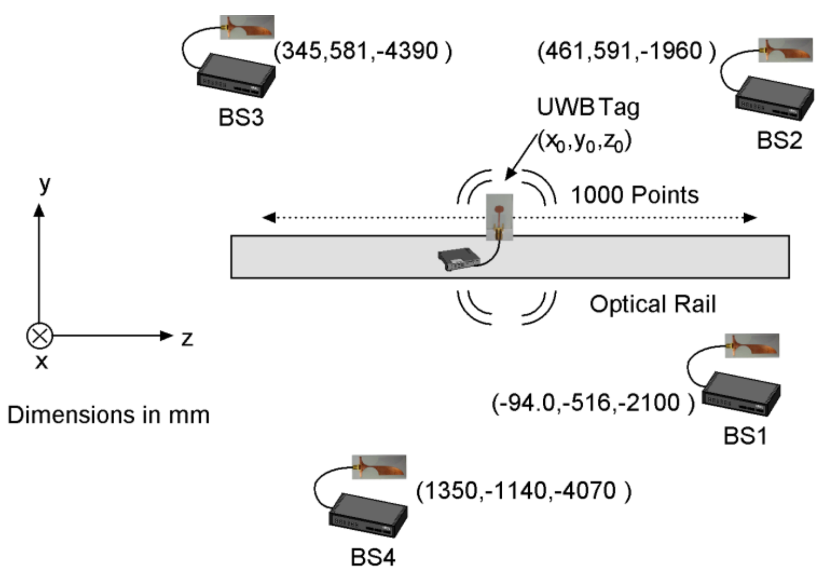

Figure 6-12: Optical rail experimental setup where four base stations are positioned at distinct 3-D locations and the UWB tag is moved along an optical rail while 1000 3-D points are taken in real-time, utilizing the UWB transmitter and receiver architectures in Figure 6-3.

along with jitter from the triggering clocks and local oscillators and also AWGN from active devices. Figure 6-13 shows average overall RMSE for simulating the optical rail experiment where the expansion factor α is varied from 1000-20,000. As α increases, more UWB pulses are averaged to create the time expanded pulse, which lessens the jitter effects since they do not scale with α. Conversely, as α increases, the time scaling effects become more pronounced since the reconstructed pulse spans a greater number of clock cycles. The optimal expansion factor found is $\alpha = 2500$. It should be noted that in the static case, the time scaling effects can be removed through a calibration procedure, as done in [93], whereas in the dynamic case, it is harder to completely remove them, although an excellent dynamic calibration method is

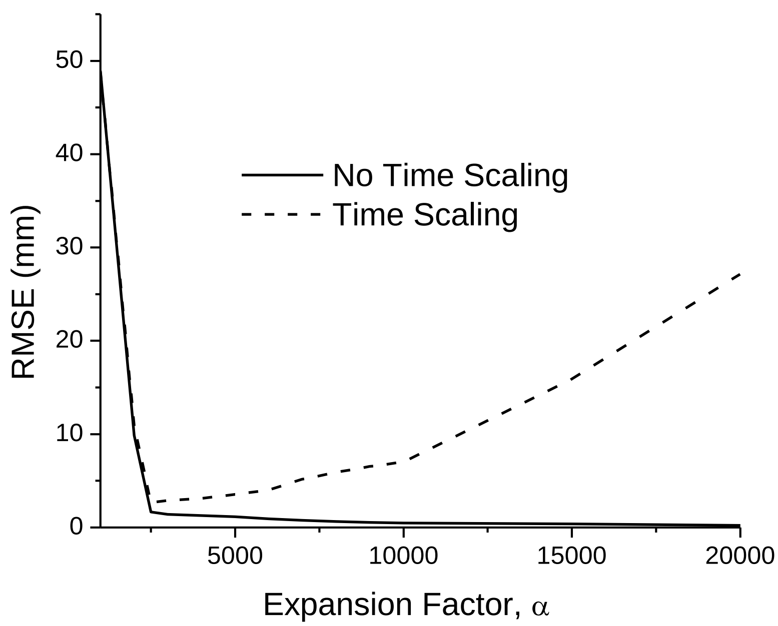

Figure 6-13: Average 3-D RMSE obtained by simulating the optical rail experiment with no channel effects incorporating leading-edge detection, a modulation factor $\beta = 5$, a 21-sample MIQR filter, and 5x averaging of the TDOA results. The effects of time scaling increase proportionally with the expansion factor and cause a trade-off between mitigating jitter/AWGN effects and mitigating time scaling effects. $\alpha = 2500$ is considered the optimal expansion factor for minimizing the combined effects of jitter, AWGN, and time scaling.

outlined in [93]. Therefore, in the static case after calibrating out the time scaling effects, it is possible to get extremely low errors of less than 0.1 mm when averaging large numbers of pulses.

Next, as shown in Table 6-3, a comparison of the error obtained by the five ranging algorithms is given for different cases involving I and Q channels. The optical rail experimental setup was simulated for $\alpha = 2500$ and $\beta = 5$ with a 21-sample MIQR filter and 5x averaging of the TDOA results. As mentioned in [19], the final system architecture relies solely on one channel: I or Q. This simulation was setup to analyze the I/Q mismatch seen experimentally and outlined in [19]. As shown in Table 6-3, when no multipath interference is present in the received signal, all five ranging algorithms provide comparable results. Use of either the I or Q channel with the TDOA algorithm produces almost identical results. When the combined $I^2 + Q^2$ signal is used, with the channels correctly aligned, a marginal improvement in overall RMSE of 0.16-0.19 mm is seen. Conversely, when the I and Q channels of the $I^2 + Q^2$ signal are not aligned, the overall RMSE degrades substantially for all five algorithms. Since it would greatly increase the complexity of the system to correctly align the I and Q channels (random phase variations in the time extended signals are introduced by the sampling mixers), only the single I channel is used at each base station.

Given the dependency of the system on the single I channel, another concern, as outlined in [19], are shoulder effects introduced by the carrier leakage $\Delta\omega_{eq}$ (shown in Figure 6-11). As discussed in [19], the carrier leakage is necessary for the single channel architecture but is also responsible for introducing added localization error into the received signals. Figure 6-

14a shows 1-D ranging error for different phase offsets as β is varied from 0.1-100. It should be noted that the leading-edge algorithm was used with $\alpha = 2500$ while jitter and AWGN effects were neglected for this simulation. As shown in Figure 6-14a, as β is decreased, the error after leading-edge detection substantially increases. This increase in error is due to the fact that the ripples of the carrier signal expand as β is decreased, resulting in large errors for certain phase offsets. When jitter and AWGN is added to the signal, a bimodal error distribution is seen [19],[93]. As shown in Figure 6-14b, when the energy detection architecture outlined in [19] is included in the simulation, the shoulder effects are sufficiently mitigated from the received signal to obtain mm-range 1-D ranging accuracy.

As mentioned in [18], the PDOP of the base station geometric configuration plays a crucial role in the resulting 3-D accuracy from the TDOA algorithm. Figure 6-15 shows the 3-D error from simulating the TDOA algorithm after 5x averaging, a 21-sample MIQR filter, LE

Table 6-3: Comparison of using I and Q channels.

Channel	Leading Edge RMSE (mm)	Matched Filter RMSE (mm)	Signal Strength RMSE (mm)	Iterative Peak Subtraction RMSE (mm)	First Peak Detect RMSE (mm)
I	2.70	2.68	2.70	2.68	2.70
Q	2.70	2.68	2.70	2.71	2.70
I^2+Q^2 Aligned	2.54	2.50	2.56	2.52	2.56
I^2+Q^2 Not Aligned	4.19	4.12	4.16	4.16	4.16

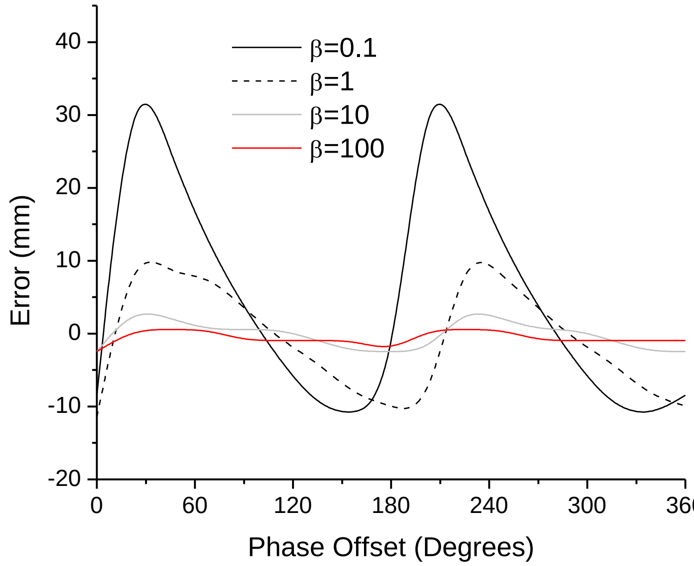

(a)

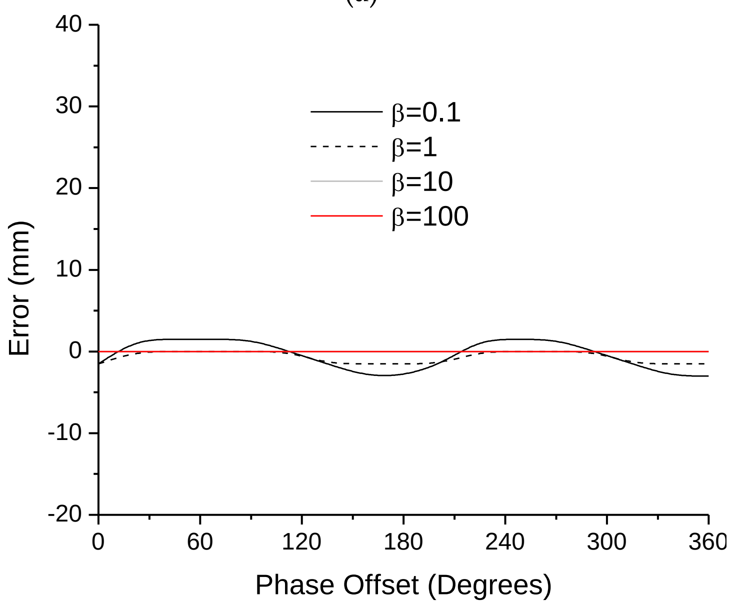

(b)

Figure 6-14: 1-D ranging error obtained by simulating the optical rail experiment with no channel effects incorporating leading-edge detection, a variable modulation factor β, and $\alpha = 2500$, neglecting jitter and time scaling effects. To illustrate the shoulder effect [19], β is varied from 0.1-100. The phase offset of the carrier leakage $\Delta\omega_{eq}$ is varied from 0-360°. The results are presented for two cases: (a) without energy detection, (b) with energy detection.

detection, $\beta = 5$, and $\alpha = 2500$. The tag starts closer to the geometric center of the base station configuration outlined in Figure 6-12. As the tag is moved along the optical rail, the PDOP and corresponding 3-D error increase while the 1-D ranging error remains nearly constant at 1.22 mm. To illustrate this effect, the RMSE from $z = -3273$ mm to $z = -3558$ mm is 2.08 mm while the RMSE from $z = -3558$ mm to $z = -3789$ mm is 2.86 mm. More discussion on the effects of PDOP, number of base station used, and base station geometric configurations is given in Section 6.4.

6.3.3 Addition of Indoor LOS and NLOS Channels

As shown in Table 6-3, when no multipath or pathloss effects are included in the

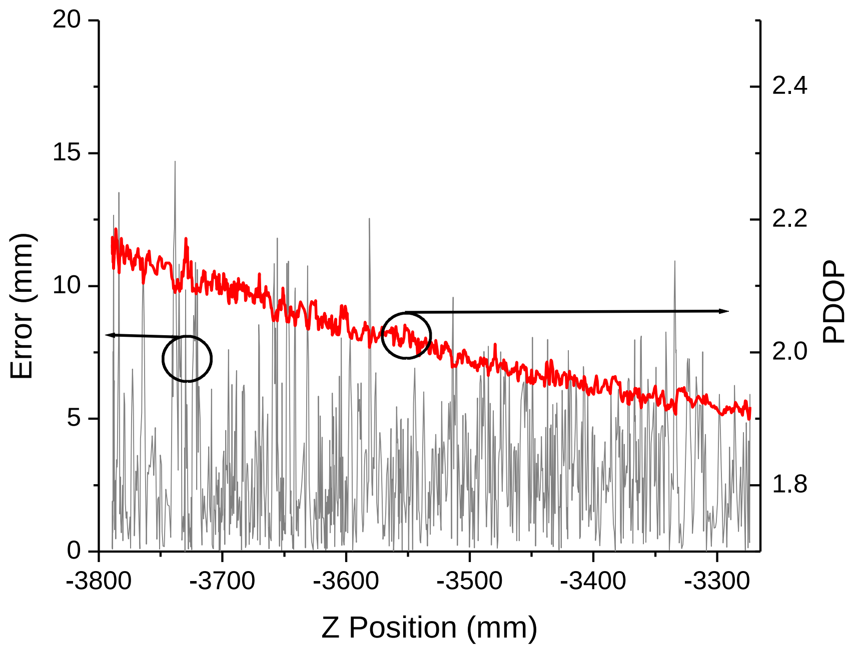

Figure 6-15: 3-D error as tag is moved along the optical rail in the $-z$ direction with the corresponding PDOP shown. No channel effects are included, leading-edge detection is used along with a modulation factor $\beta = 5$, a 21-sample MIQR filter, and 5x averaging of the TDOA results. The 1-D ranging error stays almost constant at 1.22 mm while the PDOP and corresponding 3-D error increase as the tag is moved farther along in the $-z$ direction away from the center of the base station geometric configuration.

simulation, all five ranging algorithms perform comparably. This is consistent with the illustration given in Figure 6-9. Conversely, when indoor channel effects are included in the simulation, a much larger variation in the performance of the ranging algorithms is seen. The optical rail experiment was once again simulated for various LOS and NLOS UWB channel environments utilizing the IEEE 802.15.4a channel model. As shown in Table 6-4, the leading-edge detection algorithm outperforms the other ranging algorithms in the residential,

Table 6-4: Comparison of 3-D RMSE for peak and leading edge detection algorithms in LOS indoor environments.

UWB Channel	Leading Edge RMSE (mm)	Matched Filter RMSE (mm)	Signal Strength RMSE (mm)	Iterative Peak Subtraction RMSE (mm)	First Peak Detect RMSE (mm)
Industrial LOS (CM7) no ED	7.58	45.1	42.4	44.7	48.8
Industrial LOS (CM7) with ED	6.85	108	109	108	103
Commercial LOS (CM3) no ED	4.22	360	361	359	65.8
Commercial LOS (CM3) with ED	3.18	372	372	372	144
Residential LOS (CM1) no ED	3.99	206	209	11.4	12.3
Residential LOS (CM1) with ED	3.00	205	206	203	206

Table 6-5: Comparison of 3-D RMSE for peak and leading edge detection algorithms in NLOS indoor environments.

UWB Channel	Leading Edge RMSE (mm)	Matched Filter RMSE (mm)	Signal Strength RMSE (mm)	Iterative Peak Subtraction RMSE (mm)	First Peak Detect RMSE (mm)
Industrial NLOS (CM8) no ED	241	1390	1010	994	28.8
Industrial NLOS (CM8) with ED	631	1120	743	1090	1410
Commercial NLOS (CM4) no ED	6.69	10.6	761	10.2	19.0
Commercial NLOS (CM4) with ED	5.00	126	748	124	8.69
Residential NLOS (CM2) no ED	365	97.2	157	157	192
Residential NLOS (CM2) with ED	356	94.5	103	101	373

commercial, and industrial LOS environments. The addition of energy detection, shown in Figure 6-3, does slightly improve the performance through mitigation of the shoulder effect. For all simulations in this section, the TDOA algorithm was run with 5x averaging, a 21-sample MIQR filter, $\beta = 5$, and $\alpha = 2500$. In LOS multipath conditions, the other four ranging algorithms (matched filter, SS, first peak, and iterative peak subtraction) exhibit large errors due to the ambiguity in 1-D ranging caused by multipath interference (e.g. Figure 6-10, Figure 6-16).First peak and iterative peak subtraction performed well in the residential LOS environment since the multipath peaks are spread out enough for peak detection to allow accurate ranging of the first received pulse. In order to account for the random nature of these statistical channels, 1000 channel instantiations were made for each LOS and NLOS channel. For each TDOA calculation along the optical rail (1000 total points), a random channel instance was selected for each tag-base station path from the 1000 instantiations.

For NLOS channels (results in Table 6-5), the leading-edge algorithm provides mm accuracy only when a weaker LOS signal still exists, which is typically the case in the

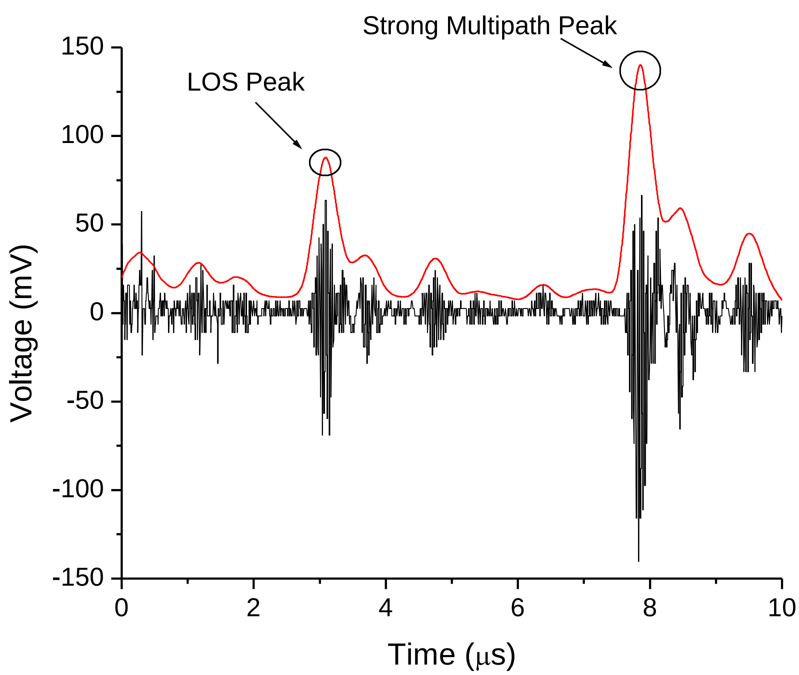

Figure 6-16: Simulated CM3 signal obtained at the UWB receiver for Tx-Rx distance of 1 m after time extension from the sampling mixer and conversion to digital. The LOS peak is highlighted as well as a strong multipath peak which arrives 4 μs after the LOS peak and causes a 1-D ranging error of 1.2 m using matched filter, iterative peak subtraction, and signal strength peak detection algorithms.

commercial NLOS channel (Figure 6-17b). When no LOS signal is present, typical of residential and industrial NLOS channels, leading-edge detection produces large ranging errors and is not an ideal ranging technique. Figure 6-17 provides example residential, commercial, and industrial NLOS received signals. As shown in Table 6-5, a first peak detect algorithm with no energy detection outperforms leading-edge detection in residential and industrial NLOS conditions. It is therefore necessary to detect when LOS versus NLOS conditions exist at the UWB receiver and switch ranging algorithms accordingly. More information on detecting NLOS conditions and ranging algorithms optimized for NLOS can be found in [209],[210].

6.3.4 Comparison with Experimental Results

A direct comparison of simulation results to experimental results is possible since the simulated scenario was first run as an actual experiment. Table 6-6 shows the RMSE for the optical rail experiment for actual experimental results compared to simulations with energy detection using industrial LOS (CM7), commercial LOS (CM3), and residential LOS (CM1). It should be noted that for all simulations the TDOA algorithm was run with 5x averaging, the leading-edge detection algorithm, a 21-sample MIQR filter, $\beta = 5$, $\alpha = 2500$. Figure 6-18 compares the simulation results for CM7 and CM3 with experimental results for all 1000 points while Figure 6-19 compares experimental results with simulation results for the residential LOS (CM1) channel. As shown in Figure 6-18, the CM7 channel introduces errors larger than actually observed experimentally. The RMSE for commercial LOS (3.18 mm) and residential LOS (3.00 mm) is much closer to the actual experimental error of 4.39 mm. As shown in Figure 6-19,

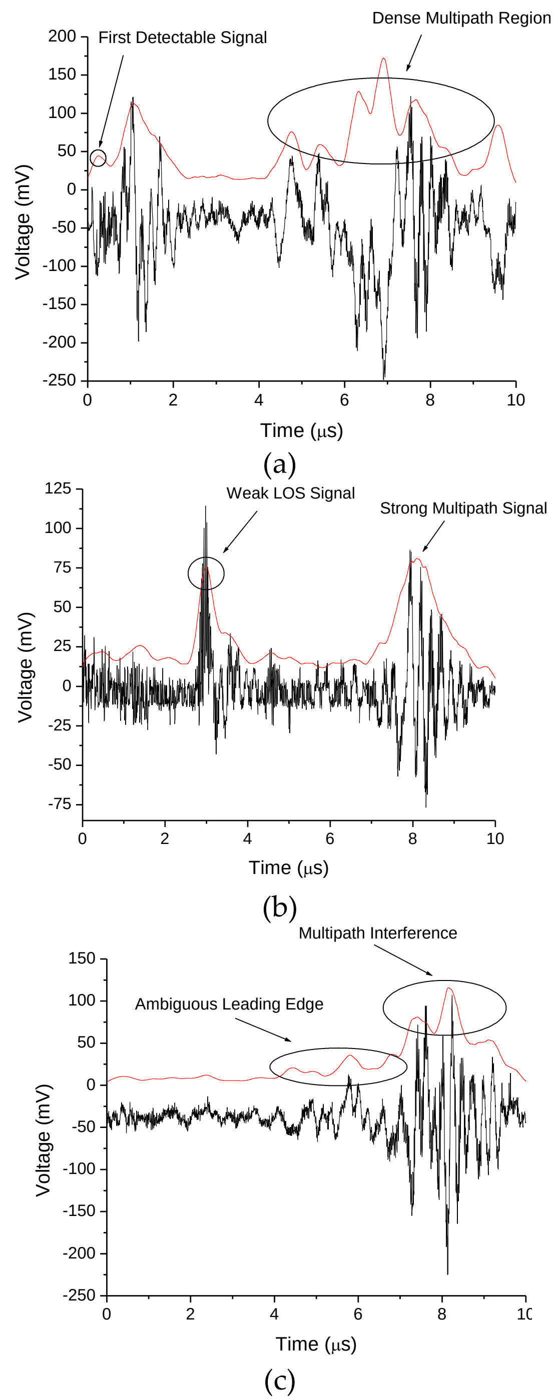

Figure 6-17: Examples of received signals. (a) CM8 received signal highlighting the need to detect the first signal above the noise floor instead of trying to resolve the arrival of the peak in the dense multipath region. (b) CM4 received signal highlighting the weaker LOS signal which still provides accurate ranging compared to the strong multipath signal. (c) CM2 received signal where the leading edge is distorted. Since the multipath signals can be resolved, iterative peak subtraction or a matched filter provides the best performance.

experimental results are most similar to a residential LOS environment while errors from the commercial LOS environment have less correlation.

6.4 Simulations for Different Base Station Configurations

The various base station configurations were adapted from experiments undertaken in various configurations of the four to six base stations to test their ability to localize the 3-D position of the tag over 8 distinct points. This setup is shown in Figure 6-20 [18]. The same experimental setup was simulated using the framework outlined in Section 6.1. For all simulations the TDOA algorithm was run with 5x averaging, a 21-sample MIQR filter, $\beta = 5$, $\alpha = 2500$. The residential LOS (CM1) UWB channel model was used as well as an ideal scenario [18] where a tag was moved along an optical rail with six base stations present while using with no multipath interference or pathloss. The results in Table 6-7 use the leading-edge detection and iterative peak subtraction ranging algorithms. LE represents the best ranging

Table 6-6: Comparison of simulated and experimental results for optical rail experiment.

Type	RMSE (mm)
Experiment	4.39
Simulation CM7 with ED	6.85
Simulation CM3 with ED	3.18
Simulation CM1 with ED	3.00

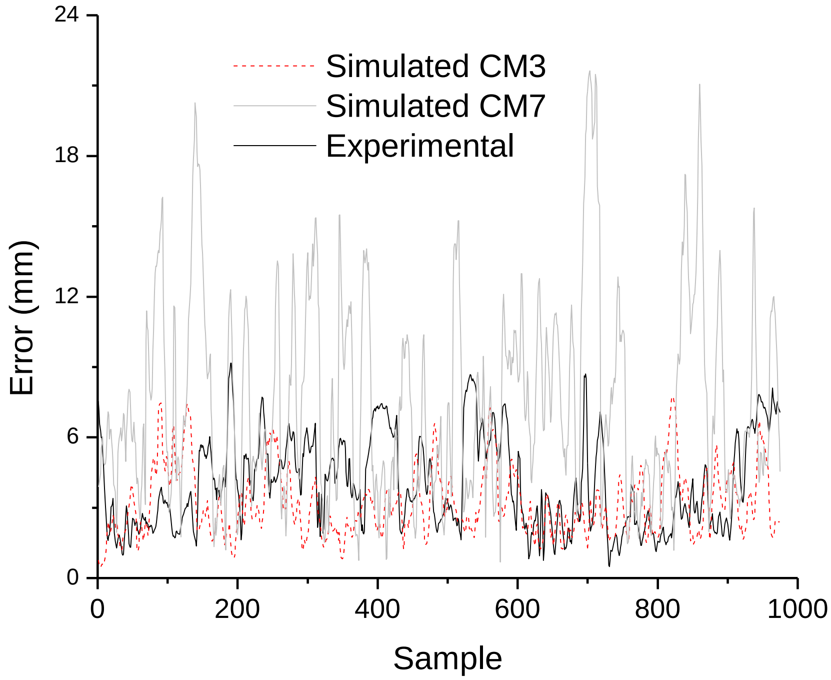

Figure 6-18: Comparison of final 3-D error from optical rail experiment, CM3 simulation, and CM7 simulation over 1000 points along the optical rail.

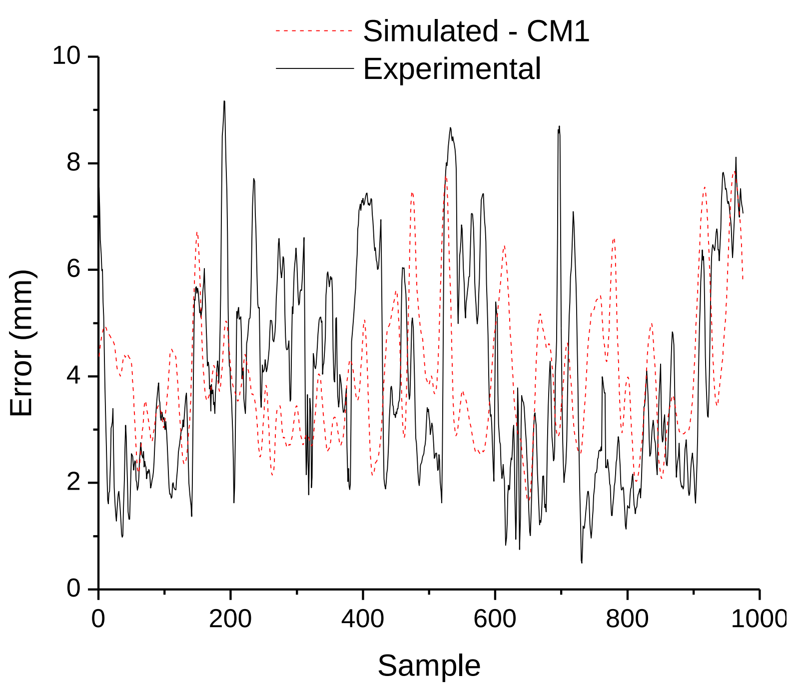

Figure 6-19: Comparison of final 3-D error from optical rail experiment and CM1 simulation.

solution and IPS was the algorithm used in [18] for the experiments. Similar to the setup in [18], the PRF clocks were synchronized in these simulations.

As shown in Table 6-7, use of LE detection outperforms the experimental results even in CM1 multipath conditions. IPS performs worse than the observed experimental results in CM1 multipath conditions. When no multipath interference or pathloss exists in the UWB channel, simulated results using IPS significantly outperform the experimental results, suggesting multipath interference and pathloss constitute the largest sources of error in this experiment. The geometric PDOP plays a significant role in the final 3-D accuracy obtained from the TDOA calculation. As shown in Figure 6-21, the error in the x-dimension is much larger than y and z while performing TDOA of the tag position using the experimental setup in Figure 6-20d and LE for the ranging algorithm. As shown in Figure 6-22, this is caused by the much larger PDOP in the x-dimension compared to y and z. The flexibility of this simulation framework allows easy adaptation to new experimental setups such as the multi-base station optical rail experiment outlined in this section.

Table 6-7: Results for multi-base station experiments.

BS Configuration	Experiment Mean Error (mm)	Simulation Mean Error LE CM1 (mm)	Simulation Mean Error IPS CM1 (mm)	Simulation Mean Error IPS no MP (mm)	Mean PDOP
6 BS	2.45	1.59	3.06	0.48	1.88
5 BS	3.13	2.07	4.16	0.53	2.02
4 BS - Figure 6-20c	3.62	2.92	6.08	0.61	2.43
4 BS - Figure 6-20d	43.3	19.1	68.1	5.11	20.6

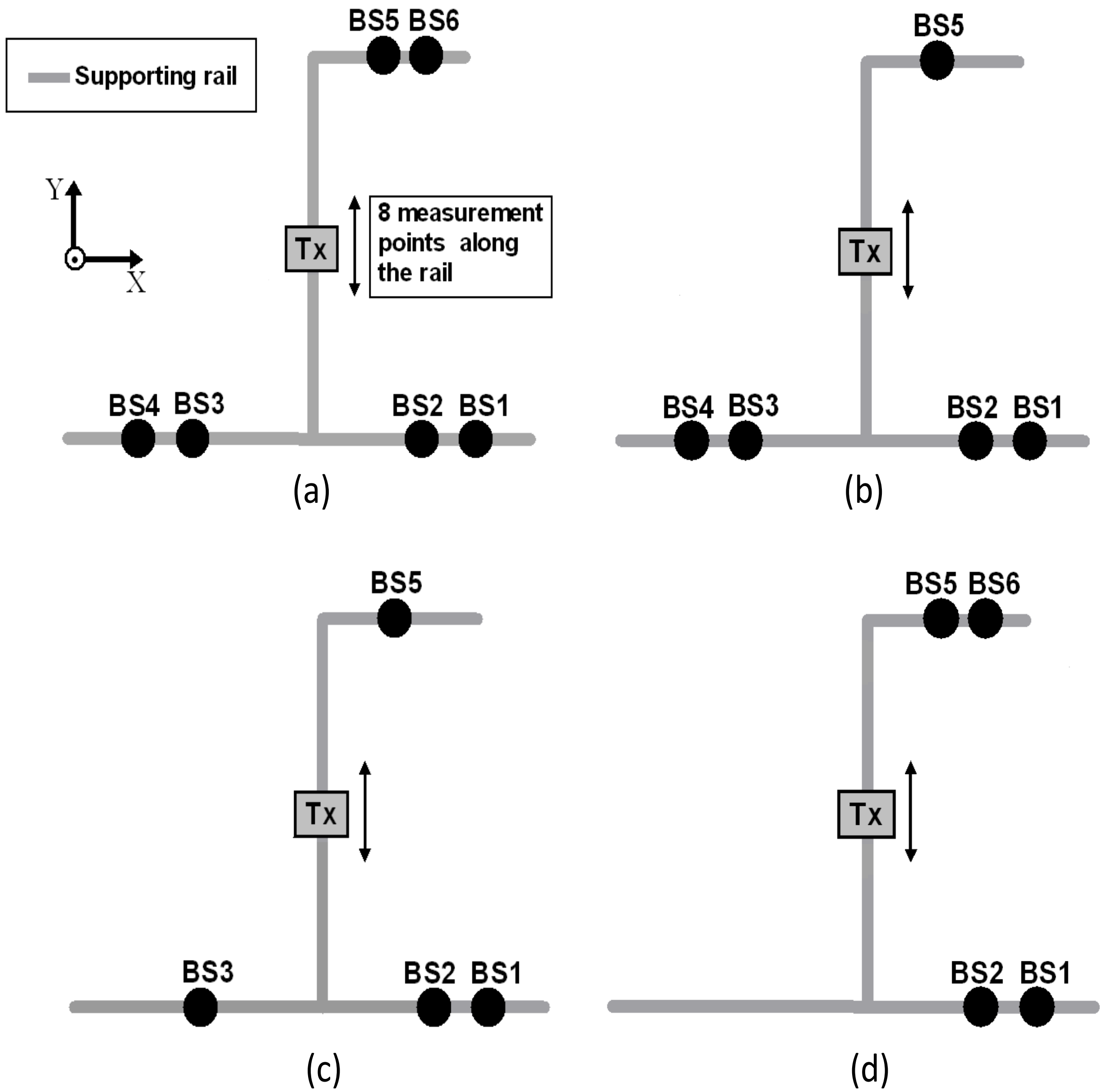

Figure 6-20: 3-D synchronized localization experiments: (a) 6 base stations. (b) 5 base stations. (c) 4 base stations with low PDOP. (d) 4 base stations with poor coverage in x-direction resulting in high PDOP [18].

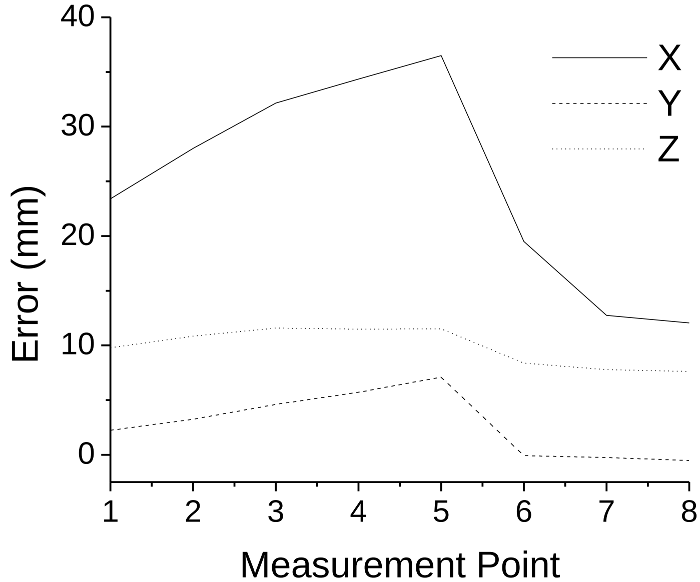

Figure 6-21: Comparison of x,y,z error for all points in simulating the multi-base station experiment outlined in Figure 6-20d using leading-edge detection. Substantially larger errors are observed in x; z also has higher error than y.

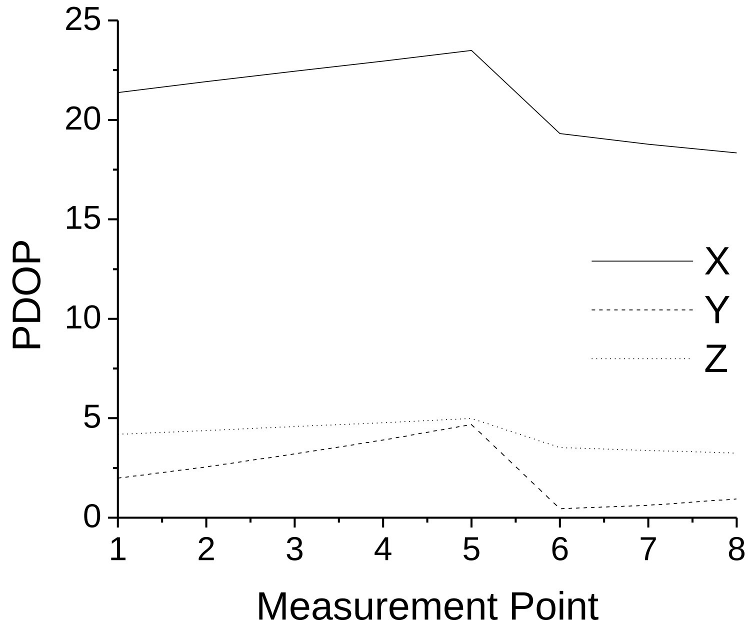

Figure 6-22: Comparison of PDOP in the x,y,z dimensions for simulating the experiment outlined in Figure 6-20d. The PDOP in the x-dimension is much greater than y,z. Also, the PDOP in the z-dimension is consistently greater than y.

6.5 ADC Effects and Automatic Gain Control

As mentioned in [211], automatic gain control and ADC selection play a critical role in the performance of UWB receivers. The simulation results are shown in Figure 6-23, Figure 6-24, Figure 6-25, and Figure 6-26. All of the simulation results use the industrial LOS channel model to add significant multipath interference and pathloss to the UWB signals at the receivers. Figure 6-23 shows how the AGC increases the SNR of the received pulse and how the SNR is instrumental in ensuring correct operation of the leading-edge detection algorithm. For example, as shown in Figure 6-24, when the SNR drops below 6 dB, the leading-edge detection algorithm fails regardless of the ADC. Figure 6-25 shows the quantization-noise-to-signal-ratio of the received UWB pulses versus distance for three different ADCs: 105 MSPS, 10 bit (currently used in the first generation system), 400 MSPS, 12 bit (commercially available for relatively cheap), and 3 GSPS, 8 bit. The 3 GSPS, 8 bit ADC is currently top of the line technology and represents the upper limit of technology available for the ADC. As shown in Figure 6-25, the QNSR of the 105 MSPS ADC is relatively high for all distances (e.g. -8 dB) whereas the 3 GSPS ADC has a low QNSR for short distances but it drastically increases as the Tx-Rx distance moves towards 4 m. Although there is significant variation among the ADCs in terms of QNSR, as shown in Figure 6-24, the ADCs perform almost identically in terms of the most important parameter: accurate leading-edge detection of the incoming UWB pulse for a given SNR. All three ADCs fail as the SNR of the incoming pulse drops below 6 dB. Finally, in Figure 6-26, the addition of AGC significantly increases the operating range between the transmitter and receiver by increasing the SNR of the received UWB signal (Figure 6-23). This analysis shows how the UWB positioning system would benefit greatly from at least one stage of AGC while it depends little on ADC performance mainly because of the use of the sub-sampling mixer in the UWB receiver, which reduces the bandwidth of the received UWB signal to less than 50 MHz. The leading-edge detection algorithm provides a robustness to ADC limitations such as QNSR, which only adds to its importance in overall system performance.

6.6 Extension to Other UWB Systems

A novel simulation framework has been introduced which was used in simulating and understanding the operation of the 1st generation indoor UWB positioning system. The complete simulation framework allows the system to be tested and characterized by using its most critical parameter as the final result: real-time 3-D positioning accuracy. Unless actual

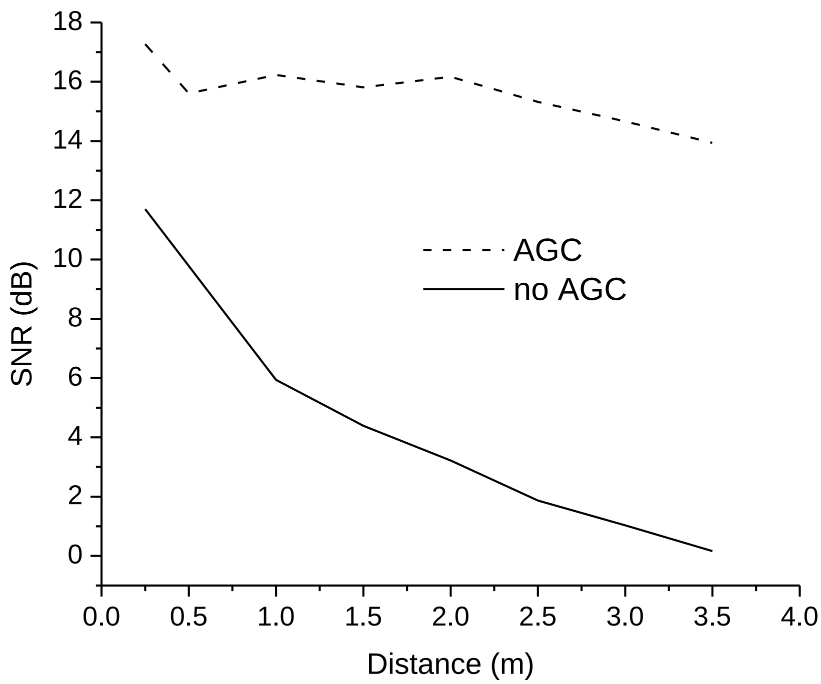

Figure 6-23: SNR of received UWB pulse vs. distance between transmitter and receiver with and without automatic gain control.

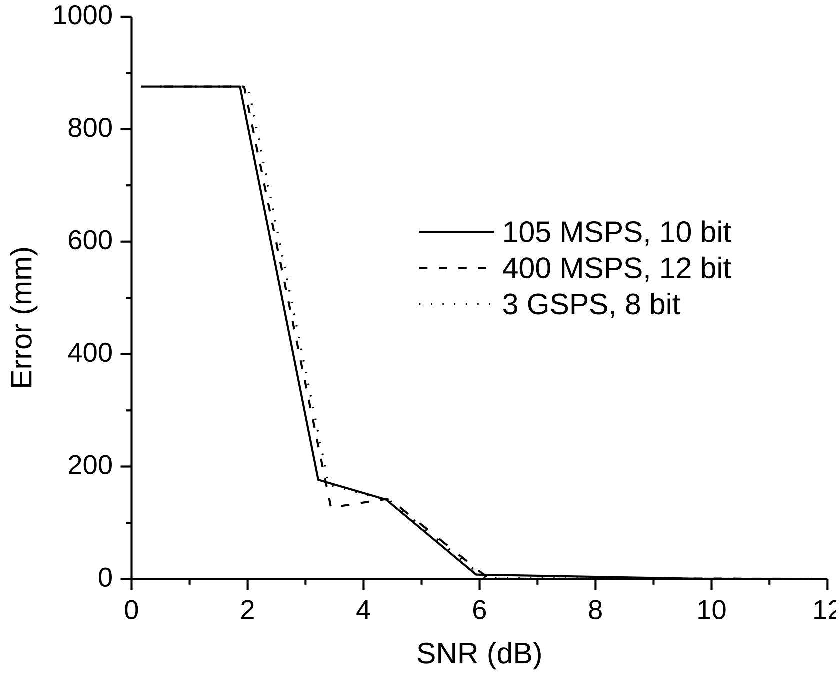

Figure 6-24: Simulated leading-edge detection 1-D error vs. SNR of received UWB pulse for three ADCs.

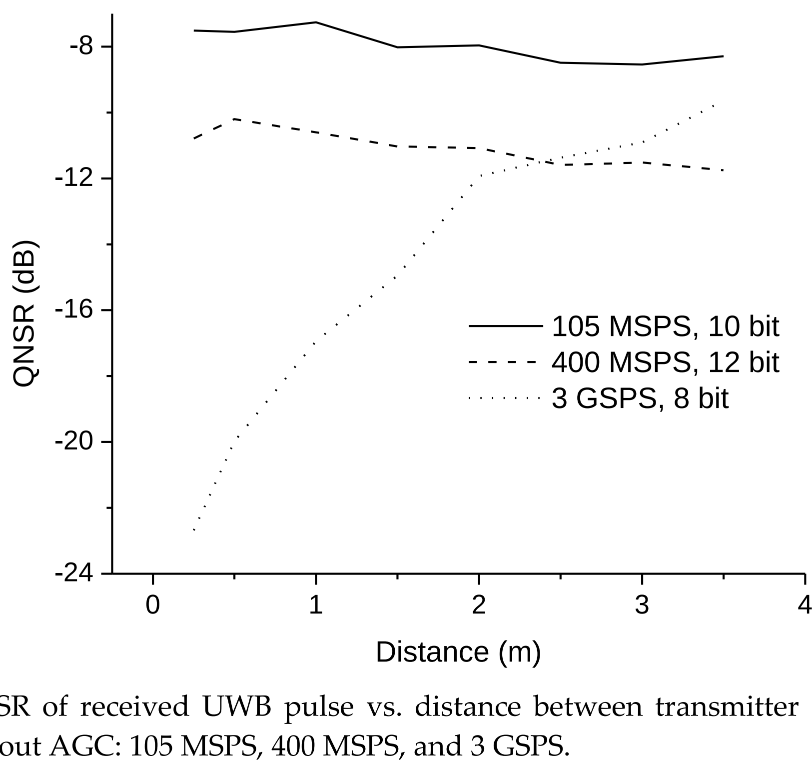

Figure 6-25: QNSR of received UWB pulse vs. distance between transmitter and receiver for three ADCs without AGC: 105 MSPS, 400 MSPS, and 3 GSPS.

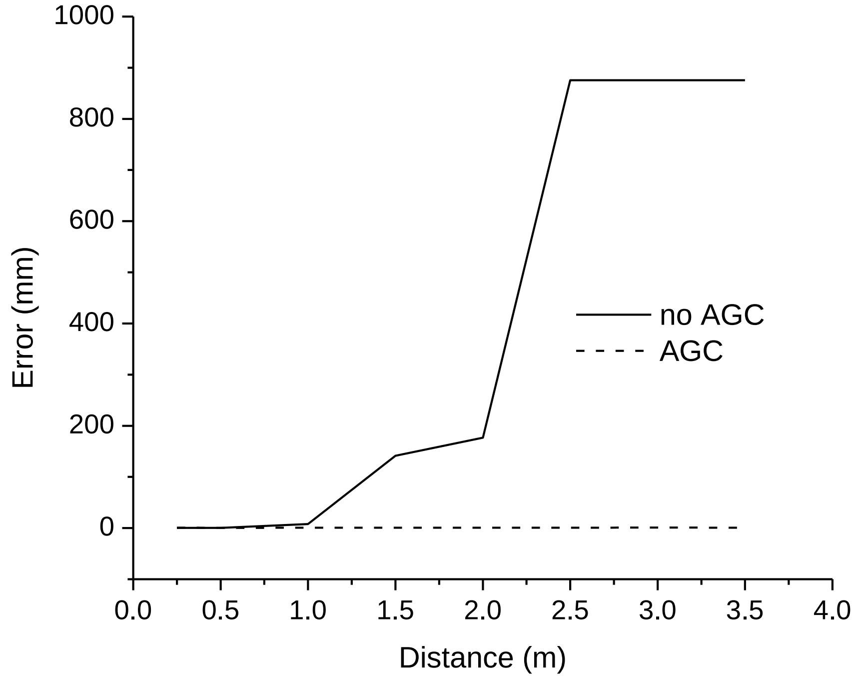

Figure 6-26: Simulated leading-edge detection 1-D error vs. distance between transmitter and receiver in the industrial LOS channel with and without automatic gain control.

experimental setups are simulated, such as the optical rail experiments outlined in Section 6.3, and all relevant aspects of the system taken into account (i.e. analog and digital portions of the transmitter and receiver, antenna effects, final processing of data on a computer, channel effects, geometric or other environmental effects, etc.), it is difficult or impossible to accurately simulate the performance of a complex wireless system such as the 1st generation UWB indoor positioning system outlined in Chapter 5. This methodology for simulating all aspects of a complex wireless system is gaining momentum for both communication and radar systems as simulation tools become more robust. Recently, this same framework has been utilized in simulating the performance of a see-through-wall radar UWB imaging system [212],[213]. This overall framework is general and the underlying simulation tools robust which allows it to be tailored to any given wireless system, both narrowband and wideband. Given the need for rapid prototyping combined with the cost of constructing experimental prototypes, it is critical that comprehensive simulation frameworks receive more attention and be included in the early stages of the design process for new wireless systems.

7. A Multi-Tag Development Platform for High Accuracy Indoor UWB Localization

Essential to an operational UWB localization system is a multi-tag access scheme based on wireless digital communication to enable the tracking of multiple assets simultaneously. A 2.4 GHz communications link is introduced into the UWB positioning system. Section 7.1 discusses a minimum shift keying approach based on Zigbee-like COTS. This opens up the ability for network operation in UWB localization. Section 7.2 provides an overview of the complete multi-tag UWB development platform. Finally, Section 7.3 discusses the integration of MMIC analog front-ends at both the UWB transmitter and receiver of the UWB multi-tag development platform outlined in Section 7.2.

7.1 2.4 GHz Minimum Shift Keying for Multi-Tag Access

The tag-controller architecture utilizes a TI MSP430 microcontroller in conjunction with the TI CC2500 MSK transceiver which are connected through a serial peripheral interface bus. The integrated solution is the TI EZ430-RF2500 module which contains both of these chips as well as a USB interface for JTAG programming of the device. The SimpliciTI ad-hoc, low power network protocol is used to allow ad-hoc network operation [214]. This is implemented on the TI MSP430F2274 microcontroller to allow a TDMA ad-hoc network scheme.

Extensive work has been done in standardizing multi-tag access for various UWB applications by the IEEE 802.15 task groups. This includes UWB-impulse response for low data rate applications (802.15.4a task group) and changes to the physical layer and media access control layer to be amended to 802.15.4-2006 standard for RFID applications (802.15.4f task group) [215]. The standards constructed by these task groups are instrumental in determining the future direction of research and development both in academia and industry. This multi-tag access scheme falls within the low data rate applications included in the 802.15.4-2006 standard and is extendable to meet the newly created criteria agreed upon by the 802.15.4f task group.

The physical layers considered for use by the IEEE 802.15.4f task group are shown in Table 7-1. Data was obtained from presentations made by each company at the September 2009 meeting of the task group [216]. The proposals for the physical layer are divided between solutions based on UWB communication and more conventional 2.4 GHz Zigbee protocols. UWB implemented in CMOS technology yields the best performance in terms of lower power (1-60 mW), longer operating ranges (>250 m for coherent receiver architectures), and higher data rates (1-6 Mbps), although the hardware required to support UWB communication is still in its infant stage. In the UWB systems, a tradeoff exists between data rate and operating range (e.g. the DecaWave proposal has a range of 940 m for 110 kbps while only 238 m for 6800 kbps). Also, non-coherent UWB receivers provide a simpler architecture compared to coherent receivers but typically have only 50-70% the range of a coherent receiver. Although UWB-IR is not tied to any specific modulation technique (many different schemes could be used including PPM, OOK, BPSK, and pulse shape modulation), the 802.15.4f task group chose OOK for the final UWB modulation scheme due to its simplified implementation architecture, lower transmit and receive power, and adequate performance for RFID applications [217]. An analysis by Ubisense using P-Aloha modified for UWB OOK showed a maximum throughput of 40,000 tags and 95% packet success rate for 1000 tags transmitting blink signals at 1 s intervals.

The theoretical bit-error-rate for UWB OOK, PPM, and BPSK as well as 2.4 GHz minimum shift keying for an AWGN channel is shown in Figure 7-1. A theoretical analysis on UWB BER performance can be found in [218]. It is apparent from Figure 7-1 that MSK and BPSK achieve better BER performance compared to PPM and OOK. However, both MSK and BPSK rely on accurate phase information, which requires an accurate channel estimation at the receiver. As discussed in [218], even when analyzing the BER in realistic channel environments including the residential LOS IEEE 802.15.4a channel model, BPSK only achieves a 3-4 dB improvement compared to simplified approaches such as PPM and OOK. Also, BPSK requires an accurate channel estimation, which is a large assumption for indoor environments with a dense number of scatterers.

As previously mentioned, UWB OOK schemes are the preferred choice for RFID applications for many reasons including long battery life, simplified transmitter and receiver architectures, and not needing an accurate channel estimation to transmit and receive digital information. Unfortunately, low power CMOS UWB transceivers are still a maturing technology. Successful designs can be found both from research groups [65],[66] and in industry [64]. However, these components are not for sale commercially, which prevents current researchers from moving directly into a UWB physical layer. Instead, the second generation UWB positioning system outlined in this chapter uses the 2.4 GHz physical layer currently being constructed by the 802.15.4f task group which closely follows the MSK scheme outlined by Ubisense in Table 7-1 [217]. With development tools readily available at low cost, this provides a viable alternative for multi-tag access while the technology needed for the UWB physical layer continues to mature.

The overall specifications for the multi-tag UWB positioning system are shown in Table 7-2 where the RF system has an operating range of 100 m while the UWB system range is limited to 13 m. The power consumption is dependent on the refresh rate of the tag (3.8-10.3 mW for refresh rates of 1-20 Hz). Battery lifetime ranges from 10-27 days depending on the refresh rate (20-1 Hz). The 2.4 GHz RF transmit power is -1 dBm while the UWB transmit power

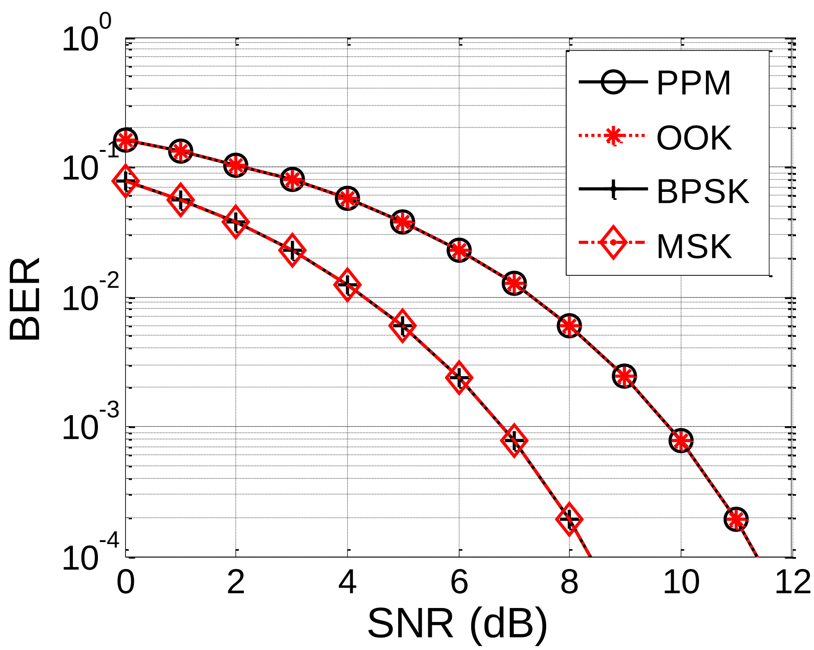

Figure 7-1: Comparison of theoretical bit-error-rates for UWB modulation schemes (PPM, OOK, BPSK) and narrowband 2.4 GHz MSK in AWGN channel.

Table 7-1: Comparison of technologies available for indoor RFID applications.

Technology	Modulation Type	Frequency (GHz)	Refresh Rate (Hz)	Number of Tags	Positioning Accuracy	Range (m)	Data Rate (Mbps)	Battery Life (Days)
Wi-Fi 802.11b	DSSS	2.40-2.48	>1000	32	> 3 m	1-100	11	0.5-5
Bluetooth	GFSK, DPSK	2.40-2.48	>1000	7	1-2 m	1-10+	0.72-3	1-7
802.15.4f UWB	OOK	5.90-7.10 6.00-8.50 7.20-10.2	<1	Unlimited	5-30 cm	49-280	1-2	100-1000+
802.15.4f 2.4 GHz	MSK	2.40-2.48	<1	Unlimited	> 50 cm	1-100	0.25	100-1000+
Zigbee	MSK	2.40-2.48	<1	Unlimited	> 50 cm	1-100+	0.25	100-1000+
This Work	MSK	2.40-2.48 5.40-10.6	<1-20	1000 to 50 per piconet	5-10 mm	1-100 <13	0.25	10-27+

Table 7-2: UWB positioning system link and power budget.

RF Operating Range	100 m
UWB Operating Range	13 m
3-D UWB Positioning Accuracy	5-10 mm
Power Consumption (1 Hz Refresh Rate)	3.8 mW
Power Consumption (20 Hz Refresh Rate)	10.3 mW
Number of Tags (20 Hz Refresh Rate)	50
Number of Tags (1 Hz Refresh Rate)	1000
Battery Lifetime (20 Hz Refresh Rate)	10 days
Battery Lifetime (1 Hz Refresh Rate)	27 days
UWB Transmit Power	-7.8 dBm
UWB Bandwidth	5.4-10.6 GHz
UWB Receiver Sensitivity	-75.3 dBm
RF Transmit Power	-1 dBm
RF Bandwidth	650 kHz
RF Receiver Sensitivity	-88 dBm
RF Modulation	MSK

is -7.8 dBm integrated across the whole frequency range of the UWB signal (5.4-10.6 GHz). The UWB receiver sensitivity of -75.3 dBm is limited by the wide bandwidth of the UWB signal (5.2 GHz bandwidth) compared to the narrowband 2.4 GHz system with a receiver sensitivity of -88 dBm. The overall multi-tag access scheme is a TDMA approach which allows for networking of the UWB tags. This concept is illustrated in Figure 7-2 where new tags are "discovered" and incorporated into the overall wireless sensor network. It should be noted that the networks are limited by the range of the UWB signals (13 m from Tx-Rx). Additional base stations are needed to expand the overall coverage of the system.

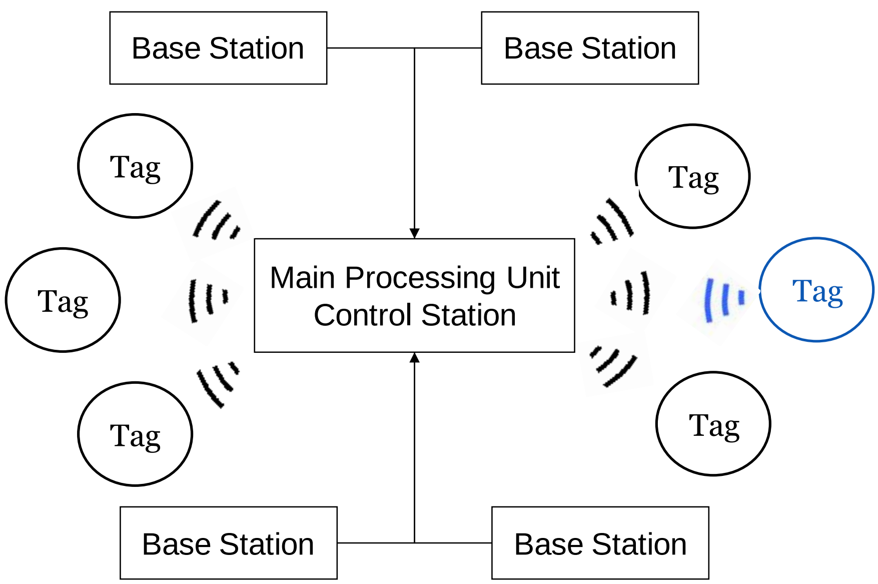

Figure 7-2: Time division multiple access where the main processing unit broadcasts all tag IDs in a round-robin fashion and the base stations localize the tag 3-D positions.

7.1.1 Experimental Setup

One EZ430-RF2500 module (termed the Access Point MCU) is needed at the CPU and is directly connected to the FPGA through two digital lines, comprising the main control station. Figure 7-3 shows the control station architecture where the Access Point MCU asynchronously transmits tag IDs to the FPGA to label incoming TDOA packets with the correct tag ID. Figure 7-5 shows example serial data output by the Access Point MCU to the computer to collect and process TDMA information by the C++ software application. Figure 7-4 shows a block diagram of the experimental system where the Access Point MCU communicates with the tag MCUs to implement the TDMA scheme.

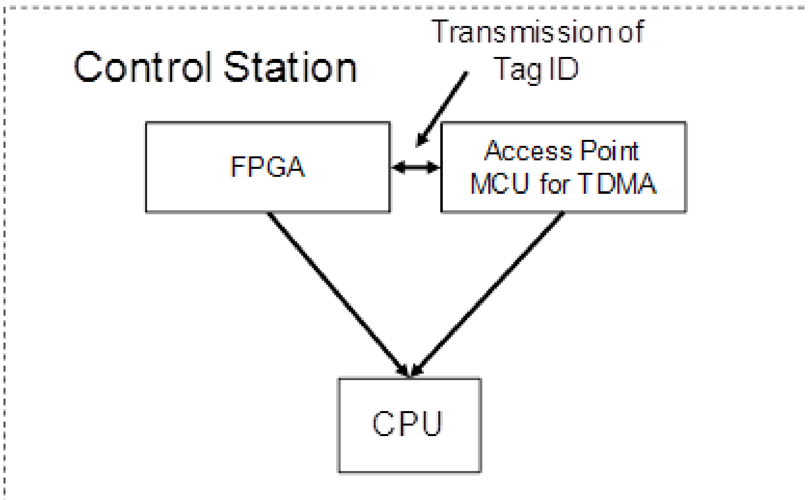

Figure 7-3: Control station architecture where Access Point MCU sends tag IDs to the FPGA for synchronous tagging of the TDOA data for TDMA approach.

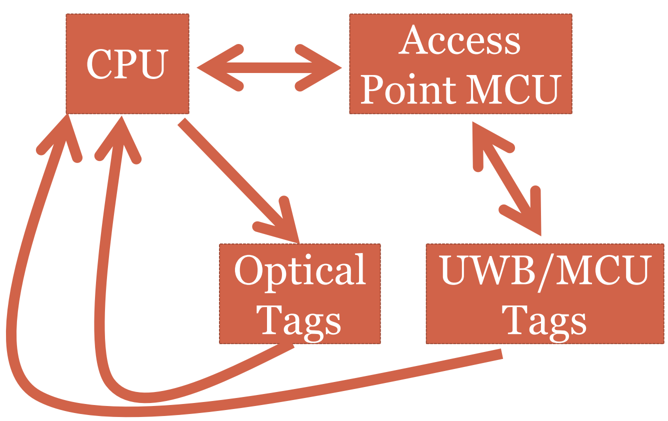

Figure 7-4: Block diagram of experimental setup outlining the role of a computer to collect data from the MCU access point, UWB positioning system, and optical tracking system. The CPU can send configuration signals to the MCU. The MCU-MCU tag-access point communication is also highlighted.

$0001, 86.1F,3.8,020,N#,002
T1
$HUB0, 97.1F,3.5,000,N#,009
$0004, 81.3F,4.9,033,N#,001
T2
T3
$0002, 84.7F,3.6,022,N#,002
T4
T1
$0003, 83.1F,2.9,026,N#,002
T2
T3
T4
T1
T2

Figure 7-5: Example serial data received during one second at the CPU from the access point microcontroller while communicating with four tags. The data includes the current tag transmitting for TDMA and a general status update for each tag as well as the access point.

7.2 UWB Multi-Tag Development Platform

The tag-controller architecture builds off of the 2.4 GHz system discussed in Section 7.1 while expanding the system to 10 functional tags fully integrated into the overall UWB positioning system which includes receiver and control station digital processing and a C++ software application for real-time location system functionality. The UWB multi-tag development platform consists of a 10 tag system where each tag is an integrated system using either wall power or a 9 V battery for power with its own transmitter 10 MHz system clock. The tags are integrated into the digital processing done at the UWB receivers and the UWB control station as well as the C++ UWB software application.

7.2.1 Integrated UWB Tag

A block diagram of the UWB integrated tag is shown in Figure 7-6. The tag consists of a DC power board fabricated on FR4 substrate. The DC power board includes a 9 V battery holder and a jack for wall power. DC-DC converters are used to supply the RF board with +5 V, -5 V, and 3.3 V. Load switches reside on the DC power board. The DC power board is shown in Figure 7-8. These load switches are controlled by the TI MSP430-RF2500 2.4 GHz MCU module to switch on and off power to the UWB tag to implement the TDMA multi-tag scheme. The RF board is outlined in Figure 7-7 where a 10 MHz Vectron TCXO drives a TI 2674 op amp which drives a step recovery diode UWB pulse generator. The UWB pulse is upconverted via a Hittite H506 VCO and amplified by a Hittite H441 medium power amplifier. The pulse is transmitted via a UWB monopole antenna. The complete integrated tag is shown in Figure 7-9

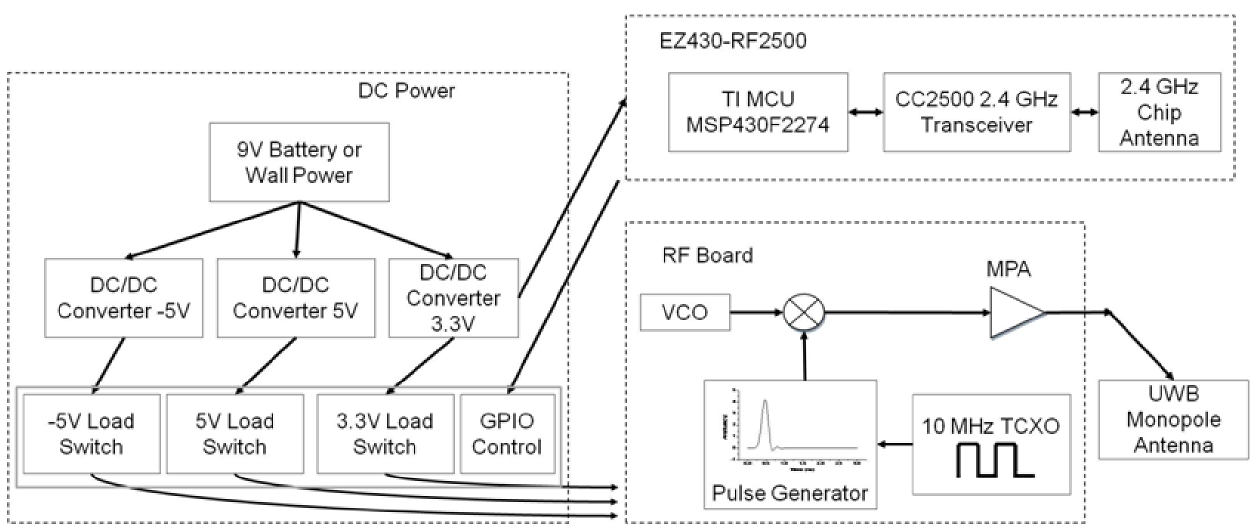

Figure 7-6: Block diagram of integrated UWB tag including the RF board containing the UWB pulse generator, VCO, mixer, and amplifier. A separate DC power board contains the DC-DC converters and load switches used to switch on and off the power to the RF board to implement the TDMA scheme.

and Figure 7-10 where the MCU board connects to the RF board, and the RF and DC power board lock together via two 40 pin Samtec connectors. The tag has a relatively high load power requirement when fully operating of 1008 mW. When DC-DC converter losses are included, the tag consumes around 1.5 W of power when transmitting UWB pulses. In its low power state when UWB transmission is turned off, the tag consumes around 200 mW of power. As discussed in Section 7.3, future work is being done to incorporate MMIC front-ends into the tag and receivers to significantly reduce operating power requirements. Figure 7-11 shows baseband pulses from all 15 tags where the green pulse is from a discrete (ideal) pulse generator and the black pulses are from the integrated tags. The pulse amplitude across

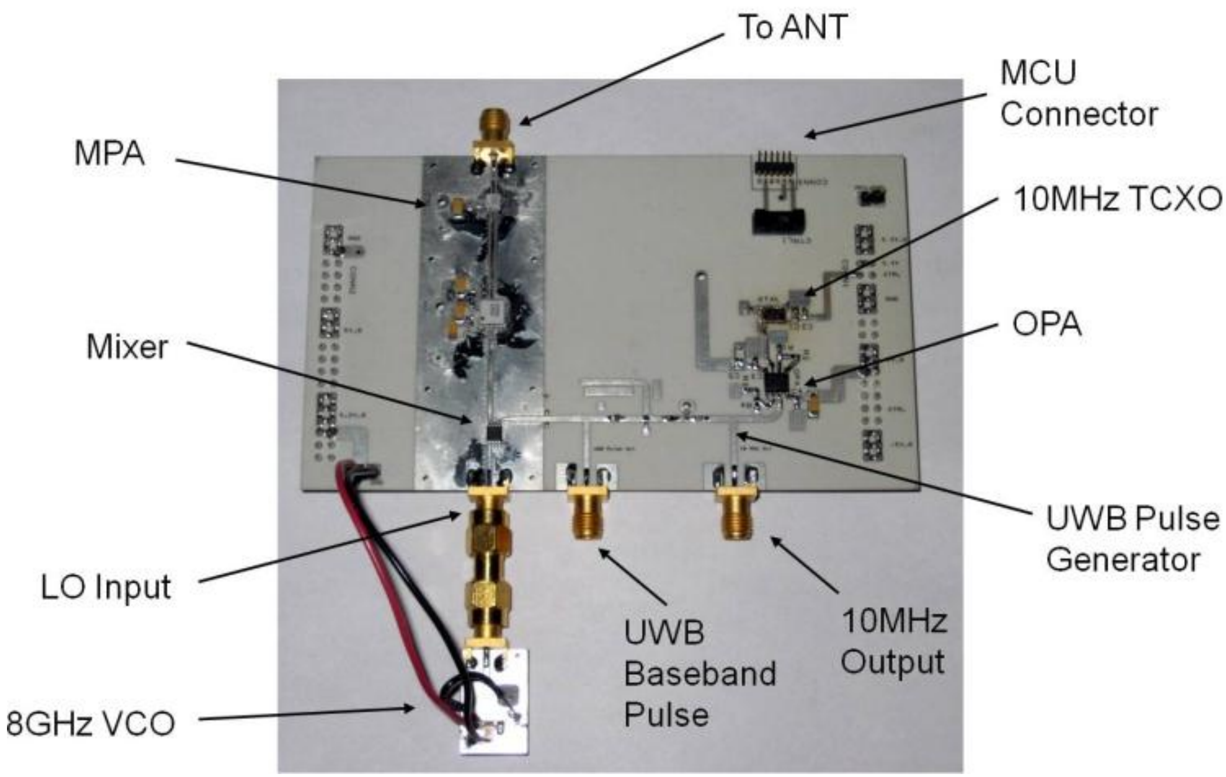

Figure 7-7: Integrated tag RF board including 10 MHz clock, high slew rate op amp, step recovery diode pulse generator, mixer, VCO, and medium power amplifier. A 6-pin connector is used to connect the MCU board to the RF board.

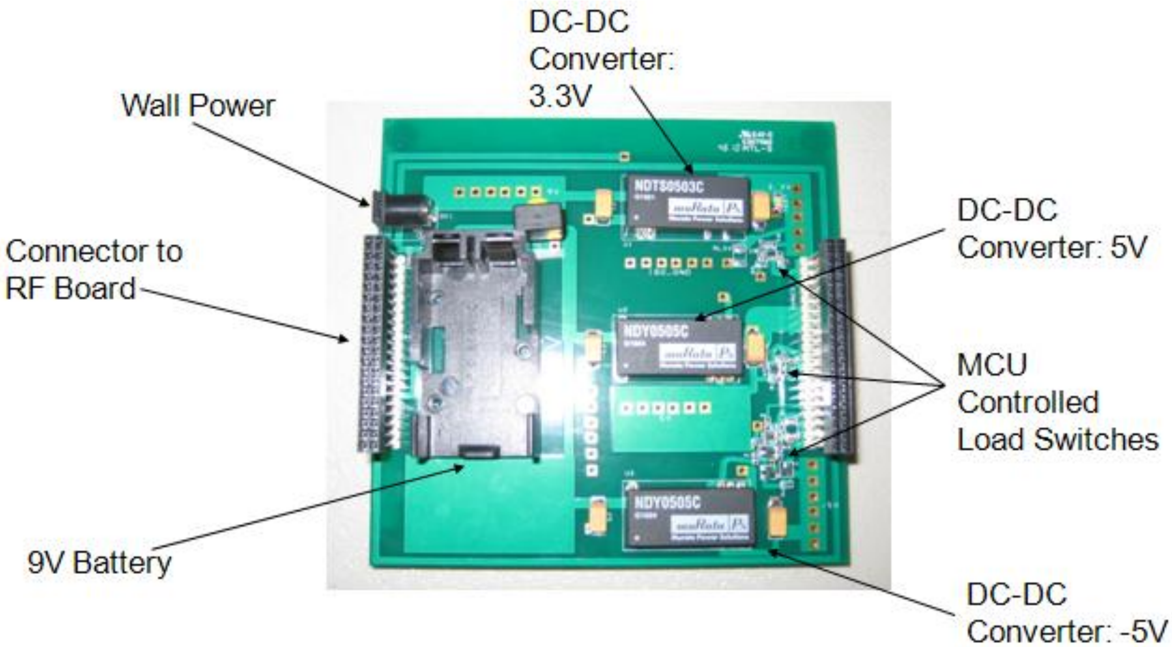

Figure 7-8: DC power board which includes wall power or power via a 9V battery. Connectors are used to directly connect the RF board shown in Figure 7-7. DC-DC converters are used to supply the RF board with +5V, -5V, and +3.3V. Load switches allow the DC power to the tag to be turned on and off and are controlled by the tag MCU. This provides the underlying time division multiple access functionality.

the 15 tags has some variation, and some of the integrated tags exhibit more ringing than the reference tag (green). Overall, all of these signals are usable for UWB indoor positioning and can be processed using the leading-edge detection algorithm outlined in Chapter 9. Figure 7-12 shows the upconverted UWB pulse from an integrated tag (black) as well as the upconverted UWB pulse from the reference transmitter (green) in the frequency domain. The -10 dB bandwidth of the reference transmitter is around 1.5 GHz larger than the integrated tag. The reduction in bandwidth is most likely caused by the integrated RF board shown in Figure 7-7. Variation exists when comparing the frequency spectrum of the upconverted signal across all 15 tags. Ultimately, these variations do not have a significant effect on the positioning accuracy since the UWB receivers are able to sub-sample the downconverted UWB pulses and digitally located the pulse leading edge. Thus, it can be inferred that the integrated tag is a viable solution for achieving millimeter 3-D dynamic accuracy for multiple, independent tags in real-time.

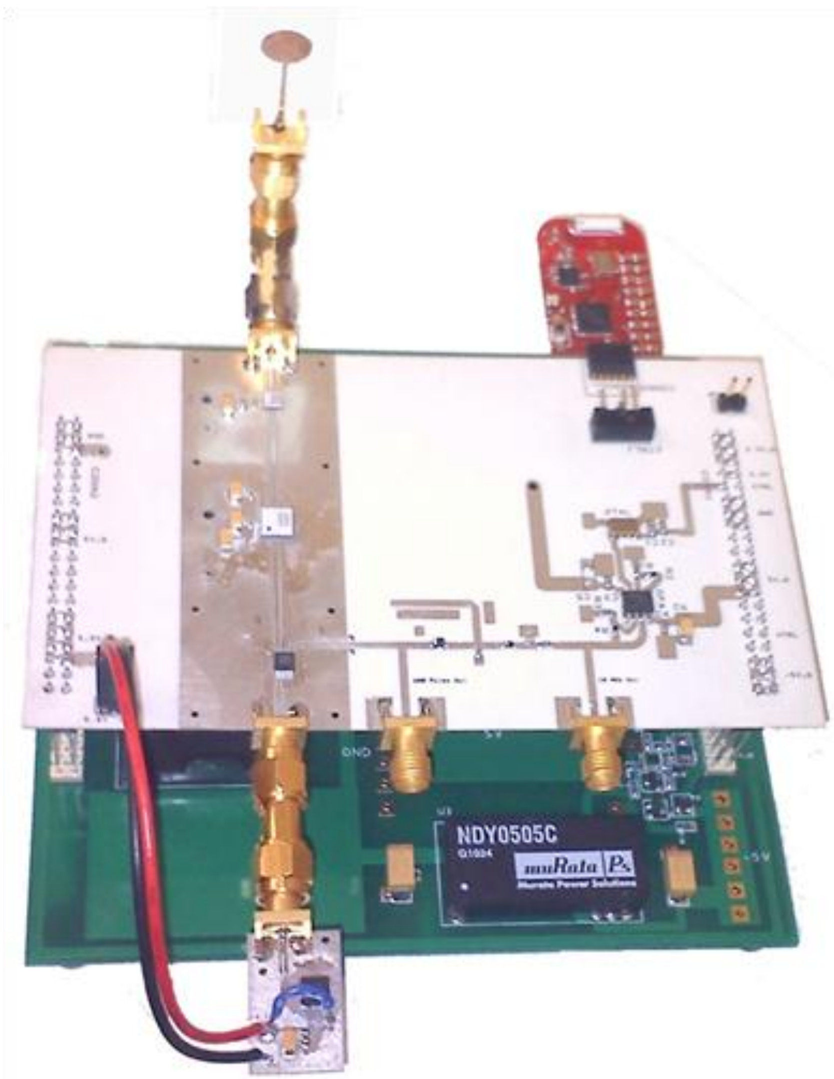

Figure 7-9: Integrated tag including DC power board, RF board, MSP430-EZ2500 microcontroller board, VCO connected via external SMA connector, and monopole UWB antenna.

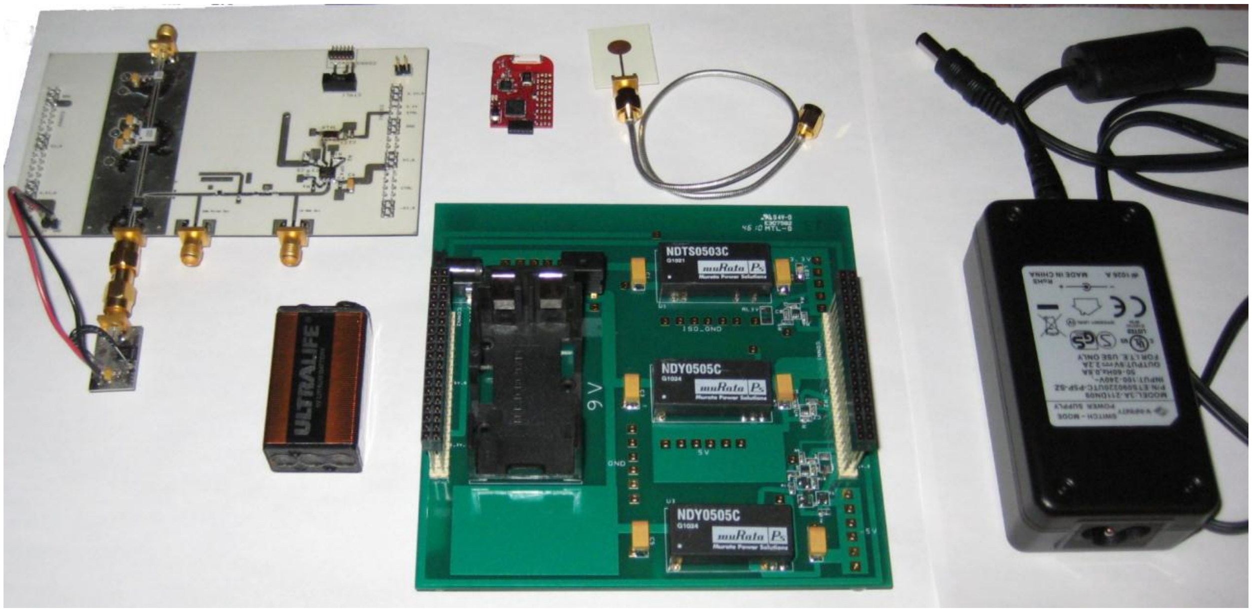

Figure 7-10: Integrated tag components including DC power board, RF board, MSP430-EZ2500 microcontroller board, VCO connected via external SMA connector, monopole UWB antenna, 9V battery, and 9V AC/DC power converter.

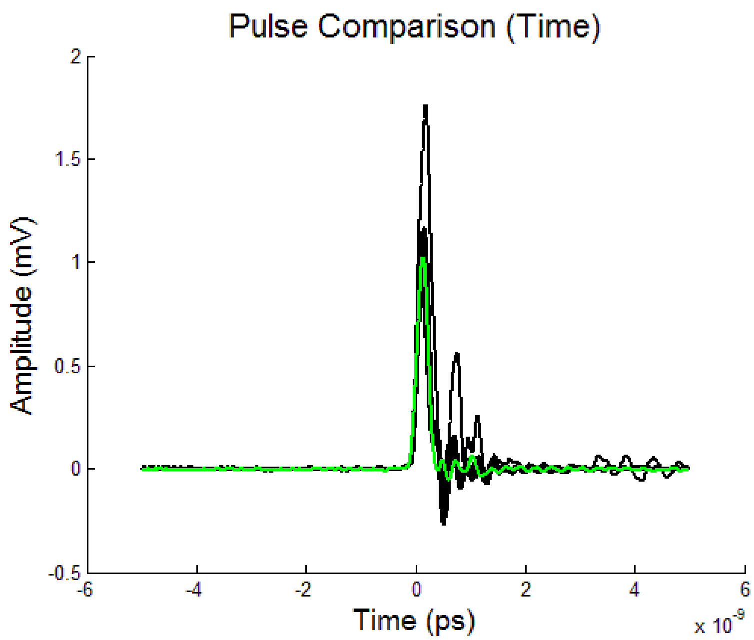

Figure 7-11: Baseband UWB pulses from the 15 tags (in black). A reference pulse from a separate SRD-based pulse generator (green). The pulse amplitude across the 15 tags has some variation, and some of the integrated tags exhibit more ringing than the reference tag. Overall, all of these signals are usable for UWB indoor positioning.

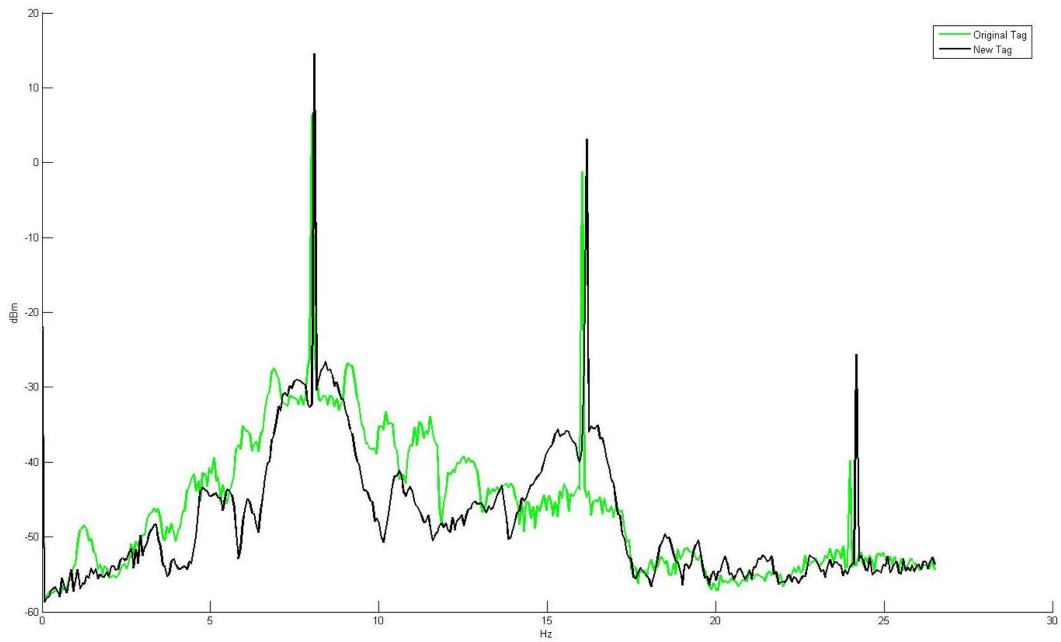

Figure 7-12: Upconverted UWB pulse in the frequency domain: integrated tag (black), discrete tag (green).

7.2.2 UWB Energy Detection Receiver

Figure 7-13 shows the block diagram for the UWB non-coherent receiver [219]. The transmitted UWB pulse is received by a single element Vivaldi directional antenna. It then goes through a 5-11 GHz bandpass filter, three stages of amplification, and is downconverted by a broadband squaring mixer designed by Elkhouly [219]. The signal is then lowpass filtered, goes through two stages of baseband amplification, is subsampled to time extend by a factor of 2500, reducing the bandwidth of the pulse from 3 GHz to around 1.2 MHz. The signal is then passed through a 105 MSPS ADC, the leading-edge is located via the FPGA implemented algorithm discussed in Chapter 9. The final range difference data for all four UWB receivers is fed to the computer via an RS232 serial connection with baud rates of up to 460,800. Figure 7-14 shows the UWB non-coherent receiver outlined in the block diagram in Figure 7-13.

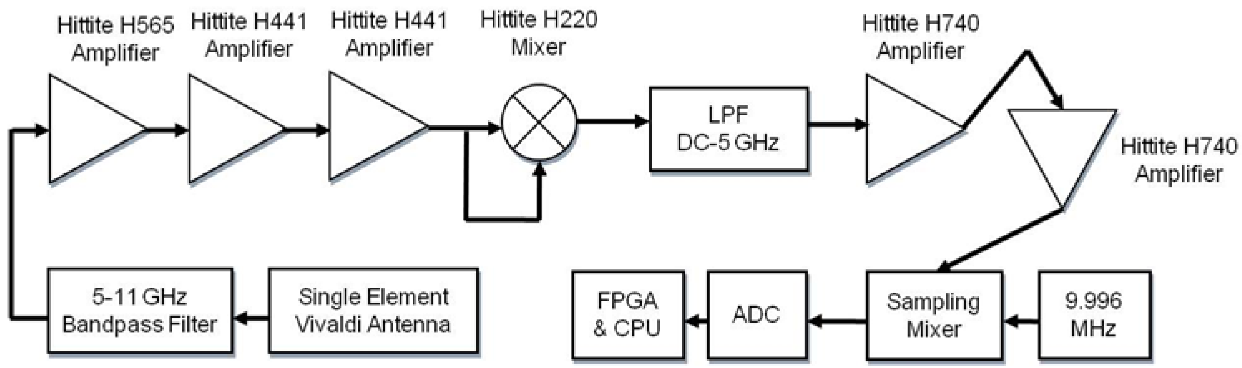

Figure 7-13: Block diagram of the UWB receiver where a single element Vivaldi antenna is connected to a 5-11 GHz band-pass filter, goes through three stages of amplification followed by a squaring mixer, then is low-pass filtered, goes through two stages of baseband amplification, and is sub-sampled to be 2500 times larger in the time domain. The signal is then converted to digital and processed on a FPGA before being fed to a C++ application on a computer via a serial connection [219].

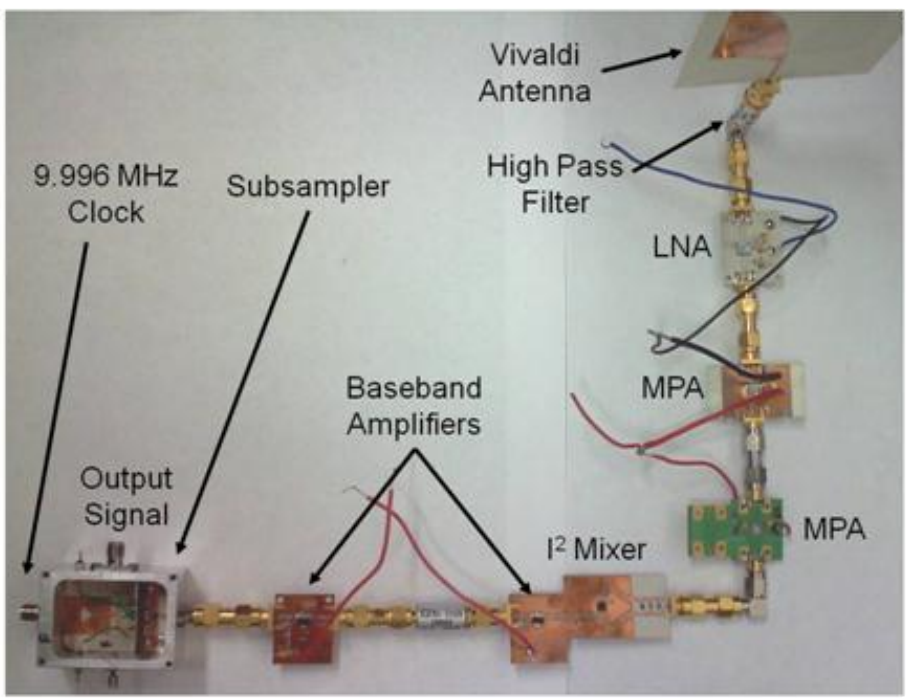

Figure 7-14: UWB energy detection receiver including a front-end band-pass filter, one low noise amplifier, two medium power amplifiers, a squaring mixer [219], two baseband amplifiers, and the sub-sampling mixer.

7.2.3 Digital Processing and Real-Time Software Integration

The microcontroller at the UWB control station turns tags on and off in a round robin fashion to implement the TDMA scheme. The control station consists of a TI EZ430-RF2500 USB dongle connected to the computer and an FPGA Spartan 3E evaluation board which is connected to the computer via an RS232 serial connection. A Perle RS232 to Ethernet device is inserted between the FPGA control station board and the computer to allow for data rates of up to 460,800 (limit of the RS232 chip on the FPGA evaluation board). Tag IDs are picked by the control station microcontroller as shown in Figure 7-15. The current tag ID is sent to the control station FPGA which then broadcasts the current tag ID to all base station FPGAs to synchronize the reception of UWB localization pulses with the correct tag ID. Figure 7-16 shows the MCU control signals from tags 1 and 2 which are used in turning on and off the load switches which supply DC power to the RF board of each integrated tag. Each tag is allocated 7 ms time bins to transmit UWB pulses before switching to the next tag. The C++ software application currently supports up to 10 tags operating simultaneously. Figure 7-17 shows UWB pulse trains for tags 1 and 2 captured with an 8 GHz real-time oscilloscope. A 160 μs latency in UWB pulse train transmission is observed when switching between tags 1 and 2. This is due to the

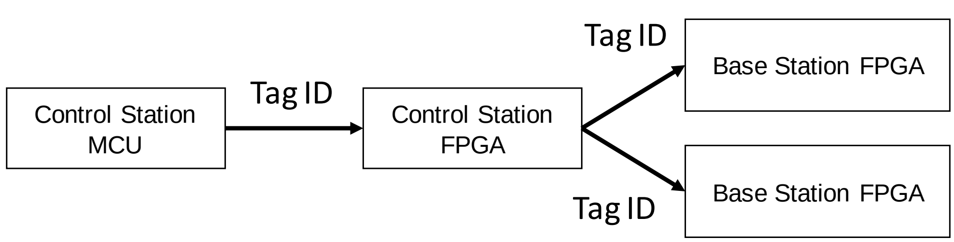

Figure 7-15: The current tag ID is sent from the control station microcontroller to the control station FPGA. From the control station FPGA, the tag ID is sent to all base station FPGAs to synchronize the current tag ID.

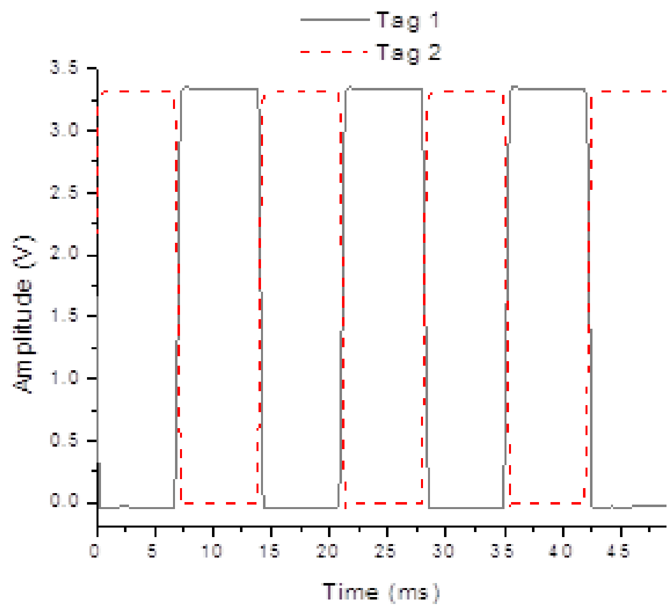

Figure 7-16: MCU control signals for tags 1 and 2 over a 50 ms time period broken into 7 ms transmitting intervals for each tag.

microcontroller processing associated with switching between tags at the control station MCU. This results in a 2.3% reduction in transmission of UWB pulses for a time bin size of 7 ms. Larger time bin sizes will result in lower and lower percentage reductions since the 160 μs latency will occur will less and less frequency. Figure 7-18 shows the time differences received at the computer via the C++ software application for tags 9 and 13 where the tags are left in static positions. The time differences represent the raw data used to calculate the tag 3-D position. As shown in Figure 7-18, the time differences can be seen switching between the current location of tags 9 and 13. A roughly 20% reduction in the overall system update rate is observed when switching between multiple tags with a time bin of 7 ms. This occurs because UWB positioning data packets are corrupted at the UWB receivers for the short time interval surrounding the switch from one tag to the next (illustrated for two tags in Figure 7-17).

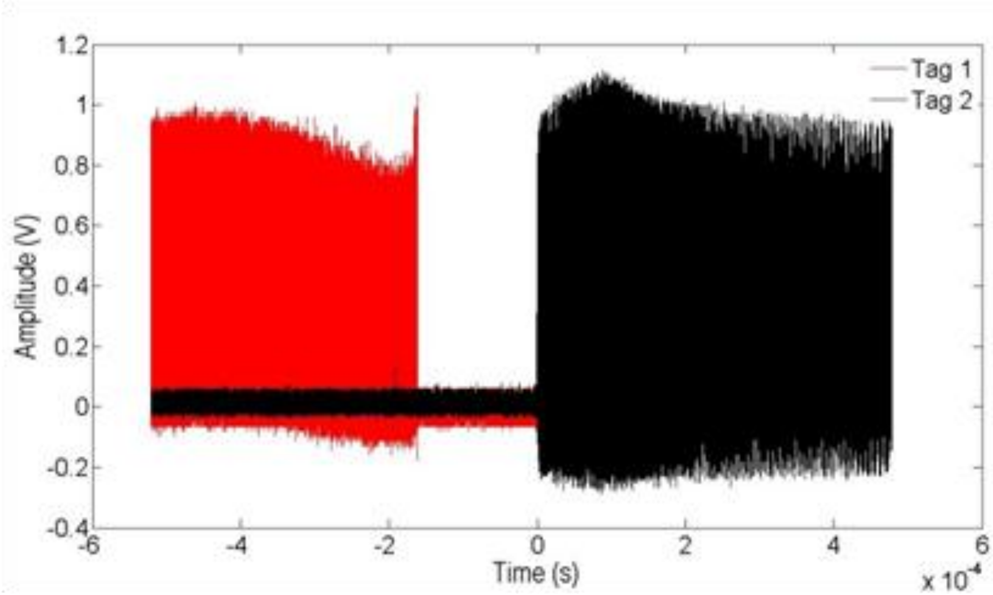

Figure 7-17: Baseband UWB pulse trains for tags 1 and 2 where a 160 μs latency occurs between turning off and on tags 1 and 2. Obtained by an 8 GHz real-time sampling oscilloscope.

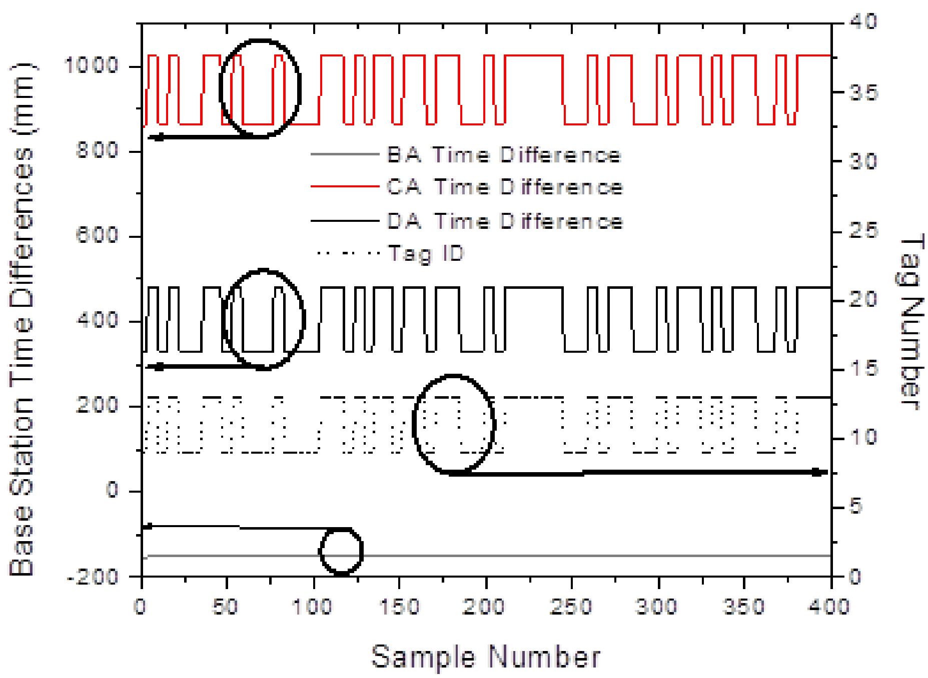

Figure 7-18: Time differences received at the computer where two distinct bands can be seen representing the 3-D positions of tags 9 and 13.

The C++ software application is outlined in Figure 7-19, Figure 7-20, and Figure 7-21. The multi-tag display window shown in Figure 7-19 displays the currently connected tags including their 3-D position, 3-D error (if being tracked by an optical probe), refresh rate (in Hz), signal strength which corresponds to the 2.4 GHz MCU link, temperature as calculated by the MCU, and battery voltage. A tag can be designated as the static tag. More information on the static tag is outlined in Section 7.2.4. The Record Data checkbox allows recording CSV data for each tag. The Calibrate button can be used to perform a 3-D calibration for each tag as outlined in Section 7.2.5. Figure 7-20 shows the TDMA window. The time interval allocated to each tag can be set here as well as the duty cycle for how much of that time interval the tag is turned on. The default settings are 7 ms time interval and 100% duty cycle (for high accuracy real-time tracking). Low power operation could consist of a 1000 ms time interval with a 1% duty cycle. The tag calibration setup window is shown in Figure 7-21. This window can be used to save and load tag calibration files. These files contain 3-D calibration matrix data for 4 base station and 5 base station experiments, the number of 3-D points used in the calibration process, the tag scale factor (measured experimentally) which is a number to convert from raw time difference information to millimeters, the current static tag (tag number), the static tag reference time differences, the cable length offset (in time differences), and a 3-D XYZ offset to account for the optical probe tip being offset from the phase center of the tag monopole antenna.

Figure 7-19: C++ software application for displaying and collecting multi-tag data. This includes information for each tag such as 3-D position, 3-D error (if being tracked by an optical tracker), refresh rate (Hz), signal strength (from 2.4 GHz MCU), temperature (from MCU), and battery voltage. Each tag can be calibrated separately. Each tag can be tracked by an optical probe. A static tag is used to filter out receiver clock jitter and drift.

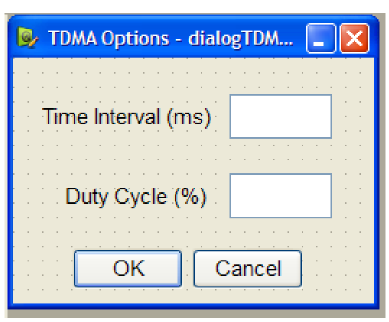

Figure 7-20: Time division multiple access parameters can be configured in the software and distributed to all tags via the 2.4 GHz communication link. This includes time interval (per tag, one time slice) and duty cycle which it is turned on within that time interval as a percentage.

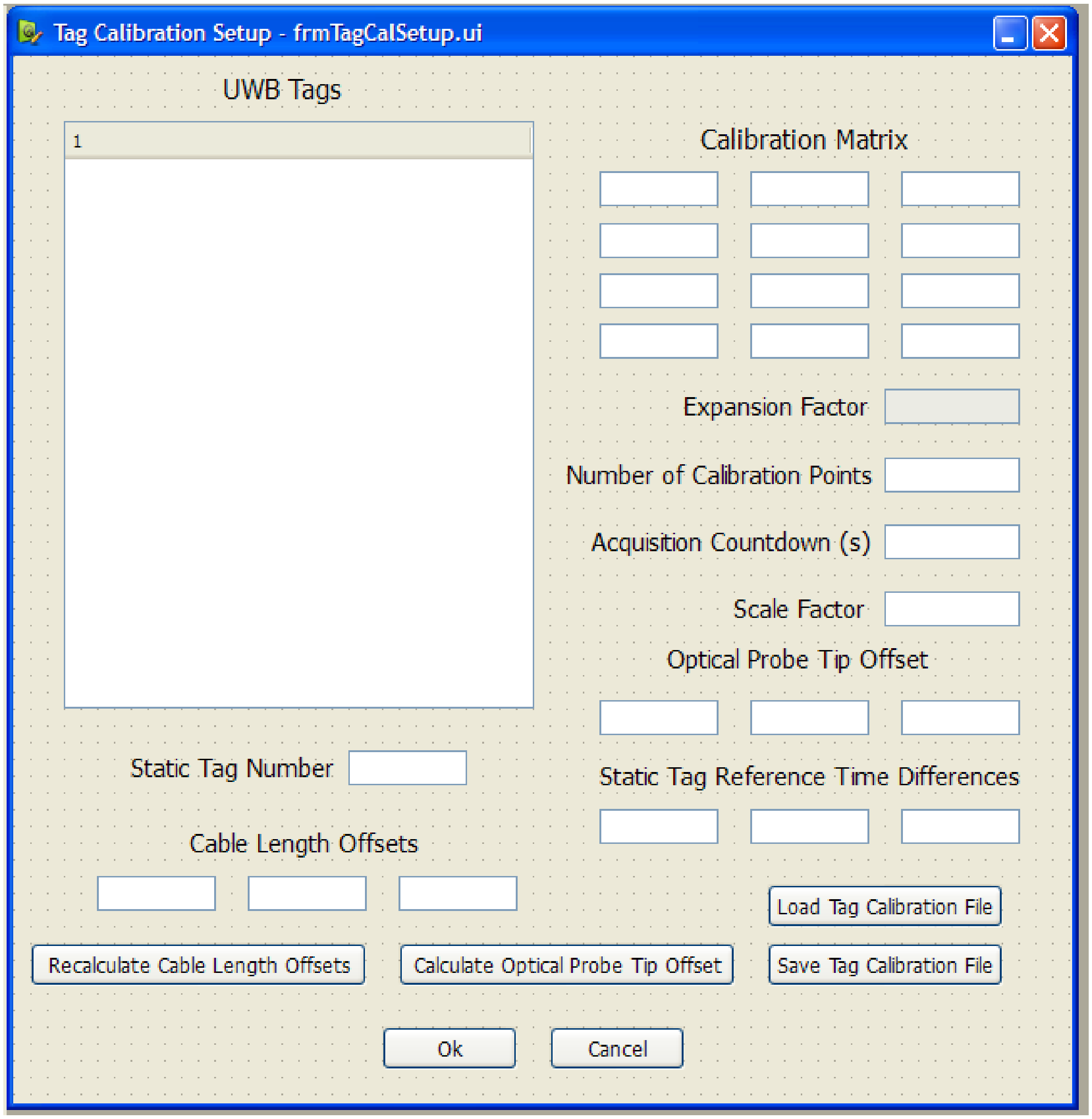

Figure 7-21: Tag calibration setup window. Used for setting tag calibration matrices as well as setting tag scale factors, cable length offsets (time differences) and the static tag reference point (in terms of time differences).

7.2.4 Static Tag Integration

The use of a sub-sampling mixer combined with the fact that precise ranging measurements on the order of 1-40 ps are needed for millimeter 3-D positioning cause this UWB indoor positioning system to have a high sensitivity to clock jitter and drift. Figure 7-22 illustrates the jitter and drift observed in the received range difference signals for a tag in a static location over a period of 23 minutes. Significant effects are observed including errors as high as 30-40 mm for each time difference. This causes 3-D positioning errors of 30 mm or more. These extremely large errors must be mitigated for the system to achieve consistent millimeter 3-D accuracy. Figure 7-23 shows one range difference signal for two tags at static positions over

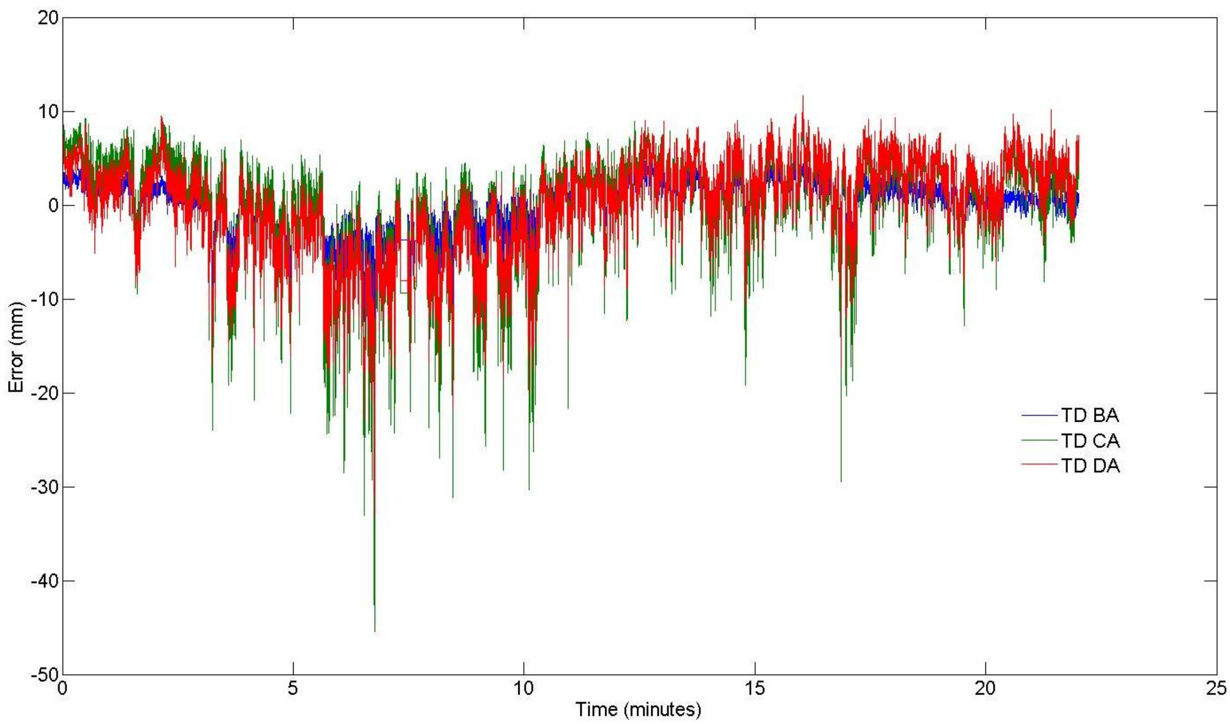

Figure 7-22: Measured receiver clock jitter and drift over a 23 minute interval caused by the 9.996 MHz signal used by the sub-sampling mixer to sub-sample the incoming UWB pulses. The clock jitter and drift can cause up to 30-40 mm of error in each measured range difference. This can cause 3-D positioning errors of 30 mm or more.

a time period of 20-30 s. There is a high correlation of the jitter and drifting between the two tags. This supports the hypothesis that the main source of error is receiver clock jitter and drift. The tags have a TCXO Vectron VTC4 crystal which has low drifting and jitter which can be removed by averaging signals on the receiver side. The receiver clock jitter and drift observed in Figure 7-22 and Figure 7-23 is due to the 9.996 MHz signal used by the sub-sampling mixer, which is currently supplied by a Tektronix AFG 3102 function generator. Since this drifting and jitter is consistent across all operating tags, it can be removed by using a static tag. Figure 7-24 shows the range differences for a 2nd tag over a time period of 25 minutes. Both tags are left in static positions. The first tag is designated the static tag and used to directly calculate the clock jitter and drift signal shown in Figure 7-22. The static received signal from the 2nd tag does not contain large drifting and jitter and contains mainly white Gaussian noise which can be removed by further averaging of the received signals. The C++ software application discussed in Section 7.2.3 has complete integration for the use of a static tag to remove the outlined receiver clock jitter and drift.

7.2.5 Cable Length Offsets

As discussed in [93], bias offsets exist in the path lengths from the UWB antennas to the point at the control station FPGA where the time differences are calculated. These static path lengths must be calibrated out of the system to remove the static bias errors they cause in performing the TDOA calculations. Using the same technique outlined in [93], these static path length biases are calculated using a single point where the optical system provides ground truth

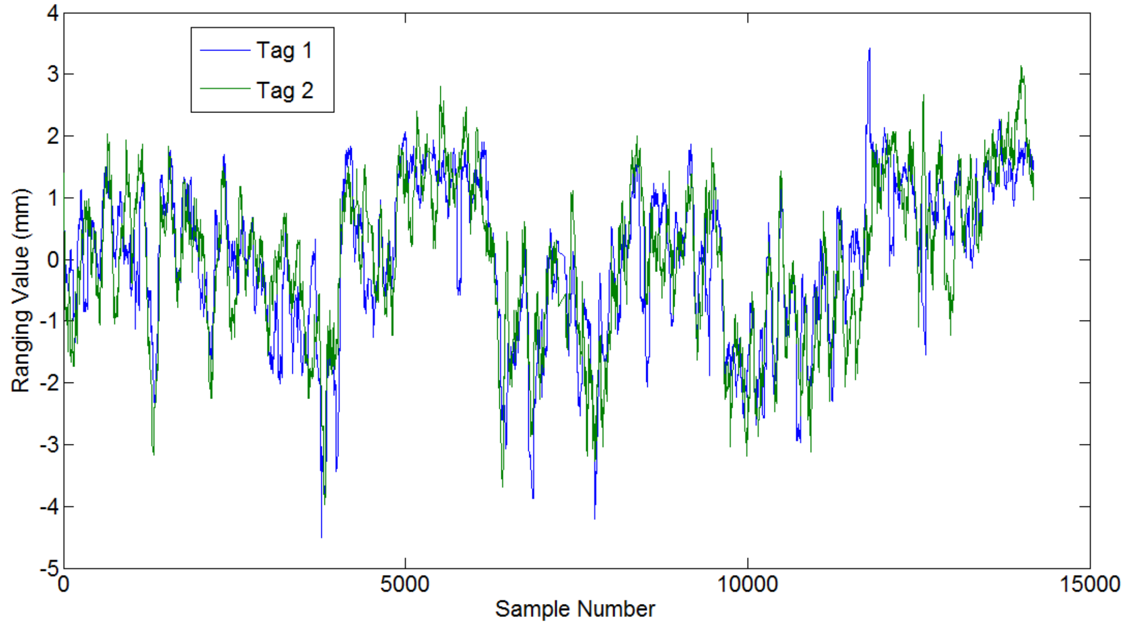

Figure 7-23: Received signal over 15000 samples (20-30 seconds) for one range difference for two different tags in static locations. The jitter and drift observed in the two signals correlates well, indicating that the main source of clock jitter and drift is from the UWB receivers and is therefore similar across all tags.

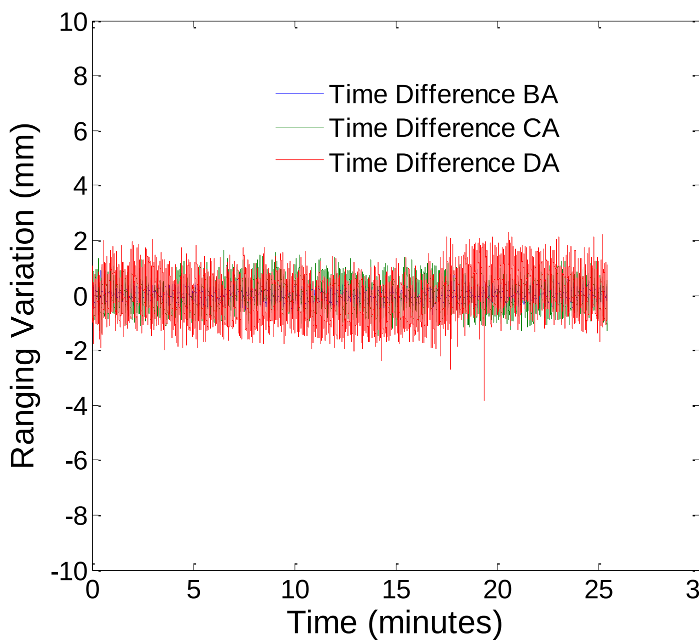

Figure 7-24: Measured receiver clock jitter and drift for a 2nd tag using the 1st tag as a static tag to calculate and remove the receiver clock jitter and drift. A nice Gaussian white noise is observed while the jitter and drift effects outlined in Figure 7-22 and Figure 7-23 are removed.

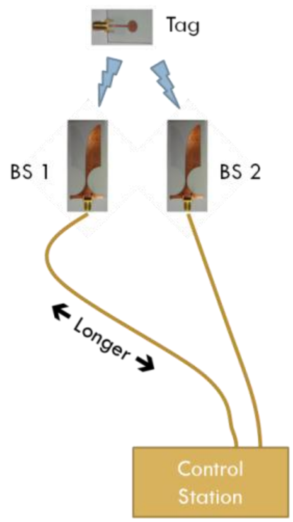

Figure 7-25: Illustration of cable length offsets which require a static calibration for removal in the C++ software [93].

information. Once the cable length offsets have been calculated, they are subtracted from new range difference data for every tag for every subsequent TDOA calculation. The cable length offset calibration is needed in addition to the use of a static tag (discussed in Section 7.2.4).

7.2.6 Tag Scale Factors

Each of the 10 tags contains its own Vectron VTC4 TCXO 10 MHz clipped sine wave clock which drives the transmission of UWB pulses. The VTC4 crystal has a stability of ±0.5 ppm and jitter of less than <30 ps (measured). The ±0.5 ppm stability can become an issue since 2500 pulses are required for each pulse obtained in the subsampling process. At f=10 MHz, stability of ±0.5 ppm translates into ±5 Hz. This translates into a 0.13% scaling error in the subsampling process when a Δf=4 kHz frequency offset is used between f_{Tx} and f_{Rx}. For example, if the scale factor is set at 2500, this error would cause it to fluctuate between 2497-2503.

In addition to instability in the transmitter clocks, there is instability in the receiver clocks. This includes the 9.996 MHz signal distributed to the subsamplers in addition to the FPGA clocks at the base stations and control station. The 9.996 MHz clock has the greatest effect since it is used in the subsampling process. The 9.996 MHz square wave signal is currently generated with a Tektronix AFG 3102 function generator. The Tektronix AFG 3012 function generator has a stability of ±1.0 ppm and jitter of <200 ps as defined in its specifications. The jitter and instability of the Tektronix AFG 3012 function generator results in jitter and drifting which is clearly illustrated in static scenarios such as those of Figure 7-22 and Figure 7-23. The jitter and instability over long time periods (1-30 minutes) cause triangulation errors of 10-40 mm and necessitates the addition of a static tag to the UWB real-time location system as discussed in Section 7.2.4. The stability of ±1.0 ppm occurs in addition to the stability of the Vectron VTC4 of ±0.5 ppm. This results in a worst case combined stability for the transmitter and receiver clocks of ±1.5 ppm. This translates into an uncertainty of ±15 Hz in the frequency offset $\Delta f = f_{Tx} - f_{Rx}$. With f_{Tx} = 10 MHz and f_{Rx} = 9.996 MHz, Δf = 4 kHz ± 15 Hz. The ±15 Hz instability results in a scaling error of 0.38%. For a scale factor of 2500, the instability causes the actual scale factor to lie between 2491-2509.

Finally, the Spartan 3E evaluation board has an Epson SG-8002JF 50 MHz clock source with stability of ±50 ppm. This has only a minimal effect since it will only effect each digital sample after subsampling. For example, instead of each digital sample being spaced 20 ns apart, this introduces an uncertainty that the samples will be 19.999-20.001 ns apart (an uncertainty of around 1 ps per digital sample). Since this 1 ps uncertainty is added after subsampling, it is equivalent to a 0.4 fs uncertainty before subsampling. The Epson SG-8002JF 50 MHz clock source has a measured jitter value of around 200 ps. This is much smaller than the 200 ps of jitter introduced by the 9.996 MHz clock which is included in the subsampled signal as jitter 2500x larger (500 ns). 200-500 ns jitter is observed experimentally in the raw output leading-edge signals from the base station FPGAs.

In order to verify this analysis of the tag scale factors, the scale factor for each of the 10 tags was measured experimentally. This was done by measuring the number of 50 MHz clock cycles (20 ns spaced digital samples) that occurred between each successive UWB pulse leading-edge. This was repeated for 100,000-300,000 consecutive UWB pulse cycles for each of the 10 tags. Examples of the raw data obtained from this analysis are shown in Figure 7-26 and Figure 7-27. As shown in Figure 7-26 and Figure 7-27, there is typically a spread of around 10 digital samples (200 ns) caused by the jitter in the received UWB pulse, but ultimately the period is well defined with a standard deviation of 1-2 digital samples (20-40 ns). A summary of the scale factor analysis for all 10 tags is presented in Table 7-3. As shown in Table 7-3, the measured scale factors vary between 2489.7-2492.2. This translated into a scale factor error of 0.23%-0.41%. These values are consistent with the theoretical analysis which suggested a worst case scale factor of 0.38% when taking into account the transmitter 10 MHz clock and the receiver 9.996 MHz clock. The dynamic calibration procedure described in Section 7.2.7 is used to measure and remove the scale factor error. The dynamic calibration also helps to mitigate phase center error caused by the shifting of the receiver antenna phase centers as the tag moves around the view volume.

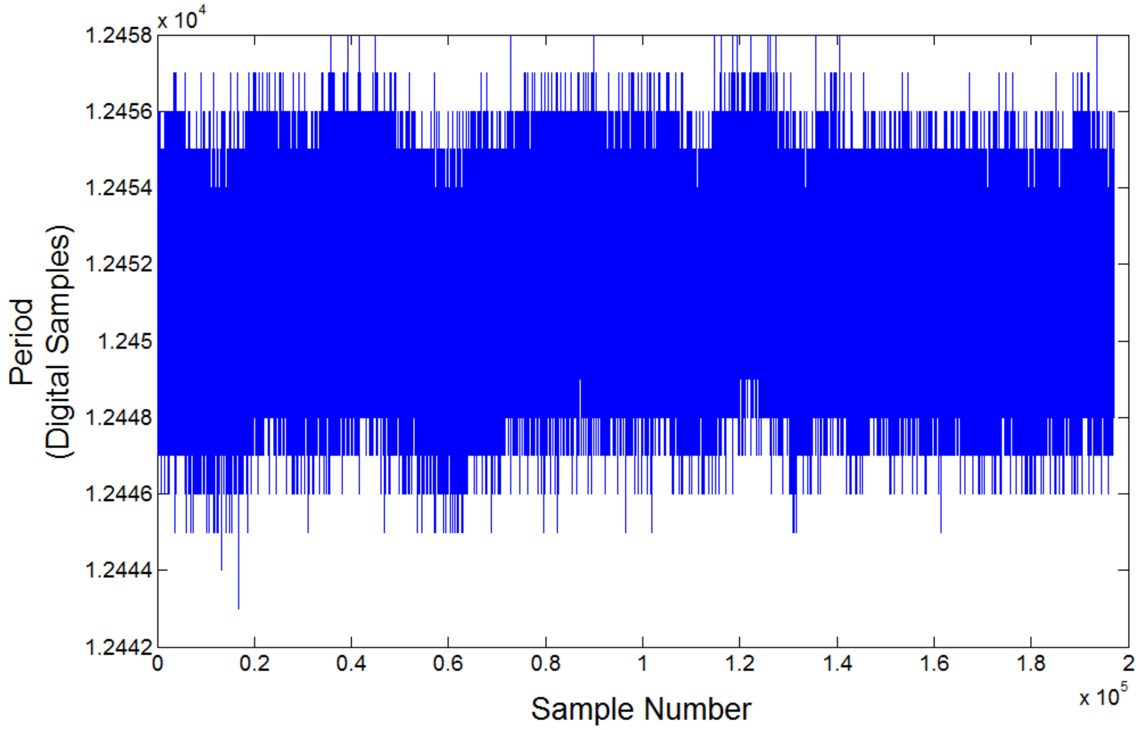

Figure 7-26: Period between successive leading-edges of the UWB pulse train from Tag 2 in digital samples spaced 20 ns apart for almost 200,000 successive UWB pulses.

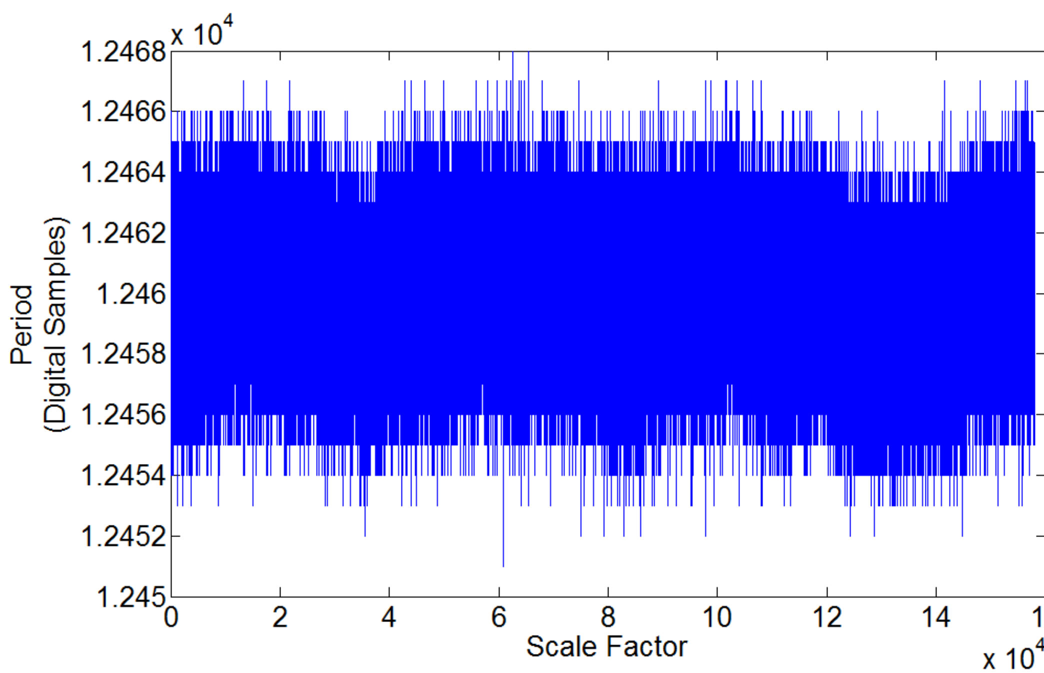

Figure 7-27: Period between successive leading-edges of the UWB pulse train from Tag 9 in digital samples spaced 20 ns apart for almost 160,000 successive UWB pulses.

Table 7-3: Summary of measured tag scale factors for all 10 operational UWB tags.

Tag Number	Period (Digital Samples)	Scale Factor	Scale Factor Error (%)
2	12,451 ± 1.7	2490.3	0.39
4	12,462 ± 2.1	2492.3	0.31
5	12,450 ± 2.0	2490.0	0.40
8	12,464 ± 1.8	2492.9	0.29
9	12,460 ± 2.0	2492.0	0.32
10	12,471 ± 1.7	2494.2	0.23
12	12,458 ± 1.7	2491.6	0.34
13	12,450 ± 1.7	2490.0	0.40
14	12,464 ± 1.7	2492.8	0.29
15	12,449 ± 2.1	2489.7	0.41

Ultimately, the accuracy of the system is limited by the 1-D ranging accuracy of the UWB base stations, receiver antenna phase center variation, and geometric dilution of precision. The scale factor error of 0.23%-0.41% is negligible when compared to receiver antenna phase center variation and geometric dilution of precision as discussed in Section 7.2.7. Dynamic accuracy is limited by tag update rate in addition to 1-D ranging accuracy of the UWB base stations, receiver antenna phase center variation, and geometric dilution of precision. Finally, the measurement of tag accuracy introduces another source of error: synchronization errors when comparing dynamic data from the UWB positioning system and the optical tracking system.

7.2.7 Dynamic Calibration

A dynamic 3-D calibration procedure helps in removing errors observed dynamically across many points within the view volume. These errors include uncertainty in the base station antenna phase center measurement used in the TDOA calculations, base station phase center variation as the tag moves around the view volume and changes its relative angle to each base station Vivaldi antenna, and any additional bias in the range difference data not initially seen at the static point used in calculating the cable length offsets (the dynamic calibration provides a more accurate cable length offset estimate obtained using a larger dataset with a more accurate representation of the entire view volume). The dynamic calibration can even help mitigate the synchronization error that can occur in attempting to align the dynamic data from the UWB and optical positioning systems.

It should be noted that 3-D dynamic experiments can be run without performing the dynamic 3-D calibration procedure outlined in this section. This can be seen by looking at the range difference data in Figure 7-28. Figure 7-28 shows dynamic range difference data (BA, CA, DA) for the UWB positioning system and the optical tracking system for Tag 10. A static tag is used to mitigate system clock jitter and drift effects (as outlined in Section 7.2.4). Cable length offsets have been calculated to align the UWB and optical range difference data at a single point in the view volume (Section 7.2.5). Finally, the measured tag scale factor for Tag 10 has been applied to the UWB range difference data (Section 7.2.6). As shown in Figure 7-28, the range difference data for the optical and UWB systems has good correlation. The 3-D RMS error of the UWB range difference data versus the optical range difference data is 13.9 mm. This does not translate directly into 3-D X,Y,Z error but provides a baseline value that is indicative of the final 3-D positioning error after the TDOA calculation. After the dynamic 3-D calibration is performed, the 3-D RMS error is reduced to 10.3 mm. This provides a welcome 26% reduction in error but still shows that more error exists within the UWB positioning data which the dynamic 3-D calibration did not remove. Thus, it can be inferred that the dynamic 3-D calibration procedure does mitigate error within the system but is not a "catch all" calibration and must be used in conjunction with other error mitigation techniques in the quest for sub-millimeter 3-D accuracy.

The dynamic 3-D calibration procedure is outlined in [93] and is termed the System Time-Scale and Offset Calibration in [93]. It is reproduced here using the same equations and nomenclature described in [93]. This algorithm requires a reference positioning system (the optical tracking system) denoted R while the UWB positioning system pseudo ranges are denoted as P. A least squares approach is used to solve for a homogeneous transformation matrix which best aligns the UWB range difference coordinate frame with the optical range difference coordinate frame. As shown in (7-1), Δr_{1k}^{t} represent the range differences computed using the reference positioning system (optical tracking system). $\Delta \rho_{1k}^{t}$ represent the range differences computed by the UWB positioning system as shown in (7-2). t represents the time index or sample index of the acquired ranges. The homogeneous transformation matrix H is solved for in the linear system which equates the UWB range differences ΔP to the optical reference positioning system range differences ΔR. ΔP and ΔR are defined in (7-4) and (7-5). The resulting linear system is defined in (7-3). The homogeneous transformation matrix H is defined in (7-6). As mentioned in [93], ΔP and ΔR must be full rank in order to ensure H provides an accurate least squares estimate of the homogeneous transformation matrix. The antenna of a UWB tag must be rigidly attached and statically calibrated to the optical probe in order to obtain range difference data from both positioning systems simultaneously.

An example transformation matrix H is shown in (7-7). This transformation matrix corresponds to the raw data shown in Figure 7-28. As can be seen in (7-7), the transformation

$$\Delta r_{1k}^{t} = r_1^t - r_{k+1}^t \tag{7-1}$$

$$\Delta \rho_{1k}^{t} = \rho_1^t - \rho_{k+1}^t \tag{7-2}$$

$$\Delta P = H \Delta R \tag{7-3}$$

$$\Delta P = \begin{bmatrix} \Delta\rho_{11}^{1} & \cdots & \Delta\rho_{1k}^{1} & 1 \\ \vdots & \ddots & \vdots & 1 \\ \Delta\rho_{11}^{N} & \cdots & \Delta\rho_{1k}^{N} & 1 \end{bmatrix} \tag{7-4}$$

$$\Delta R = \begin{bmatrix} \Delta r_{11}^{1} & \cdots & \Delta r_{1k}^{1} \\ \vdots & \ddots & \vdots \\ \Delta r_{11}^{N} & \cdots & \Delta r_{1k}^{N} \end{bmatrix} \tag{7-5}$$

$$H = \begin{bmatrix} s_{11} & s_{12} & s_{13} & d_1 \\ s_{21} & s_{22} & s_{23} & d_2 \\ s_{31} & s_{32} & s_{33} & d_3 \\ 0 & 0 & 0 & 1 \end{bmatrix} \tag{7-6}$$

$$H_{Example} = \begin{bmatrix} 0.942 & 0.047 & -0.038 & -28.5 \\ 0.005 & 0.972 & 0.007 & 7.62 \\ -0.049 & 0.051 & 0.937 & -40.1 \\ 0 & 0 & 0 & 1 \end{bmatrix} \qquad (7\text{-}7)$$

mainly occurs as a scale factor along the diagonal (s_{11}, s_{22}, s_{33}) combined with translation offsets d_1, d_2, and d_3. There is a small amount of correlation among the off-diagonal scale factors, but this contribution is negligible compared to the main diagonal. The translation offsets d_1, d_2, and d_3 represent a corrected estimate of the cable length offsets with less error than the original estimate since some of the error inherent to the single point cable length offset calibration (Section 7.2.5) has been removed. The scale factors s_{11}, s_{22}, and s_{33} represent a

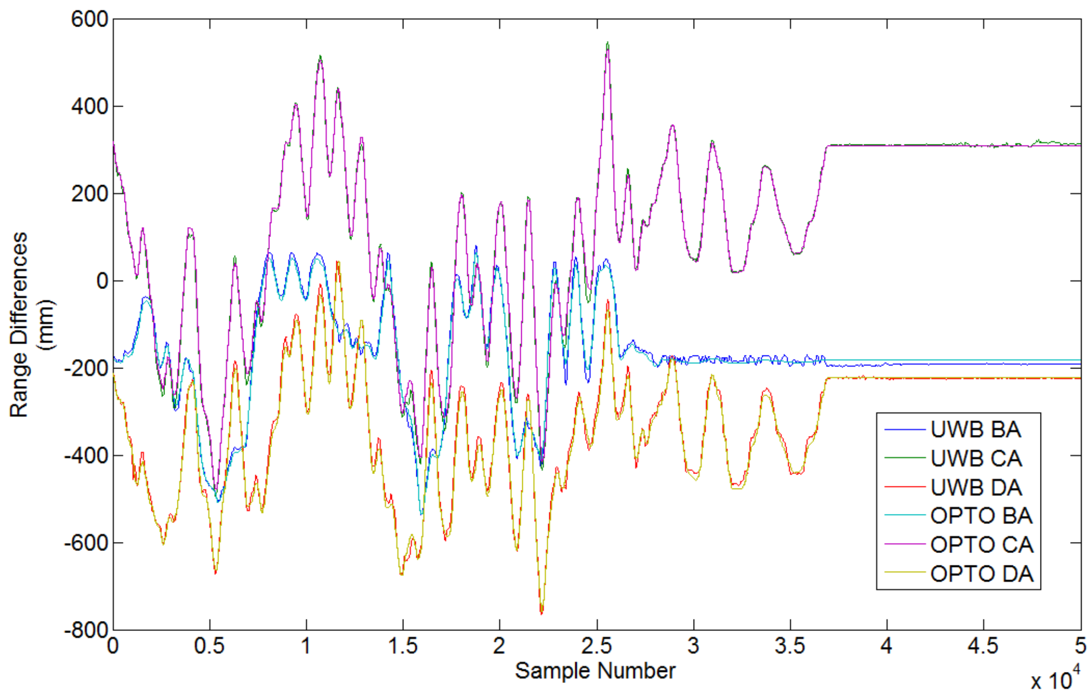

Figure 7-28: Raw range difference data for base station B minus base station A (BA), base station C minus base station A (CA), and base station D minus base station A (DA) for both the optical and ultra-wideband positioning systems as the tag is moved around the view volume. The cable length offsets have already been applied, a static tag is used, and the tag scale factor has already been applied. Good correlation is observed when comparing the range differences between the two systems.

scaling of the range differences applied to the non-calibrated UWB BA, CA, and DA range differences. For the example transformation matrix $H_{Example}$, $s_{11} = 0.942$, $s_{22} = 0.972$, and $s_{33} = 0.937$. This constitutes a 5.8% scale reduction for BA, a 2.8% scale reduction for CA, and a 6.3% scale reduction for DA. The effects of these scale reductions can be seen in Figure 7-29, Figure 7-30, Figure 7-31, Figure 7-32, Figure 7-33, Figure 7-34, and Figure 7-35. The zoomed-in plots of Figure 7-30, Figure 7-32, and Figure 7-34 illustrate how the dynamic calibration mitigates errors in the UWB range difference data. Figure 7-35 shows the 3-D range difference error before and after the dynamic calibration. 3-D range difference error is defined in (7-8) and incorporates error from UWB BA, CA, and DA range differences. A 26% reduction in error is

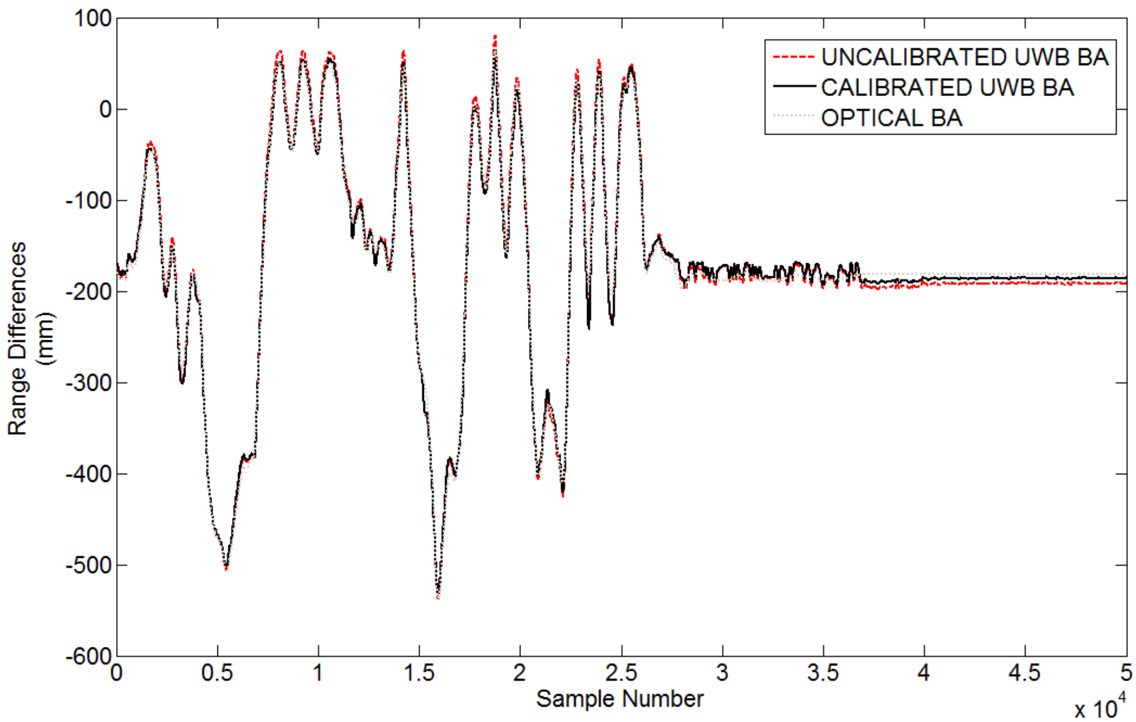

Figure 7-29: Raw range difference data for base station B minus base station A (BA) for both the optical and ultra-wideband positioning systems as the tag is moved around the view volume. Both uncalibrated and calibrated UWB range difference curves are shown. The calibrated UWB range differences better fit the optical BA range differences.

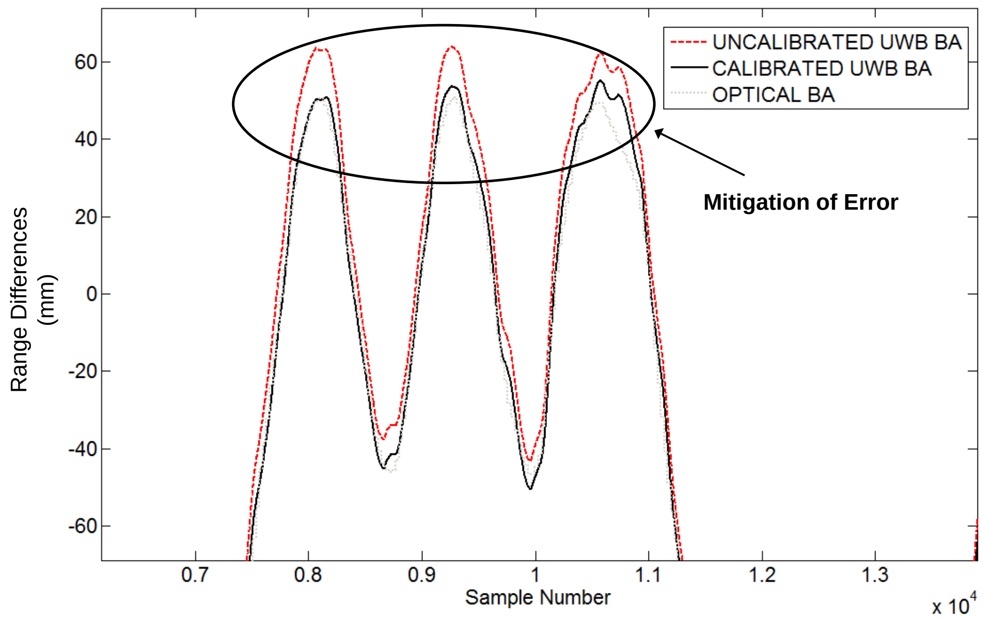

Figure 7-30: A zoomed-in view of the raw range difference data for base station B minus base station A (BA) for both the optical and ultra-wideband positioning systems as the tag is moved around the view volume. The calibrated UWB range differences have a 5.8% scale reduction which provides a noticeably better fit to the optical range difference data, especially at the extremities of the view volume.

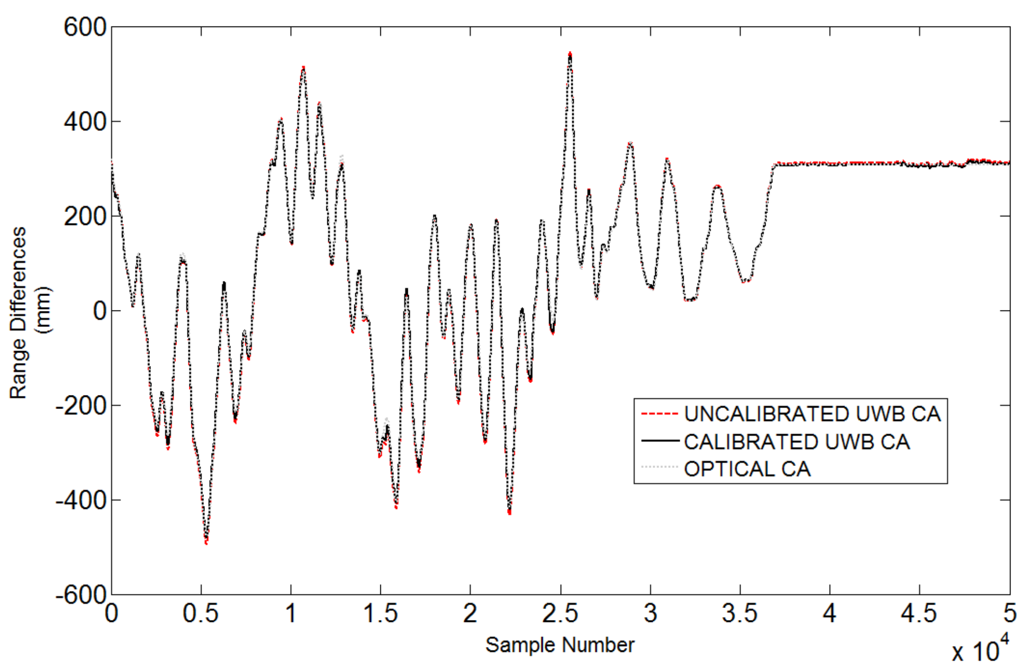

Figure 7-31: Raw range difference data for base station C minus base station A (CA) for both the optical and ultra-wideband positioning systems as the tag is moved around the view volume. The calibrated UWB range differences better fit the optical CA range differences.

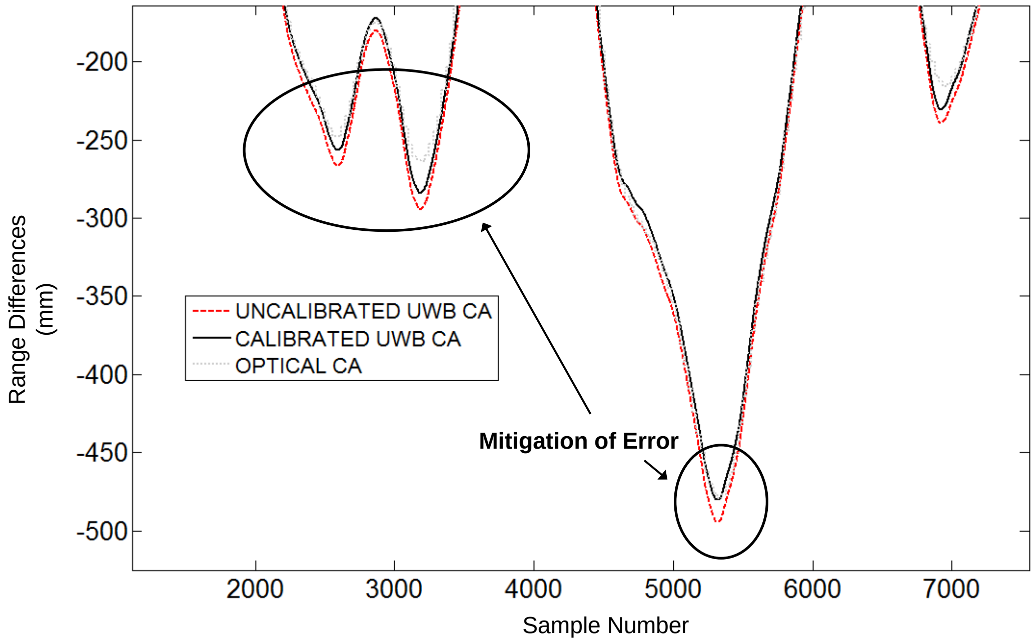

Figure 7-32: A zoomed-in view of the raw range difference data for base station C minus base station A (CA) for both the optical and ultra-wideband positioning systems as the tag is moved around the view volume. The calibrated UWB range differences have a 2.8% scale reduction which provides a noticeably better fit to the optical range difference data, especially at the extremities of the view volume.

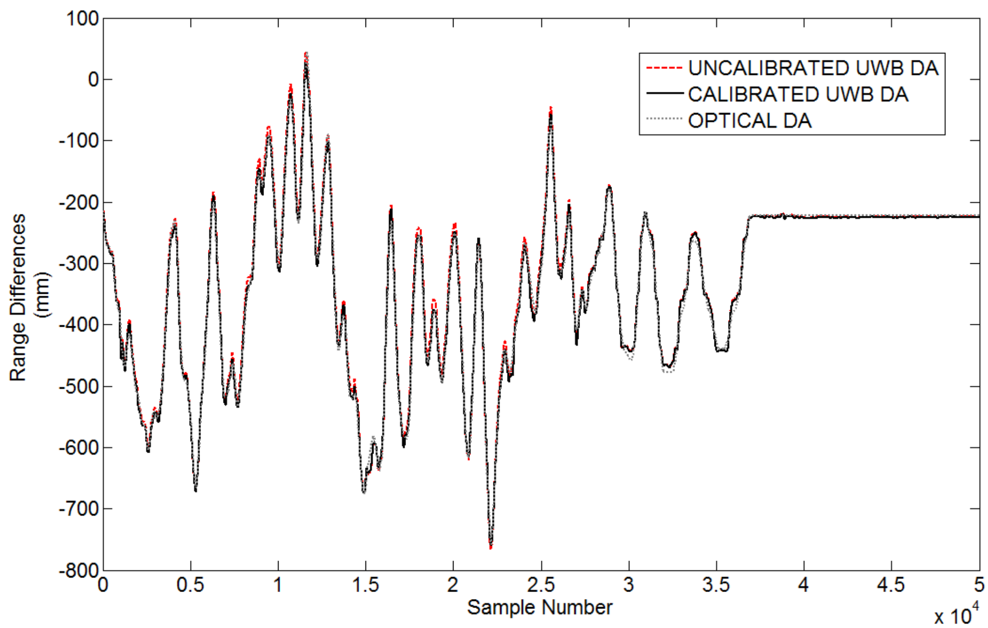

Figure 7-33: Raw range difference data for base station D minus base station A (DA) for both the optical and ultra-wideband positioning systems as the tag is moved around the view volume. The calibrated UWB range differences better fit the optical DA range differences.

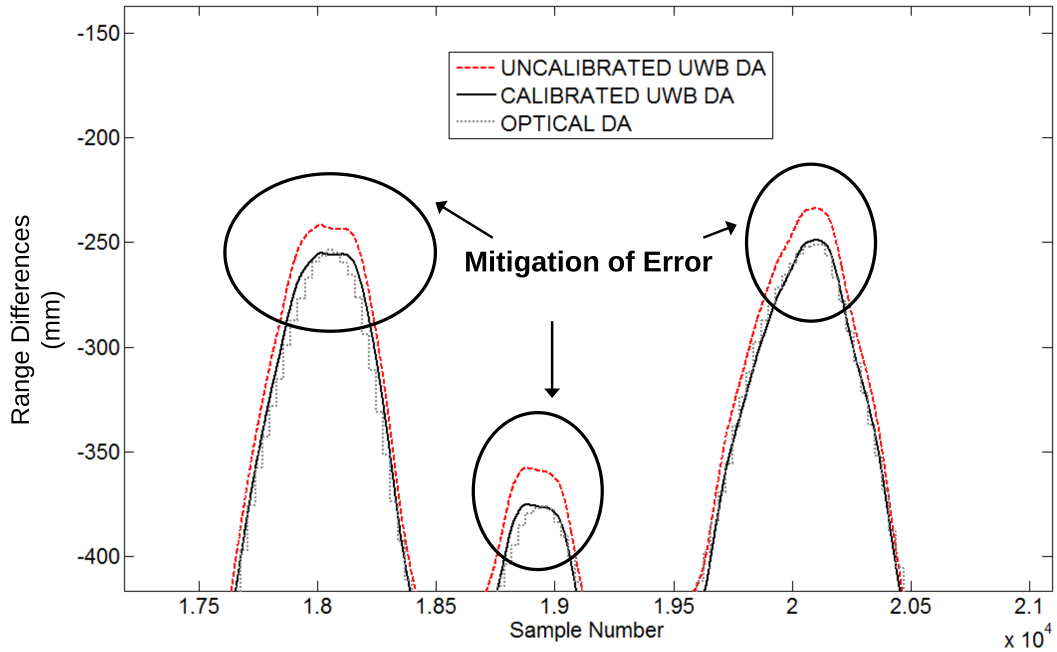

Figure 7-34: A zoomed-in view of the raw range difference data for base station D minus base station A (DA) for both the optical and ultra-wideband positioning systems as the tag is moved around the view volume. The calibrated UWB range differences have a 6.3% scale reduction which provides a noticeably better fit to the optical range difference data, especially at the extremities of the view volume.

observed for the calibrated 3-D range difference error versus the non-calibrated 3-D range difference error.

$$3D\ Range\ Difference\ Error = \sqrt{(BA_{UWB} - BA_{OPTICAL})^2 + (CA_{UWB} - CA_{OPTICAL})^2 + (DA_{UWB} - DA_{OPTICAL})^2} \quad (7\text{-}8)$$

A plausible error source which would necessitate scaling reductions in the BA, CA, and DA range differences, such as the 5.8% reduction for BA, 2.8% reduction for CA, and 6.3% reduction for DA observed here, is an inaccurate initial estimate of the base station phase center 3-D positions. Figure 7-36 shows a typical measurement of the base station Vivaldi phase center while Figure 7-37 shows how there is actually a range of uncertainty in this measurement since

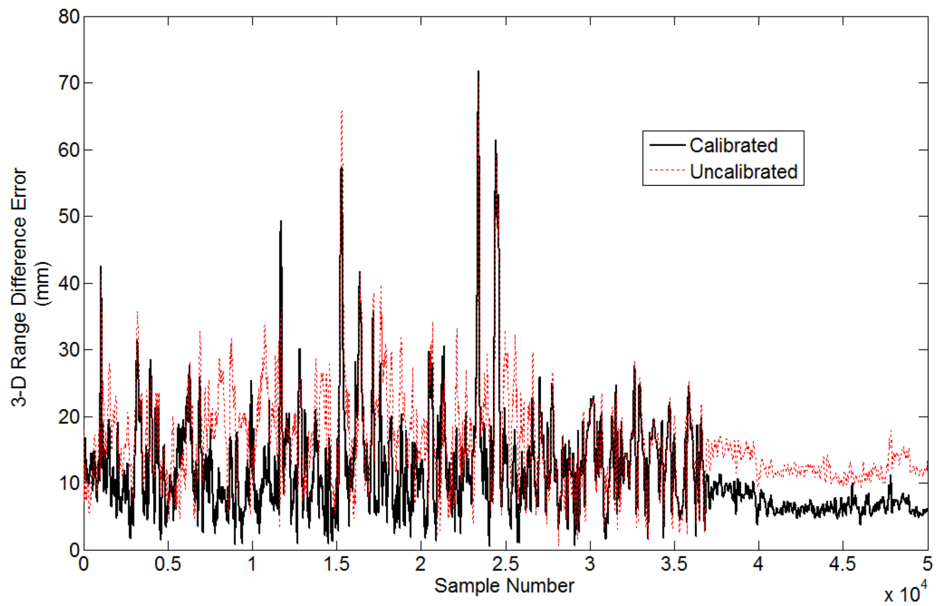

Figure 7-35: The 3-D range difference error (defined in (7-8)) for all 50,000 calibration points before and after the dynamic calibration (applying *H*). The dynamic calibration provides a 26% reduction in RMS 3-D range difference error (reduced from 13.9 mm to 10.3 mm).

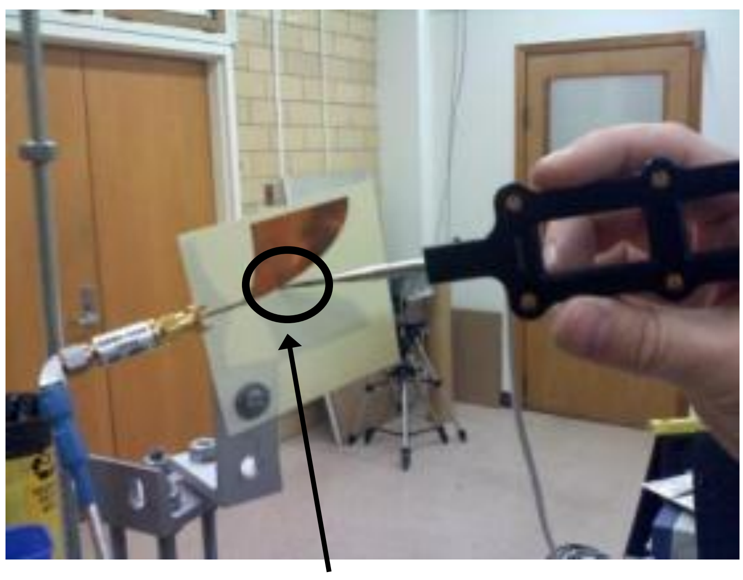

Figure 7-36: An optical probe is used to estimate the base station Vivaldi antenna phase center. This 3-D position is used in calculating the reference optical range differences for dynamic calibration. This 3-D base station position is also used in the TDOA calculation for the UWB positioning system.

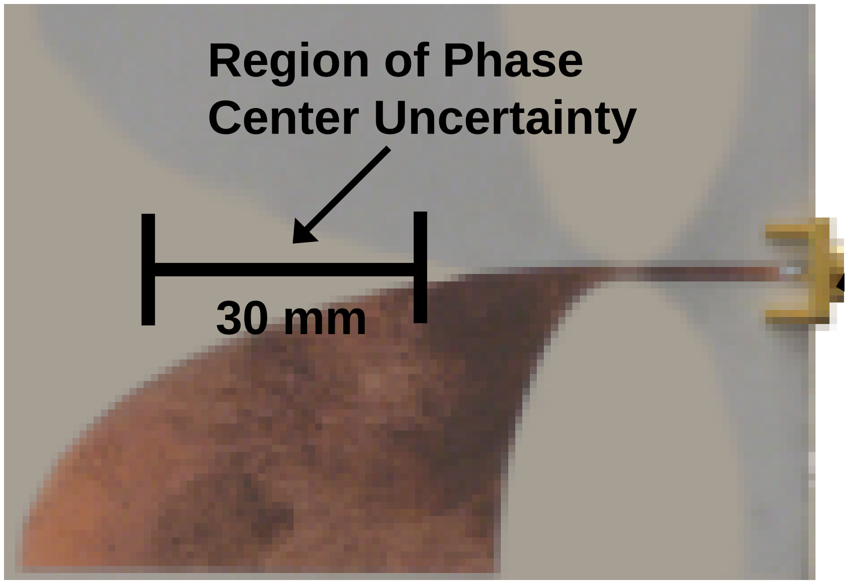

Figure 7-37: A roughly 30 mm range of uncertainty is introduced in measuring the UWB base station Vivaldi phase centers. This can translate into 10-60 mm of systematic error in the BA, CA, and DA range differences when comparing optical and UWB range difference data.

the actual phase center position is unknown. This range of uncertainty is estimated at 30 mm per base station. For a worst case analysis, we will assume that each base station (A,B,C,D) has a 30 mm offset in its actual phase center versus the measured phase center as shown in Figure 7-38. This offset will cause scaling between the UWB and optical range differences as the tag is moved around the view volume because the UWB range differences are inherently using the actual phase center while the measured optical range differences rely on the measured phase center 3-D points to compute the optical range differences.

A simulation of this effect is outlined in Figure 7-38, Table 7-4, Table 7-5, and Table 7-6. The phase center of each base station was measured with the optical tracking system. The 3-D measured positions are provided in Table 7-4. An offset was introduced in the general direction of where the actual phase center may be located (its actual position is not known). The offset

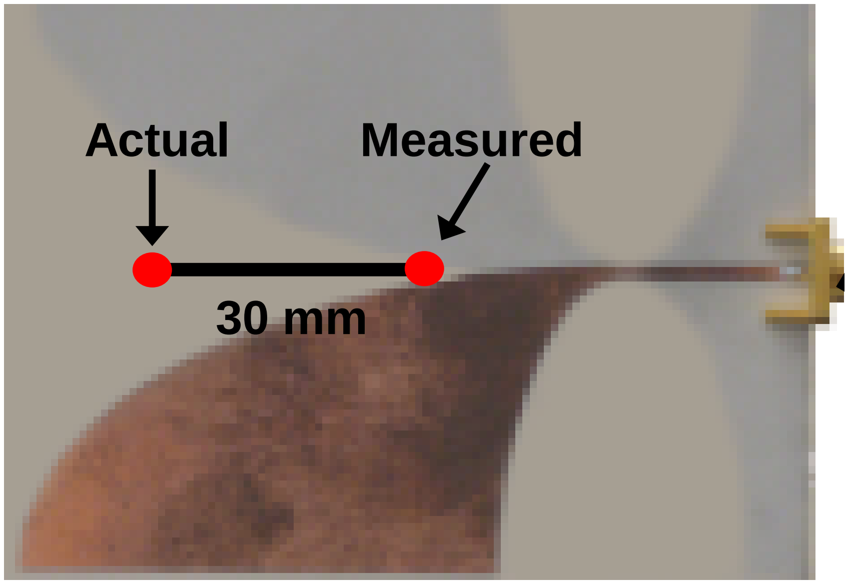

Figure 7-38: For a worst case analysis, a 30 mm offset is introduced between the measured phase center and the actual phase center of the Vivaldi base station antenna for a simulation of its effect on the UWB positioning system dynamic behavior.

Table 7-4: Simulated phase center offsets introduced to analyze the effect of phase center offsets in observed scaling error in the range difference data for dynamic experiments.

Base Station	Measured Phase Center (x,y,z)	Actual Phase Center (x,y,z)	3-D Difference (mm)
A	(-838.4, -570.9, -3763.0)	(-825, -557, -3759)	19.7
B	(255.5, -274.8, -2680.1)	(257, -272, -2708)	28.1
C	(-44.1, 333.2, -5790.5)	(-54, 326, -5765)	28.3
D	(-703.9, 517.9, -2964.2)	(-693, 526, -2981)	21.6

phase center 3-D positions represent the actual 3-D phase centers of the UWB base station antennas and are outlined in Table 7-4. The 3-D difference between the measured and actual phase center is also shown in Table 7-4 with maximum differences of < 30 mm. Table 7-5 contains the resulting range differences for three tag locations around the view volume for both the optical and UWB tracking systems. The three tag locations provide values across the view volume spanning 1.6 m across. The phase center offsets cause the UWB and optical range differences to vary with the most significant differences observed at the edges of the view volume since the base station antennas are oriented towards the center of the view volume, which provides some mitigation to the effect of the phase center offset on the observed range differences at the center versus the edges. Table 7-6 shows the spread in millimeters of the range differences for BA, CA, and DA across the three simulated tag points as well as the associated scale difference caused by the phase center offset. As shown in Table 7-6, the phase center offset causes a 1.54% scale difference for BA, a 0.86% scale difference for CA, a and 1.12% scale difference for DA. These scale differences are smaller than the observed scale differences from the full dynamic calibration (5.8% for BA, 2.8% for CA, and 6.3% for DA). Still, they are within 25%-55% of the magnitude of the observed scale differences from the dynamic calibration (1.54% versus 2.8%-6.3%). Also, in a real dynamic calibration, the phase center can vary in its position dynamically, which could potentially increase the observed scale differences between the two systems compared to the initial phase center offset. Finally, the dynamic calibration itself is quite sensitive to the input data from the UWB and optical positioning systems which makes it likely that a rather large variation of scale differences can be observed when performing a series of calibrations, which is indeed the case. Experimentally, scale differences from 0.3%-15% were observed when calibrating the system 20-30 times with different input data. More work is needed to understand the effects the phase center has on the system. The

Table 7-5: Simulated tag 3-D points and corresponding range differences for the UWB and optical tracking systems. The optical tracking system uses the measured phase center base station positions while the UWB positioning system uses the actual phase center positions.

Tag 3-D Position (x,y,z)	UWB Range Differences (BA, CA, DA)	Optical Range Differences (BA, CA, DA)
(12, 12, -4200)	(434, 494, 395)	(446, 504, 395)
(80, 300, -3500)	(-280, 996, -315)	(-276, 1001, -318)
(-40, -300, -5000)	(821, -502, 786)	(842, -484, 795)

Table 7-6: Results from the simulated analysis which shows that biases in the measured phase center 3-D positions of the base station antennas introduce scaling effects of 1-2% into the range differences of the UWB system compared to the optical system.

Range Difference	Optical Spread (mm)	UWB Spread (mm)	Scale Difference (%)
BA	1101	1118	1.54
CA	1498	1486	0.86
DA	1101	1114	1.12

uncertainty in the initial phase center 3-D position combined with the uncertainty in the dynamic phase center position as the tag moves around the view volume is clearly a major source of error. The phase center effects combined with geometric dilution of precision and 1-D ranging accuracy pose the greatest hurdles to achieving sub-millimeter 3-D accuracy.

7.3 MMIC Transmitter and Receiver Integration

The UWB group at the University of Tennessee is working with Dr. Schumacher and his doctoral student Dayang Lin at the University of Ulm in Germany to integrate MMIC analog RF front-ends at both the UWB tags and receivers used in the University of Tennessee UWB indoor real-time location system. The MMIC energy detection receiver designed by Dr. Schumacher's group has already been incorporated into the University of Tennessee UWB positioning system. The MMIC UWB transmitter will be incorporated in the future through a new integrated tag design to replace the current tag design described in Section 7.2.1. A discussion of the MMIC integration is outlined here since it will greatly improve the reliability while shrinking the tag and receiver form factors and lowering power consumption for both the tag and receiver.

7.3.1 Transmitter Front-End

The non-coherent UWB positioning system currently being used for indoor positioning at the University of Tennessee is outlined in Section 7.2 and discussed in [220]. As discussed in Section 7.2.1, the power requirement of the transmitter (or tag) is over 1 W, which restricts the use of this system in low power applications. Figure 7-39a outlines the current discrete tag which utilizes a VCO and MPA as well as a step recovery diode-based pulse generator causing the large power requirement of around 1 W. The corresponding picture of the discrete tag is shown in Figure 7-40a. The block diagram of the SiGe MMIC-based UWB transmitter is shown in Figure 7-39b where a cross-coupled oscillator core is transiently turned on by a current spike generated by a Schmitt trigger driving a current mirror. An integrated board design with the MMIC at the feed point of the UWB dipole antenna is shown in Figure 7-40b. More details on the MMIC design can be found in [221]. The MMIC-based transmitter is more compact and only has a load requirement of 6 mW for operation (1.5 V, 4 mA).

7.3.2 Receiver Front-End

A block diagram of the discrete UWB non-coherent receiver is shown in Figure 7-41a including directional Vivaldi antenna, bandpass filter, three stages of amplification, squaring mixer, lowpass filter, baseband amplification, and subsampling mixer. Figure 7-42a shows a picture of this receiver chain. The main restrictions of the discrete receiver include power consumption (2.15 W load requirement) and size. Figure 7-41b shows a block diagram of the MMIC-based receiver where the amplifiers, squaring mixer, and lowpass filter have been replaced by an integrated SiGe MMIC chip. Figure 7-42b shows a picture of the UWB non-coherent receiver using the integrated SiGe MMIC front-end. More information on the design of the MMIC non-coherent receiver front-end can be found in [222]. The MMIC receiver provides a significant reduction in the size of the RF front-end and reduces total power consumption including DC-DC converter losses from more than 3 W to around 190 mW. Figure 7-43a shows experimental signals at the transmitter. The MMIC UWB pulse falls below the Federal Communications Commission limits of -41.3 dBm/MHz and consequently only has a peak-to-peak voltage of around 250 mV whereas the discrete tag is around 1 V peak-to-peak. Figure 7-43b shows experimental signals at the receiver after subsampling. The discrete transmitter was used for the signals received in Figure 7-43b. Both the discrete and MMIC receivers produce a strong subsampled pulse of around 1 μs width and 1 V amplitude.

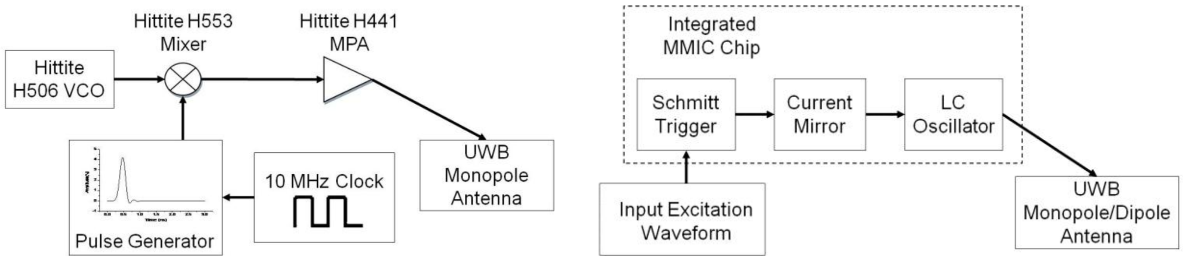

(a) (b)

Figure 7-39. Block diagram of UWB transmitter front-ends: (a) discrete, (b) integrated into a MMIC chip [221].

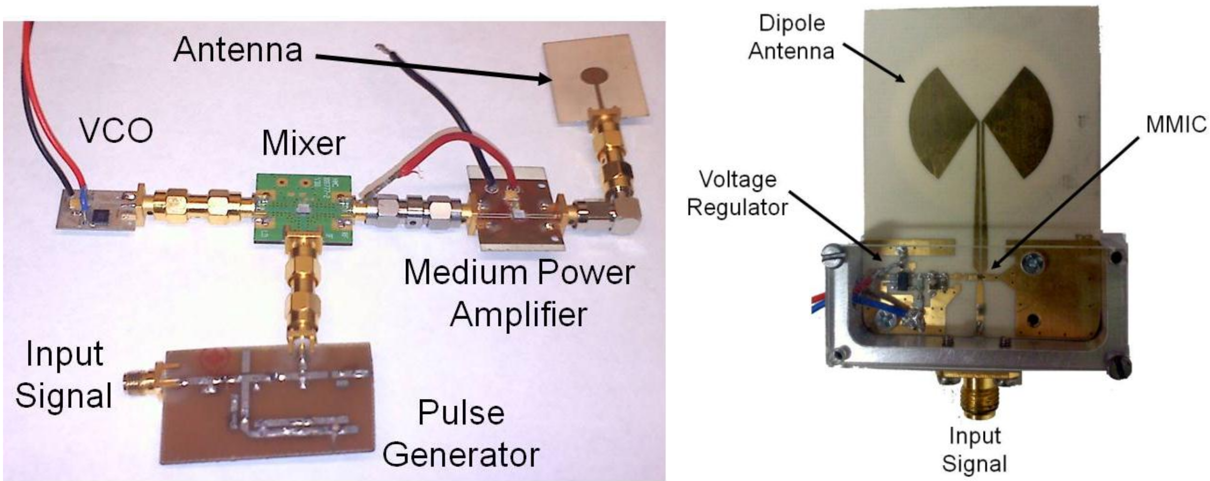

(a) (b)

Figure 7-40. UWB transmitter front-ends: (a) discrete, (b) integrated into a MMIC chip [221].

7.3.3 Experimental Results

Static and dynamic real-time experiments were undertaken to compare the high accuracy localization performance of the discrete and MMIC front-ends. The leading-edge of the UWB pulses was located via a FPGA algorithm after the subsampled pulse was digitized. The time difference is used in the time difference of arrival algorithm and represents the difference in samples as measured by the FPGA between two channels. This sample difference is then converted to millimeters using the FPGA clock period and subsampling expansion factor. Figure 7-44 shows raw static data comparing the time difference of two discrete and two MMIC

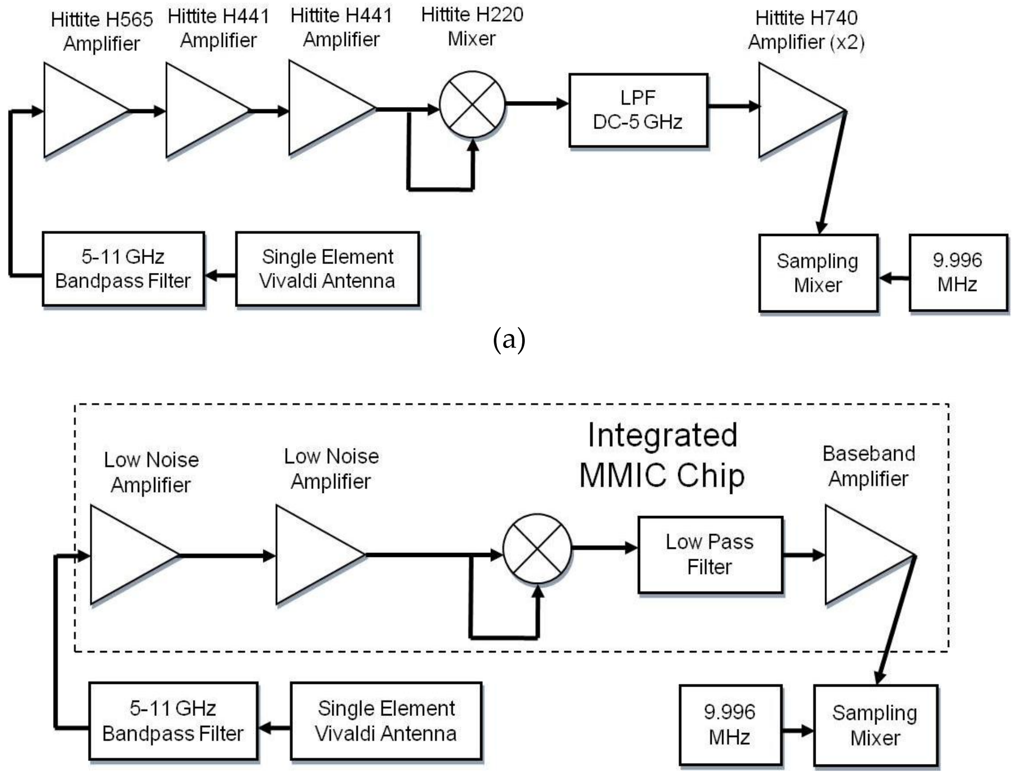

(a) (b)

Figure 7-41. Block diagram of UWB receiver front-ends: (a) discrete, (b) integrated into a MMIC chip [222].

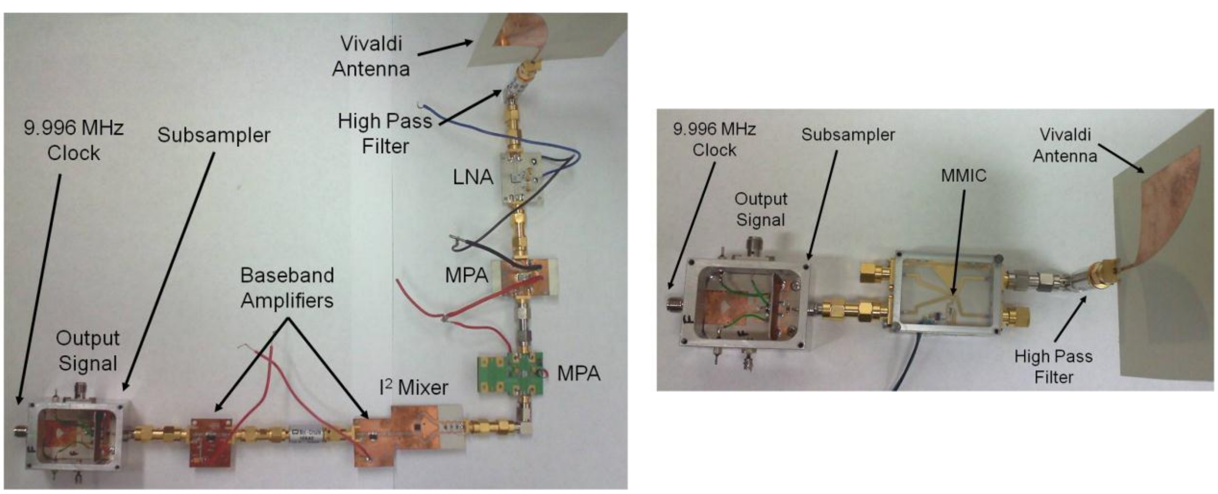

(a) (b)

Figure 7-42. UWB receiver front-ends: (a) discrete, (b) integrated into a MMIC chip [19].

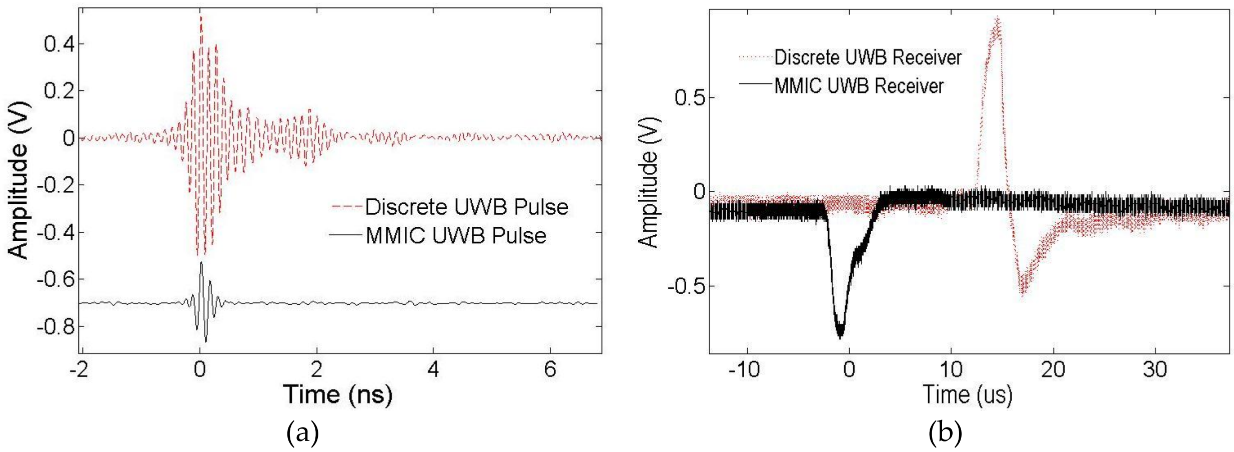

Figure 7-43. Experimental signals: (a) transmitted UWB pulse, (b) received UWB pulse after subsampling.

front-end receivers. The raw standard deviations are 11.2 mm and 9.59 mm for the discrete and MMIC receivers. Figure 7-45 shows the same time differences after applying a 300 sample moving window averaging filter. The standard deviations are reduced to 0.58 mm and 0.64 mm for the discrete and MMIC receivers. Figure 7-46 shows how the standard deviation decreases for larger averaging windows with no difference between discrete and MMIC receivers. Figure 7-47 shows a dynamic experiment where a tag moves freely around the view volume causing dynamic changing of the time differences. The optical tracking system is calibrated to the UWB tag and all four UWB receivers to provide 3-D real-time reference data. As shown in Figure 7-47, the UWB and optical systems follow identical trends within a few millimeters. Figure 7-48 shows the absolute difference between the time differences for the UWB positioning system versus the optical positioning system. The MMIC receivers have a RMSE of 2.56 mm while the discrete receivers have a RMSE of 4.47 mm over all 10,000 samples.

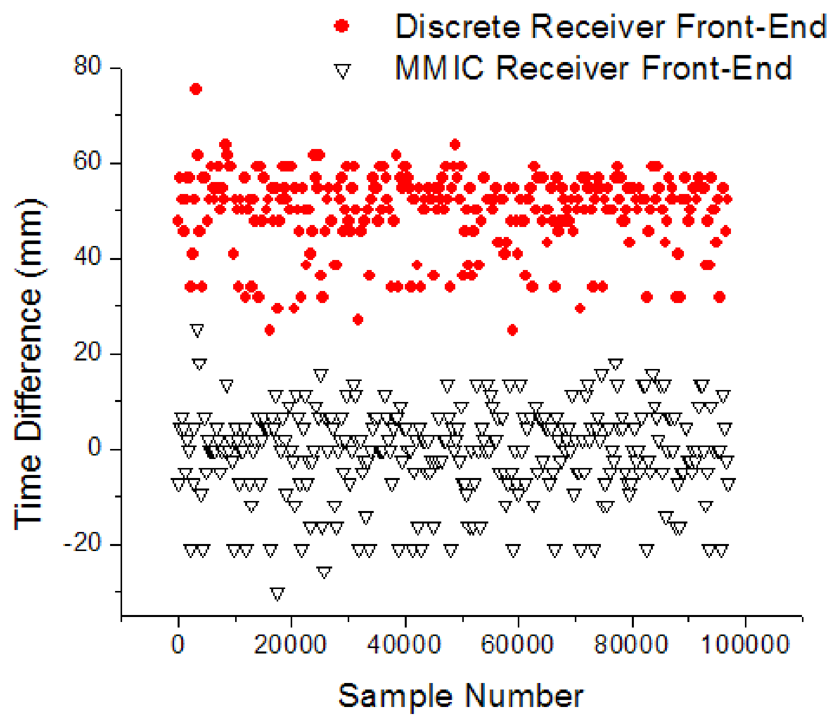

Figure 7-44. Raw time difference static data for two discrete front-end receivers versus two MMIC receivers in millimeters with MMIC data offset to zero for illustration.

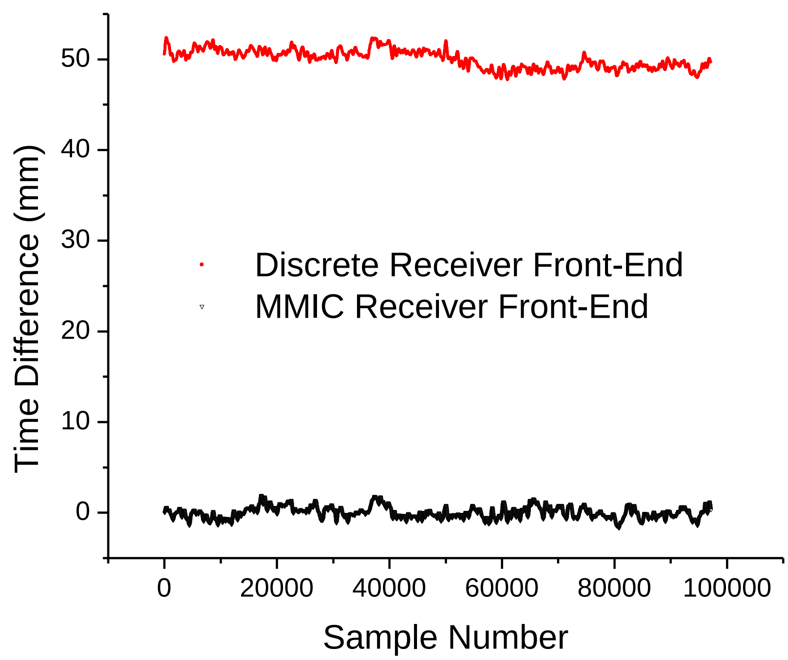

Figure 7-45. Time difference static data for two discrete front-end receivers versus two MMIC receivers in millimeters after applying a 300 sample averaging window.

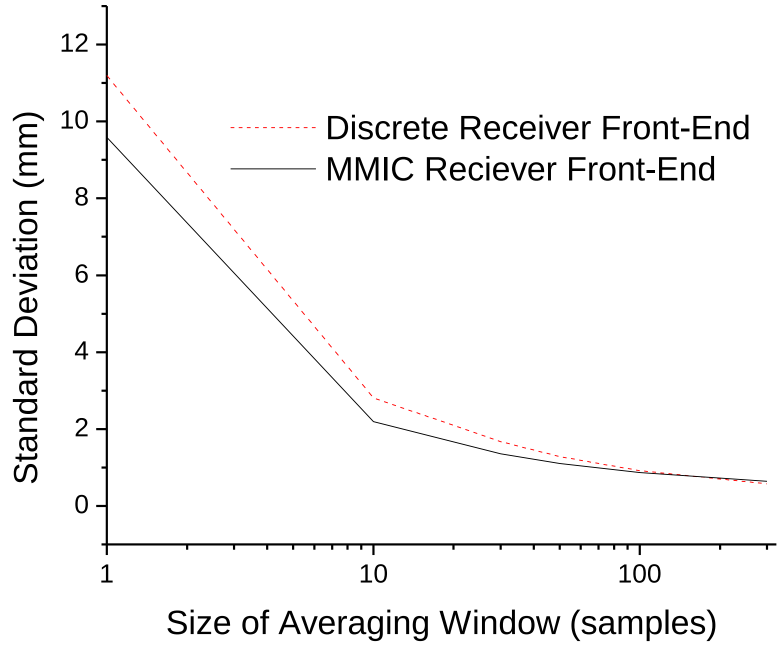

Figure 7-46. Standard deviation of static time differences comparing two discrete receiver front-ends to two MMIC receiver front-ends with a variable averaging window size.

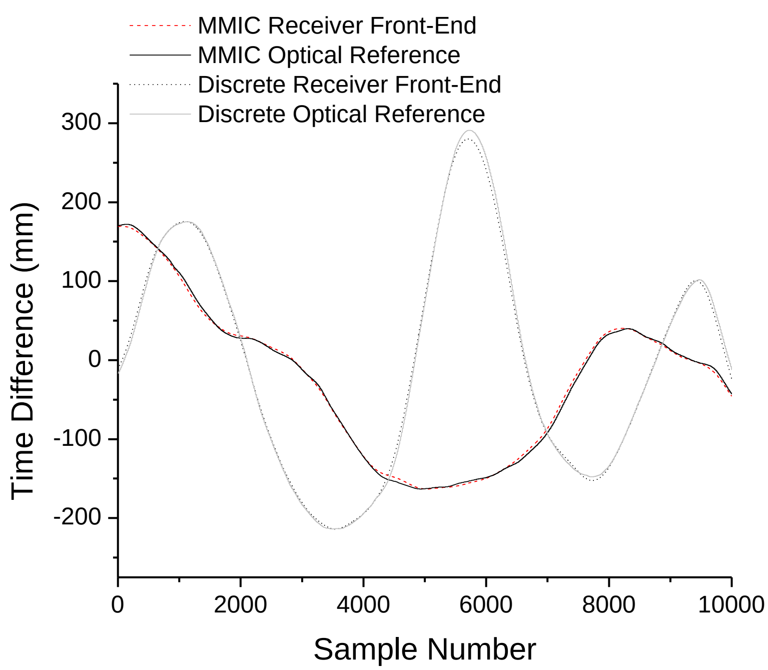

Figure 7-47. Dynamic time differences in millimeters as the tag is moved freely in the view volume comparing two discrete and two MMIC receiver front-ends. An optical tracking system provides 3-D real-time reference data.

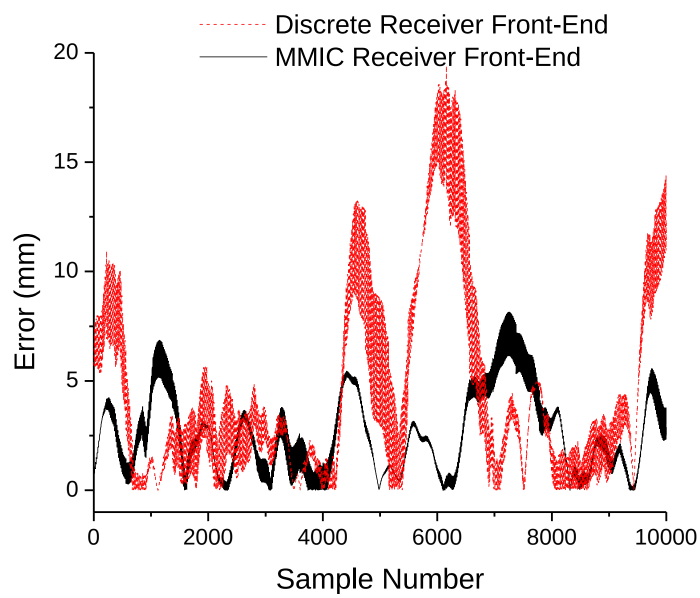

Figure 7-48. Ranging errors in the dynamic time differences shown in Figure 7-47 when comparing the UWB time difference data to the optical (ground truth) time difference data.

7.3.4 Conclusion

Work is currently being done towards integrating MMIC front-ends into the UWB transmitter and receiver chains to reduce power consumption and size. As discussed in Section 7.3.3, the performance of the discrete and MMIC receiver front-ends was similar in both static and dynamic experiments, showing the potential of MMIC front-ends in future systems targeting high accuracy indoor positioning. Future work includes the design and integration of a tag using the MMIC UWB transmitter into the UWB development platform outlined in Section 7.2.

8. A Multi-Tag Development Platform for High Accuracy Indoor UWB Localization: Experimental Analysis

8.1 Overview

The Multi-Tag Development Platform is outlined in Chapter 7. It contains an integrated tag design with 10 operational tags, an energy detection receiver with squaring mixer, DSP for leading-edge detection and multi-tag support, and real-time dynamic operation via a C++ software application with user interface. Results are presented in this chapter for four base station scenarios using the Multi-Tag Development Platform. This includes 3-D dynamic and static experiments with multiple tags operating simultaneously. An analysis of the errors observed in these experiments is also provided.

8.2 Real-Time Four Base Station Experiments

Experiments were undertaken using four base stations to resolve the 3-D positions of one or more tags. The cable length offsets were removed and a 3-D dynamic calibration was performed as discussed in Chapter 7. Also, a static tag was used to mitigate receiver clock jitter and drift effects as discussed in Chapter 7. Figure 8-1 shows the frequency response of the two averaging filters which can be applied independently to the dynamic UWB positioning data. The regular tracking mode averaging filter has a 3 dB passband of 15 Hz which can capture relatively quick 3-D motion compared to the high accuracy track mode. The high accuracy track mode has a 3 dB bandwidth of 8 Hz. The regular track mode can pick-up quick motions such as the tag vibration outlined in Figure 8-2. The high accuracy track mode may still pick-up at

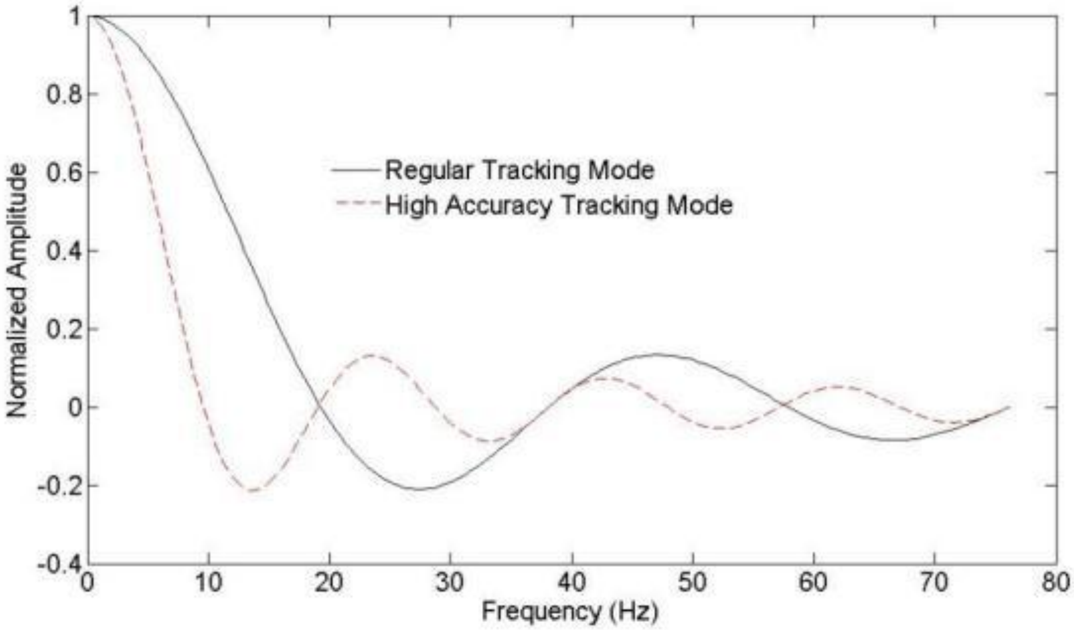

Figure 8-1. Two different sized averaging filters are applied to the 3-D UWB dynamic positioning data. The regular tracking mode detects frequencies in the 3-D motion of up to 15 Hz while the high accuracy tracking mode provides better accuracy but at the expense of detecting only 8 Hz of 3-D motion.

least some of this motion, although with decreased sensitivity. Figure 8-3 outlines the overall system refresh rate and individual tag refresh rate for up to 10 tags. The maximum system update rate is around 1300 Hz due to baud rate limitations with the control station RS-232 link (described in Chapter 9). A 20% reduction in overall system update rate occurs when tracking multiple tags due to lost packets during the tag switches TDMA process. The individual tag update rate decreases as more tags are added since each tag gets fewer and fewer time slices allocated to it.

8.2.1 Optical Rail Experiments with Optical Tracking

Optical rail experiments were undertaken where one tag was placed in a static location

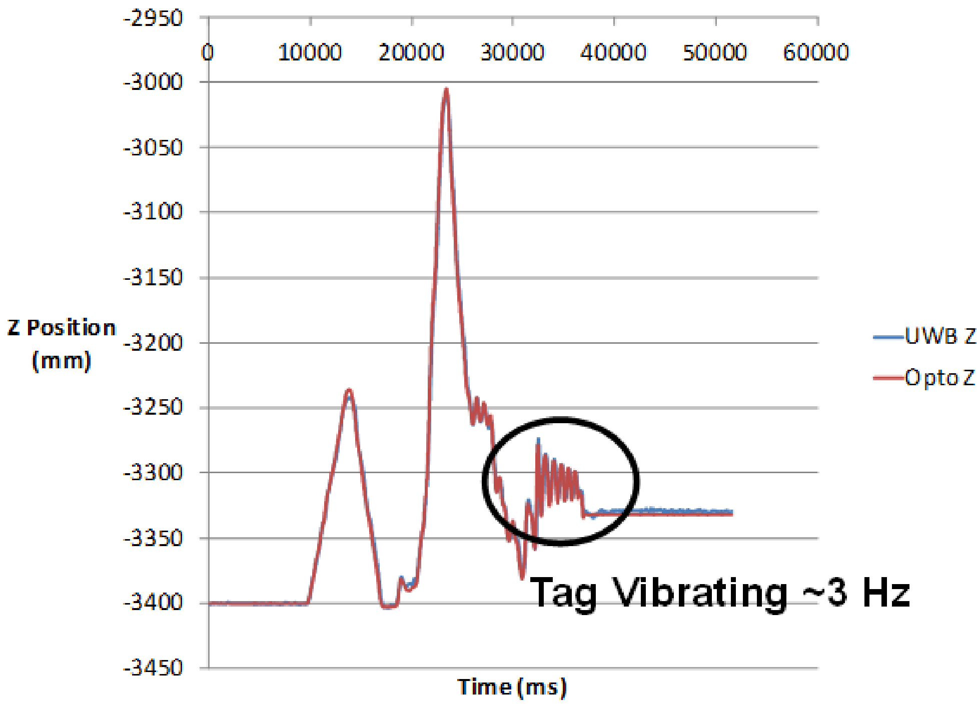

Figure 8-2. 3-D dynamic experiment where UWB and optical systems are calibrated together. A 3 Hz vibration of the tag as it is placed back on the optical rail is detected by both the UWB and optical tracking systems. These results are for Tag 13.

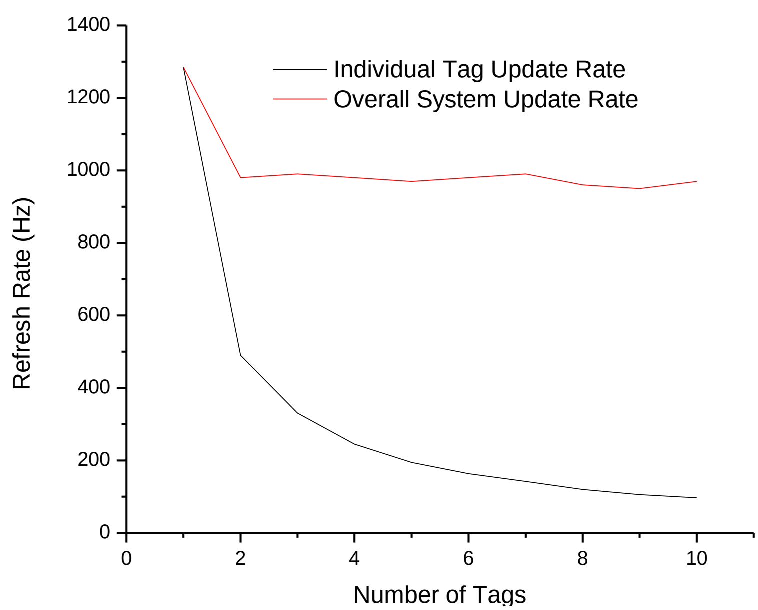

Figure 8-3. System and individual tag refresh rate versus the number of tags for up to 10 tags. The overall update rate with a single tag is around 1300 Hz. Only 1000 Hz total update rates can be achieved for multi-tag tracking since around 20% of the data is lost during the tag switching process.

while the other tag was moved along the optical rail with an infrared tracking probe from the Optotrak 3020 rigidly attached and the UWB and optical tracking systems calibrated to one another. This experimental setup is shown in Figure 8-4. Typical experimental results for the optical tracking experiment are shown in Figure 8-5. The majority of movement occurs in the Z dimension, so only the Z dimension is shown. There is good agreement between the optical and UWB tracking systems. Typical 3-D dynamic error across the 10 tags is around 6-8 mm 3-D for the optical rail experiment using the regular tracking mode 15 Hz averaging filter.

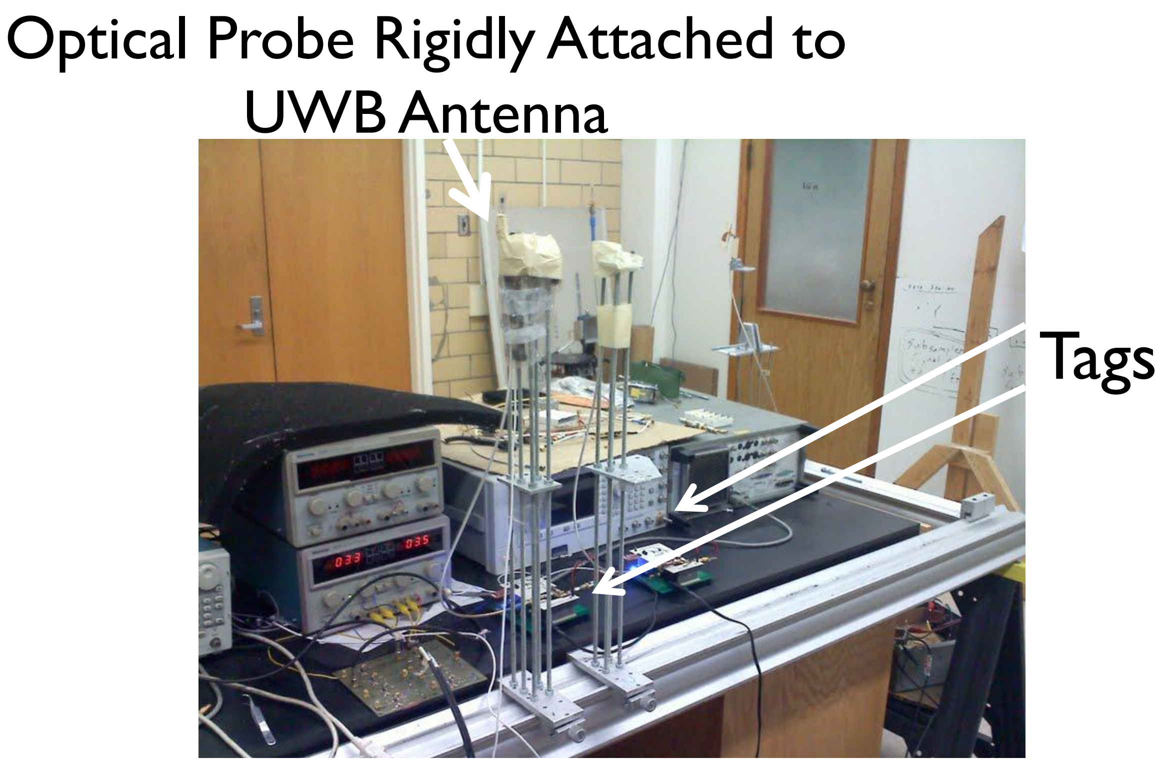

Figure 8-4. Experimental setup for optical rail experiments where one tag serves as the static tag while the other tag is moved along the optical rail with an infrared 6 DOF probe rigidly attached to it.

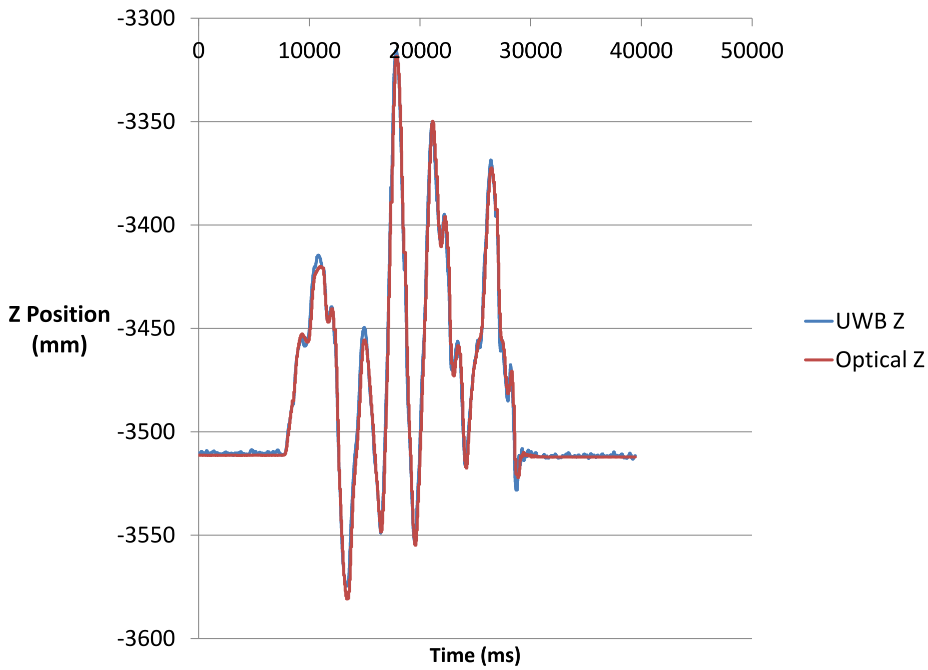

Figure 8-5. Typical optical rail experiment where the majority of 3-D motion is along the Z axis. The optical tracking system and UWB positioning system track together with around 6-8 mm of 3-D dynamic error. These results are for Tag 8.

8.2.2 Free Motion Experiments with Optical Tracking

Freeform motion experiments were undertaken using the same experimental setup shown in Figure 8-4. In the freeform dynamic experiment, the tag is moved around continuously through the view volume in a random fashion with some quick turning and accelerating. Typical 3-D results from the freeform experiments are shown in Figure 8-6, Figure 8-7, and Figure 8-8. Overall the UWB and optical data track together well. There is still 5-7 mm of 3-D dynamic error between the two systems. One reason for this error is the phase center bias outlined in Section 7.2. The freeform experiments showcase the robustness of this system in detecting quick and changing motions around the view volume. A summary of freeform 3-D dynamic experiments is provided in Table 8-1. Overall the tags perform similar to one another

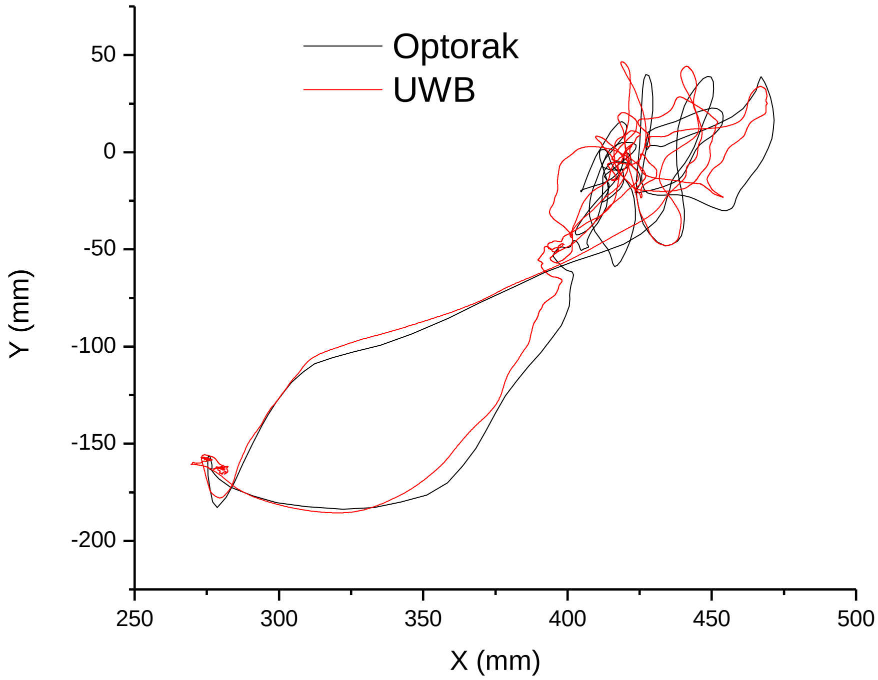

Figure 8-6. X-Y cross section showing optical and UWB data for a dynamic freeform experiment for Tag 10. Good agreement can be seen between the UWB and optical tracking systems, although certain 3-D locations have more error than others.

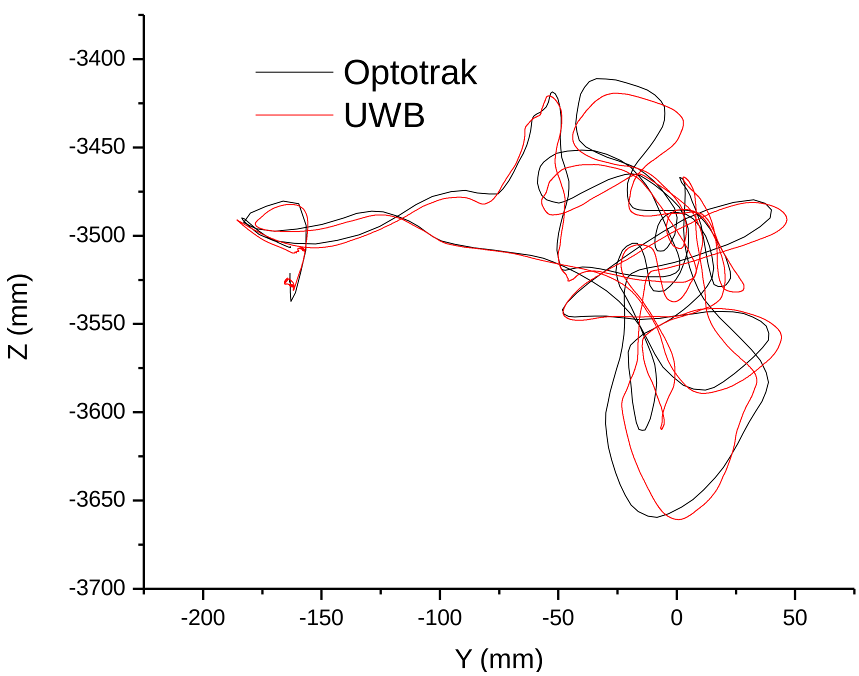

Figure 8-7. Y-Z cross section showing optical and UWB data for a dynamic freeform experiment for Tag 10. Good agreement can be seen between the UWB and optical tracking systems.

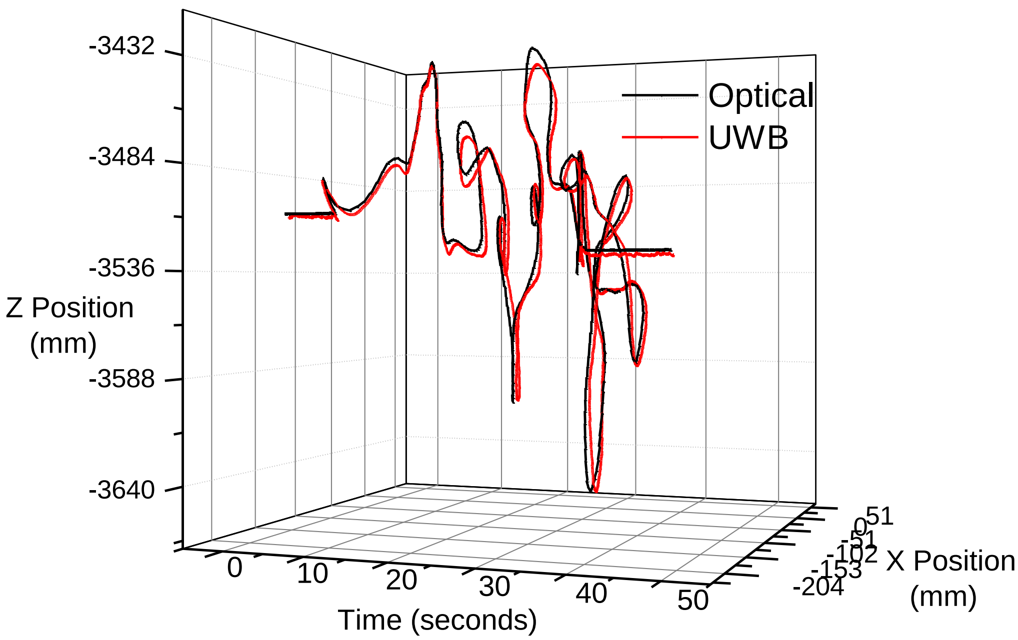

Figure 8-8. X-Z cross section with time also displayed for Tag 10 to show the real-time tracking of the UWB positioning system by the optical tracking system.

with 5.56-7.12 mm 3-D RMSE measured for the high accuracy track mode and 7.56-11.6 mm 3-D RMSE for the regular track mode. These experiments were performed three times per tag and averaged to get consistent results. The overall average across all 10 tags was 9.54 mm 3-D RMSE for regular tracking mode and 6.71 mm for high accuracy track mode. These results are promising, especially since the tag is a standalone system and this was a freeform experiment which typically causes more error than other types of experiments with less dynamic motion. Also, the tag is using a VCO rather than a low phase noise local oscillator. The VCO was a serious detriment to the 1st generation system outlined in Chapter 5.

8.2.3 Two Tag Dynamic Experiments

Currently only one optical probe is integrated into the UWB positioning system, so it is

Table 8-1: Error summary of 3-D dynamic experiments where a tag is moved freely in the view volume and tracked by the optical tracking system. A static tag is used to remove receiver clock jitter and drift.

Tag	80 Sample Average 15 Hz Passband 3-D RMS Error (mm)	160 Sample Average 8 Hz Passband 3-D RMS Error (mm)
2	7.56	5.56
4	11.6	6.67
5	10.1	6.99
8	8.62	6.98
9	9.79	7.01
10	9.08	7.04
12	10.1	7.12
13	9.23	7.00
14	9.81	6.61
15	9.53	6.14
Average	9.54	6.71

not possible to get 3-D accuracy for both tags. Nonetheless, experiments can be run to verify visually and within the context of the experiment that multiple tags are tracking dynamically at the same time. Figure 8-9 shows an X,Y,Z plot of the 3-D position of two tags as the rigid body both of them are attached to begins to move. The UWB positioning system can handle tracking up to 10 tags simultaneously, so as expected tracking two simultaneously works well.

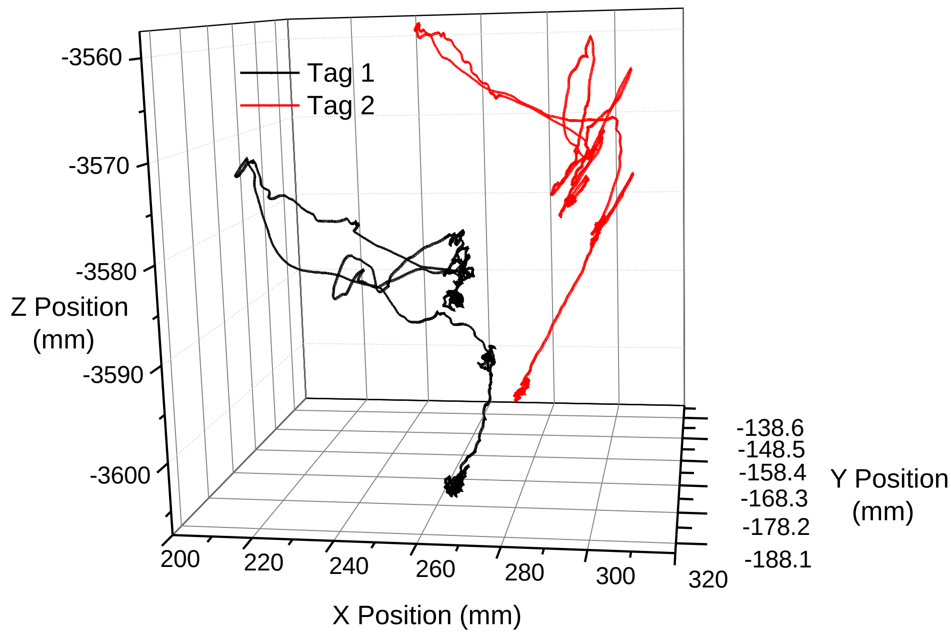

Figure 8-9. X,Y,Z plot of the 3-D position of two separate tags as they are moved dynamically while attached to the same rigid body. Accuracy was not measured but is estimated at 6-7 mm 3-D RMSE.

8.3 Analysis of Observed Errors

The results presented in this chapter of 6-9 mm of 3-D RMSE are promising since an integrated tag is being used which has a noisy VCO as its LO source, and many real system design features have been incorporated into the multi-tag UWB development platform. Unfortunately, the goal of this project is sub-millimeter accuracy, so there are still more hurtles to overcome in the pursuit of sub-millimeter 3-D wireless accuracy. Figure 8-10 shows dynamic data for the X dimension where X has a higher PDOP when compared to Y and Z (around 2). This causes reduced range resolution and higher errors in the X dimension. Figure 8-11 shows the Y dimension for the same experiment. The Y dimension in this case does not have significant added PDOP but rather contains phase center bias and error which is easily

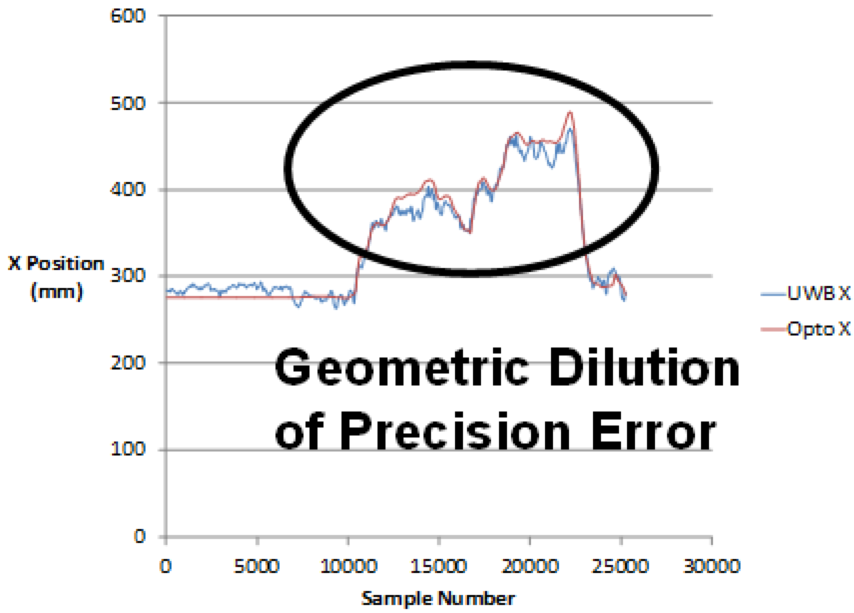

Figure 8-10. X position of Tag 10 in a dynamic freeform experiment where increased error and instability caused by a high geometric dilution of precision in the X direction can be seen.

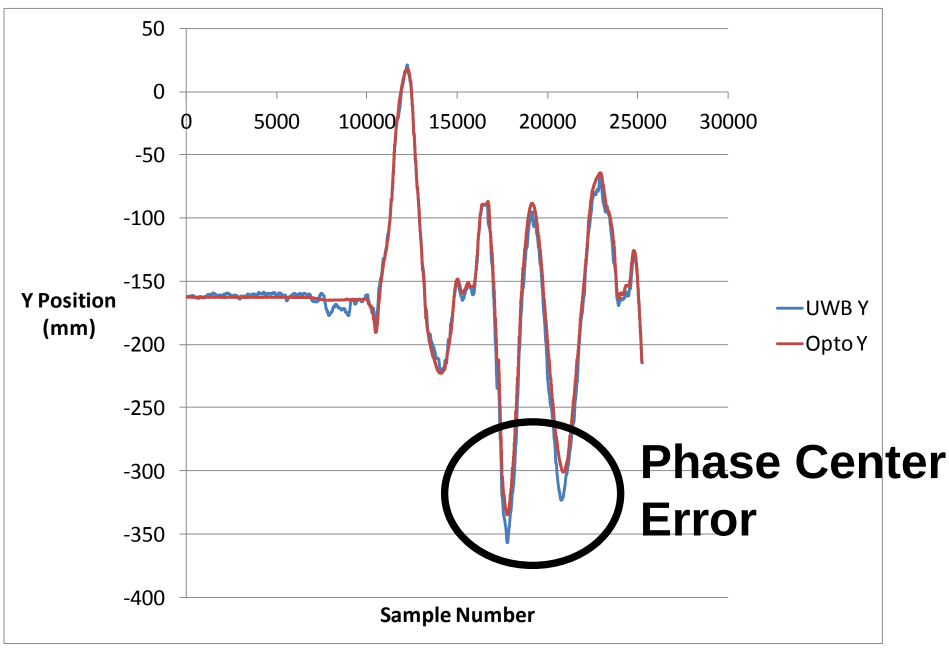

Figure 8-11. Y Position of Tag 10 in a dynamic freeform experiment. The large offsets are indicative of phase center error which ultimately causes these types of scaling errors.

observed in the extreme locations of the view volume such as those locations outlined in Figure 8-11. Figure 8-12 is the Z dimension for the same experiment. No noticeable PDOP effects or phase center biasing effects are observed. Finally, Figure 8-13 illustrates how phase center biasing and dynamic phase center variation can cause areas of significant bias in the range differences. Some locations within the view volume have little to no effects from phase center biasing while other locations see significant bias effects.

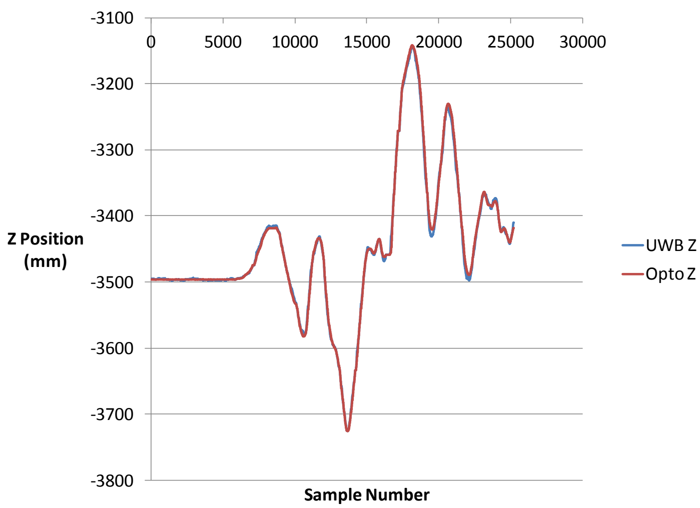

Figure 8-12. Z position of Tag 10 where the other error sources (geometric dilution of precision and phase center biasing) do not occur to large extent.

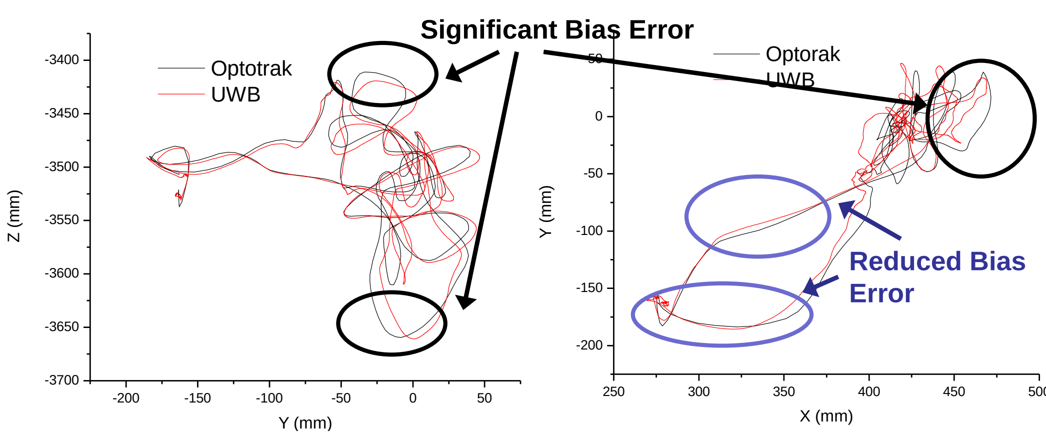

Figure 8-13. X,Y,Z cross sections with focus on significant bias error locations versus reduced bias error locations. This variation in bias error is most likely caused by dynamic base station phase center variation.

8.4 Five Base Station Optical Rail Experiment

An experiment was run using five base stations while tracking Tag 13 dynamically along the optical rail. The experimental setup is shown in Figure 8-14 where Tag 9 is used as the static tag and Tag 13 is tracked dynamically along the optical rail. Experimental results from the five base station experiment are shown in Figure 8-15, Figure 8-16, and Figure 8-17. Figure 8-15 shows the X position in mm for the optical rail experiment for both the optical and UWB tracking systems. Figure 8-16 and Figure 8-17 show the Y and Z position in mm for the optical rail experiment for both the UWB and optical tracking systems. RMSE in the X,Y,Z dimensions is 2.52 mm, 0.93 mm, and 1.83 mm. This results in a total 3-D RMSE of 3.26 mm. 130 range

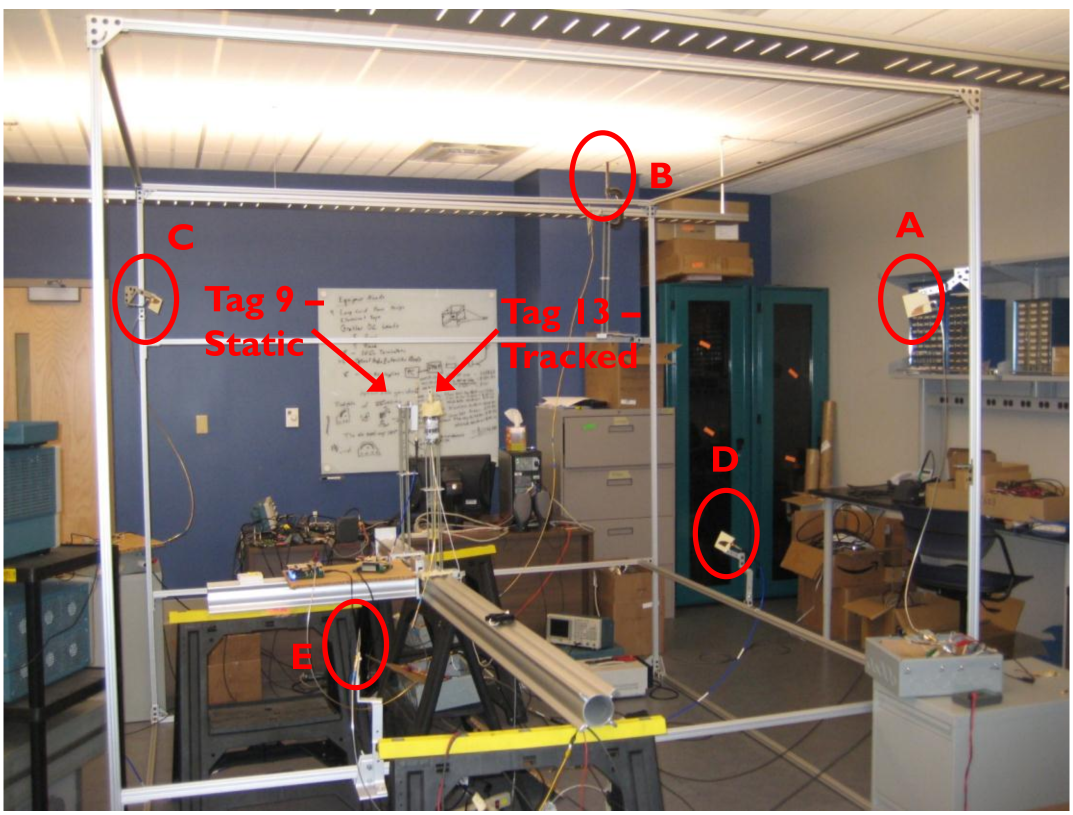

Figure 8-14. Experimental setup where dynamic (Tag 13) and static (Tag 9) tags are positioned on an optical rail. Five base stations are positioned around the tags (A,B,C,D,E) in a geometrical setup with low PDOP.

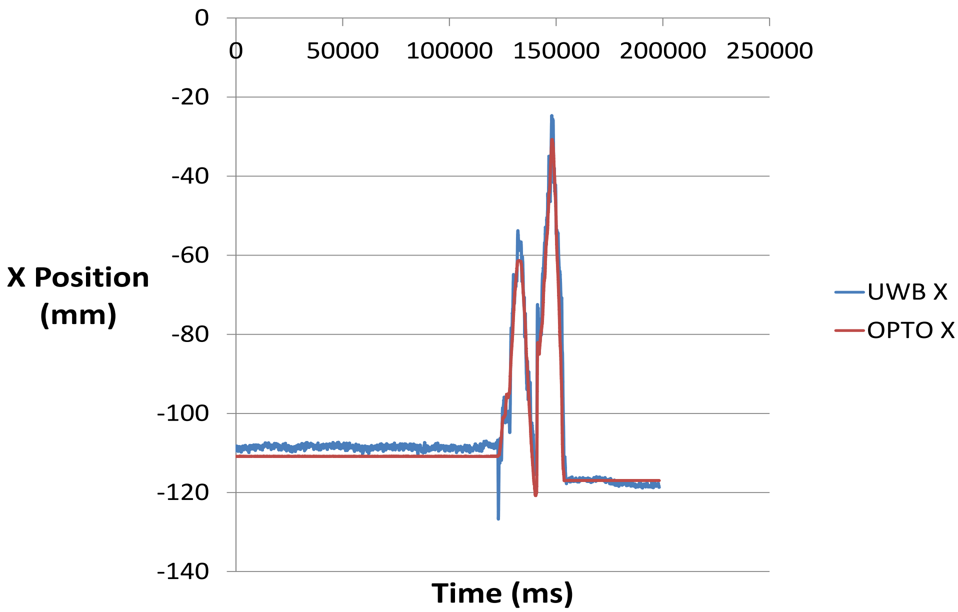

Figure 8-15. X position values for both the UWB and optical tracking systems for an optical rail experiment where Tag 13 is dynamically moved along the optical rail. The RMSE in the X dimension is 2.52 mm.

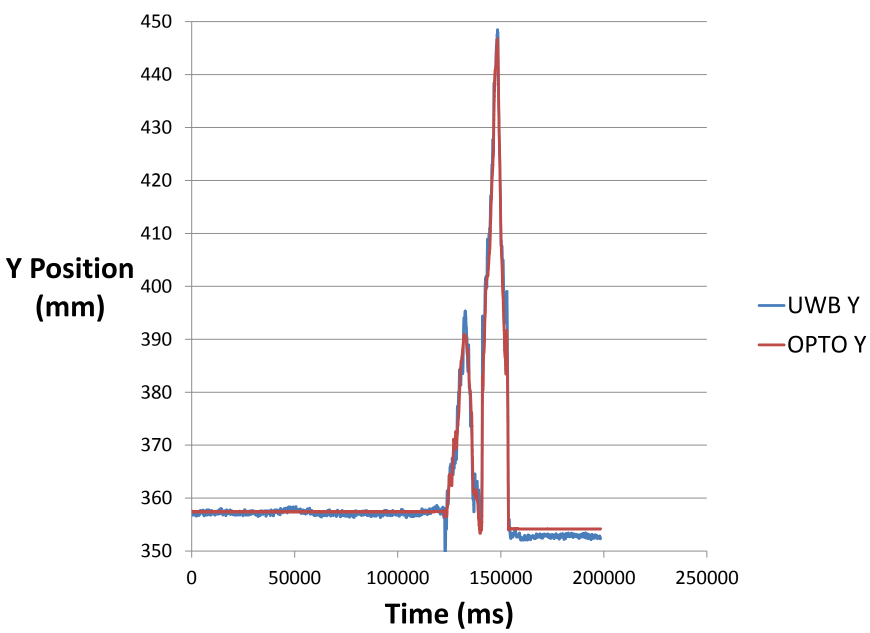

Figure 8-16. Y position values for both the UWB and optical tracking systems for an optical rail experiment where Tag 13 is dynamically moved along the optical rail. The RMSE in the Y dimension is 0.93 mm.

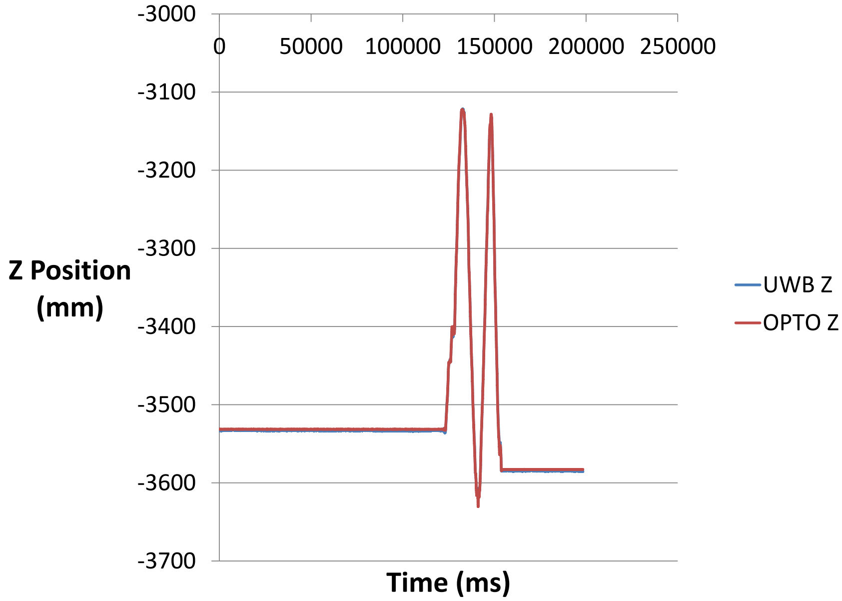

Figure 8-17. Z position values for both the UWB and optical tracking systems for an optical rail experiment where Tag 13 is dynamically moved along the optical rail. The RMSE in the Z dimension is 1.85 mm.

differences were averaged during this experiment. The 3-D RMSE of 3.26 mm is the best achieved for a dynamic optical rail experiment and represents a 50% reduction in error compared to the optical rail experiments performed with four base stations discussed in Section 8.2.1 resulting 6-8 mm of 3-D error.

8.5 Four Base Stations versus Five Base Stations

As mentioned in Section 8.4, the optical rail experiment with five base stations resulted in 3-D error of 3.26 mm while optical rail experiments with four base stations resulted in 6-8 mm of 3-D error as discussed in Section 8.2.1. The improvement in accuracy occurs for two reasons: (1) a five base station dynamic calibration is more accurate than a four base station dynamic calibration, and (2) the geometric PDOP is less for a five base station experimental setup versus four base station. Figure 8-18 shows the range differences for both the optical and UWB tracking systems after solving for the homogeneous transformation matrix from the dynamic calibration process. The additional information provided by an extra range difference link helps improve the accuracy of the resultant homogeneous transformation matrix, thus improving the overall 3-D accuracy of the UWB positioning system. Figure 8-19 and Figure 8-20 show the X,Y,Z PDOP for a four base station and five base station optical rail experiment. As shown in Figure 8-19, the four base station experiment has a total 3-D PDOP around 2.40 (X=2.22,Y=0.77,Z=0.50) while the five base station experiment has a total 3-D PDOP around 1.58 (X=1.45,Y=0.52,Z=0.34). This is a 34% reduction in 3-D geometrical error. The improved dynamic calibration combined with the improved PDOP account for the 46%-60% reduction in 3-D error when comparing four base station versus five base station optical rail experiments.

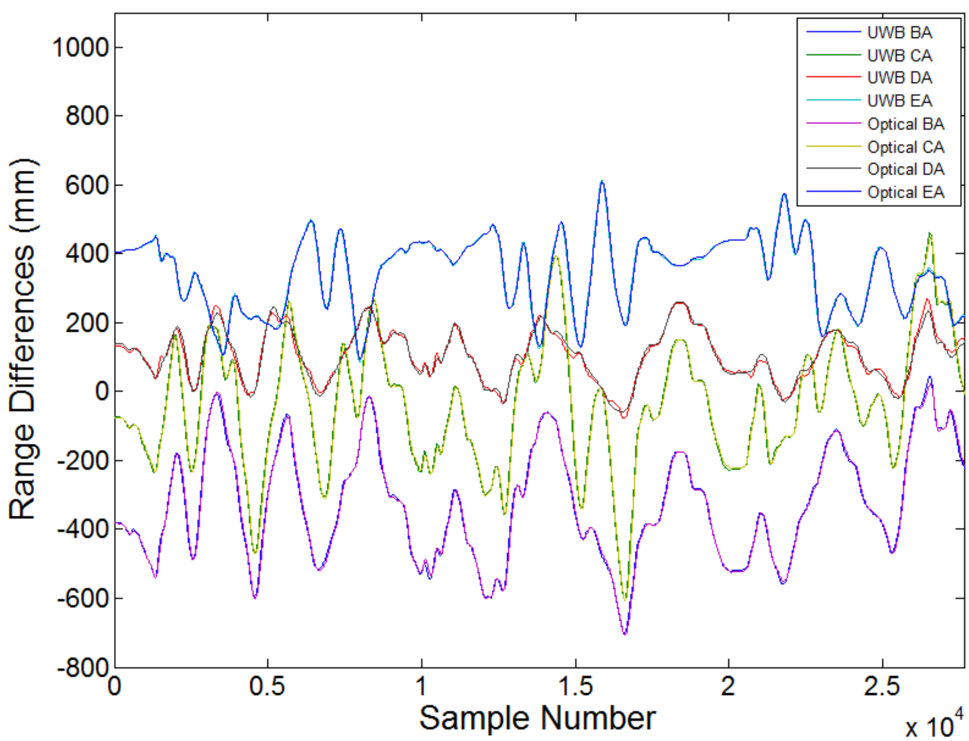

Figure 8-18. Five base station calibration data where the optical and UWB range differences BA, CA, DA, and EA are calibrated together via a homogeneous transformation matrix.

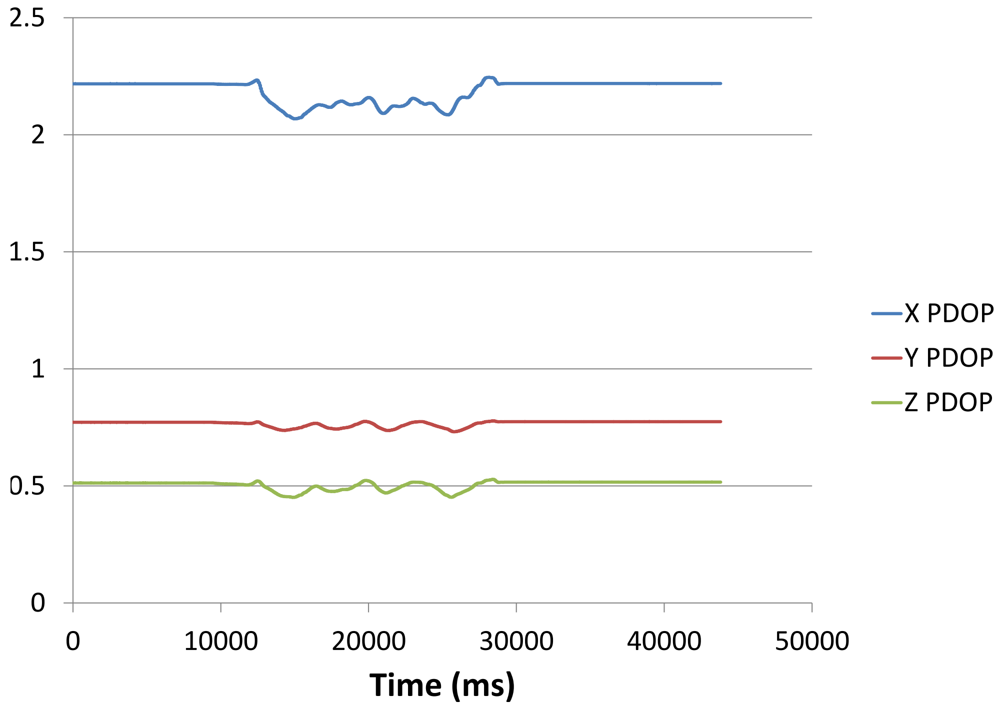

Figure 8-19. PDOP data for a four base station optical rail experiment showing the PDOP in X,Y,Z. The total PDOP is 2.40 (X=2.22,Y=0.77,Z=0.50).

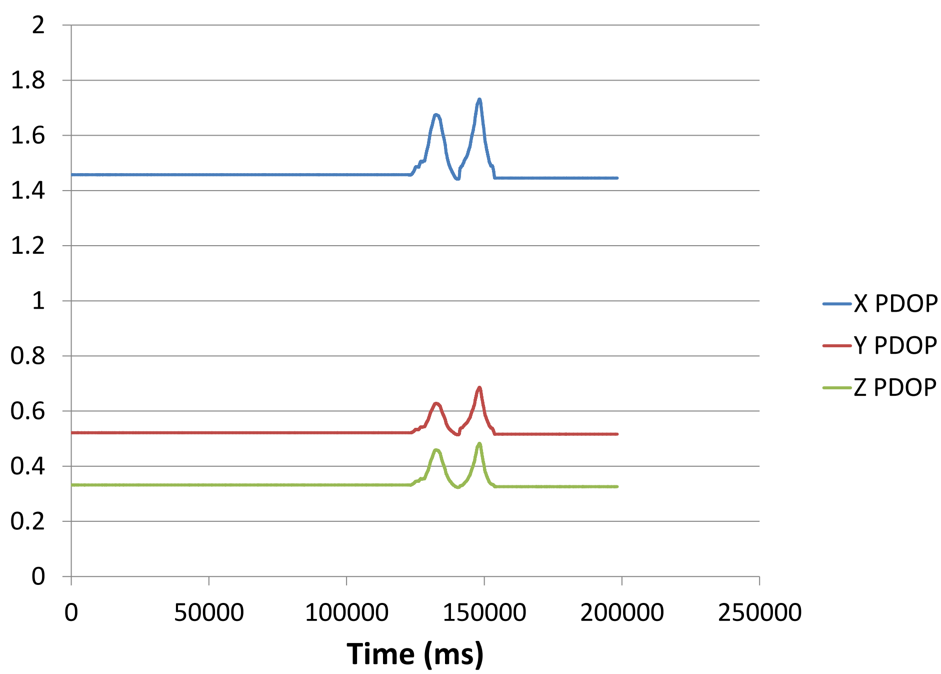

Figure 8-20. PDOP data for the five base station optical rail experiment showing the PDOP in X,Y,Z. The total PDOP is 1.50 (X=1.45,Y=0.52,Z=0.34).

8.6 Conclusion

Dynamic 3-D data has been presented for the 10 tags which are part of the UWB Multi-Tag Development Platform. This includes optical rail and freeform dynamic experiments using four base stations. Additional error sources observed during this experimental analysis have also been highlighted. The UWB Multi-Tag Development Platform consistently achieves 6-9 mm 3-D accuracy in freeform dynamic experiments across a large portion of the view volume (50 cm x 20 cm x 20 cm) using four base stations. The five base station optical rail experiment yielded a 46%-60% reduction in 3-D error compared to the four base station optical rail experiment. This reduction in error is due to the increased accuracy of the dynamic calibration and the 30%-40% reduction in PDOP when using five base stations compared to four base stations. The second generation multi-tag UWB positioning system achieves comparable 3-D dynamic accuracy to the first generation system outlined in Chapter 5 even after the addition of integrated tags and base stations and the removal of low phase noise LOs from the transmitter and receiver for four base station experiments. Five base stations increases the accuracy to 3-4 mm dynamic 3-D accuracy which provides a 2-3 mm improvement in 3-D accuracy compared to the first generation system outlined in Chapter 5.

9. UWB Receiver-Side Digital Signal Processing for High Accuracy Indoor Localization

A pronounced need exists for adaptive techniques in receiving and processing of UWB signals at base stations and communications receivers. This is due to the wide range of indoor environments which UWB signals travel through from the transmitter to receiver(s). For example, the signal may be either LOS or NLOS, which fundamentally changes its characteristics and therefore how it should be processed at the receiver. Adaptive techniques are needed which are implemented on programmable digital hardware (i.e. FPGAs) to accurately detect the nature of the incoming UWB signals so that appropriate mitigation techniques can be used either on the FPGA or in the software. An overview is provided here of the digital signal processing techniques used in the UWB real-time location system which are implemented on an FPGA. This includes peak and leading-edge detection, noise estimation, and signal-to-noise ratio calculations. Effects of low signal-to-noise ratios on UWB leading-edge detection is discussed in Section 9.5 to provide background and an understanding of the effects low SNR and NLOS signals have at the UWB energy detection receiver. Chapter 10 provides a more formalized discussion of non-line-of-sight detection and mitigation including experimental results using the UWB multi-tag development platform outlined in Chapter 7 and Chapter 8. Section 9.6 discusses an adaptive leading-edge detection algorithm which utilizes SNR and received pulse slew rate to first determine LOS or NLOS and then uses an adaptive technique to apply a matched filter to the incoming UWB signal. The matched filter helps to increase the SNR of the LOS UWB pulse by up to 5-7 dB. Simulation results are included in

Section 9.6. The FPGA used at the UWB base stations and UWB control station is the Spartan 3E evaluation board with a Xilinx Spartan-3 XC3S200 FPGA (and in some cases the Xilinx Spartan-3 XC3S1000 FPGA). The transmission of range difference and SNR data to the computer via an RS-232 serial connection is discussed in Section 9.7.

9.1 UWB Pulse Analog-to-Digital Conversion

The raw UWB signal after sub-sampling (see Section 5.2.3) is shown in Figure 9-1. The sub-sampling process extends the pulse from 300 ps FWHM to 0.7-1.0 μs FWHM using a 2500 expansion factor. The received UWB pulse after passing through a 50 MSPS 10-bit Analog Devices AD9216 ADC evaluation board is shown in Figure 9-2. The UWB pulse is intact, but a slight ringing is introduced by the RF transformer at the differential input of the ADC. The RF transformer resonates around 100 kHz and saturates for low frequency signals (< 50 kHz), effectively making the input signal high pass filtered at around 100-300 kHz. This effect is shown in Figure 9-3 and effectively limits the usable expansion factor for the UWB system. As shown in Figure 9-3, the 50 kHz sine wave passes the input RF transformer without attenuation while the 30 kHz, 20 kHz, and 10 kHz sine waves become more and more attenuated.

Table 9-1 shows the sub-sampled -10 dB bandwidth and FWHM for different expansion factors. At a 2500 expansion factor, the UWB pulse is transmitted successfully with no amplitude reduction and slight ringing as shown in Figure 9-2. At a 10,000 expansion factor, the UWB pulse is transmitted through the RF transformer but causes extreme amounts of ringing which makes it unusable for localizing in the UWB positioning system. This effect is shown in

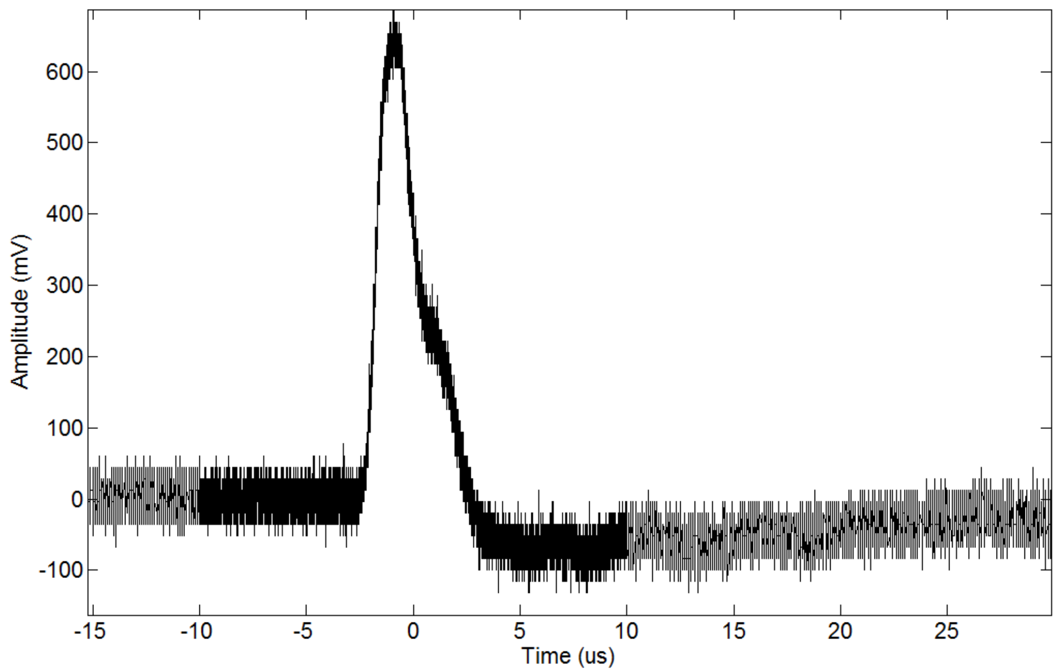

Figure 9-1: Raw received UWB pulse using a 2500x expansion factor before analog-to-digital conversion. No ringing is observed in the UWB pulse when compared to Figure 9-2.

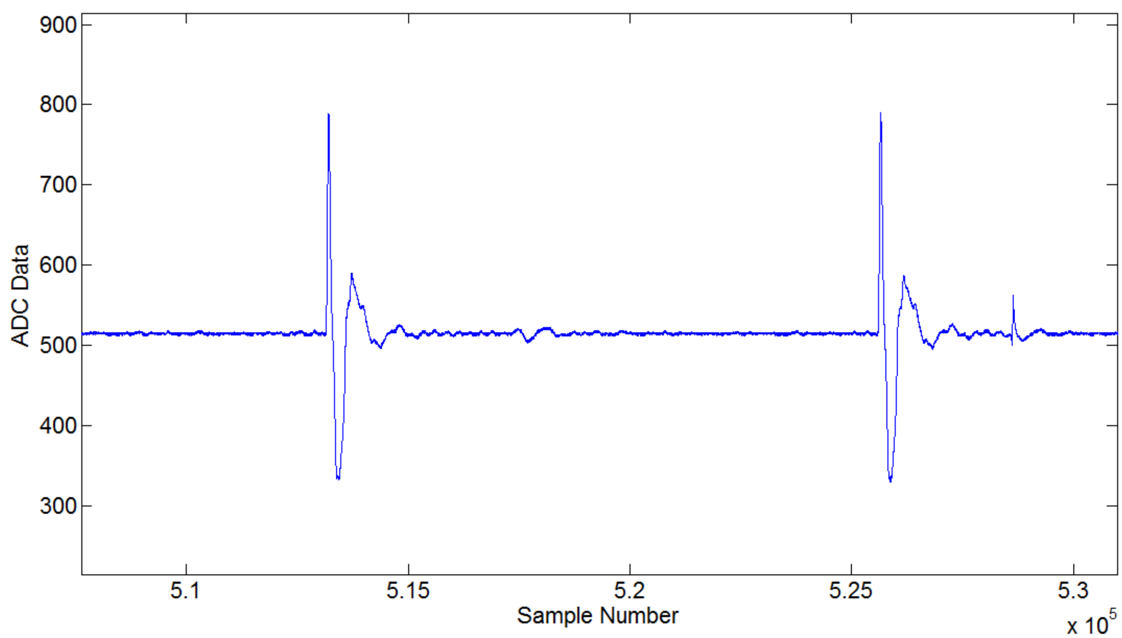

Figure 9-2: Raw received UWB pulse using a 2500x expansion factor after analog-to-digital conversion. A slight ringing is introduced by the high pass filter on the ADC which can be observed immediately after the initial UWB pulse. The original shape of the UWB pulse before analog-to-digital conversion is shown in Figure 9-1.

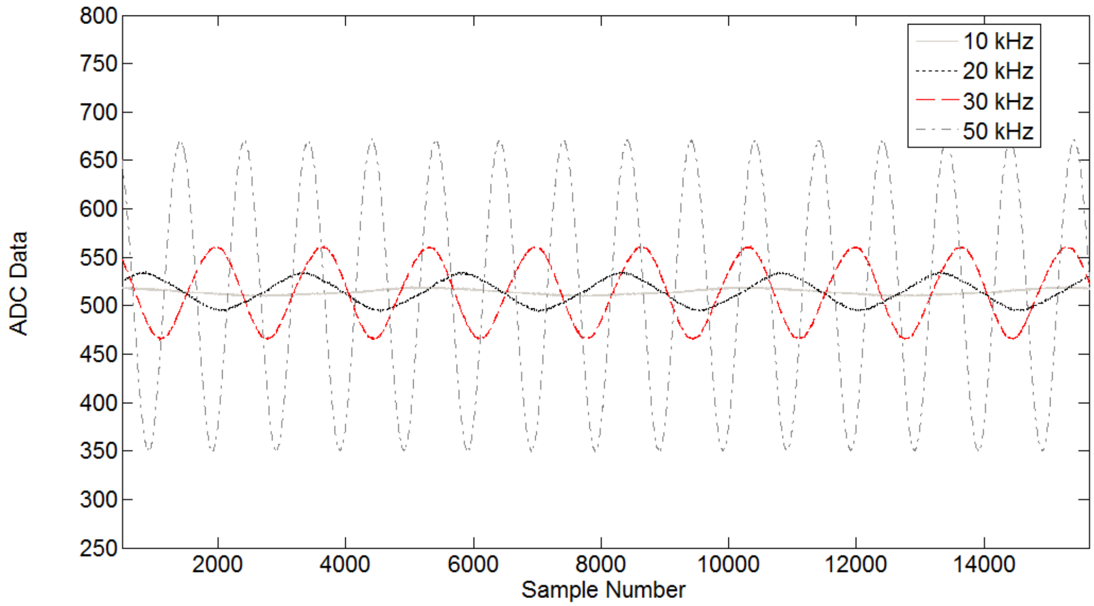

Figure 9-3: Output sine wave signals for input sine waves of 500 mVpp with frequencies of 10 kHz, 20 kHz, 30 kHz, and 50 kHz. The signals attenuate significantly when comparing 50 kHz to 10 kHz. This is the saturation effect of the RF transformer which effectively limits the input signal to a frequency bandwidth of 50 kHz and above (a high pass filter with a 50 kHz cutoff).

Table 9-1: Sub-sampled 300 ps UWB pulse -10 dB bandwidth and FWHM for different expansion factors.

Expansion Factor	UWB Pulse -10 dB Bandwidth	Pulse FWHM
1000	DC - 3 MHz	300 ns
2500	DC – 1.2 MHz	750 ns
5000	DC – 600 kHz	1.5 μs
10,000	DC – 300 kHz	3 μs
100,000	DC – 30 kHz	30 μs

Figure 9-4 where the UWB pulse with 10,000 expansion is shown before and after analog-to-digital conversion. Before the ADC, the UWB pulse has a typical pulse shape while after the ADC, the pulse has an extreme amount of ringing. At a 10,000 expansion factor, the -10 dB bandwidth is 300 kHz, which is greatly distorted and resonated by the RF transformer at the differential input of the ADC. Finally, Figure 9-5 shows a 30 μs UWB pulse with 100,000 expansion factor. The bandwidth of this signal is 30 kHz, and it is almost completely attenuated by the RF transformer at the differential input of the ADC. Given the input frequency constraints of the ADC differential input RF transformer, an expansion factor of 2500 is used to ensure the received UWB signal has minimal ringing, minimal distortion, and a higher digital sample period (for 2500, each sample is spaced 8 ps apart).

9.2 UWB Peak Detection

The first step in localizing the sub-sampled UWB pulses is detection of the UWB pulse peak. The pulse peak is important for multiple reasons which include its use as a trigger to reset

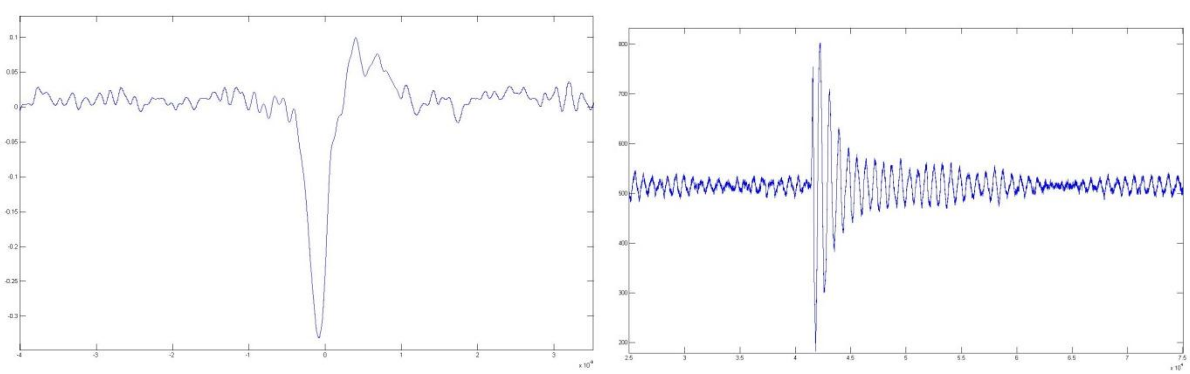

(a) (b)

Figure 9-4: (a) 3 μs UWB pulse at a 10,000 expansion factor before analog-to-digital conversion, (b) 3 μs UWB pulse at a 10,000 expansion factor after analog-to-digital conversion where a large amount of ringing is evident which is caused by the RF transformer at the differential input of the analog-to-digital converter.

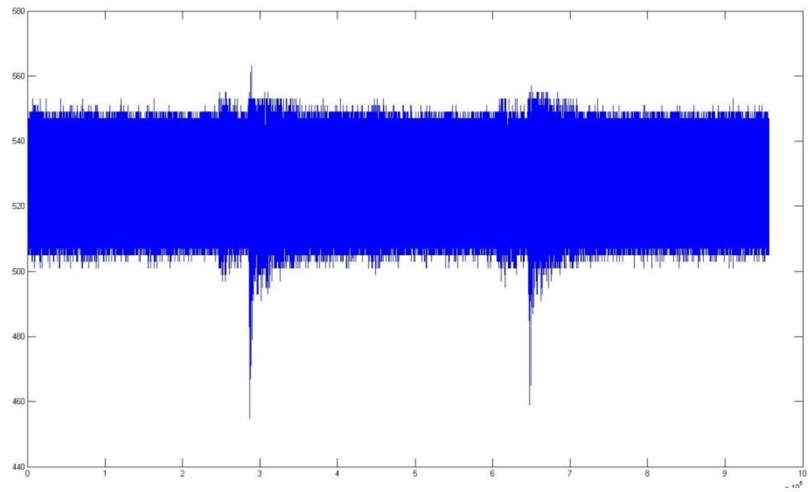

Figure 9-5: 30 μs UWB pulse at a 100,000 expansion factor after analog-to-digital conversion where the UWB pulse has been almost completely attenuated by the ADC input RF transformer.

the UWB base station peak and leading-edge detection algorithms as well as its use in the signal-to-noise ratio calculation which can then be used for NLOS detection and mitigation as discussed in Chapter 10. Figure 9-6 shows the absolute value of the received UWB signal. The

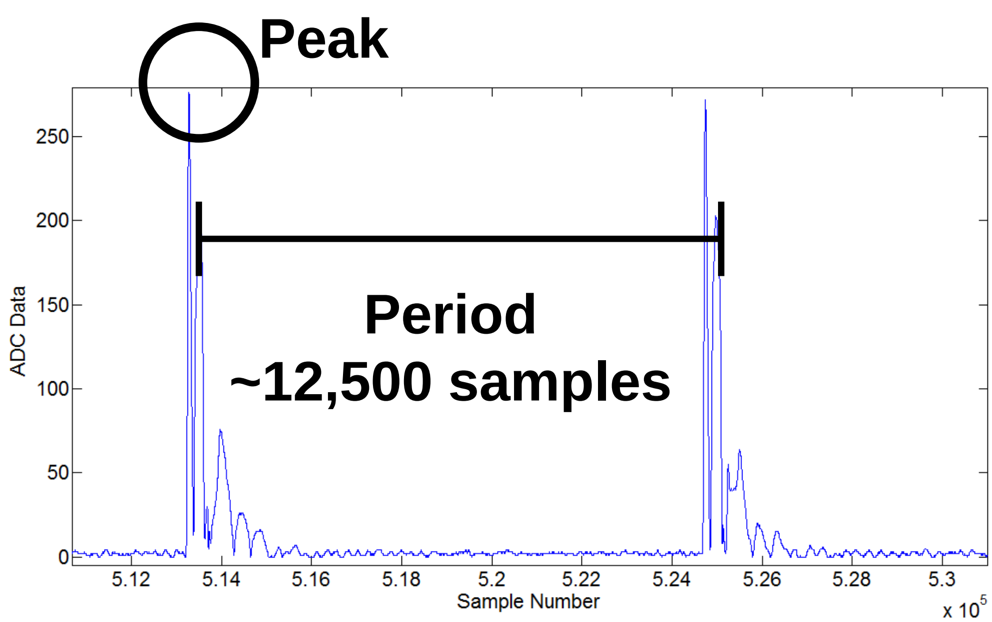

Figure 9-6: Absolute value of the received UWB pulse. The peak can easily be located by using a search window which is a substantial size of the UWB pulse period of around 12,500 digital samples. A window size of 5/8 of the period is used which equates to 7812 samples.

peak is located by using a moving window of 5/8 the size of the UWB pulse period. Each time a new maximum value is found, the counter resets to zero. Since the digital pulse period is 12,500 samples for a 2500 expansion factor (equates to 250 μs), the moving window is 7812 samples. This is sufficiently large to lock onto the UWB pulse peak while reducing the likelihood of false peak triggering to virtually zero. This provides a triggering capability which resets the leading-edge detection algorithm each time a new UWB pulse peak is located. Once the counter for the 7812 sample window reaches becomes greater than the window size of 7812, the peak or leading-edge time position is saved, and the FPGA switches into a hold mode and noise sampling mode. The running peak search window is shown in Figure 9-7.

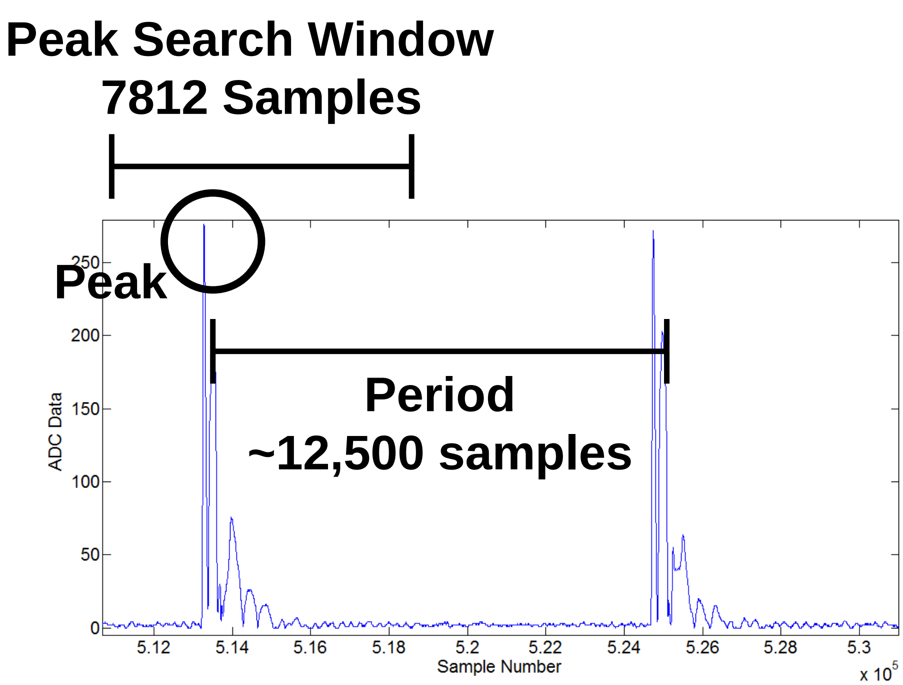

Figure 9-7: Absolute value of the received UWB pulse. The peak search window is 7812 samples or 5/8th of the overall UWB pulse period of 12,500 samples.

9.3 UWB Leading-Edge Detection

Leading-edge detection is the most robust ranging algorithm for accurate estimation of the time-of-arrival of a UWB pulse. It is used in commercial UWB indoor positioning systems [13] as well as in research-related UWB positioning systems [19]. The first generation leading-edge detection algorithm designed by Merkl is described in [93] and outlined in Section 5.2.6. It uses two max windows of 16 and 256 samples and the ratio between them to detect the leading-edge of the incoming UWB pulse. The 3-D dynamic results from the 1st generation UWB indoor positioning system outlined in Chapter 5 were obtained with Merkl's max ratio leading-edge detection algorithm implemented on an FPGA. Chapter 6 provides simulation results which further support the robustness of leading-edge detection for indoor LOS environments. Figure 9-8 shows a received UWB pulse and highlights the leading edge of the pulse. The leading-edge can be detected with a high accuracy of 10-20 ps (3-6 mm) for the raw signal compared to 30-300 ps (9-90 mm) for peak detection of a high SNR UWB pulse signal. This is possible because of the high slew rate of the leading-edge when compared to the peak of the UWB pulse. Figure 9-9 shows the error in millimeters for a tag in a static position for both the leading-edge detection and peak detection algorithms. As shown in Figure 9-9, leading-edge detection has much less variation (11.1 mm) compared to 76.5 mm for peak detection. Error due to clock jitter and drift and AWGN combine with uncertainty in the leading-edge to cause the raw error to be 11.1 mm instead of the theoretical uncertainty given the slew rate of the leading-edge of 3-6 mm.

The leading-edge digital sample position is calculated by first detecting the UWB pulse peak from the previously received UWB pulse. For example, for the signal in Figure 9-7, the

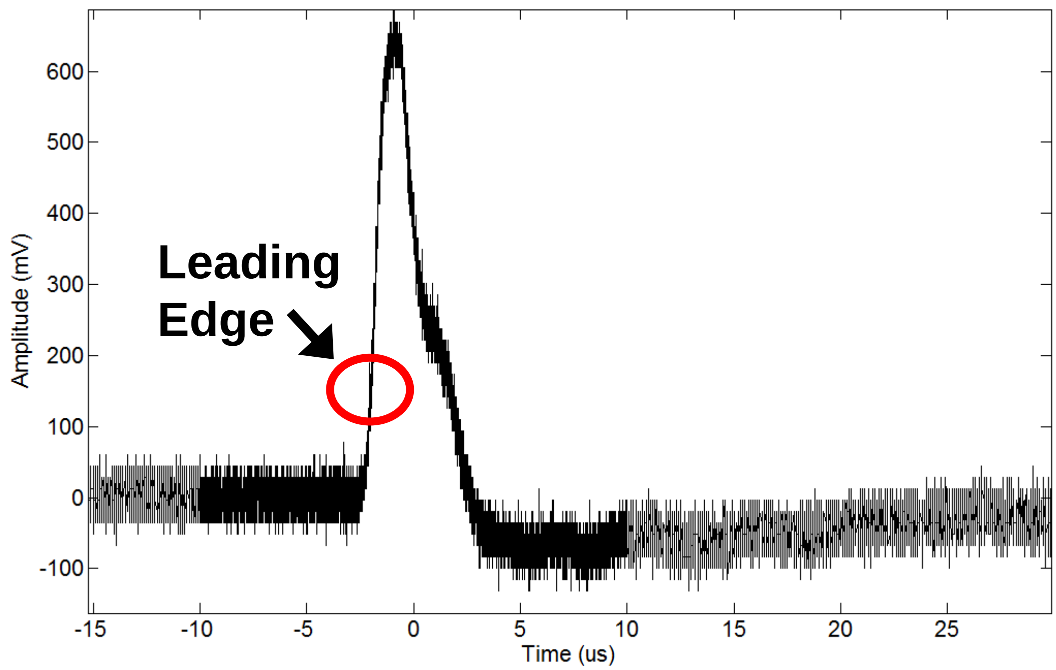

Figure 9-8: UWB pulse before the ADC where the high slew rate leading-edge can be seen and provides a much sharper trigger point for resolution of the time-of-arrival (10-20 ps) when compared to the peak of the UWB pulse (30-300 ps for high SNR signals).

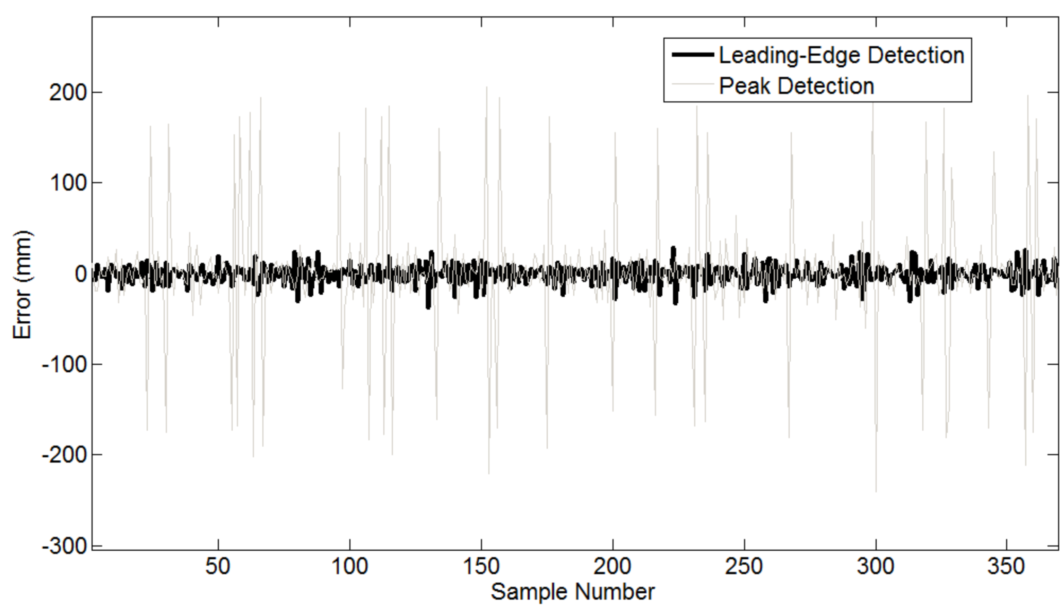

Figure 9-9: Variation in millimeters for a tag in a static location comparing raw output data from the peak and leading-edge detection algorithms. The leading-edge detection algorithm has a standard deviation of 11.1 mm compared to a standard deviation of 76.5 mm for peak detection.

peak value is around 290. The threshold for the leading-edge detection algorithm is set to 1/4th the magnitude of the UWB peak value. In this case, the leading-edge detection threshold is set to 72. A final comparison is done to make sure the current leading-edge threshold is above the noise floor of the incoming signal. The noise floor calculation is discussed in Section 9.4. Results for the leading-edge detection algorithm are outlined in Figure 9-10 where a tag is left in a static location and 10,000 consecutive leading-edge detection measurements are taken. The raw leading-edge data has a standard deviation of 11.1 mm while the standard deviation drops to 0.60 mm with the application of a 10-sample averaging filter. The complete leading-edge detection algorithm is outlined in Figure 9-11. This algorithm is used to provide data for the NLOS detection and mitigation outlined in Chapter 10.

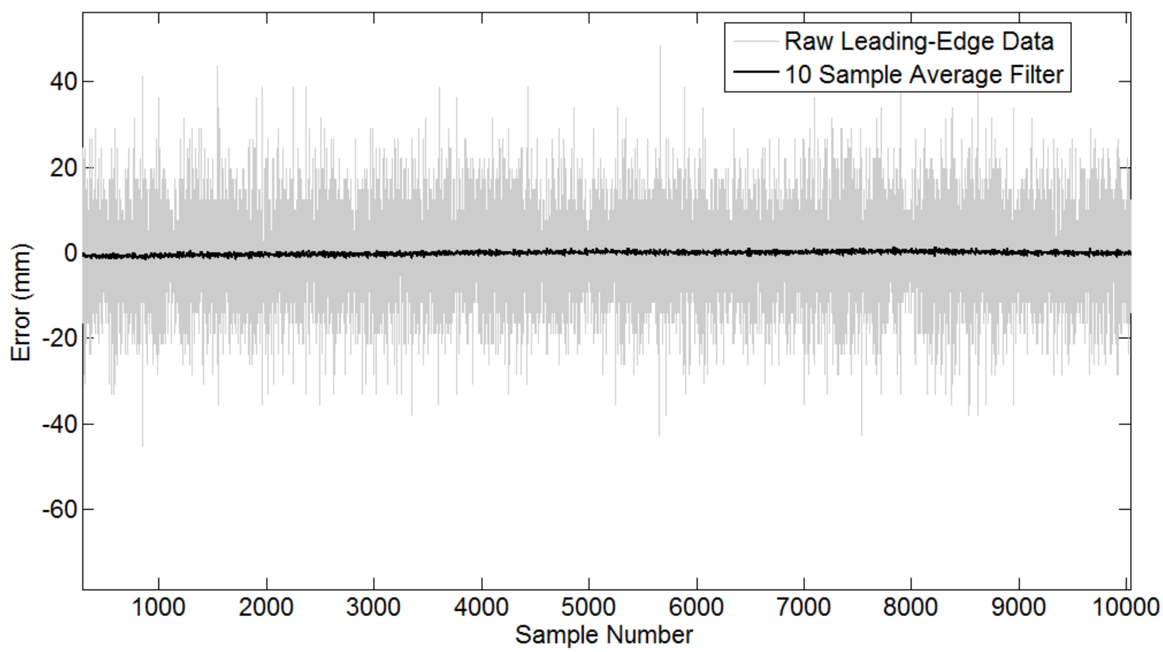

Figure 9-10: Variation in millimeters for a tag in a static location for 10,000 consecutive UWB pulse leading-edge calculations. The raw leading-edge detection data has a standard deviation of 11.1 mm while the application of a 10-sample averaging filter reduces the standard deviation to 0.60 mm. The leading-edge detection data is Gaussian and is easily filtered.

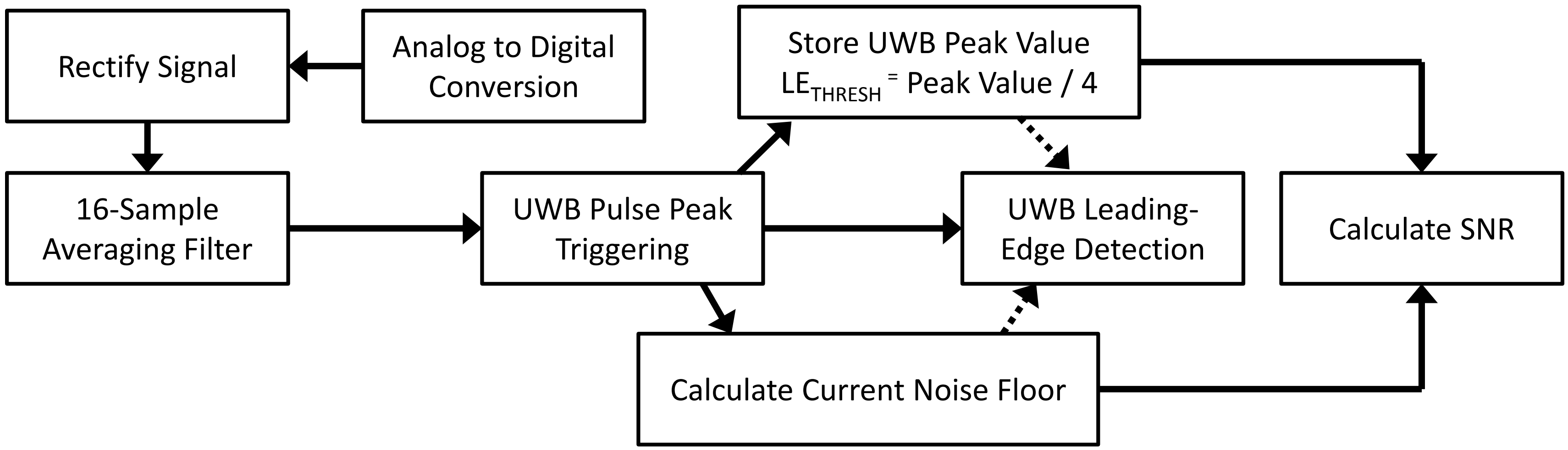

Figure 9-11: Leading-edge detection algorithm implemented on the base station FPGA which uses a rectified signal which undergoes a 16-sample averaging filter. This signal is used in triggering the algorithm off of the UWB pulse peak. The peak value is used to set the leading-edge detection threshold. The noise floor is calculated as discussed in Section 9.4. Finally, the peak and noise values are used to calculate the UWB SNR.

9.4 Noise Estimation

The noise in the received UWB pulse signal is estimated by first triggering the leading-edge detection algorithm off of the received UWB pulse peak as discussed in Section 9.2. Once the peak triggering is set, then a window is allocated for the received signal noise estimation. This process is outlined in Figure 9-12 where two separate moving windows are allocated: one for leading-edge and peak detection, the other for noise sampling and estimation. Currently the maximum value found within the noise sampling window is stored and used as the current noise level of the UWB signal. As shown in the leading-edge detection algorithm in Figure 9-11, the noise value is located after the received signal is rectified and sent through a 16-sample averaging filter. A typical noise signal is shown in Figure 9-13. The noise signal was measured

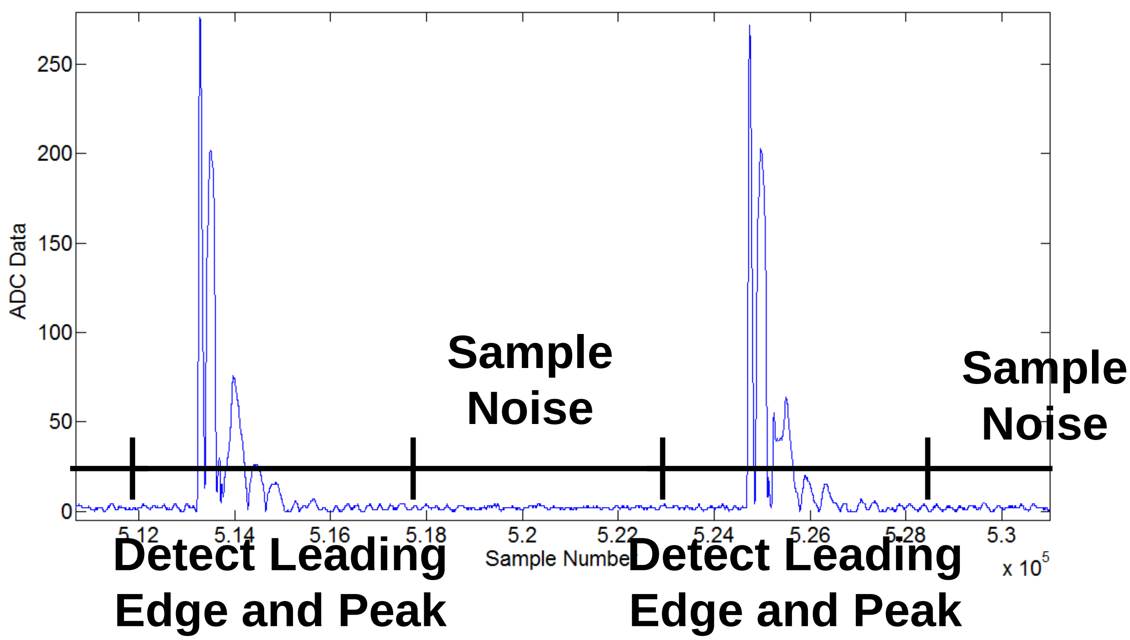

Figure 9-12: Received UWB pulse peak triggering process where a window is first allocated for peak and leading-edge detection followed by a separate time window allocated for noise sampling and estimation.

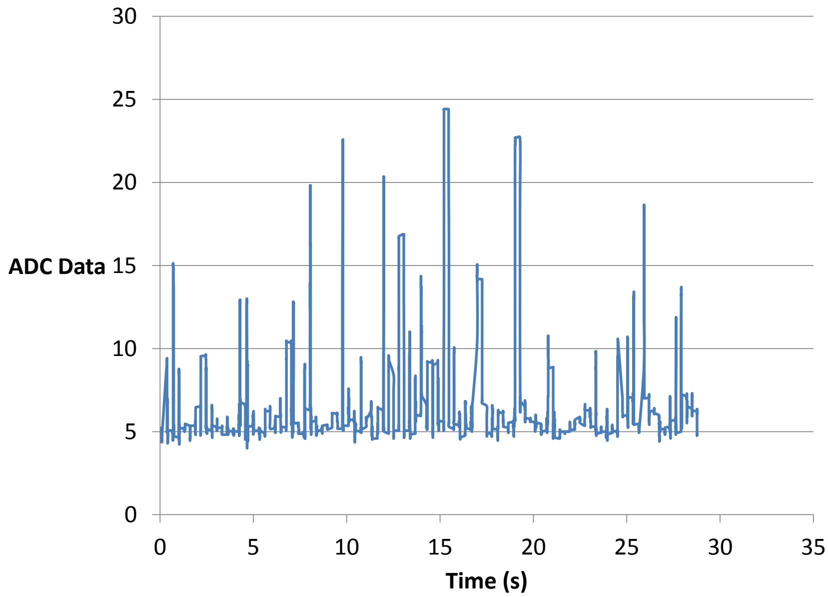

Figure 9-13: A typical noise signal measured over a time period of 30 s. Values fluctuate from 5-25 as measured by the 10-bit ADC.

over a 30 s period from a UWB receiver while the tag was left in a static location. The data values from the 10-bit ADC vary from 5-25 for this example signal.

9.5 Signal-to-Noise Ratio Calculation

The UWB peak value and noise value are used to calculate the SNR of the received UWB pulse. Peak detection is discussed in Section 9.2 while noise estimation is outlined in Section 9.4. The SNR is calculated using (9-1)

$$SNR = 20\ \log_{10}\left(\frac{Voltage\ Peak\ Val}{Voltage\ Noise\ Val}\right) \qquad (9\text{-}1)$$

where the peak value is calculated as discussed in Section 9.2 and the noise value is calculated using the method outlined in Section 9.4. The SNR can be solved for exactly when the peak and noise data is sent to the computer, as discussed in Section 9.8. Conversely, the SNR is estimated on the FPGA using (9-2)

$$SNR = \frac{420}{64} * Round\left(\log_2\left(\frac{Voltage\ Peak\ Val}{Voltage\ Noise\ Val}\right)\right) \tag{9-2}$$

where the *log₂ (Voltage Peak Val / Voltage Noise Val)* is estimated to the nearest power of two. The resultant possible SNR values output directly to the FPGA seven segment display include 0, 6, 13, 19, 25, 32, 39, 45 (or 0, 6, D, 13, 19, 20, 27, 2D in hex). The FPGA calculated SNR values are useful for quick system checking and debugging.

Figure 9-14 shows the raw UWB received signal after the ADC. Variations in the UWB pulse peak amplitude can be captured in variations of the SNR of the received UWB pulses. Figure 9-15 shows the SNR in dB for a UWB receiver where a hand is purposely waived in front of the UWB receiver during the 20-30 s time interval. This effectively blocks the LOS path and causes a reduction in SNR from 28 dB to 6-15 dB. Finally, the SNR for five base stations over a

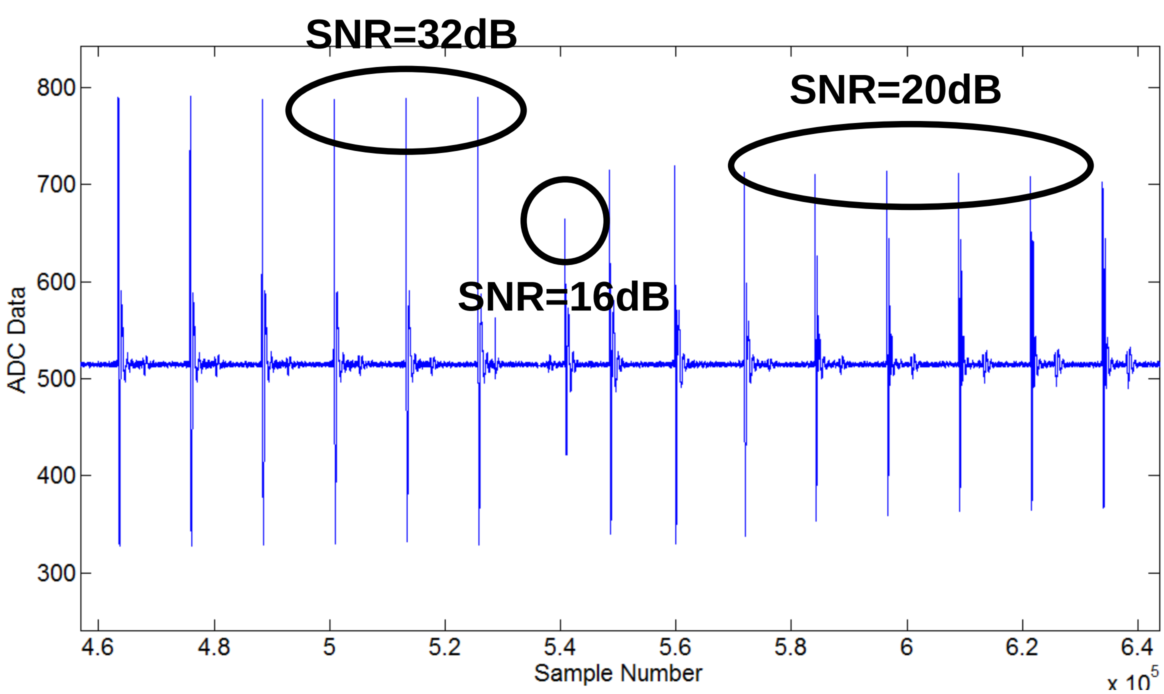

Figure 9-14: Raw UWB signal after the ADC where various UWB pulse peak heights can be seen to illustrate variations in the SNR of the received UWB signal.

140 s time period is shown in Figure 9-16. The tag is kept in a static location over this time period. The SNRs of the five base stations vary between 25-38 dB but illustrate a strong link between the tag and the five base stations. The SNR of the UWB signal is used in NLOS detection and mitigation as discussed in Chapter 10.

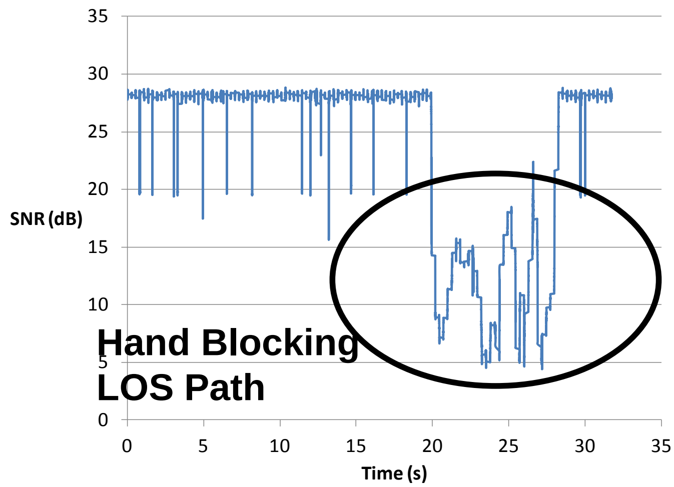

Figure 9-15: The SNR received at a UWB receiver over a 30 s period where hand blocking occurs between 20-30 s. This hand blocking reduces the LOS UWB pulse and consequently the SNR drops from 28 dB to between 6-15 dB.

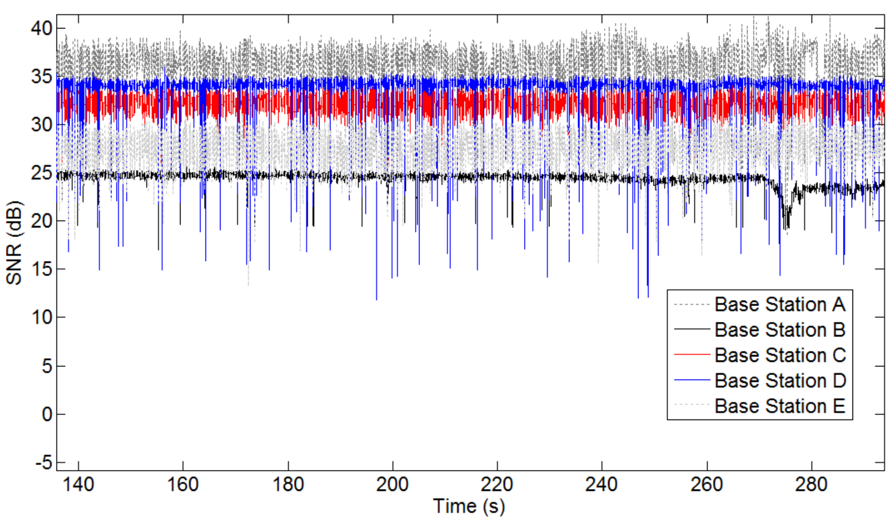

Figure 9-16: The SNR for five base stations (A, B, C, D, E) for a static scenario where the tag is kept in a static location. The SNRs of the base stations vary between 25-38 dB but illustrate a strong UWB link between the tag and the five base stations.

9.6 Effects of Low Signal-to-Noise Ratios on Leading-Edge Detection

As discussed in Section 6.3.3, Section 6.5, Section 9.8, and [93], the deterioration of the SNR of the received UWB pulse can have significant effects in the operation of the leading-edge detection algorithm. Since a ratio of 1/4th is used in detecting the UWB pulse leading-edge, when the SNR drops to below 6 dB, the leading-edge detection algorithm begins to detect noise instead of the actual pulse leading-edge. This is clearly illustrated in Figure 9-17 where in a simulated scenario as the SNR of the received UWB signal drops below 6 dB, the leading-edge detection ranging error increases from around 1 mm to almost 1000 mm. Therefore, an SNR below 12 dB indicates potential NLOS conditions where larger errors in leading-edge detection ranging can occur. This LOS/NLOS detection scheme is outlined in more detail in Chapter 10.

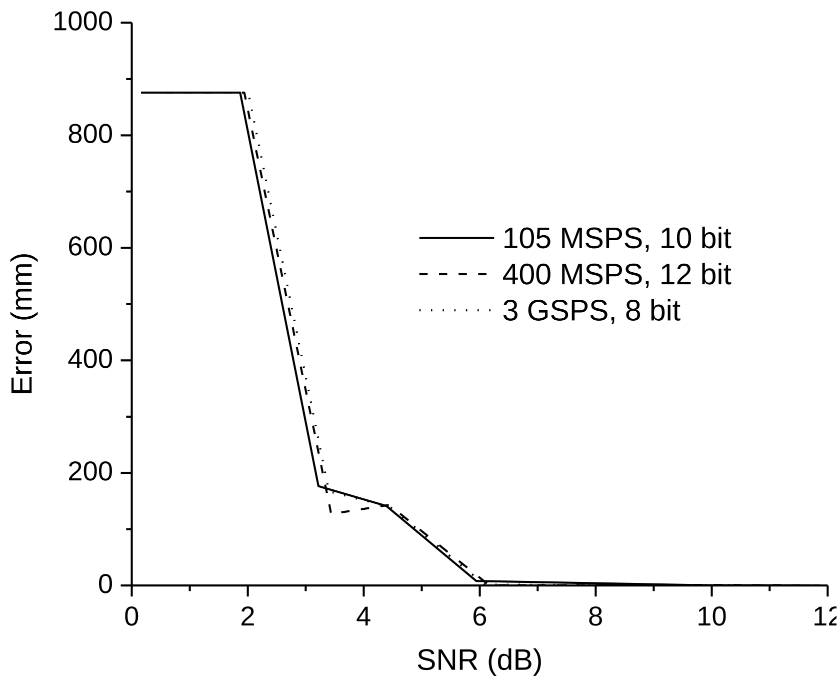

Figure 9-17: Simulated leading-edge detection 1-D error vs. SNR of received UWB pulse for three ADCs.

9.7 UWB Control Station Processing

The UWB control station FPGA calculates the range differences (in digital samples) between the reference base station A and the other base stations (B, C, and D for four base station experiments and B, C, D, and E for five base station experiments). The range difference calculations are relative to base station A. The results are sent via an RS-232 serial port connection to the computer for further processing. The complete process of digital data passing from the base station FPGAs to the control station FPGA to the computer is outlined in Figure 9-18. The base station FPGAs provide two-channel support. Three base station FPGAs support up to six operational UWB base stations. A confirmed leading-edge detection is sent to the control station FPGA as a digital zero-to-one transition. Peak and noise values for the UWB received signals are also sent to the control station FPGA. The control station FPGA broadcasts the current tag ID to the base station FPGAs. This allows UWB peak values to be stored individually for each tag currently connected to the UWB positioning system. The time differences, the tag ID, and the peak and noise values are transmitted via RS-232 to the computer through the Perle RS-232 to Ethernet converter. The Perle RS-232 to Ethernet converter is needed to support data rates higher than 115,200 baud for the control station-computer RS-232 link. The Spartan 3E evaluation board has a Maxim MAX3232 RS232 voltage translator chip. This chip supports data rates of up to 460,800 baud. With the Perle RS-232 to Ethernet converter, data rates of up to 460,800 can be realized at the computer. Figure 9-19 shows the main window of the UWB C++ software application. Different modes can be selected depending on whether 4 or 5 base stations are connected and whether or not SNR information is desired. The UWB real-time C++ software is outlined in more detail in Chapter 7.

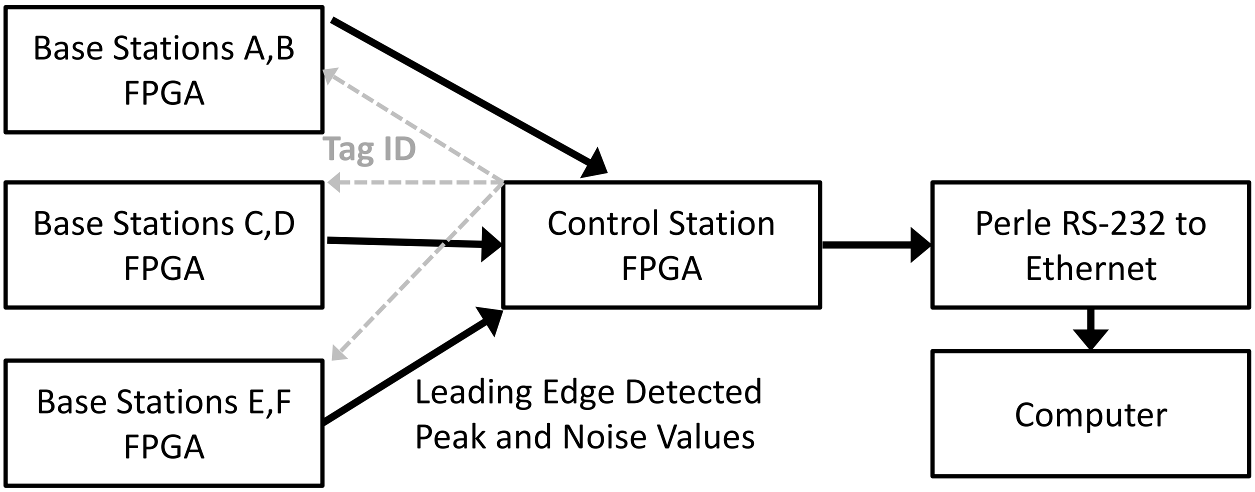

Figure 9-18: Block diagram of complete digital processing system which includes three 2-channel base station FPGAs which communicate with the control station FPGA when a leading-edge is detected for either channel. The data is transmitted from the control station FPGA through a Perle RS-232 to Ethernet converter to the computer.

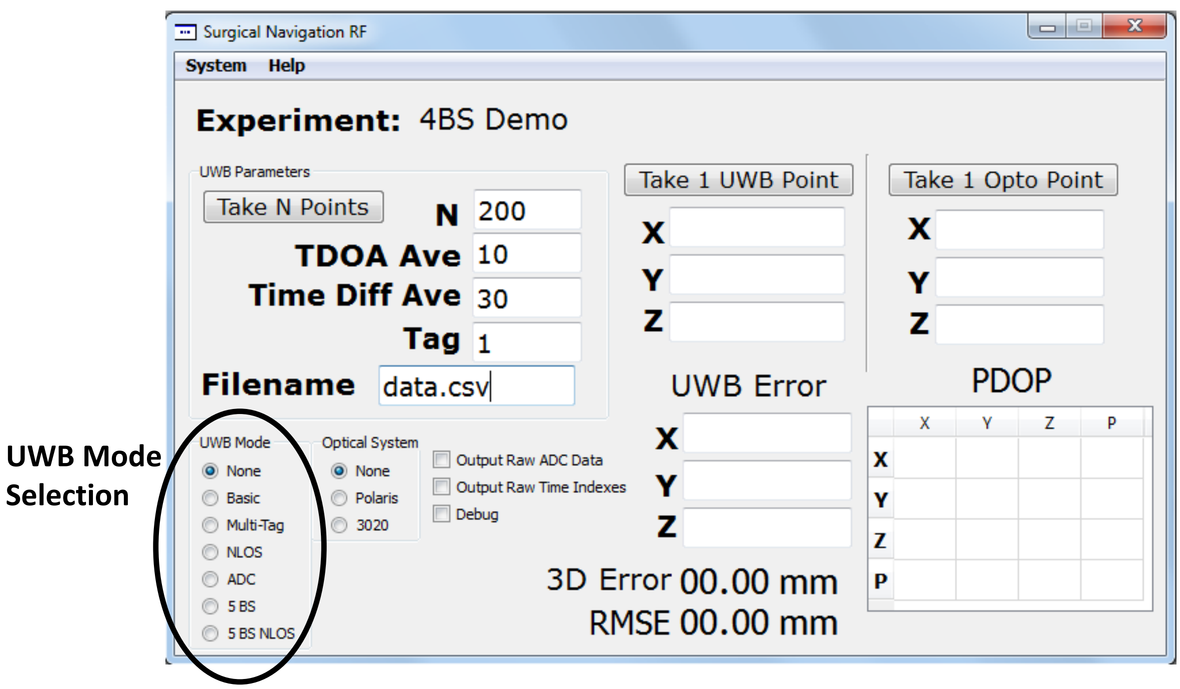

Figure 9-19: UWB mode selection in the C++ software can be used to switch between 4 base stations and 5 base stations as well as whether or not peak and noise values are transmitted to the computer (NLOS modes include peak and noise values, Multi-Tag and 5 BS do not).

9.8 Adaptive Leading-Edge Detection for Low SNR and NLOS Environments

The adaptive leading-edge detection algorithm builds off of Merkl's max-ratio leading-edge detection algorithm, which is outlined in Section 5.2.6. The adaptive portion of this algorithm builds off the basic algorithm defined in Section 5.2.6 (Algorithm 1).

Algorithm 3: Adaptive Leading-Edge Detection

Results from the basic leading-edge detection algorithm are shown in Figure 6-24 for three different ADCs versus signal-to-noise ratio in an industrial LOS environment defined by the IEEE 802.15.4a channel model with $\alpha = 2$. As shown in Figure 6-24, the basic leading-edge detection algorithm fails for $\mathrm{SNR} < 6dB$. Conversely, for $\mathrm{SNR} > 6dB$, sub-mm accuracy is achieved with the algorithm functioning properly.

$$\mathrm{r_{SNR}} = \frac{\sigma_{\mathrm{V\_pulse}}}{\sigma_{\mathrm{V\_noise}}} = 10^{\frac{\mathrm{SNR}}{20}} \tag{9-3}$$

where $\sigma_{\mathrm{V\_pulse}}$ is the standard deviation of the UWB pulse portion of the received signal in Volts and $\sigma_{\mathrm{V\_noise}}$ is the standard deviation of the noise in Volts. Instead of solving for (9-3), $\mathrm{r_{SNR}}$ can be approximated by

$$\mathrm{r_{SNR}} \cong \frac{\mathrm{max}\_n_2\_pulse[t]}{n_{noise}} \tag{9-4}$$

where $\mathrm{max}\_n_2\_pulse[t]$ is the maximum value of the larger moving window as it traverses over the UWB pulse and n_{noise} is the maximum value obtained when sampling the UWB signal during the 2nd half of the 10 MHz clock cycle [93]. A SNR of 6dB corresponds to $\mathrm{r_{SNR}} = 2$. Since $\alpha = 2$, it can be seen that the algorithm fails when $\mathrm{r_{SNR}} \leq \alpha$. When the received signal goes below this threshold, the comparator operation performed in (5-6) fails since $\max\_n_1[t] * \alpha$ could return values greater than $\max\_n_2[t]$ even when detecting noise rather than an UWB pulse even if $\max\_n_2[t]$ is greater than the noise threshold $thresh$. The additional adaptive steps needed for low SNR and NLOS situations are outlined in Steps 1-3.

1. The adaptive portion of the algorithm is added by including an additional check

$$if\ (\mathrm{r_{SNR}} \leq \alpha)\ then\ \hat{y}[t] = h[t] \otimes g[t] \tag{9-5}$$

   where $g[t]$ is the template signal shown in Figure 9-20 and $\otimes$ denotes the convolution operator. The new match filtered signal $\hat{y}[t]$ is then run through the original leading-edge detection algorithm outlined in Section 5.2.6.

2. Besides detecting low SNR conditions, NLOS conditions must also be detected since, as shown in Figure 9-21, the received signals have a much lower slew rate, which causes ambiguity in detecting the leading-edge of the incoming signal. The slew rate can be estimated using a window around the leading-edge estimate

$$r_{slew} \cong \max\_n_1[t+30] - \max\_n_1[t-30] \tag{9-6}$$

   where the slope over 61 samples of the max window $\max\_n_1[t]$ is used in estimating the slew rate.

3. As shown in Figure 9-21, another concern in NLOS conditions is the presence of strong multipath components shifted a significant distance in time from the weaker LOS signal. A 2nd check is needed when determining whether or not the received signal is NLOS,

σ_{LE}, which represents the standard deviation in the leading-edge time sample value over the previous five received pulses. Combining Step 2 with σ_{LE} gives

$$if\ (\ r_{slew} \leq \beta)\ OR\ (\sigma_{LE} \geq \gamma)\ \ First\_detect\ \ and\ \ NLOS = true \tag{9-7}$$

where β and γ are empirically derived thresholds and $First\_detect$ is a simplified algorithm where the first detectable sample in $y[t]$ above $thresh$ is considered the leading-edge. $First\_detect$ is only run in NLOS situations. Additionally, the fact that the received signal is NLOS can be sent to the computer and either discarded or used in the final TDOA algorithm similar to [223] where realistic error models for NLOS received signals were used in a global maximum likelihood scheme for the ranging estimates in the final TDOA calculation.

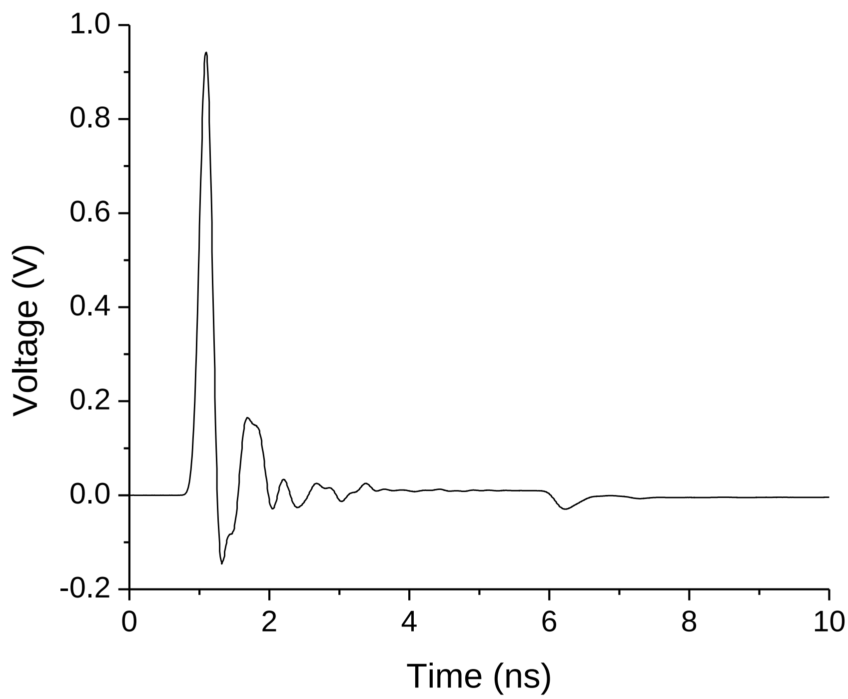

Figure 9-20: Simulated baseband UWB Gaussian pulse used as a template signal for the matched filter outlined in Step 1.

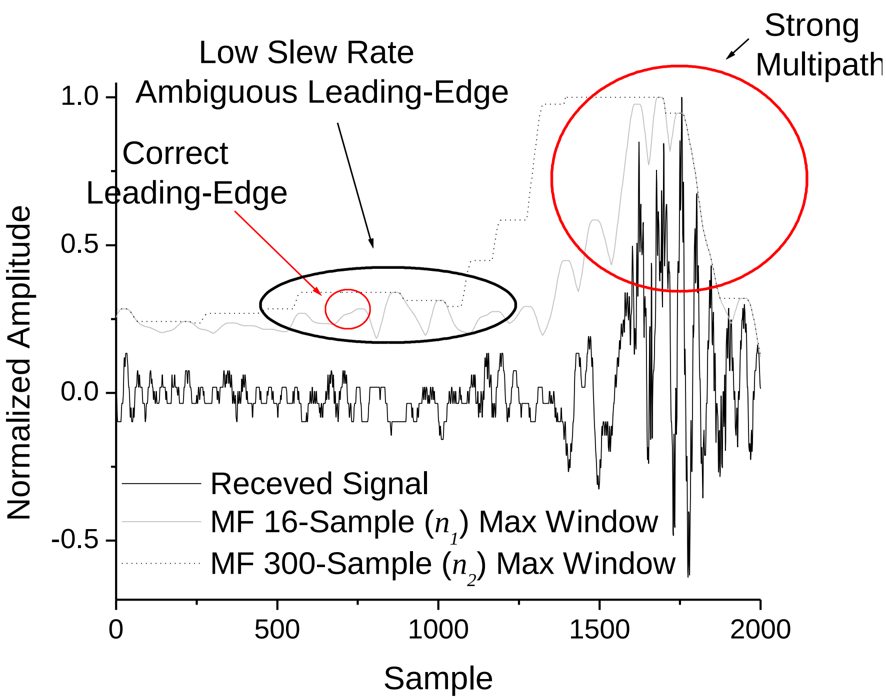

Figure 9-21: Simulated UWB received signal using the UWB IEEE 802.15.4a residential NLOS channel. The low slew rate of the NLOS leading-edge is highlighted as well as the strong multipath interference which arrives almost 1000 samples after the original weak LOS signal.

9.8.1 Simulation Results

The simulation framework outlined in Chapter 6 was used to test the adaptive scheme in comparison to the basic leading-edge detection algorithm. The entire UWB positioning system is simulated including the analog portions of the Tx and Rx in ADS, the UWB channel in Matlab (IEEE 802.15.4a to simulate different environments), and the sub-sampling mixer in Agilent ADS. The signal is first converted to digital by a 10 bit, 105 MSPS ADC. Next, the signal is sent to the FPGA where the leading-edge algorithm is run. The final processing is done on a computer to run the TDOA algorithm. Figure 9-22 shows an example received signal sent through an industrial LOS channel with the Tx-Rx 3 m apart. Significant noise and multipath mask the LOS pulse causing a SNR = -2.61dB. Figure 9-23 shows the same signal after (5-3) with max_$n_1[t]$ and max_$n_2[t]$ overlayed. Since $r_{SNR} < \alpha$, noise is detected rather than the UWB pulse leading-edge. Figure 9-24 shows the same signal after (5-3) with the application of the MF in (9-5) overlayed by max_$n_1[t]$ and max_$n_2[t]$. The new SNR = 4.11dB and is detectable by the leading-edge algorithm since the MF significantly reduces the noise in the signal allowing correct detection of the leading-edge. Figure 9-25 shows SNR versus Tx-Rx distance for the industrial LOS environment where the addition of a MF increases the SNR by an average of 5.82dB. Conversely, as shown in Figure 9-26, in high SNR situations, such as the residential LOS environment with the Tx-Rx separated by 2 m, the addition of a MF reduces the SNR by 3.3dB, showing the need for a MF only in low SNR situations. 20 instantiations of the commercial and industrial LOS IEEE 802.15.4a channels were tested with a Tx-Rx distance of 2-8 m. An average SNR increase of 5.42dB and 3.42dB was obtained with application of a MF for the industrial and commercial LOS channels. In NLOS situations, the use of $First\_detect$ applied to five instantiations of the residential, commercial, and industrial NLOS channels with Tx-Rx distances of 1-5 m yielded on average 1-D ranging accuracy of 12.5 mm, 19 mm, and 29.5 mm compared to an average of 350 mm, 31 mm, and 225 mm for the normal leading-edge algorithm.

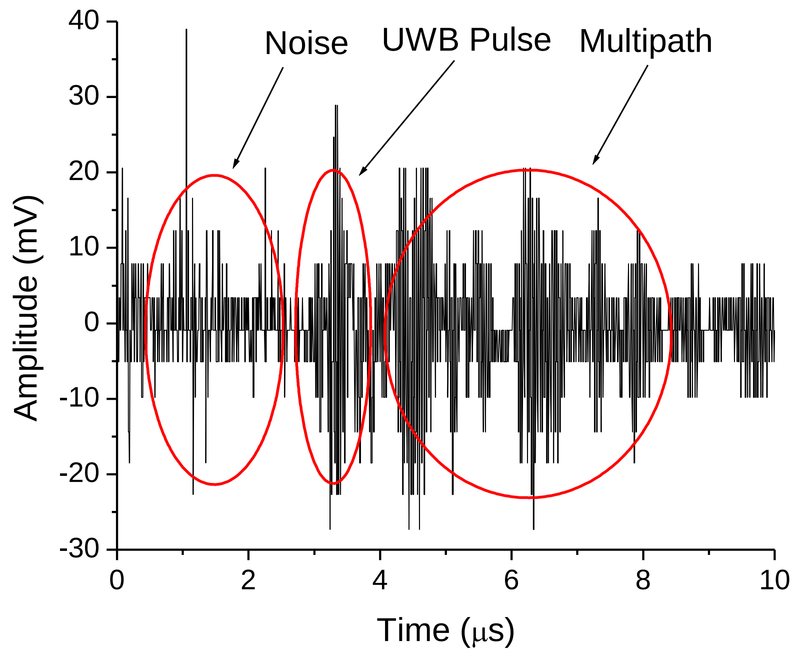

Figure 9-22: Simulated UWB time-extended signal where the Tx-Rx are 3 m apart in an industrial LOS environment defined by the IEEE 802.15.4a channel model and no automatic gain control is used in the UWB receiver creating a weak signal. Electrical noise, multipath interference, and quantization noise are observed. SNR = -2.61dB.

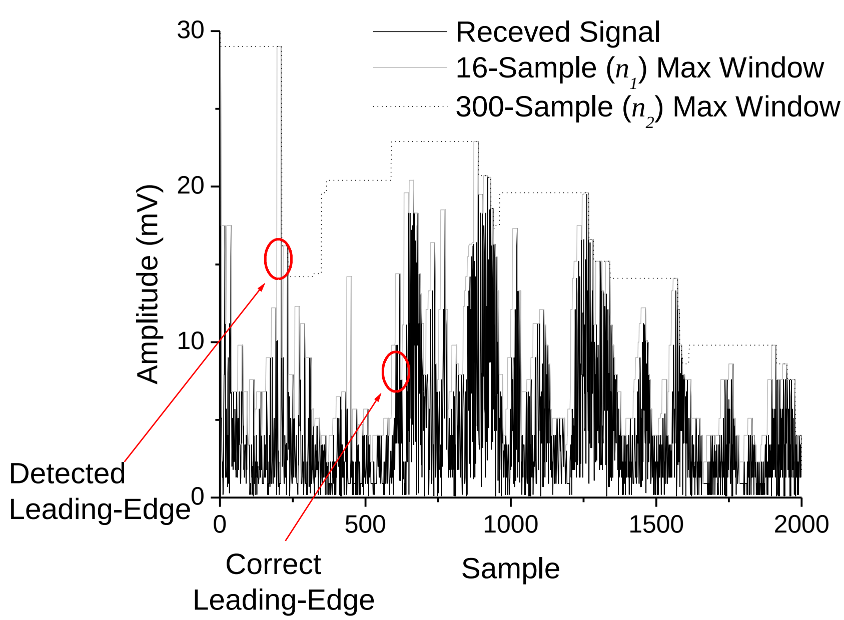

Figure 9-23: Simulated UWB received signal from Figure 9-22 where the basic leading-edge algorithm is run with $\alpha = 2, n_1 = 16, n_2 = 300$. Since the SNR = -2.61dB, the leading-edge algorithm incorrectly detects the noise at the beginning of the signal (sample 11) rather than the correct UWB leading-edge (sample 595).

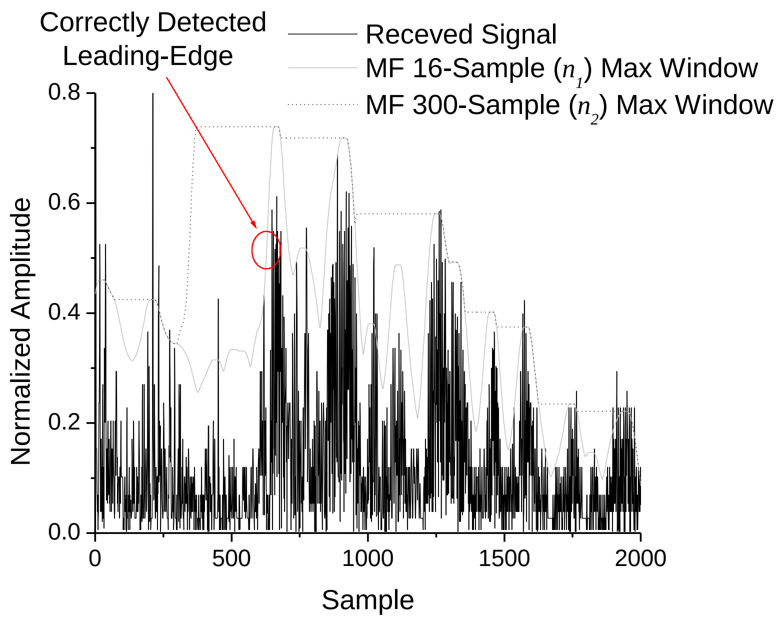

Figure 9-24: Simulated UWB received signal from Figure 9-22 where the adaptive leading-edge algorithm is run with $\alpha = 2, n_1 = 16, n_2 = 300$, and the template shown in Figure 9-20. Since the new SNR = 4.11dB after applying a matched filter, the adaptive algorithm has no problem locating the correct UWB leading-edge (sample 595).

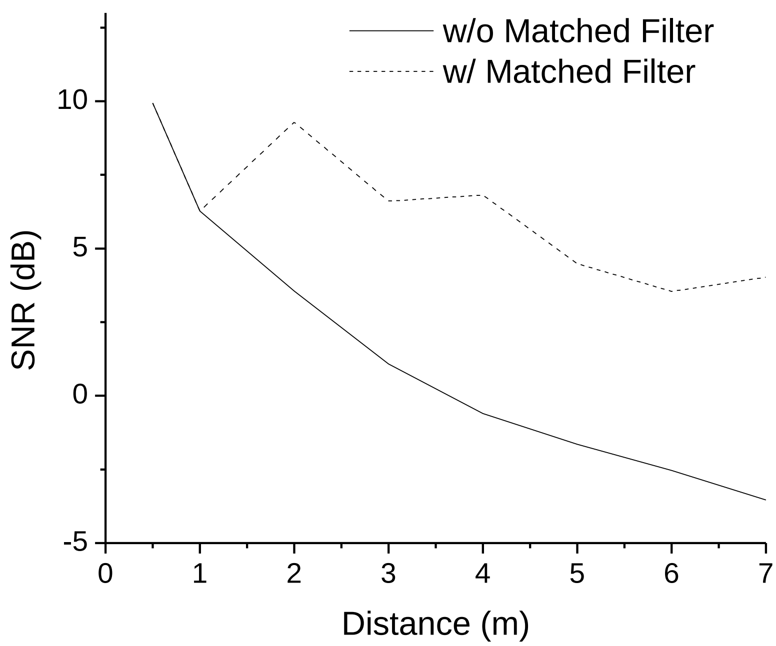

Figure 9-25: SNR versus Tx-Rx distance for standard leading-edge algorithm versus adaptive leading-edge algorithm. The UWB channel environment is the IEEE 802.15.4a industrial LOS channel. On average the addition of a MF increases the SNR by 5.82dB in low SNR conditions (when original signal $y[t]$ has SNR below 6dB).

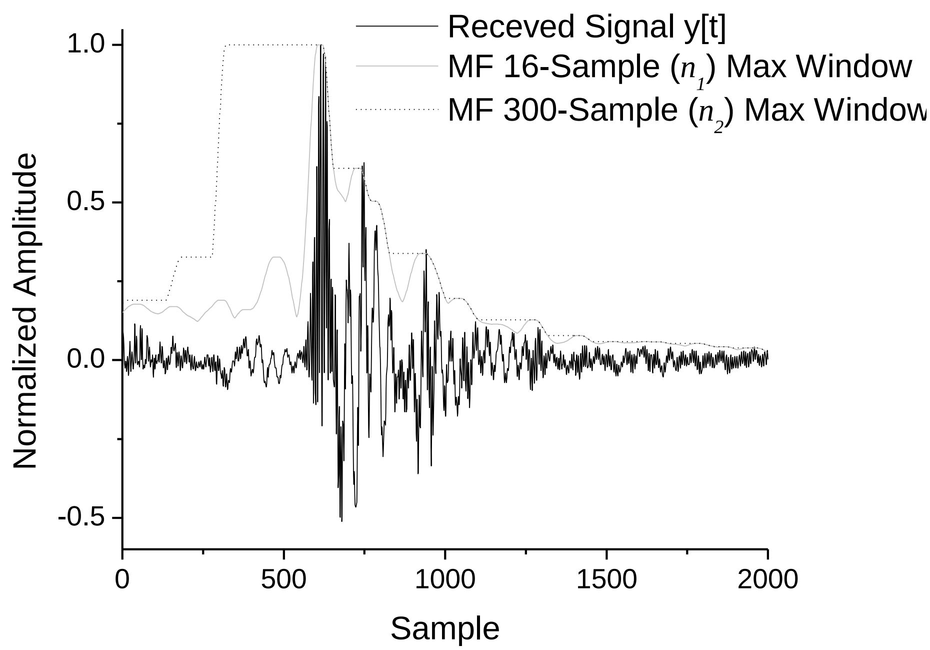

Figure 9-26: Simulated UWB received signal using the UWB IEEE 802.15.4a residential LOS channel with Tx-Rx distance of 2 m. The SNR of $y[t]$ is 17.7dB. After applying a MF, the SNR drops to 14.4dB.

10. Non-Line-of-Sight Detection and Mitigation for High Accuracy Indoor UWB Localization

The quality of the wireless link between the tag and the base station plays a key role in the quality of the positioning data. This is true for all wireless positioning systems which use time-of-flight information to estimate ranges and ultimately perform 2-D or 3-D positioning. For example, redundant GPS satellites (more than the minimum number of four) are always visible at any point within the United States and most locations around the world. Ten or more GPS satellites can be visible at any one location on the earth. This provides a high level of redundancy in case one or more of the links are attenuated, partially blocked, or fully blocked. Partially blocked wireless signals can be reflected off of metal structures while attenuated wireless signals transmit directly through a lossy medium en-route to the final destination. In order to achieve ranging accuracy of five millimeters, accurate timing resolution of better than 20 picoseconds is required. This difficult requirement of 20 picoseconds creates a pronounced need for wireless links between the tag and base stations which are of high quality throughout the volume of interest. The real-time detection of poor link quality and NLOS conditions is outlined in this chapter. FPGA digital signal processing combined with real-time detection and mitigation algorithms implemented in software is required to detect and mitigate the effects of poor link quality and, in the worst case scenario, NLOS conditions.

10.1 Overview

The detection and mitigation of NLOS conditions for the high accuracy UWB indoor positioning system outlined in Chapter 7 is a difficult problem which requires a system-level approach and real-time operation to provide successful operation in dynamic scenarios. The detection of poor link quality and NLOS conditions is first outlined. This occurs both at the FPGA-level and also within the C++ software application. The mitigation of the effects of poor link quality and NLOS conditions must also be implemented at the system-level – both on digital hardware and in the real-time software application. Experiments are run to analyze the LOS versus NLOS wireless link behavior within the high accuracy UWB indoor positioning system. A mitigation strategy is introduced which relies on both peak detection and leading-edge detection ranging algorithms and utilizing the link SNR.

10.2 Experimental Setup

The experimental setup used in analyzing the UWB wireless link for LOS versus NLOS is shown in Figure 10-1. Partial (30-40%) and almost full blockage (95%) is introduced in the UWB wireless link path between the transmitter and base station. This is done by placing persons within the LOS link path for partial blockage and cupping the receive antenna at close range for near full blockage. Near full blockage corresponds to the low SNRs observed in Section 10.3 and 10.4. Figure 10-4 outlines the C++ software application where real-time tag information is displayed and recorded along with link information (LOS/NLOS) and link SNR. This setup is used in the experimental analysis outlined in Sections 10.3 and 10.4.

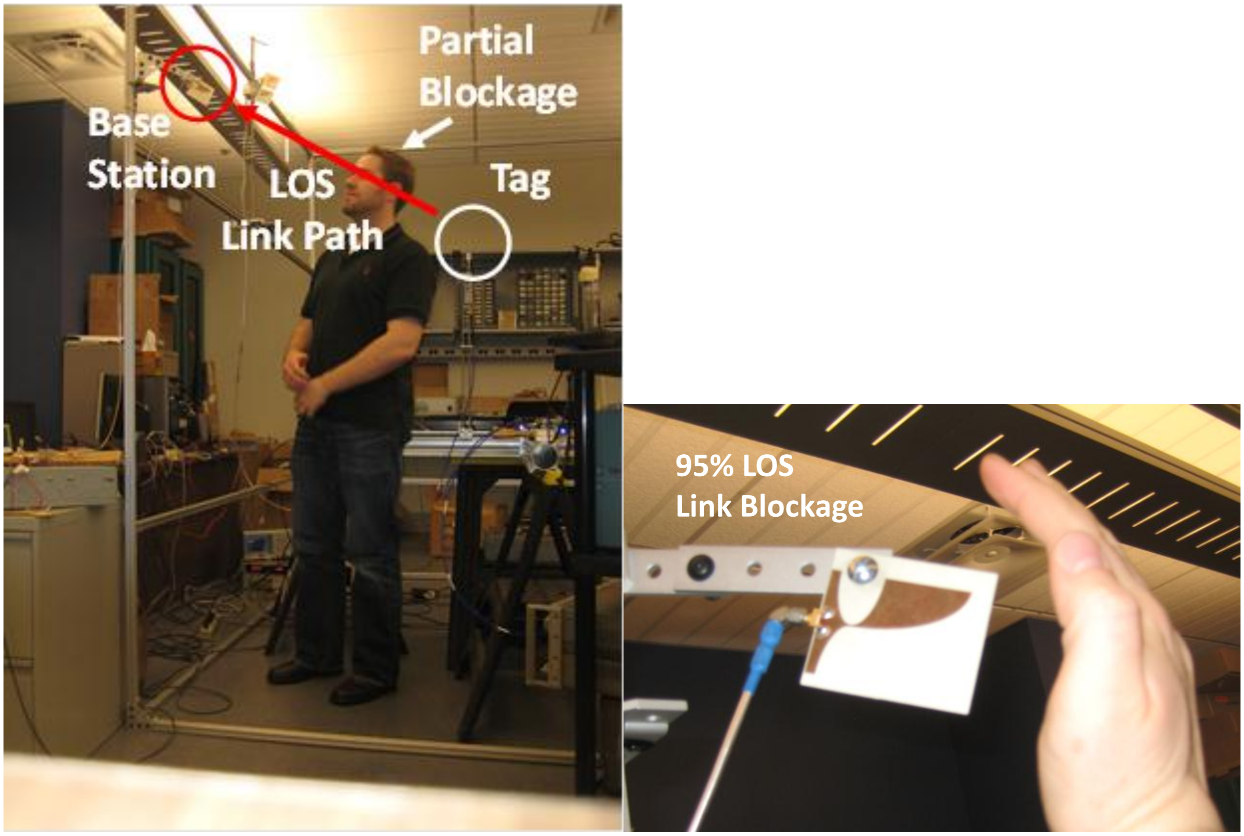

(a) (b)

Figure 10-1: Experimental setup where partial blockage is introduced in the LOS link path: (a) 30-40% blockage, (b) 95% blockage.

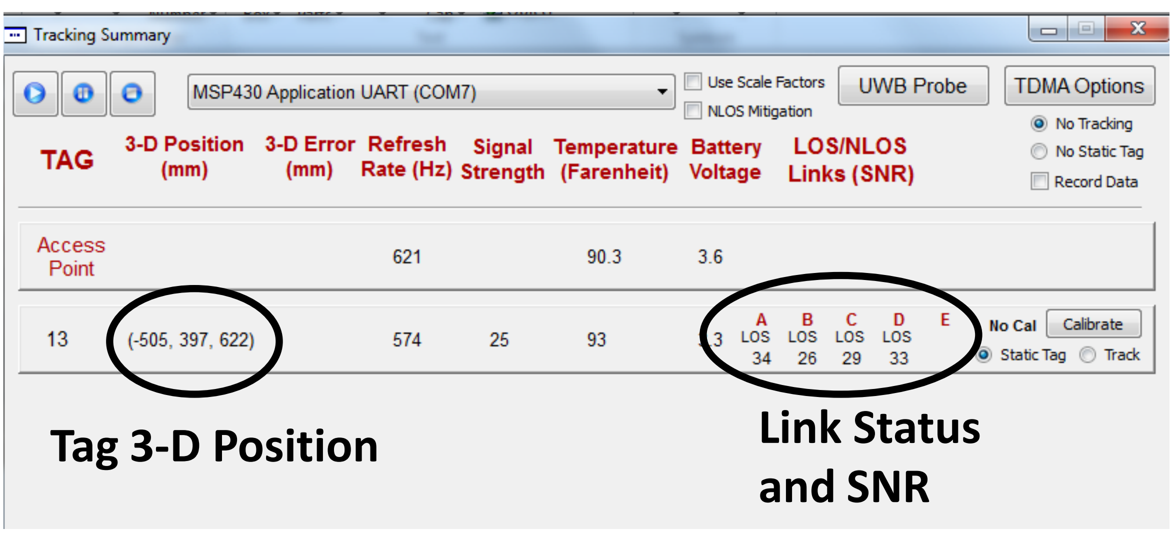

Figure 10-2: Software application where 3-D tag position and base station link status (LOS versus NLOS) and base station SNR are displayed and output to a CSV file in real-time.

10.3 Detection

The initial detection of NLOS conditions has to be done in real-time on dedicated digital hardware. The first measurement which provides the bulk of the information on whether or not an NLOS link exists is the signal-to-noise ratio. The FPGA-implemented SNR calculation algorithm is outlined in Section 9.5. The SNR of the received UWB signal as seen by the FPGA is defined as follows

$$SNR = 20\ \log_{10}\left(\frac{Voltage\ Peak\ Val}{Voltage\ Noise\ Val}\right) \tag{10-1}$$

where the voltage peak value and the voltage noise value of the received UWB signal is measured in digital samples after passing through the ADC. Figure 10-3 shows the received UWB signal after taking the signal absolute value and passing the signal through a 16-sample averaging filter. This signal is typical of a strong received UWB pulse where the transmitter and receiver. The peak value in digital samples is 285 while the noise floor is 8. This corresponds to a SNR of 40 dB using (10-1). In practical operation, the SNR at each link for a strong UWB pulse typically lies between 20-40 dB. As the SNR degrades below 20 dB and approaches 10 dB and below, the leading-edge detection will fail as it is trying to locate the leading-edge at 1/4th the amplitude of the peak of the received UWB signal which lies below the noise floor of the received signal. Wireless signal propagation conditions which cause the SNR to degrade to 10 dB and below are typically caused by partial or close to complete blockage of the path between the transmitted wireless signal and the base station receiver.

Figure 10-4 shows the raw peak values for a transmitter-base station wireless link. The typical values around 70 digital samples (150 mV) are indicative of a strong link where the UWB pulse signal is received consistently. The three dips illustrate a human hand moving towards and away from the base station antenna to cause partial blockage up to 95% blockage. Figure 10-5 shows the corresponding SNR for the received UWB pulse signal shown in Figure 10-4. The SNR for a strong LOS link is typically 25-27 dB. When partial to 95% blockage occurs, the SNR is reduced to less than 5 dB. As shown in Figure 10-6, the quick degradation of the SNR causes large ranging errors for the FPGA-implemented leading-edge detection algorithm outlined in Section 9.3 of up to 2 m. Figure 10-7 shows the leading-edge ranging error versus SNR. As the SNR drops below 10-12 dB, the leading-edge algorithm fails to locate the UWB pulse resulting in large errors. Given the relationship between received signal SNR and the

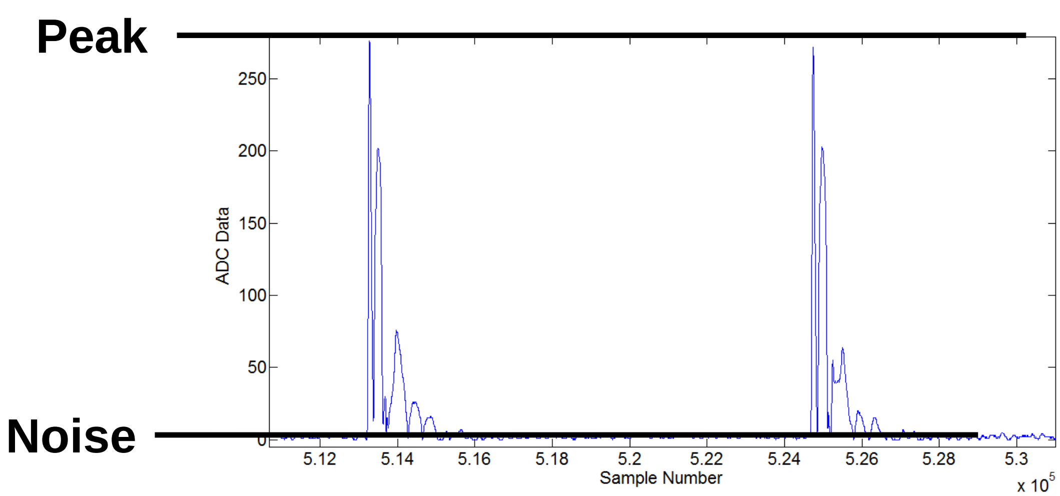

Figure 10-3: Typical received UWB pulse after taking the absolute value of the raw signal and passing it through a 16-sample averaging filter. The amplitude between the peak of the UWB signal and the noise floor is shown to highlight the high SNR's which can typically be achieved when operating with LOS links.

performance of the leading-edge detection algorithm, an SNR threshold of 12 dB is used to detect LOS versus NLOS link conditions.

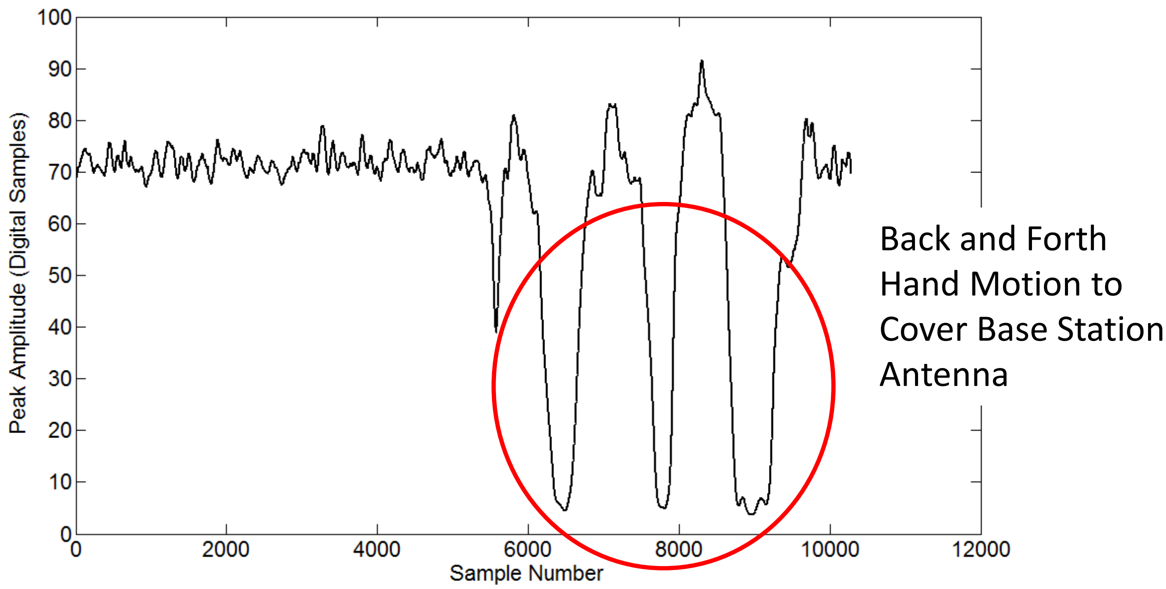

Figure 10-4: Experimental data measuring the peak of the UWB pulses in digital samples. The peak value decreases rapidly as a human hand approaches and almost completely covers the antenna. The quick reduction in link quality is easily measured by measuring the UWB pulse peak values.

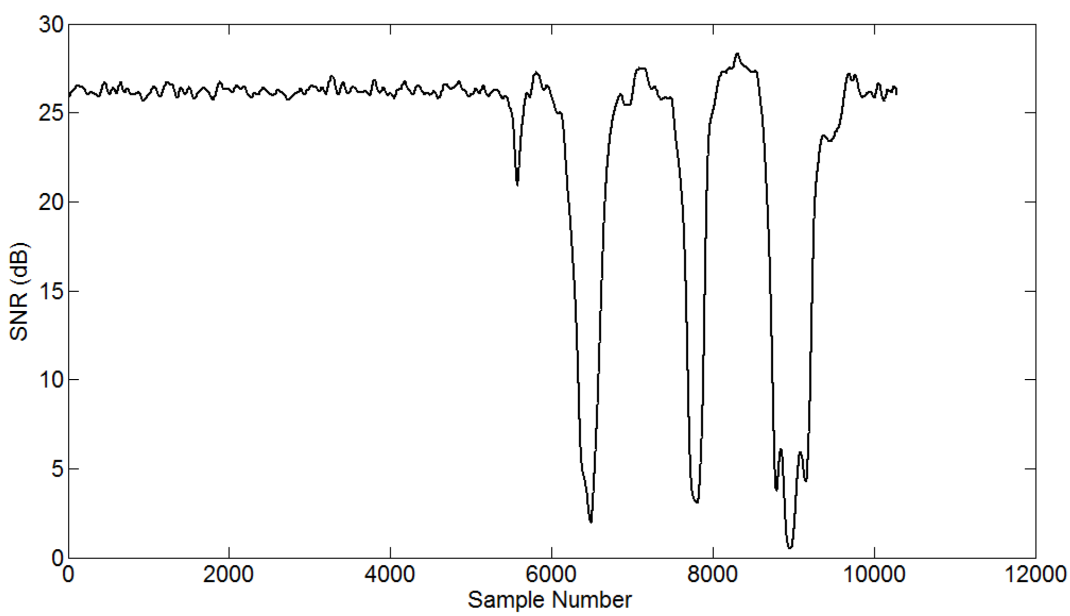

Figure 10-5: The received UWB pulse signal from Figure 10-4 expressed as SNR in dB.

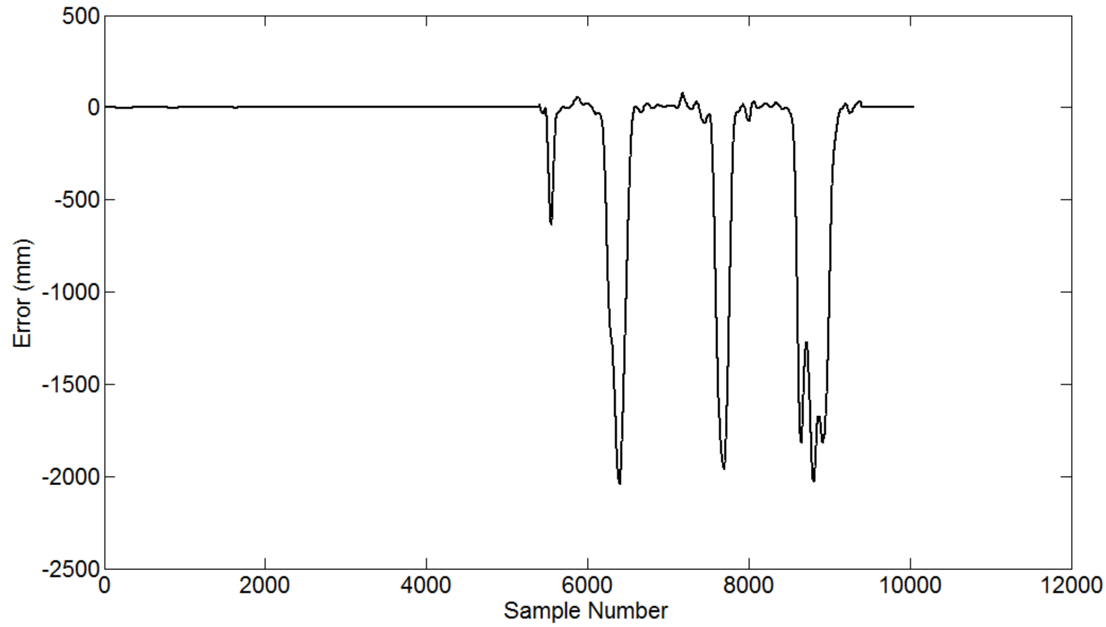

Figure 10-6: Range difference corresponding to the UWB base station where the NLOS blockage occurred. Extremely large ranging errors are observed on the order of two meters.

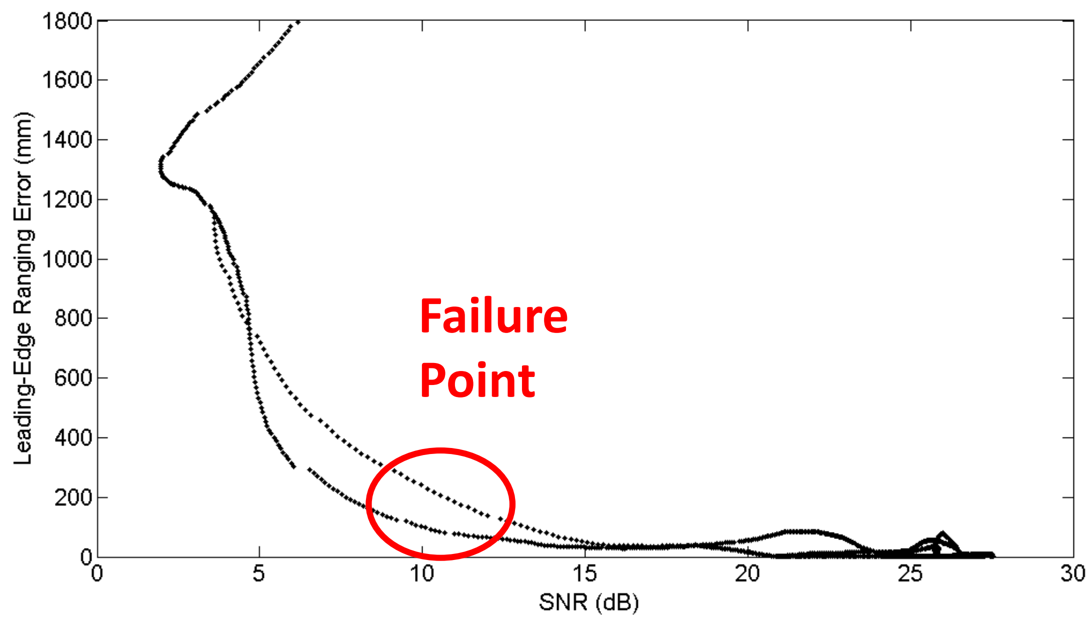

Figure 10-7: Leading-edge algorithm ranging error for one base station versus SNR from the experimental results outlined in Figure 10-5 and Figure 10-6. The leading-edge detection algorithm fails around when the SNR reaches 10-12 dB. At this signal level, the leading-edge (1/4th peak amplitude) will often drop below the noise floor, resulting in large ranging errors (1000 mm or greater).

10.4 Mitigation

As discussed in Section 10.3, the leading-edge detection algorithm will routinely fail for SNR values of less than 12 dB. The first step in dealing with NLOS conditions is detecting when they happen. The next step in providing robust indoor UWB positioning in such conditions is to mitigate the ranging errors once NLOS conditions have been detected. Since the leading-edge algorithm fails below 12 dB, FPGA-implemented peak detection, outlined in Section 9.3, provides a better ranging technique since the UWB peak can still be located for a SNR above zero. Figure 10-8 outlines the sequence of states for NLOS detection and mitigation which includes NLOS detection (SNR < 12 dB), switching of the ranging algorithm to peak detection, and, as a last resort, elimination of this base station from the tag TDOA calculation. If the UWB link improves (SNR increases above 12 dB), leading-edge detection is re-enabled. Figure 10-9 shows the SNR for an experiments similar to that done for leading-edge detection in Section 10.3 where a tag is left in a static location and LOS blockage is introduced dynamically between the tag and one of the base stations. This results in drops in SNR to below 5 dB as shown in

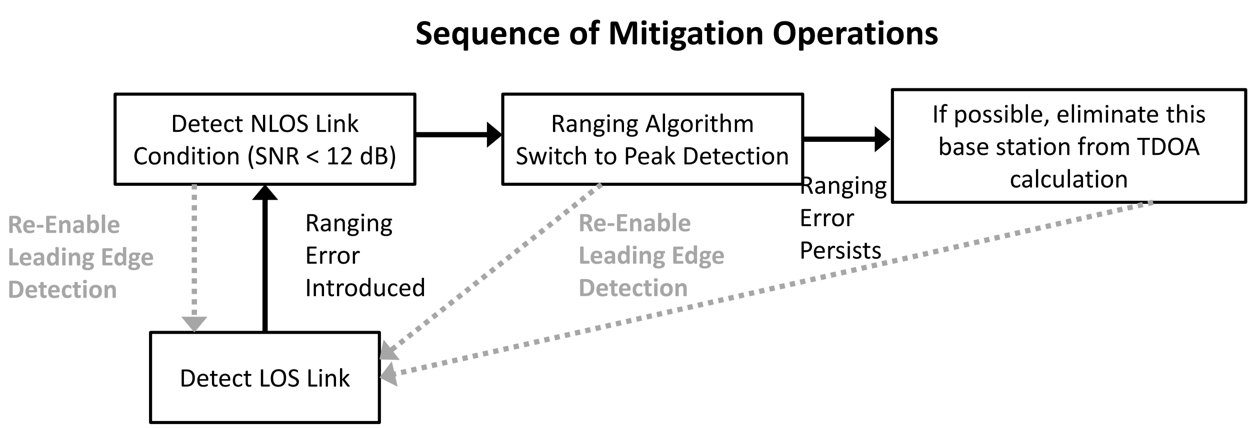

Figure 10-8: Block diagram of NLOS detection and mitigation steps including a return to a LOS link.

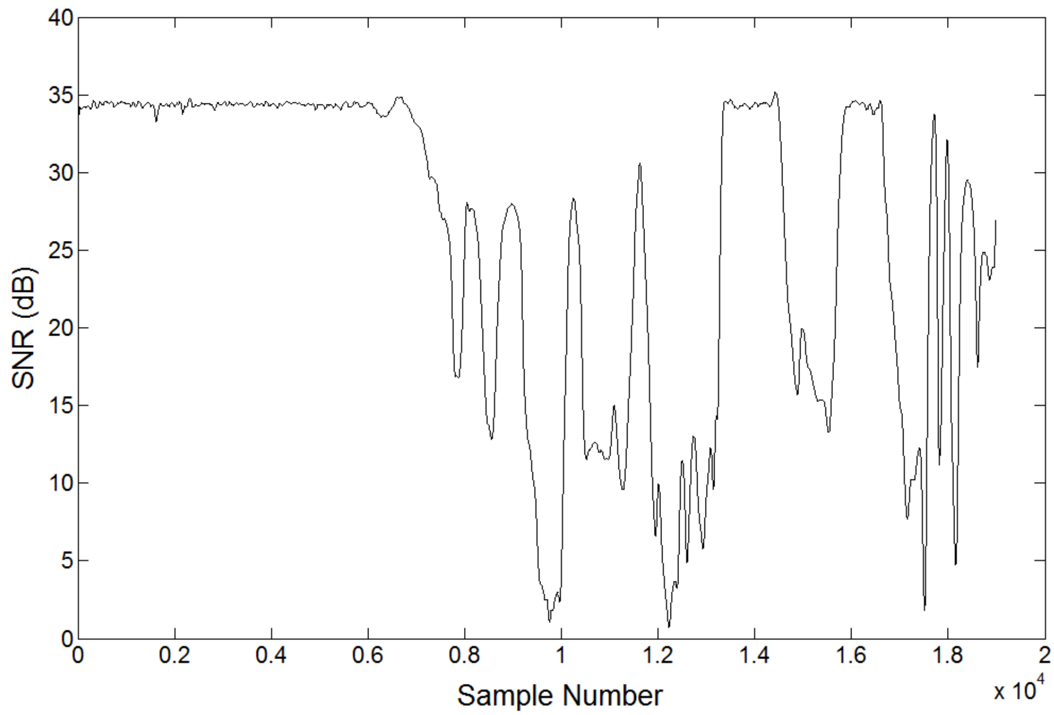

Figure 10-9: SNR for an experiment where a tag is left in a static location and extreme LOS blockage is introduced.

Figure 10-9. The resulting ranging error for peak detection is outlined in Figure 10-10. It can clearly been seen in Figure 10-10 that peak detection is more robust to ranging errors than leading-edge detection as the ranging errors are smaller and less frequent given the low SNR conditions compared to leading-edge detection in Figure 10-6. Figure 10-11 shows the SNR versus peak detection ranging error for the experiment outlined in Figure 10-9 and Figure 10-10. The failure point for peak detection is around 4-5 dB compared to 10-12 dB for leading-edge detection as shown in Figure 10-7. Peak detection only fails when the received UWB pulse peak shrinks to within the noise floor of the received signal.

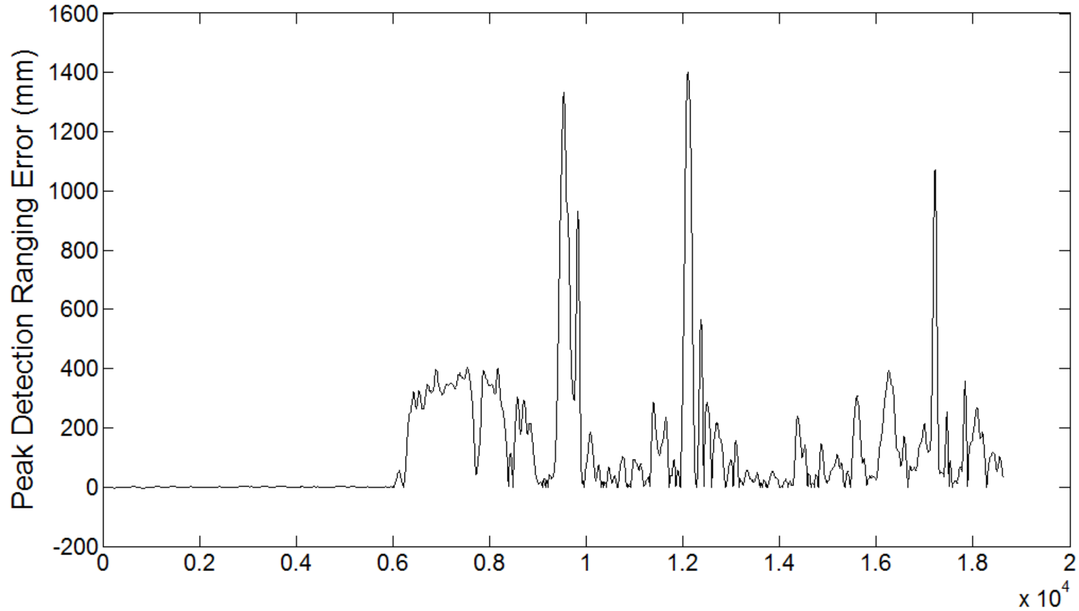

Figure 10-10: Peak detection ranging error for the poor SNR scenario outlined in Figure 10-9.

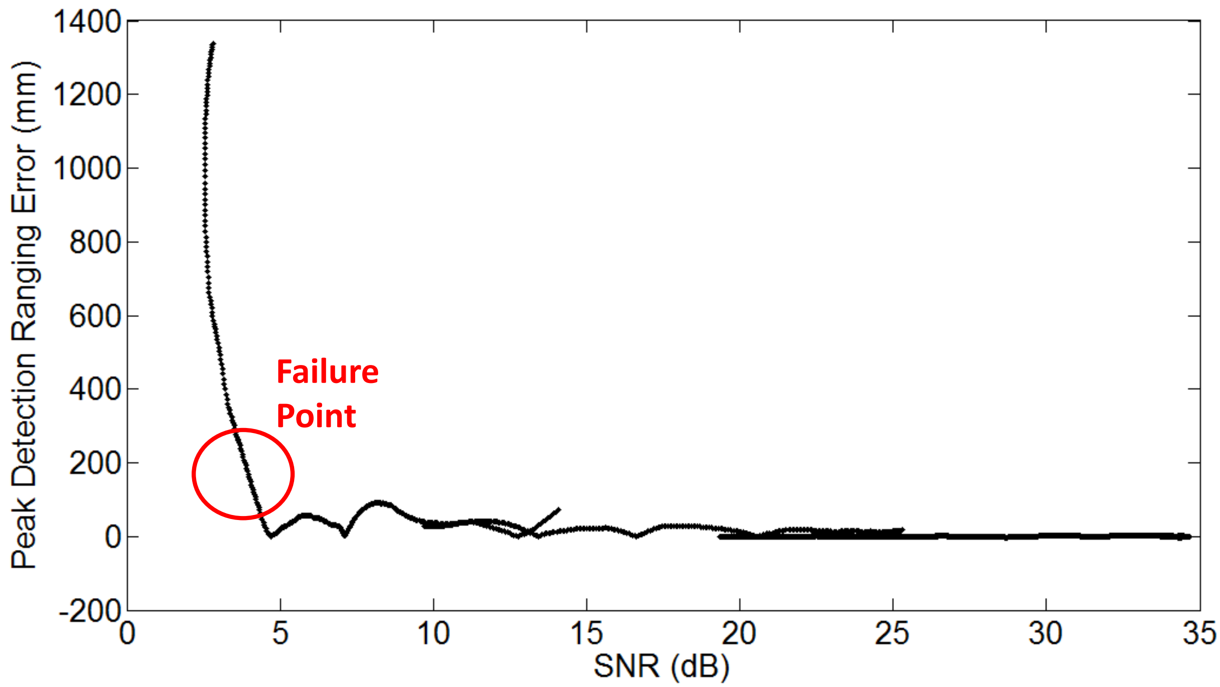

Figure 10-11: Peak detection algorithm ranging error for one base station versus SNR from the experimental results outlined in Figure 10-9 and Figure 10-10. The peak detection algorithm fails when the SNR reaches 4-5 dB. This is a 6-7 dB improvement over the leading-edge detection algorithm as shown in Figure 10-7.

11. Towards Sub-Millimeter Accuracy in UWB Positioning for Medical Environments

Advances in UWB and other enabling technologies has resulted in higher achievable accuracy for wireless sensor networks, which has opened up new applications including smart medical instruments, surgical navigation, and tracking in wireless body-area-networks. To realize the potential of these approaches as transformative technologies, additional research is needed in three main areas: (1) investigation of system-level design concerns and comprehensively quantifying their effects on overall system accuracy (e.g. UWB receiver leading-edge detection algorithms, Tx/Rx system architectures, local oscillator phase noise sensitivity, etc.); (2) realization of novel UWB system architectures through integrated RF front-ends with MIC and MMIC technologies; (3) quantifiable testing of the system performance in realistic hospital environments in terms of dynamic 3-D accuracy using novel, real-time testing platforms.

The potential exists to fundamentally change the achievable accuracy of indoor wireless localization systems to millimeter and sub-millimeter accuracy for an array of new location-aware clinical applications including smart medical instruments, surgical navigation, and wireless body-area-networks. The proposed novel UWB localization techniques have a strong potential to be transformative by overcoming inherent limitations of current RTLS that have been exhaustively investigated and developed into commercial products. Also, comprehensive development and testing platforms for UWB localization systems in clinical settings are needed to optimize these systems for hospital use. The impact of this work will be felt not only by engineers working towards high accuracy UWB localization systems for dense indoor environments in applications such as surgical navigation and location-aware smart sensing medical instruments, but for scientists working in fundamental areas including microwave-based biological sensors and characterization of biological tissues at microwave frequencies. Successful development of high accuracy UWB localization systems would have a direct and significant impact on indoor wireless positioning systems, surgical navigation, wireless bio-sensors, and biological sensing – fields that rely critically on high accuracy localization and accurate detection of changes in dielectric properties at microwave frequencies.

Although these technologies can be scaled and applied to any UWB-available frequency range, it is advantageous to utilize the 3.1-10.6 GHz and 22-29 GHz bands allocated for UWB use by the FCC in 2002. The rationale for using these bands is (1) the 3.1-10.6 GHz band has received enormous interest in designing UWB communication, imaging, and localization systems for a wide array of indoor applications with existing commercial devices and chipsets available and (2) the 22-29 GHz band will have less indoor interference, allow for smaller circuit, chip, and antenna design, provide an attractive testing platform for MMIC technology, and mature MMIC devices are available. The mature technologies available at these frequencies ensure a higher likelihood of success in the commercialization and realization of these systems.

11.1 Challenges in High Accuracy UWB Positioning Systems

Many challenges exist when building an indoor UWB positioning system targeting millimeter or sub-millimeter 3-D dynamic accuracy. This includes the noise and sensitivity of the UWB receiver, antenna phase center variation, time scaling, jitter, and degradation due to overall system calibration. Each of these challenges is discussed with focus on how each affects the UWB positioning system designed at The University of Tennessee.

11.1.1 Noise and Sensitivity at the UWB Receiver

When analyzing the sensitivity of the UWB receiver to AWGN and SNR, the leading-edge detection algorithm implemented on the FPGA must be examined in further detail to understand the overall limitations of the current system in terms of ranging accuracy. As discussed in Chapter 9 and Chapter 10, the leading-edge detection algorithm fails when the UWB pulse peak SNR drops to around 10-12 dB (leaving the leading edge near the noise floor). The general consensus on UWB ranging is that a high SNR is needed for any chance at accurate positioning, placing a restriction on the robustness of the current system to keep SNRs above 10-12 dB. Another limitation of the current system is the dynamic range of the UWB receiver which limits the current operating range of the system to 5 m. Finally, as discussed in Section 4.3.3, the system currently operates from 5.4-10.6 GHz, which makes it *susceptible* to narrowband, high power IEEE 802.11a/n interferers (see Section 4.4) and needs to be addressed at the design level of the proposed advanced positioning system to achieve sub-mm accuracy.

11.1.2 Antenna Phase Center Variation

When attempting to achieve millimeter and sub-mm accuracy, *phase center variation of the antennas* at the Tx/Rx is an important source of error which needs to be taken into account. The transmitter employs a UWB monopole antenna which provides an omni-directional radiation pattern with minimal phase center variation while the receiver utilizes a single element Vivaldi antenna for a radiation pattern directed at the view volume of interest. As shown in Figure 11-1, noticeable variation of the phase center is observed in both the E and H cuts especially for angles greater than ±30°. High accuracy positioning systems must employ calibration techniques to remove the phase center effects. For example, antennas used for GPS systems go through an advanced automated calibration process which uses high precision robots to move the antennas to 6000-8000 distinct points in calibrating out phase center effects.

11.1.3 Time Scaling, Jitter Effects, and System Calibration

More challenges appear in achieving high accuracy real-time indoor positioning when moving to the *system-level*. *Cable length effects* at the UWB receivers must be accounted for and statically calibrated out of the system. *Time scaling effects* due to system clock drift must be characterized and calibrated out of the final TDOA calculations in a dynamic manner when

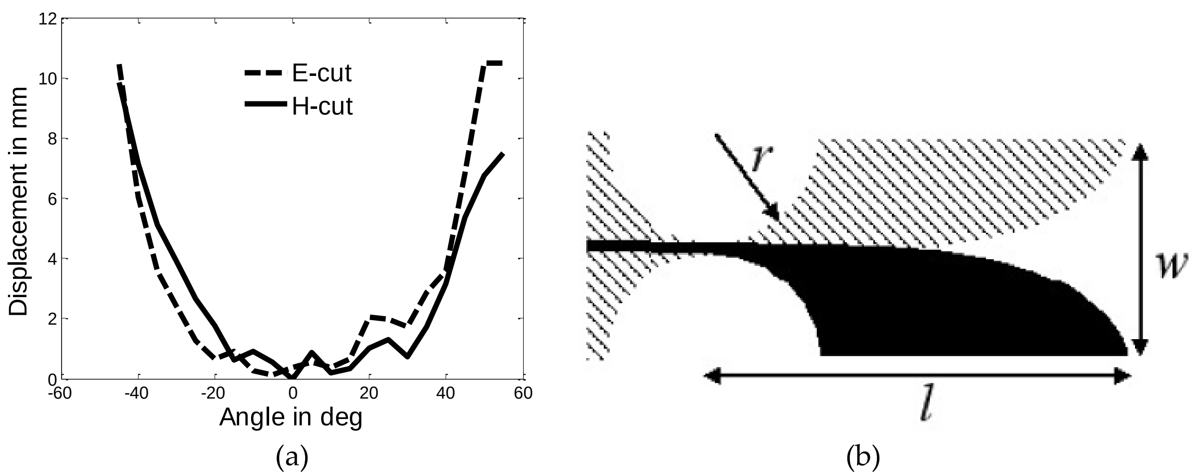

Figure 11-1: (a) Experimentally measured phase center variation of single element Vivaldi antenna in receiving an up-converted UWB pulse (5.4-10.6 GHz bandwidth), (b) single element Vivaldi antenna.

moving around the view volume. Time scaling effects change across the view volume due to the differences in LOS ranges between the tag and each base station. *All of these effects must be addressed at the system-level and mitigated in a comprehensive manner to ensure optimum performance in achieving millimeter and sub-mm accuracy.*

11.2 Future Work

To realize the potential of the 2nd generation carrier-based UWB positioning approach as a transformative technology for millimeter/submillimeter accuracy in dense indoor environments, the future research should be focused in three primary areas: (1) investigation of system-level design concerns and comprehensively quantifying their effects on overall system accuracy through development of a novel system-level simulation framework (e.g. UWB receiver leading-edge detection algorithms, Tx/Rx system architectures, local oscillator phase noise sensitivity, etc.); (2) realization of novel UWB system architectures through integrated RF front-ends with MIC and MMIC technologies; (3) quantifiable testing of the system performance in realistic hospital environments in terms of dynamic 3-D accuracy using novel, real-time testing platforms. Specific issues to be investigated and approaches to be taken in these three areas are described in the following subsections.

11.2.1 System-Level Design and Simulation Framework

Many challenges exist in designing a comprehensive system-level simulation framework for the 2nd generation UWB positioning system. The simulation framework is covered in detail in Chapter 6. In order to simulate the entire system, both the analog and digital portions must be taken into account in varying levels of complexity. No commercially available simulation tools exist which have the capability to simulate all of these disparate components. *The current simulation framework needs to be extended into an even more robust solution where a C++ interface ties together the underlying disparate applications and additional simulation tools such as HFSS, Insite, and CST can be used for even more accurate simulations of (1) antennas in realistic operating environments, (2) site specific UWB indoor channels, (3) simulation of phase center effects for orientation-specific cases where various input waveforms can be analyzed, and (4) integration with MMIC simulation tools to quantitatively evaluate designed MMIC components in realistic operating environments*.

11.2.2 Novel UWB Positioning System Architectures

Given the *many limitations* of the current positioning system, *numerous novel hardware components* developed from the system-level perspective are needed at the UWB mobile tag, the base stations, and the main control unit to attain the targeted 1-2 millimeter or submillimeter positioning accuracy. Figure 11-2 outlines the proposed positioning system which includes many new critical additions to the system compared to the original architecture including (1) *dielectric resonator oscillator* circuits at the mobile tag and base stations to meet the criteria of low phase noise LOs which is *critical in reducing overall system jitter* for submillimeter accuracy; (2) *adaptive leading-edge detection* implemented on a FPGA at the UWB receivers to extend system operation into *low SNR and NLOS conditions* to ensure system operation even in dense indoor environments with extreme pathloss; (3) *automatic gain control* at the UWB receiver *to extend the system dynamic range* and to ensure, combined with adaptive-leading edge detection, operation in low SNR and even NLOS environments; (4) a *front-end bandpass filter* at the UWB receiver to mitigate the effects from high power IEEE 802.11a/n interferers which potentially exist in hospital environments; (5) narrowband (Bluetooth) and UWB (carrier-based on-off-keying) *multi-tag access schemes* building a *foundational framework to incorporate networking schemes* into future system architectures for optimum system scalability; (6) *MMIC integrated designs building on the 1st generation MIC solutions* for the RF front-ends at the mobile tag and base stations for *minimal size, reduced power consumption, and optimum system performance*.

11.2.2.1 Dielectric Resonator Oscillator

A dielectric resonator oscillator provides *substantially lower phase noise* LO signals compared to a free running VCO, *critical to achieving submillimeter accuracy*. A series- feedback topology is proposed, which consists of a resonator network, a feedback element, a bias and an output matching network. The proposed architecture includes a high performance 100 MHz OCXO as the reference clock and a phase locked loop consisting of a phase detector, loop filter, voltage controlled DRO, and prescaler. Preliminary simulation results show a 40 dB improvement at a 1 kHz offset is obtained versus a commercially available free-running VCO [224].

11.2.2.2 Adaptive Leading-Edge Detection

As discussed previously, the current leading-edge detection algorithm has *significant limitations in low SNR and NLOS environments* when the SNR of the received pulse falls below the predefined threshold value. An adaptive framework is needed to *sense* low SNR and

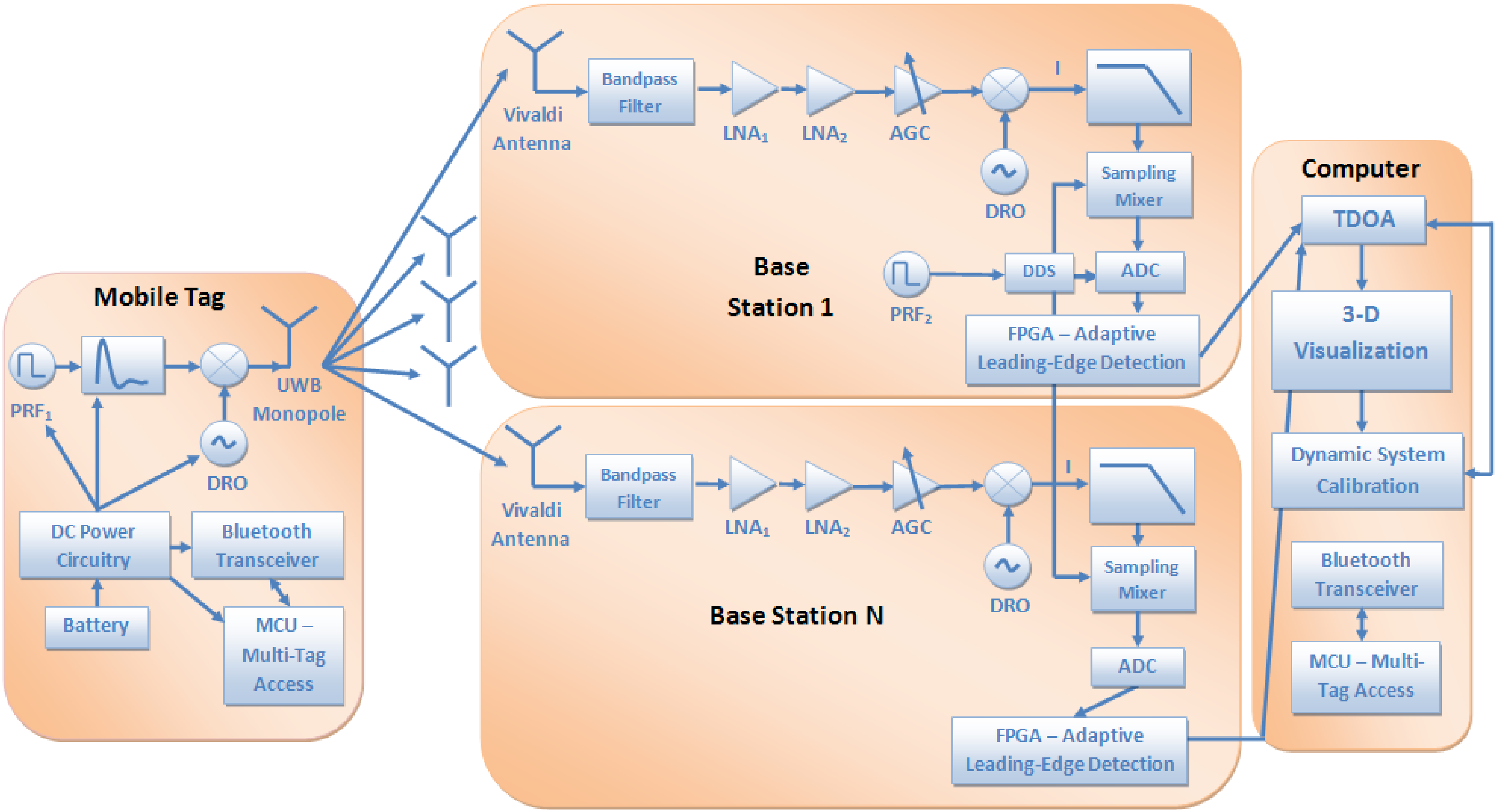

Figure 11-2: Proposed UWB system architecture which incorporates a Bluetooth-based multi-access scheme, dielectric resonator oscillators for reduced phase noise, automatic gain control for increased operating range, a front-end bandpass filter to mitigate IEEE 802.11a/n interferers, adaptive leading-edge detection for system operation in low SNR and NLOS environments, and dynamic system calibration to mitigate adverse effects including jitter, system clock drift (time scaling), and cable length and phase center variation.

NLOS conditions and *adapt* by switching ranging algorithms on the fly. Also, the use of *adaptive thresholding algorithms* will be explored to further increase the capabilities of the UWB receivers to perform accurate submillimeter ranging even in dense multipath environments. Using the max window of the leading-edge detection algorithm and the noise estimate, the SNR of the received signal can be estimated on the FPGA. An *adaptive matched filter scheme* is proposed where multiple matched filters are applied, and the one with the largest SNR is selected prior to running the leading-edge detection algorithm. r_{SNR} is a scalar estimate of the SNR used to switch on the adaptive matched filter step. Simulation results in realistic indoor environments showed that the SNR is increased by almost 8 dB after application of a matched filter. For NLOS scenarios, the slew rate r_{slew} of the detected leading edge is significantly reduced. This is combined with substantially more uncertainty σ_{LE} in detecting the received UWB signal. Metrics should be added to test for these conditions in the FPGA architecture and using a first detect approach where the leading-edge of the received signal is considered the first signal detected 3σ above the current noise level. Preliminary results show an order of magnitude improvement in 1-D ranging in NLOS environments (see Chapter 9).

11.2.2.3 Automatic Gain Control

As shown in Figure 11-2, an automatic gain control block is incorporated into the advanced system to *significantly increase the dynamic range of the UWB receiver*. We propose implementing this block by combining a variable voltage attenuator, variable gain amplifier, and power detector controlled by the FPGA for 60-70 dB dynamic range improvement.

11.2.2.4 Front-End Bandpass Filter

Interference from high power sources (e.g. IEEE 802.11a/n WLAN) operating in the 5.725-5.875 GHz ISM band pose a *significant concern* for our UWB positioning system operating from 5.4-10.6 GHz. As discussed in Chapter 4, a WLAN interferer is placed 2 m away from the UWB base station in a simulated environment. The high power source saturates the UWB receiver. A *multi-stage bandpass filter using ground plane aperture techniques* is needed in the RF front-end. Simulation results in Chapter 4 show that this addition to the system successfully mitigates high power interference from WLAN sources, although a drop in SNR of 4-6 dB is incurred from the bandpass filter. Also, even though pulse distortion is added by the bandpass filter, the leading-edge detection algorithm does not rely on pulse shape information, so this has no adverse effects on the ranging performance.

11.2.2.5 MMIC Integrated Components

The current hardware needs to be extended, with designs such as the base station RF front-end in Figure 11-3, *to integrated MMIC chips*. This will minimize the size of the RF front-ends at the tag and base stations, reduce power consumption, and optimize performance.

11.2.3 Quantitative Testing and Analysis

A critical aspect of this work is experimental testing and characterization of the harsh operating conditions found in medical environments. As shown in Figure 11-4, a real-time experimental testing platform which utilizes an optical tracking system for ground truth is currently employed for experimental analysis of the system. This needs to be extended to a real-time

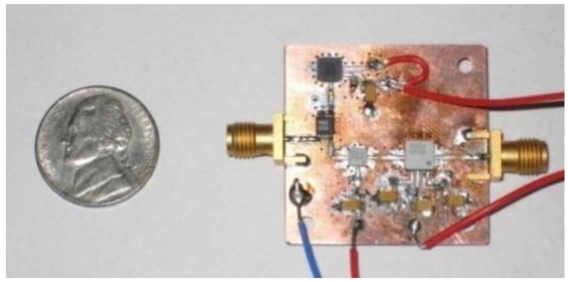

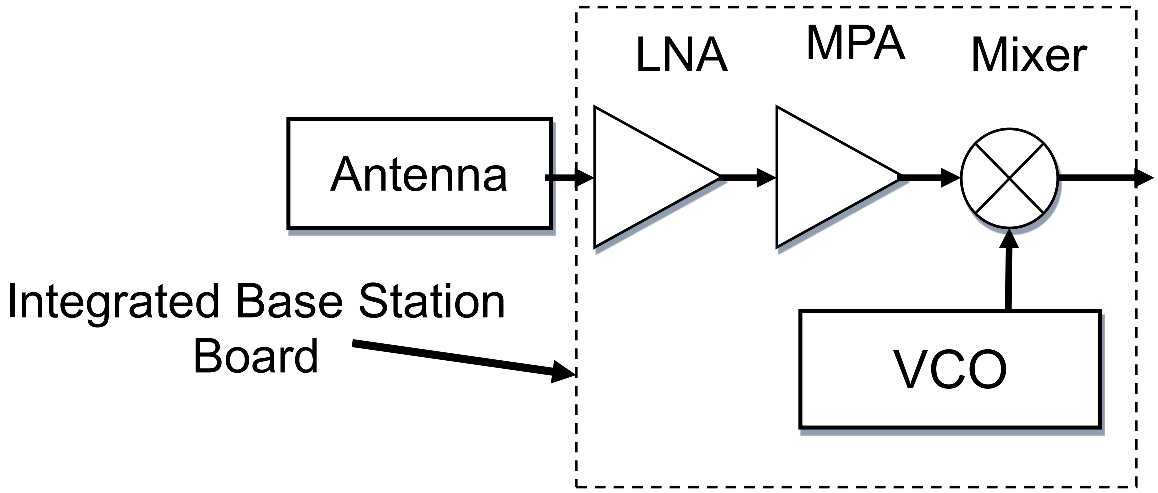

Figure 11-3: Current integrated base station where commercially available chips are used.

testing platform to run experiments in hospital environments (e.g. Figure 11-4b). Also, *dynamic self calibration techniques are needed in the system to remove time scaling effects, geometric effects, and phase center effects.* Building on this experimental testing platform, the analysis can be taken one step further by better quantifying the channels typically found in a hospital environment. For example, in [141] an experiment was run in the operating room during a live orthopedic surgery where the pathloss of the operating room channel was fit to the IEEE 802.15.4a channel model and showed it is most similar to an industrial or residential LOS scenario. Even more quantitative approaches are needed which includes developing customized comprehensive channel models for various medical environments which builds on these preliminary results and allows quick and accurate characterization of UWB communication and localization systems in these harsh medical environments.

11.3 Conclusion

The research outlined for future work offers *fundamentally novel approaches for precise localization in harsh indoor environments*. The incentive for pursuing this research is to *address the central difficulties in high accuracy localization systems to achieve a 3-D real-time accuracy of 1-2 mm and even sub-mm*. The goals for future work to extend this UWB positioning system to 1-2 mm or even sub-millimeter 3-D dynamic accuracy are outlined in Table 11-1. The main tasks include to (1) develop a comprehensive simulation platform for realistic prototyping of high accuracy UWB positioning systems, (2) develop various novel hardware components including MMIC integrated solutions needed to transform overall system performance into the submillimeter range, and (3) experimentally test hardware components in the 3.1-10.6 GHz and 22-29 GHz

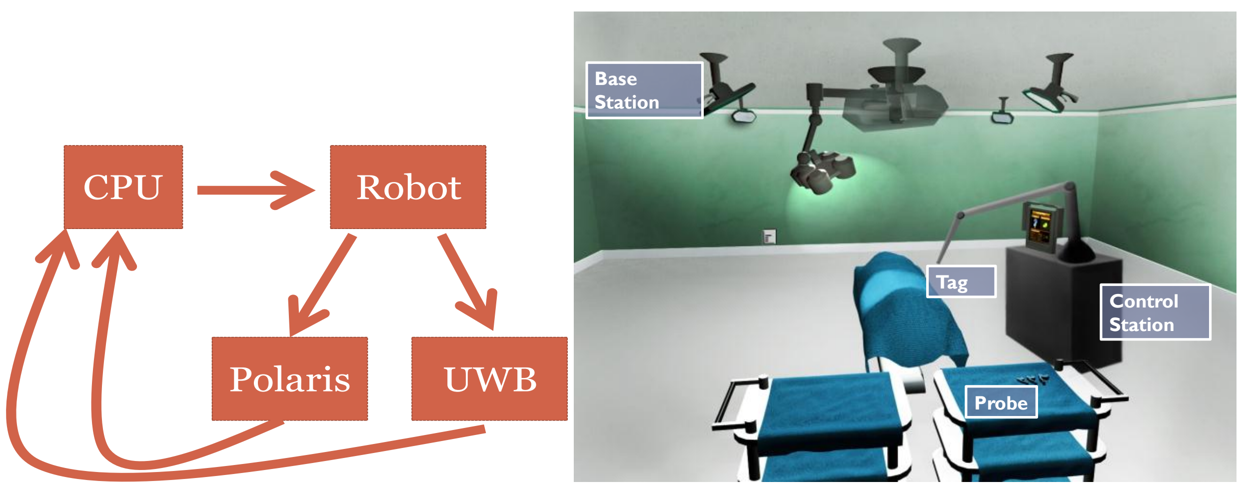

(a) (b)

Figure 11-4: (a) Real-time measurement setup (b) proposed setup for positioning in surgical navigation.

bands in realistic medical environments with real-time testing platforms.

Future trends in UWB precise positioning show its convergence with UWB digital communication in WSNs outlined by the IEEE 802.15.4a standard. MMIC technology, ultra-low-noise oscillators, extremely low jitter-clocks, and wired/wireless synchronization of various base stations are the driving forces for these new systems since they facilitate eliminating various localization errors associated with current technologies. Among the anticipated technical benefits are:

(1) A fundamentally new approach for the integration of the pulser, medium power drivers, LNA, and sub-sampler using MMIC circuits.

(2) To push positioning to mm or even sub-mm accuracy so that it can be used for surgical operations that require such accuracy, replacing optical and electromagnetic methods which suffer from LOS limitations and susceptibility to metallic interference.

(3) Extend the range to 10-20 m and simultaneously track many targets (e.g. 100+).

The direct beneficiaries of this work are researchers who rely directly on UWB technology but can also include biomedical researchers looking for robust wireless solutions for smart surgical tools and wireless sensors. Moreover, the evolution of UWB positioning technology provides new and expanded opportunities to develop and apply fast A/D conversion, advanced signal processing, asset tracking, microwave, wireless communications, and precise localization to unique applications and environments. This work is

Table 11-1: Technical goals for future work

Research Topic	Goal
Simulation Framework	Development of a comprehensive C++ application which interacts with ADS, Matlab, HFSS, etc. and is freely downloadable on the web
Dielectric Resonator Oscillator	Integration of DRO and PLL technology into tags
Adaptive Leading-Edge Detection	FPGA experimental implementation of adaptive leading-edge detection and testing of algorithm in realistic environments
Automatic Gain Control	Development of experimental design and integration with base station RF front-end
IEEE 802.11a/n Interference	Development of novel bandpass filters and experimental testing in the presence of interferers
Integration of RF Front-ends	Simulation and experimental chip testing of MMIC RF front-ends for the UWB tag and base stations
Quantitative Testing and Analysis	Real-time experimental testing in hospital environments. Development of customized channel models for various medical environments.

interdisciplinary/multidisciplinary by nature and provides stimulus to multiple fields needing advanced wireless paradigms where the application is driven by the need for millimeter 3-D accuracy or greater even while operating in challenging indoor environments.

12. Discussion

This dissertation provides an overview of wireless positioning systems targeting medical applications with focus on ultra-wideband indoor positioning applied to millimeter 3-D real-time tracking. The developed UWB real-time location system can achieve 3-10 mm of 3-D accuracy as demonstrated by the real-time dynamic 3-D experiments outlined in Chapter 8. The second generation system builds off of the first generation UWB positioning system outlined in Chapter 5. The second generation UWB positioning system addresses the main limitations of the first generation system which include: (1) low phase noise local oscillators required at both the tag and receiver, (2) no multi-tag real-time tracking support, (3) real-time operation limited to four base stations, (4) no non-line-of-sight support, and (5) no testing of the first generation system in an actual OR environment or characterization of the OR environment for UWB signal transmission.

The second generation UWB positioning system outlined in this dissertation (Chapters 7-10) addresses all of these limitations. The second generation UWB positioning system has been developed using a system-level design approach where multiple system blocks have been developed concurrently. As discussed in Chapter 8, the addition of a fifth base station provides a significant 45%-60% reduction in 3-D RMSE for a dynamic optical rail experiment (reduced error to 3-4 mm from 6-8 mm). The use of redundant base stations combined with more robust dynamic calibration and new dynamic phase center mitigation techniques are needed for a future system to achieve sub-millimeter 3-D accuracy. Also, improvements to the leading-edge detection FPGA algorithm and automatic gain control at the UWB receiver will surely improve system performance both in terms of accuracy and operating range. Finally, an improved digital board at the UWB receiver which allows for expansion factors of greater than 2500 and can achieve higher digital sampling rates of greater than 50 MSPS and more bit resolution (> 10 bits) could bring performance and accuracy improvements to the system.

The second generation UWB positioning system supports tracking of multiple tags utilizing a TDMA approach. Integration of the multi-tag tracking is done both at the UWB transmitter and also at the UWB receiver and main control station including the computer. A tradeoff exists between the achievable dynamic accuracy and number of tags being tracked since each tag is allocated fewer and fewer time slices when using a TDMA multi-tag approach. Experimental analysis shows that the UWB positioning system can track multiple tags with 6-8 mm of 3-D accuracy in a four base station setup while five base stations improves accuracy by 45%-60%. NLOS conditions can cause large ranging errors. This occurs at low SNRs including less than 10-12 dB for leading-edge detection. Detection of NLOS conditions and mitigation via either switching to peak detection or excluding low SNR tag-base station links is needed to ensure the system is robust to potential NLOS links.

The main contributions presented in this dissertation are summarized here. A system-level simulation framework has been developed using Matlab and ADS to analyze the performance of the UWB indoor positioning system and to characterize various sources of error including clock jitter and drift and multipath interference and is outlined in Chapter 6. Simulation results were compared with experimental results. The effects of the indoor channel were quantified using the IEEE 802.15.4a channel model for both LOS and NLOS environments.

The operating room channel was characterized for UWB signal transmission in Chapter 4. This includes frequency domain and time domain experiments with fitting of the experimental results to the IEEE 802.15.4a channel model. This includes implications of the UWB operating room channel on UWB indoor localization systems. Experimental analysis of electromagnetic interference in the operating room was performed as part of the operating room channel characterization.

A UWB multi-tag tracking development platform was developed and is outlined in Chapter 7. This includes an integrated tag design with DC power board, RF board, and 2.4 GHz digital communication link. Ten integrated tags are functional and have been tested to successfully operate in the UWB positioning system. The multi-tag functionality is integrated into the base station and control station FPGA digital signal processing and also the real-time software application.

Experimental analysis of the UWB Multi-Tag Development Platform is outlined Chapter 8. This includes 3-D dynamic experiments with one or two tags. This also includes an analysis on the dynamic 3-D accuracy of four base station TDOA versus five base station TDOA.

An experimental analysis of NLOS detection and mitigation techniques was performed and is discussed in Chapter 9 and Chapter 10 using the UWB Multi-Tag Development Platform outlined in Chapter 7. This includes FPGA-based SNR calculations and C++ software integration for LOS/NLOS detection with discussion of the effects of NLOS and low SNR channels on ranging techniques including leading-edge detection and peak detection.

Recent publications related to the work in this dissertation include [179],[219],[220],[225]-[231]. It should be noted that [179] is a journal article published in the IEEE Transactions on Microwave Theory and Techniques, [225] is a book chapter, and [226] a magazine article published in the IEEE Microwave Magazine. The remaining publications are from IEEE conference proceedings.

12.1 Future Work

Many improvements can be made to future UWB positioning systems to enhance the operating range and accuracy performance including automatic gain control, dynamic phase center mitigation, redundant base station configurations, and more robust digital hardware at the UWB receiver. In addition to these improvements, future work to further develop this system for real-time tracking in medical applications including computer assisted surgery can be broken down into three main research categories:

1. Development and testing of ultra-wideband probes for rigid body tracking, resolving 3-D orientation, and further improvements in 3-D dynamic accuracy as outlined in Figure 12-1.
2. The integration of the ultra-wideband positioning system with mature inertial measurement system technology for real-time rigid body tracking and 3-D orientation resolution. The ultra-wideband positioning system and inertial measurement system provide redundant technologies for real-time rigid body tracking to further improve dynamic accuracy and system robustness. This concept is illustrated in Figure 12-2.

3. The integration of MMIC analog RF front-ends at both the UWB transmitter and receiver as discussed in Section 7.3. Integrated RF front-ends will reduce the form factor of both the UWB transmitter and receiver while also reducing power consumption and making the overall system more robust and useable.

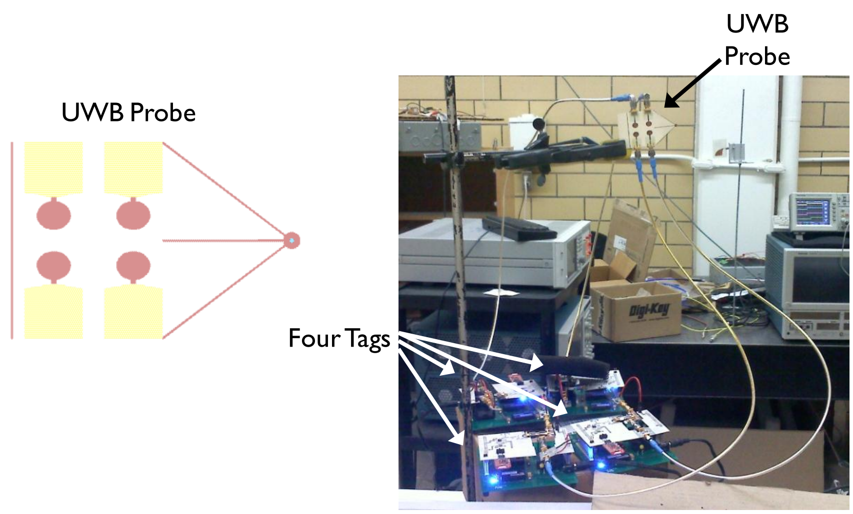

Figure 12-1: Experimental setup showing four tags connected to an ultra-wideband probe containing four monopole antennas in a known geometrical configuration.

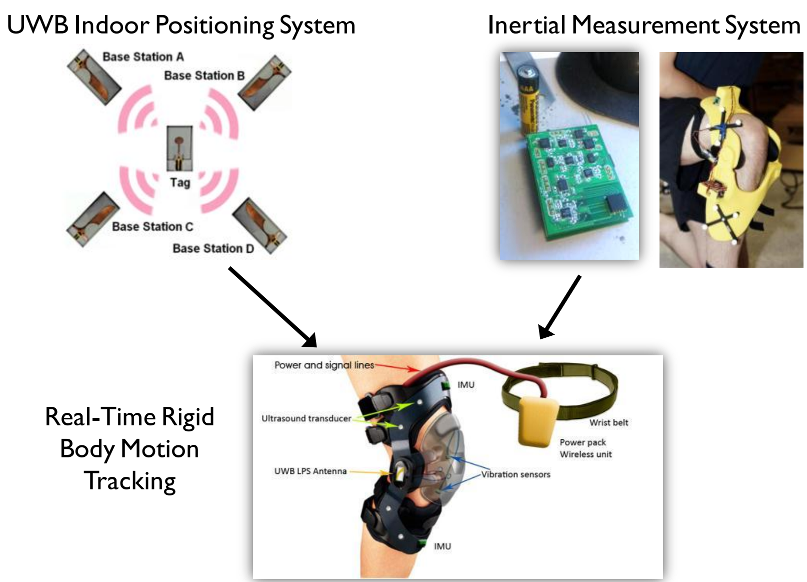

Figure 12-2: Integration of the ultra-wideband positioning system and inertial measurement systems for highly accurate real-time 3-D tracking of rigid bodies for applications such as real-time tracking of the tibia and femur.

References

1. "RTLS and Wireless Technologies," Venture Development Corp., RFID Business Planning Service 2005-2006, http://www.pencomputing.com/news/news_rtls.html.

2. "RFID Forecasts, Players and Opportunities 2009-2019," Summary, IDTechEx, Cambridge, MA, 2009, http://www.idtechex.com/research/reports/rfid_forecasts_players_and_opportunities_2009_2019_000226.asp.

3. M. Vossiek, L. Wiebking, P. Gulden, J. Wieghardt, C. Hoffman, P. Heide, "Wireless local positioning," *IEEE Microwave Magazine*, vol. 4, 2003, pp. 77 – 86.

4. Federal Communications Commission, "The first report and order regarding ultra-wideband transmission systems," FCC 02-48, ET Docket No. 98-153, 2002.

5. N. Patwari, J. Ash, S. Kyperountas, A. Hero III, et al., "Locating the nodes: cooperative localization in wireless sensor networks," *IEEE Signal Processing Magazine*, vol. 22, 2005, pp. 54 – 69.

6. E. Kaplan, *Understanding GPS: Principles and Applications*, Boston, MA: Artech House, 1996.

7. A. Stelzer, K. Pourvoyeur, A. Fischer, "Concept and application of LPM-A novel 3-D local position measurement system," *IEEE Trans. Microwave Theory and Tech.*, vol. 52, 2004, pp. 2664 – 2669.

8. M. Pichler, A. Stelzer, P. Gulden, C. Seisenberger, M. Vossiek, "Phase-error measurement and compensation in PLL frequency synthesizers for FMCW sensors—I: context and application," *IEEE Trans. Cir. and Sys. I*, vol. 54, 2007, pp. 1006 – 1017.

9. LPR-2D, Symeo, 2009, http://www.symeo.com/cms/upload/PDF/Datasheet_LPR-2D.pdf.

10. L. Wiebking, M. Glanzer, D. Mastela, M. Christmann, M. Vossiek, "Remote local positioning radar," in *IEEE Radio and Wireless Symp.*, 2004, pp. 191 – 194.

11. S. Roehr, M. Vossiek, P. Gulden, "Method for high precision radar distance measurement and synchronization of wireless units," in *IEEE International Microwave Symp.*, 2007, pp. 1315-1318.

12. R. Fontana, "Recent system applications of short-pulse ultra-wideband (UWB) technology," *IEEE Trans. Microwave Theory and Tech.*, 52(9), 2004, pp. 2087 – 2104.

13. Dart Ultra-Wideband System, Zebra Enterprise Solutions, (2011, Aug. 9). [Online]. Available: http://www.zebra.com/.

14. “Hardware datasheet,” Ubisense, Cambridge, UK, 2007, http://www.ubisense.net.

15. Z. Low, J. Cheong, C. Law, W. Ng, Y. Lee, “Pulse detection algorithm for line-of-sight (LOS) UWB ranging applications,” *IEEE Ant. and Wireless Prop. Letters*, vol. 4, 2005, pp. 63 – 67.

16. R. Zetik, J. Sachs, R. Thomä, “UWB localization - active and passive approach, in *Proceedings of the 21st IEEE IMTC*, vol. 2, 2004, pp. 1005-1009.

17. C. Meier, A. Terzis, S. Lindenmeier, “A robust 3D high precision radio location system, in *IEEE International Microwave Symp.*, 2007, pp. 397 – 400.

18. M. Mahfouz, C. Zhang, B. Merkl, M. Kuhn, A. Fathy, “Investigation of high accuracy indoor 3-D positioning using UWB technology,” *IEEE Transactions on Microwave Theory and Techniques*, 56(6), 2008, pp. 1316-1330.

19. C. Zhang, M. Kuhn, B. Merkl, A. Fathy, M. Mahfouz, “Real-time non-coherent UWB positioning radar with millimeter range accuracy: theory and experiment,” *IEEE Transactions on Microwave Theory and Techniques*, 58(1), 2010, pp. 9-20.

20. B. Waldmann, R. Weigel, P. Gulden, “Method for high precision local positioning radar using an ultra wideband technique,” in *IEEE International Microwave Symp.*, Atlanta, USA, 2008, pp. 117-120.

21. C. Meier, A. Terzis, S. Lindenmeier, “Investigation and suppression of multipath influence on indoor radio location in the millimeter wave range,” in *Conf. Wave Prop. Comm., Microwave Sys. Nav.*, Chemnitz, Germany, 2007, pp. 21-24.

22. Thomas E. McEwan, “Radiolocation system having writing pen application,” U.S. Patent 6,747,599, June, 2004.

23. G. Ossberger, T. Buchegger, E. Schimback, A. Stelzer, R. Weigel, “Non-invasive respiratory movement detection and monitoring of hidden humans using ultra wideband pulse radar,” in *IEEE International Conf UWB Sys. Tech.*, Kyoto, Japan, 2004, pp. 395-399.

24. A. Fujii, H. Sekiguchi, M. Asai, S. Kurashima, H. Ochiai, and R. Kohno, “Impulse radio UWB positioning system,” in *IEEE Radio and Wireless Symposium*, pp. 55-58, 2007.

25. A. Stelzer, C.G. Diskus, H.W. Thim, “A microwave position sensor with sub-millimeter accuracy,” *IEEE Trans. Microwave Theory and Tech.*, 47(12), 1999, pp. 2621–2624.

26. F. Ellinger, R. Eickhoff, R. Gierlich, J. Hüttner et al., “Local positioning for wireless sensor networks,” in *IEEE Globecom Workshops*, Washington DC, USA, 2007, pp. 1-6.

27. R. Mosshammer, M. Huemer, R. Szumny, K. Kurekt, J. Hittner, R. Gierlichli, “A 5.8 GHz local positioning and communication system,” in *IEEE MTT-S International Microwave Symposium*, Honolulu, USA, 2007, pp. 1237-1240.

28. P. Tragas, A. Kalis, C. Papadias, F. Ellinger, R. Eickhoff , et al., “RESOLUTION: reconfigurable systems for mobile local communication and positioning,” in *Mob. and Wireless Comm. Summit*, Budapest, Hungary, 2007, pp. 1-5.

29. R. Feger, C. Wagner, S. Schuster, H. Jäger, A. Stelzer, “A 77-GHz FMCW MIMO radar based on an SiGe single-chip transceiver,” *IEEE Trans. Microwave Theory and Tech.*, 57(5), 2009, pp. 1020 - 1035.

30. I. Guvenc, Z. Sahinoglu, P. Orlik, “TOA estimation for IR-UWB systems with different transceiver types,” *IEEE Transactions on Microwave Theory and Techniques*, 54(4), Part 2, 2006, pp. 1876 – 1886.

31. T. Buchegger, G. Obberger, A. Reisenzahn, E. Hochmair, A. Stelzer, A. Springer, ‘‘Ultrawideband transceivers for cochlear implants,’’ *EURASIP J. Appl. Signal Process*, vol. 2005, no. 18, 2005, pp. 3069–3075.

32. J. P. Lie, C. M. See, B. P. Ng, “UWB ranging with high robustness against dominant jammer and multipath,” *IEEE Microwave and Wireless Components Letters*, 15(12), 2005, pp. 907-909.

33. A. Rabbachin, I. Oppermann, “Synchronization analysis for UWB systems with a low-complexity energy collection receiver,” in *Proc. IEEE Ultrawideband Syst. Technol. Conf.*, Kyoto, Japan, 2004, pp. 288–292.

34. R.J. Fontana, F.J. Larrick, “Ultra wideband receiver with high speed noise and interference tracking threshold,” U.S. Patent 5,901,172, May, 1999.

35. C.-C. Chong, S. K. Yong, S.-S. Lee, “UWB direct chaotic communication technology,” *IEEE Antennas Wireless Propagat. Lett.*, vol. 4, 2005, pp. 316–319.

36. D. Barras, F. Ellinger, H. Jäckel, W. Hirt, "A robust front-end architecture for low-power UWB radio transceivers", *IEEE Trans. Microwave Theory Tech.*, 54(4), Part 2, 2006, pp. 1713 – 1723.

37. C. Zhang, M. Kuhn, B. Merkl, M. Mahfouz, and A. E. Fathy, “Development of an UWB indoor 3-D positioning radar with millimeter accuracy,” in *IEEE International Microwave Symp.*, 2006, pp. 106-109.

38. C. Zhang, A. Fathy, M. Mahfouz, “Performance enhancement of a sub-sampling circuit for ultra-wideband signal processing”, *IEEE Micro. and Wireless Comp. Lett.*, 17(12), 2007, pp. 873-875.

39. D. M Treyer, W. Bächtold, “Investigation of a self-calibrating SSB modulator,” *IEEE Trans. Microwave Theory and Tech.*, 53(12), 2005, pp. 3806-3816.

40. T. Copani, S. Min, and S. Shashidharan,“A CMOS low-power transceiver with reconfigurable antenna interface for medical implant applications,” *IEEE Trans. Microw. Theory Tech.*, 59(5), 2011, pp. 1369-1378.

41. A.M. Sodagar, K.D. Wise, and K. Najafi, “A wireless implantable microsystem for multichannel neural recording,” *IEEE Trans. Microw. Theory Tech.*, 57(10), Part 2, 2009, pp. 2565-2573.

42. F. Graichen, R. Arnold, A. Rohlmann, and G. Bergmann, “Implantable 9-channel telemetry system for in- vivo load measurements with orthopedic implants,” *IEEE Trans. Biomed. Eng.*, 54(2), 2007, pp. 253-261.

43. U. Kawoos, M.-R. Tofighi, R. Warty, F.A. Kralick, and A. Rosen, "In-vitro and in-vivo trans-scalp evaluation of an intracranial pressure implant at 2.4 GHz,” *IEEE Trans. Microw. Theory Tech.*, 56(10), 2008, pp. 2356-2365.

44. P. Valdastri, E. Susilo, T. Forster, C. Strohhofer, A. Menciassi, and P. Dario, "Wireless implantable electronic platform for chronic fluorescent-based biosensors,” *IEEE Trans. Biomed. Eng.*, 58(6), 2011, pp. 1846-1854.

45. F. Graichen, R. Arnold, A. Rohlmann, and G. Bergmann, “Implantable 9-channel telemetry system for in- vivo load measurements with orthopedic implants,” *IEEE Trans. Biomed. Eng.*, 54(2), 2007, pp. 253-261.

46. D.J. Young, "An RF-powered wireless multi-channel implantable bio-sensing microsystem,” *Proc. of IEEE Int. Conf. Eng. Med. Bio. Society*, Buenos Aires, Argentina, 2010, pp. 6413-6416.

47. H.-J. Lee, H.-S. Lee, H.H. Choi, K.-H. Yoo, and J.-G. Yook, "An RF circuit model for interdigital capacitors-based carbon nanotube biosensors,” *IEEE Trans. Nanotech.*, 9(6), 2010, pp. 682-686.

48. N. Laskovski, M.R. Yuce, and T. Dissanayake, "Stacked spirals for biosensor telemetry,” *IEEE Sensors Journal*, 11(6), 2011, pp. 1484-1490.

49. B. Kim, S. Uno, and K. Nakazato, "13.56 MHz-RFID biosensor with on-chip spiral inductor,” *Proc. of Int. Conf. on Enabl. Sci. Nanotech.*, Kuala Lumpur, Malaysia, 2010, pp. 1-2.

50. A.Y. Benbasat, S. Morris, J. Paradiso, "A wireless modular sensor architecture and its application in on-shoe gait analysis," *Proc. of the IEEE Sensors*, Toronto, Canada, 2003, pp. 1086-1091.

51. E.H.M. Lou, E.K. Brunton, F. Kamal, A. Renggli, K. Kemp, et al., "A low power wireless data acquisition device to monitor gait patterns for children with toe walking during daily activities," *J. Med. Devices*, 5(2), 2011, pp. 1-6.

52. W. Qu, S. Islam, M. Mahfouz, G. To, and S. Mofasta, "Micro-cantilever array pressure measurement system for biomedical instrumentation," *IEEE Sensors Journal* , 10(2), 2010, pp. 321-330.

53. B. Gyselinckx, J. Penders, and R. Vullers, "Potential and challenges of body area networks for cardiac monitoring," *J. Electrocardiol*., 40(6), Supplement, 2007, pp. S165–S168.

54. Zephyr Inc. (2011, Aug. 9). [Online]. Available: http://www.zephyr-technology.com/.

55. A. Pantelopoulos, and N.G. Bourbakis, "A survey on wearable sensor-based systems for health monitoring and prognosis," *IEEE Trans. Sys., Man, and Cyber*., Part C: App. Rev., 40(1), 2011, pp. 1-12.

56. L. Wang, G.-Z. Yang, J. Huang, J. Zhang, L. Yu, Z. Nie, and D.R.S. Cumming, "A wireless biomedical signal interface system-on-chip for body sensor networks," *IEEE Trans. Bio. Circuits and Systems*, 4(2), 2010, pp. 112-117.

57. A. Pantelopoulos and N.G. Bourbakis, "Prognosis—a wearable health-monitoring system for people at risk: methodology and modeling," *IEEE Trans. Inf. Tech. in Biomed*., 14(3), 2010, pp. 613-621.

58. P. Phunchongharn, E. Hossain, D. Niyato, and S. Camorlinga, " A cognitive radio system for e-health applications in a hospital environment," *IEEE Wireless Comm*., 17(1), 2010, pp. 20-28.

59. M. Mincica, D. Pepe, A. Tognetti, A. Lanatà, D. De Rossi, and D. Zito, "Enabling technology for heart health wireless assistance," *Proc. of IEEE Int. Conf. e-Health Net. App. Serv*., Lyon, France, 2010, pp. 36-42.

60. N. Nakajima, "Short-range wireless network and wearable bio-sensors for healthcare applications," *Proc. of Int. Symp. on App. Sci. Biomed. Comm. Tech*., Bratislava, Slovak Republic, Nov. 2009, pp. 1-6.

61. B. Shengrong, F.R. Yu, X.P. Liu, P. Mason, and H. Tang, "Distributed combined authentication and intrusion detection with data fusion in high-security mobile ad hoc networks," *IEEE Trans. Veh. Tech*., 60(3), 2010, pp. 1025-1036.

62. 1100/1101 Wireless Probes, Neoprobe, (2011, Aug. 9). [Online]. Available: http://www.neoprobe.com/Bluetooth-Wireless-Probe.html.

63. Plus Location Systems (2011, Aug. 9). [Online]. Available: http://www.plus-ls.com/datasheets/plus-asset.php.

64. DecaWave RTLS Product Description and Applications, DecaWave, Dublin, Ireland, 2012, http://www.decawave.com/.

65. Y. Zheng, M. Arusa, K. Wong, et al., "A 0.18μm CMOS 802.15.4a UWB transceiver for communication and localization," *IEEE Int. Solid State Cir. Conf.*, San Francisco, CA, 2008, pp. 118-119, 600.

66. J. Ryckaert, G. Van der Plas, V. De Heyn, et al., "A 0.65-to-1.4nJ/burst 3-to-10GHz UWB all-digital Tx in 90nm CMOS for IEEE 802.15.4a," *IEEE J. Solid State Cir.*, 42(12), 2007, pp. 2860-2869.

67. U. Varshney, "Using wireless technologies in healthcare," *Int. J. of Mobile Communications*, Vol. 4, 2006, pp. 354-368.

68. C. Pattichis, E. Kyriacou, S. Voskarides, M. Pattichis, et al., "Wireless telemedicine systems: an overview," *IEEE Antenna and Propagation Magazine*, 44(2), 2002, pp. 143-153.

69. B. Lee, J. Bishoff, G. Janetschek, P. Bunyaratevej, et al., "A novel method of surgical instruction: international telementoring," *World J. Urology*, Vol. 16, 1998, pp. 367-370.

70. F. Graichen, G. Bergmann, A. Rohlmann, "Hip endoprosthesis for in vivo measurement of joint force and temperature," *J. Biomechanics*, Vol. 32, 1999, pp. 1113-1117.

71. G. Bergmann, F. Graichen, A. Rohlmann, N. Verdonschot, G. van Lenthe, "Frictional heating of total hip implants, Part 1. measurements in patients," *J. Biomechanics*, Vol. 34, 2001, pp. 421-428.

72. B. Evans, *MEMS Capacitive Strain Sensing Elements for Integrated Total Knee Arthroplasty Prosthesis Monitoring*, Ph.D. Dissertation, University of Tennessee, 2007.

73. G. To, *Development of the Telemetrical Intraoperative Soft Tissue Tension Monitoring System in Total Knee Replacement with MEMS and ASIC Technologies*, M.Sc. Thesis, University of Tennessee, 2007.

74. E. Pritchard, M. Mahfouz, B. Evans, S. Eliza, M. Haider, "Flexible capacitive sensors for high resolution pressure measurement," in *IEEE Sensors*, Lecce, Italy, Oct. 2008, pp. 1484-1487.

75. A.V. Vorst, A. Rosen, Y. Kotsuka, *RF/Microwave Interaction with Biological Tissues*, John Wiley & Sons Inc., Hoboken,NJ, 2006.

76. L. Dubois, J.P. Sozanski, V. Tessier, J. Camart, J.J. Favre, J. Pribetich, M. Chiv′e, "Temperature control and thermal dosimetry by microwave radiometry in hyperthermia," *IEEE Trans. Microwave Theory Tech.*, 44(10), Part 2, 1996, pp. 1755–61.

77. S.O. Nelson. "Dielectric properties of agricultural products - measurements and applications," *IEEE Trans. Elec. Insul*., 26(5), 1991, pp. 845-869.

78. V. Komarov, S. Wang, J. Tang. "Permittivity and measurements," Ed. K. Chang, *Wiley Encyclopedia RF Microwave Engineering*, John Wiley & Sons, New York, 2005, pp. 3693-3711.

79. S. Gabriel, R.W. Lau, C. Gabriel. "The dielectric properties of biological tissues: III parametric models for the dielectric spectrum of tissue," *Phys. Med. Biol*., 41, 1996, pp. 2271-2293.

80. T.W. Athey, M.A. Stuchly, S.S. Stuchly. "Measurement of radio frequency permittivity of biological tissues with an open-ended coaxial line, part 1," *IEEE Trans. Microwave Theory Tech*., 30(1), 1982, pp. 82-92.

81. R. Pethig. "Dielectric properties of body tissues," *Clin. Phys. Physiol. Meas.*, 8, 1987, pp. 5-12.

82. C. Gabriel, S. Gabriel, E. Corthout, "The dielectric properties of biological tissues: I. Literature survey," *Phys. Med. Biol*., 41, 1996, pp. 2231-2249.

83. F. Duhamel, I. Huynen, A.V. Vorst, "Measurements of complex permittivity of biological and organic liquids up to 110 GHz," *IEEE MTT-S International Microwave Symp.*, Denver, CO, Vol. 1, 1997, pp. 107-110.

84. Technical Overview. Agilent 85070D Dielectric Probe Kit 200 MHz to 20 GHz, Agilent literature number 5968-5330E, 2002.

85. M. Kuhn, M. Awida, M. Mahfouz, A. Fathy, "Open-ended coaxial probe measurements for breast cancer detection," *IEEE Radio Wireless Symp.*, New Orleans, LA, 2010, pp. 512-515.

86. D. Clarke, A. Park, "Active-RFID system accuracy and its implications for clinical applications," *IEEE Symp. on Computer-Based Med. Sys.*, Salt Lake City, USA, 2006, pp. 21-26.

87. Time Domain Corp. PLUS® RTLS for Healthcare Applications, http://www.timedomain.com/healthcare.php.

88. E. Kyriacou, S. Pavlopoulos, A. Berler, M. Neophytou, et al., "Multi-purpose healthcare telemedicine systems with mobile communication link support," *BioMedical Engineering OnLine*, 2, 2003, pp. 1-12.

89. R. Carroll, R. Cnossen, M. Schnell, D. Simons, "Continua: an interoperable personal healthcare ecosystem," *IEEE Pervasive Computing*, 6(4), 2007, pp. 90-94.

90. S. Drude, "Tutorial on body area networks," IEEE 15-06-0331, July 2006, submitted to IEEE P802.15 Working Group for WPANs.

91. "Avant® 4000 wireless tabletop pulse oximeter," Nonin Medical, Inc., Plymouth, MN, 2009, http://www.nonin.com/

92. "WSR601 - wireless UWB single chip," Wisair, 2009, http://www.wisair.com/wp-content/WSR601.pdf.

93. B. Merkl, *The Future of the Operating Room: Surgical Preplanning and Navigation Using High Accuracy Ultra-Wideband Positioning and Advanced Bone Measurement*, Ph.D. Dissertation, The University of Tennessee, 2008.

94. E. Elfenbein, "The miracle of Warsaw, Indiana," March 21st, 2006, http://www.crossingwallstreet.com/.

95. A. Hodgson, "Computer-assisted orthopedic surgery," Chapter 12 in *Image-Guided Interventions, Technology and Applications*, Springer US, New York, USA, 2008.

96. B. Jaramaz, A. DiGioia III, "CT-based navigation systems," Chapter 2 in *Navigation and MIS in Orthopedic Surgery*, Springer Berlin Heidelberg, Berlin, Germany, 2007.

97. A. Wiles, D. Thompson, D. Frantz, "Accuracy assessment and interpretation for optical tracking systems," *Proc. of SPIE*, vol. 5367, 2004, pp. 421 – 432.

98. "Polaris Spectra & Polaris Vicra technical specifications," Northern Digital Inc., 2008, http://www.ndigital.com/medical/polarisfamily-techspecs.php.

99. "Optotrak Certus technical specifications," Northern Digital Inc., 2003, http://www.gaitech.net/.

100. "Flock of Birds, real-time motion tracking," Ascension Technologies Corporation, 2008, http://www.ascension-tech.com/docs/Flock_of_Birds.pdf.

101. "3D Guidance medSAFE," Ascension Technologies Corporation, 2008, http://www.ascension-tech.com/docs/3DGuide%20medSAFE.pdf.

102. J. Kowal, F. Langlotz, L. Nolte, "Basics of computer-assisted orthopaedic surgery," Chapter 1 in *Navigation and MIS in Orthopedic Surgery*, Springer Berlin Heidelberg, Berlin, Germany, 2007.

103. "MAKOplasty® brochure," MAKO Surgical Corp., 2008, http://www.makosurgical.com/.

104. K. Krackow, "Total knee arthroplasty using the Stryker Knee Trac system," Chapter 13 in *Navigation and MIS in Orthopedic Surgery*, Springer Berlin Heidelberg, Berlin, Germany, 2007, pp. 100-105.

105. National Institutes of Health, "Consensus statement on total knee replacement," *NIH Consensus and State-of-the-Science Statements*, 20(1), 2003, pp. 1–34.

106. Medtronic Navigation, Total Knee Arthroplasty Procedure, 2007, http://www.medtronicnavigation.com/.

107. C. Lüring, H. Bäthis, M. Tingart, J. Grifka, L. Perlick, "Experience with navigated total knee replacements with CT-free and CT-based VectorVision® BrainLAB navigation system," Chapter 19 in *Navigation and MIS in Orthopedic Surgery*, Springer Berlin Heidelberg, Berlin, Germany, 2007.

108. T. Mattes, R. Decking, H. Reichel, "Navigated total knee arthroplasty with the Navitrack® system," Chapter 18 in *Navigation and MIS in Orthopedic Surgery*, Springer Berlin Heidelberg, Berlin, Germany, 2007.

109. P. Ritschl, F. Machacek, R. Fuiko, "Modern navigated ligament balancing in total knee arthroplasty with the PiGalileo system," Chapter 17 in *Navigation and MIS in Orthopedic Surgery*, Springer Berlin Heidelberg, Berlin, Germany, 2007.

110. E. Stindel, J. Briard, C. Plaskos, J. Troccaz, "Navigated total knee arthroplasty and the Surgetics bone-morphing system, Chapter 16 in *Navigation and MIS in Orthopedic Surgery*, Springer Berlin Heidelberg, Berlin, Germany, 2007.

111. R. Haaker, M. Senkal, A. Ottersbach, R. Willburger, "Navigated total knee arthroplasty and the OrthoPilot system," Chapter 14 in *Navigation and MIS in Orthopedic Surgery*, Springer Berlin Heidelberg, Berlin, Germany, 2007.

112. R. Jeffery, R. Morris, R. Denham, "Coronal alignment after total knee replacement," *J. Bone Joint Surg. Br.*, 73(5), 1991, pp. 709-714.

113. J. Jenny, U. Clemens, S. Kohler, H. Kiefer, W. Konermann, R. Miehlke, "Consistency of implantation of a total knee arthroplasty with a non-image-based navigation system," *J. Arthroplasty*, 20(7), 2005, pp. 832-839.

114. M. Kelly, "Patellofemoral complications following total knee arthroplasty," *Instructor Course Lectures*, 2001, 50, pp. 403-407.

115. J. Victor, "Navigated total knee arthroplasty with the fluoroscopic Medtronic system," Chapter 22 in *Navigation and MIS in Orthopedic Surgery*, Springer Berlin Heidelberg, Berlin, Germany, 2007.

116. R. Alen, A. Tria, "Quadriceps sparing total knee arthroplasty in association with electromagnetic navigation," Chapter 28 in *Navigation and MIS in Orthopedic Surgery*, Springer Berlin Heidelberg, Berlin, Germany, 2007.

117. M. Skutek, R. Bourne, C. Rorabeck, A. Burns, S. Kearns, G. Krishna, "The twenty to twenty-five year outcomes of Harris Design-2 matte-finished cemented total hip replacement. A concise follow-up of a previous report," *J. Bone Joint Surg. Am.*, 89(4), 2007, pp. 814-818.

118. J. Masonis, B. Bourne, "Surgical approach, abductor function, and total hip arthroplasty dislocation," *Clin. Ortho. Related Research.*, 405, 2002, pp. 46-53.

119. M. Kwon, M. Kuskowski, K. Mulhall, W. Macaulay, T. Brown, K. Saleh, "Does surgical approach affect total hip arthroplasty dislocation rates?," *Clin. Ortho. Related Research.*, 447, 2006, pp. 34-38.

120. S. Parratte, J. Argenson, "Validation and usefulness of a computer-assisted cup-positioning system in total hip arthroplasty. A prospective, randomized, controlled study," *J. Bone Joint Surg. Am.*, 89(3), 2007, pp. 494-499.

121. W. Harris, "Wear and periprosthetic osteolysis: the problem," *Clin. Ortho. Related Research.*, 393, 2001, pp. 66-70.

122. D. Back, J. Smith, R. Dalziel, D. Young, J. Skinner, A. Shimmin, "Establishing a learning curve for hip resurfacing," *annual meeting of American Academy of Orthopedic Surgeons*, 2007, San Diego, USA.

123. P.Vavken, R. Kotz, R. Dorotka, "Minimally invasive hip replacement – a meta-analysis," *Z. Orthop. Unfall.*, 145(2), 2007, pp. 152-156.

124. F. Orozco, A. Ong, R. Rothman, "The role of minimally invasive hip surgery in reducing pain," *Instructor Course Lectures*, 2007, 56, pp. 121-124.

125. S. Woolson, "In the absence of evidence – why bother? A literature review of minimally invasive total hip arthroplasty," *Instructor Course Lectures*, 2006, 55, pp. 189-193.

126. I. Reininga, R. Wagenmakers, I. van den Akker-Scheek, A. Stant, J. Groothoff, S. Bulstra, W. Zijlstra, M. Stevens, "Effectiveness of computer-navigated minimally invasive total hip surgery compared to conventional total hip arthroplasty: deisgn of a randomized controlled trial," *BMC Musculoskeletal Disorders*, 8(1):4, 2007.

127. D. Attarian, T. Vail, "Medicolegal aspects of hip and knee arthroplasty," *Clin. Ortho. Related Research*, 433, 2005, pp. 72-76.

128. J. Edeen, P. Sharkey, A. Alexander, "Clinical significance of leg-length inequality after total hip arthroplasty," *Am. J. Orthopedics,* 24(4), 1995, pp. 347-351.

129. T. Visuri, T. Lindholm, I. Antti-Poika, M. Koskenvuo, "The role of overlength of the leg in aseptic loosening after total hip arthroplasty," *Italian J. Orthopedics Traumatology*, 19(1), 1993, pp. 107-111.

130. Medtronic Total Hip Replacement Procedure, 2006-2007, http://www.medtronicnavigation.com/.

131. Stryker iNstride Hip Navigation Software, 2008, http://www.stryker.com/en-us/products/Orthopaedics/ComputerAssistedSurgery/HipNavigationSurgery/iNstride/index.htm.

132. H. Kiefer, A. Othman, "Cup and stem navigation with the Orthopilot system," Chapter 43 in *Navigation and MIS in Orthopedic Surgery*, Springer Berlin Heidelberg, Berlin, Germany, 2007.

133. G. Lewinnek, J. Lewis, R. Tarr, C. Compere, J. Zimmermann, "Clinical dislocations after total hip-replacement arthroplasties," *J. Bone Joint Surg. Am.*, 60A, 1978, pp. 217-220.

134. J. Babisch, F. Layher, K. Sander, "Imageless cup and stem navigation in dysplastic hips with the Navitrack and Vector Vision systems," Chapter 44 in *Navigation and MIS in Orthopedic Surgery*, Springer Berlin Heidelberg, Berlin, Germany, 2007.

135. J. Argenson, S. Parratte, X. Flecher, J. Aubaniac, "Navigation of computer-assisted designed hip arthroplasty," Chapter 45 in *Navigation and MIS in Orthopedic Surgery*, Springer Berlin Heidelberg, Berlin, Germany, 2007.

136. H. Bäthis, L. Perlick, M. Tingart, T. Kalteis, J. Grifka, "Computer-assisted hip resurfacing," Chapter 46 in *Navigation and MIS in Orthopedic Surgery*, Springer Berlin Heidelberg, Berlin, Germany, 2007.

137. T. Hess, "Navigation for hip resurfacing," Chapter 47 in *Navigation and MIS in Orthopedic Surgery*, Springer Berlin Heidelberg, Berlin, Germany, 2007.

138. B. Jaramaz, A. DiGioia, M. Blackwell, C. Nikou, "Computer assisted measurement of cup placement in total hip replacement," *Clin. Ortho. Related Research.*, 354, 1998, pp. 70-81.

139. R. Haaker, G. Trottenberg, A. Gleichmann, "Cup and offset navigation with OrthoPilot system," Chapter 55 in *Navigation and MIS in Orthopedic Surgery*, Springer Berlin Heidelberg, Berlin, Germany, 2007.

140. M. Hartzband, G. Klein, "Navigating the two-incision total hip arthroplasty," Chapter 60 in *Navigation and MIS in Orthopedic Surgery*, Springer Berlin Heidelberg, Berlin, Germany, 2007.

141. M. Mahfouz, M. Kuhn, G. To, A. Fathy, "Integration of UWB and wireless pressure mapping in surgical navigation," in *IEEE Trans. Microwave Theory Tech.*, 57(10), Part 2, 2009, pp. 2550-2564.

142. M. Mahfouz, "Operating room of the future orthopedic perspective," in *Proc. of Cairo International Biomedical Engineering Conference*, 2008, pp. 1-9.

143. B. Merkl, M. Mahfouz, "Unsupervised three-dimensional segmentation of medical images using an anatomical bone atlas," *12th International Conference on Biomedical Engineering*, Singapore, Dec. 2005.

144. M. Mahfouz, E. Abdel Fatah, H. E. Dakhakhni, R. Tadross, R. Komistek, "Three-dimensional bone creation and landmarking using two still X-rays," in *Annual Meeting of American Academy of Orthopaedic Surgeons*, San Francisco, CA, Mar. 2008.

145. M. Mahfouz, B. Merkl, E. Abdel Fatah, R. Booth, J. Argenson, "Automatic methods for characterizing of sexual dimorphism of adult femora: distal femur," *Comp. Methods in Biomechanics and Biomedical Engr.*, 10(6), 2007, pp. 447-456.

146. M. Mahfouz, W. Hoff, R. Komistek, D. Dennis, "A robust method for registration of three-dimensional knee implant models to two-dimensional fluoroscopy images," *IEEE Trans. Med. Imag.*, 22(12), 2003, pp. 1561-1574.

147. J. Collins, "RFID remedy for medical errors," *RFID Journal*, May 28, 2004, http://www.rfidjournal.com/article/view/961/1/1.

148. N.F. Güler and U. Fidan, "Wireless transmission of ECG signal," *J. Medical Sys.*, Springer Netherlands, 30(3), 2006, pp. 231-235.

149. Application Note 3945, “Path loss in remote keyless entry systems,” Maxim-IC, Inc., Dec. 15, 2006, http://www.maxim-ic.com/appnotes.cfm/an_pk/3945.

150. “Maxim 1473 315 MHz and 433 MHz superheterodyne receiver with extended dynamic range,” Datasheet, Maxim Integrated Products, 19-2748, Rev 3, 2003.

151. A. Molisch, K. Balakrishnan, et al., “IEEE 802.15.4a channel model - final report,” Tech. Rep., Document IEEE 802.1504-0062-02-004a, 2005.

152. A.F. Molisch, D. Cassioli, C. Chong, S. Emami, A. Fort, B.. Kannan, J. Karedal, J. Kunisch, H.G. Schantz, K. Siwiak, M.Z. Win, “A comprehensive standardized model for ultrawideband propagation channels,” *IEEE Trans. Antennas and Propag*., vol. 54, Nov. 2006, pp. 3151-3166.

153. L. Hentila, A. Taparungssanagorn, H. Viittala and M. Hämäläinen, “Measurement and modelling of an UWB channel at hospital,” *IEEE International Conference on Ultra-Wideband*, Zurich, Switzerland, Sept. 2005, pp. 113-117.

154. Z. Irahhauten, H. Nikookar, G.J.M. Janssen, “An overview of ultra wide band indoor channel measurements and modeling,” *IEEE Microwave and Wireless Components Letters*, 14(8), 2004, pp. 386-388.

155. FCC Regulations, 47 CFR, 18.301, 95, Washington, D.C.

156. ERC Report 25, “Frequency range 29.7 MHz to 105 GHz and associated European table of frequency allocations and utilisations,” 1994, revised in Brugge, February 1998. European Radiocommunications Committee (ERC) within the CEPT.

157. Y. Kim, D.H. Kwon, “CPW-fed planar ultra-wideband antenna having a frequency band notch function,” *IEEE Elect. Letters*, vol. 40, 2004, pp. 403–405.

158. C. Zhang, A. Elsherbini, A.E. Fathy, M. Mahfouz, “Investigation of pulse dispersion in a carrier-based UWB system with LO leakage cancellation,” *Int. J. RF Microwave Computer-Aided Engineering*, 19(6), 2009, pp. 669-675.

159. J. Bellorado, S.S. Ghassemzadeh, L.J. Greenstein, T. Sveinsson, V. Tarokh, “Coexistence of ultra-wideband systems with IEEE-802.11a wireless LANs,” *IEEE Global Telecom. Conf.*, San Francisco, CA, Dec. 2003, pp. 410-414.

160. L. Zhu, H. Bu, K. Wu, “Broadband and compact multi-pole microstrip bandpass filters using ground plane aperture technique,” *IEE Proc. Microwaves, Ant. and Prop.*, 149(1), 2002, pp. 71-77.

161. C. Zhang and A. E. Fathy, "Reconfigurable pico-pulse generator for UWB applications," in *IEEE International Microwave Symp.*, 2006, pp. 407 - 410.

162. M. Gerding, T. Musch, B. Schiek , "A novel approach for a high-precision multitarget-level measurement system based on time-domain reflectometry," *IEEE Trans. on Microwave Theory and Tech.*, 54(6), 2006, pp. 2768 – 2773.

163. J. Han, C. Nguyen, "Coupled-slotline-hybrid sampling mixer integrated with step-recovery-diode pulse generator for UWB applications," *IEEE Trans. on Microwave Theory and Tech.*, 53(6), 2005, pp. 1875 – 1882.

164. M. M. Zinieris, R. Sloan, L. E. Davis, "A broadband microstrip-to-slot-line transition," *Microwave and Optical Technology Letters*, pp. 339-342, 1998.

165. Tektronix Electrical Sampling Modules Datasheet, http://www.tek.com/.

166. Picosecond Pulse Labs 7040 Sampler Module Datasheet, http://www.picosecond.com/.

167. M. Shinagawa, Y. Akazawa, T. Wakimoto, "Jitter analysis of high speed sampling system," in *IEEE VLSI Circuits Symposium*, Kyoto, Japan, May, 1989, pp. 95 - 96.

168. VTC4 series voltage controlled temperature compensated crystal oscillator, Vectron Int'l, Hudson, NH, 2007, p. 7.

169. Y.T. Chan, K.C. Ho, "Joint time-scale and TDOA estimation: analysis and fast approximation," *IEEE Trans. on Signal Processing,* 53(8), 2005, pp. 2625-2634.

170. J.A. Costa, N. Patwari, A.O. Hero, "Distributed weighted multidimensional scaling for node localization in sensor networks. *ACM Trans. Sen. Netw.* 2(1), 2006, pp. 39-64.

171. Application note VTC4, clippsed sine wave TCXO typical phase noise measurements, Vectron Int'l, Hudson, NH, 2007.

172. M. Tüchler, V. Schwarz, A. Huber, "Location accuracy of an UWB localization system in a multi-path environment," in *IEEE International Conf UWB,* Zurich, Switzerland, 2005, pp. 414-419.

173. H.G. Schantz, "Introduction to ultra-wideband antennas," in *IEEE Conference on Ultra Wideband Systems and Technologies*, Nov. 2003, pp. 1 – 9.

174. G. M. Wubbena, M. Schmitz, F. Menge, V. Boder, and G. Seeber, "Automated absolute field calibration of GPS antennas in real-time," in *Proc. ION GPS 2000*, 2000, pp. 2512–2522.

175. A. Elsherbini, C. Zhang, S. Lin, M. Kuhn, A. Kamel, A. E. Fathy, H. Elhennawy, "Enhancing the performance of antipodal Vivaldi antennas using a dielectric rod for high precision localization applications," in *IEEE AP-S Int. Symp.* 2007, pp. 1973 - 1976.

176. M. Kuhn, M. Mahfouz, A. Fathy, "A UWB real-time millimeter 3-D wireless positioning system," *Advances in UWB Localization and Sensing Workshop, European Microwave Conference*, Rome, Italy, Oct, 2009.

177. M. Kuhn, C. Zhang, B. Merkl, et al., "High accuracy UWB localization in dense indoor environments," in *IEEE International Conf UWB*, Hannover, Germany, 2008, vol. 2, pp. 129-132.

178. M. Kuhn, C. Zhang, S. Lin, M. Mahfouz, A. Fathy, "A system-level design approach to UWB localization," in *IEEE MTT-S International Microwave Symposium*, Boston, MA, 2009, pp. 409-412.

179. M. Kuhn, M. Mahfouz, C. Zhang, B. Merkl, A. Fathy, "A system-level simulation framework for UWB localization," *IEEE Trans. Microwave Theory Tech.*, 58(12), Part 1, 2010, pp. 3527-3537.

180. Advanced Design System (ADS), Agilent Technologies, 2009, http://www.home.agilent.com/agilent/product.jspx?nid=-34346.0.00&cc=US&lc=eng.

181. W. Eberle, *Wireless Transceiver Systems Design*, New York, NY, Springer Inc., 2008.

182. T. Kürner, M. Jacob, R. Piesiewicz, J. Schoebel, "An integrated simulation environment for the investigation of future THz communication systems: extended version," in *SIMULATION*, 84(2/3), 2008, pp. 123-130.

183. A. Lecointre, D. Dragomirescu, R. Plana, "System architecture modeling of an UWB receiver for wireless sensor network," *Embedded Computer Systems: Architectures, Modeling, and Simulation*, Lecture Notes in Computer Science 4599, Berlin, Germany, Springer Inc., 2007, pp. 408-420.

184. H. Zhai, S. Sha, V. Shenoy, S. Jung, M. Lu, K. Min, S. Lee, D. Ha, "An electronic circuit system for time-reversal of ultra-wideband short impulses based on frequency domain approach," in *IEEE Trans. Microwave Theory Tech.*, 58(1), 2010, pp. 74-86.

185. G. Manzi, M. Feliziani, P. Beeckman, N. van Dijk "Coexistence between ultra-wideband radio and narrow-band wireless LAN communication systems—part II: EMI evaluation," in *IEEE Trans. Electro. Compatibility*, 51(2), 2009, pp. 382-390.

186. G. Jue, D. Leiss, "System-level design for aerospace, defense, and SatCom applications using ADS," *Agilent AD Symposium*, Oct. 2004.

187. G. Vandersteen, P. Wambacq, Y. Rolain, P. Dobrovolný, et al., "A methodology for efficient high-level dataflow simulation of mixed-signal front-ends of digital telecom transceivers," in *Proc. ACM IEEE Design Auto.Conf.*, Los Angeles, CA, 2000, pp. 440-445.

188. G.G.E. Gielen, "Modeling and analysis techniques for system-level architectural design of telecom front-ends," in *IEEE Trans. Microwave Theory Tech.*, 50(1), 2002, pp. 360-368.

189. H. Chunxing, S. Gupta, "Statistical eye simulation and modeling high-speed serial links," Planet Analog, May 1, 2009, http://www.planetanalog.com/features/signal/showArticle.jhtml?articleID=197008439.

190. C. Zhang, A. E. Fathy, "Development of an ultra-wideband elliptical disc planar monopole antenna with improved omni-directional performance using a modified ground," in *Proc. IEEE AP-S Int. Symp.*, Albuquerque, NM, 2006, pp. 1689 – 1692.

191. J. Choi, W. Stark, "Performance of ultra-wideband communications with suboptimal receivers in multipath channels," *IEEE J. Selected Areas Comm.*, 20(9), Dec. 2002, pp. 1754-1766.

192. J. Proakis, M. Salehi, *Communication Systems Engineering, 2nd Edition*, Upper Saddle River, NJ: Pearson Education, Inc., 2002.

193. A. Saleh, R. Valenzuela., "A statistical model for indoor multipath propagation," *IEEE J. Sel. Areas Comm*., Vol. 5, Feb. 1987, pp. 128–137.

194. R. Vaughan and N. Scott, "Super-resolution of pulsed multipath channels for delay spread characterization," *IEEE Trans. Comm*., vol. 47, Mar. 1999, pp. 343-347.

195. C. Falsi, D. Dardari, L. Mucchi, and M. Z. Win, "Time of arrival estimation for uwb localizers in realistic environments," *EURASIP Journal on Applied Signal Processing*, vol. 2006, Article ID 32082, 13 pages, 2006.

196. M. Kuhn, C. Zhang, M. Mahfouz, A. Fathy, "Cross polarization effects and UWB performance of antipodal Vivaldi antennas using method of moments," URSI National Radio Science Meeting, URSI691, Ottawa, Canada, 2007.

197. R. J. Fontana, "Experimental results from an ultra-wideband precision geolocation system," *Ultra-Wideband, Short-Pulse Electromagnetics 5*, Part 2, Springer U.S., 2002, p. 215-224.

198. R. J. Fontana et al., “UWB dual tunnel diode detector for object detection, measurement, or avoidance,” U.S. Patent 6239741, May 29, 2001.

199. L. Zhao, A. Haimovich, “Performance of ultra-wideband communications in the presence of interference,” *IEEE J. Selected Areas Comm.*, 20(9), Dec. 2002, pp. 1684-1691.

200. T. Miller, L. Potter, J. McCorkle, “RFI suppression for ultra wideband radar,” *IEEE Trans. Aero. Elec. Sys.*, 33(4), Oct. 1997, pp. 1142-1156.

201. V. Mikhnev, P. Vainikainen, “A clutter reduction technique for microwave reconstruction of shallow underground targets,” *Euro. Conf. Ant. Prop.*, Nov. 2007.

202. I. O’Donnell, M. Chen, S. Wang, R. Brodersen, “An integrated, low power ultra-wideband transceiver for low-rate, indoor wireless systems,” *IEEE CAS Workshop on Wireless Comm. Networking*, Pasadena, USA, Sep. 2002.

203. S. Gezici, Z. Tian, G. Giannakis, H. Kobayashi, A. Molisch, H. Poor, Z. Sahinoglu, “Localization via ultra-wideband radios: a look at positioning aspects of future sensor networks,” *IEEE Signal Processing Magazine*, 22(4), Jul. 2005, pp. 70 – 84.

204. I. Guvenc, C. Abdallah, R. Jordan, O. Dedeoglu, “Enhancements to rss based indoor tracking systems using kalman filters,” *Int. Sig. Proc. Conf. & GSP Expo*, Dallas, USA, Apr. 2003.

205. Ekahau Real-Time Location System Brochure, Ekahau, Inc., 2008, http://www.ekahau.com/.

206. B. Alavi, K. Pahlavan, “Modeling of the TOA-based distance measurement error using UWB indoor radio measurements,” *IEEE Comm. Let.*, 10(4), Apr. 2006, pp. 275-277.

207. G. Bellusci, G. Janssen, J. Yan, C. Tiberius, “Low complexity ultra-wideband ranging in indoor multipath environments,” *IEEE/ION Pos., Loc. and Nav. Symp.*, Monterey, USA, May 2008, pp. 394-401.

208. A. Chehri, P. Fortier, P. Tardif, “On the TOA estimation for UWB ranging in complex confined area,” *URSI Int. Symp. Signals. Sys. Elec.*, Montreal, Canada, Jul. 2007, pp. 533-536.

209. M. Kuhn, J. Turnmire, M. Mahfouz, A. Fathy, “Adaptive leading-edge detection in UWB indoor localization,” in *IEEE Radio Wireless Symp.*, New Orleans, LA, 2010, pp. 268-271.

210. K. Yu, I. Sharp, Y. J. Guo, *Ground-Based Wireless Positioning*, West Sussex, United Kingdom: John Wiley & Sons Ltd., 2009.

211. Y. Vanderperren, G. Leus, W. Dehaene, "An Approach for specifying the ADC and AGC requirements for UWB digital receivers," *Inst. Engr. Tech. Seminar, UWB Technologies and Applications*, 2006, pp. 196-200.

212. Y. Wang, M. Kuhn, A. Fathy, "Advanced system level simulation of UWB three-dimensional through-wall imaging radar for performance limitation prediction," accepted in *IEEE MTT-S International Microwave Symposium*, Anaheim, CA, 2010.

213. Y. Wang, M. Kuhn, M. Mahfouz, A. Fathy, "A comprehensive system-level simulation paradigm for UWB systems," submitted to *IEEE AP-S Int. Symp.*, Toronto, Canada, 2010.

214. "Introduction to SimpliciTI," Technical Document SimpliciTI Overview (Rev. B), Texas Instruments Inc., Dec. 2008, http://focus.ti.com/lit/ml/swru130b/swru130b.pdf.

215. IEEE 802.15 Working Group for WPAN, http://ieee802.org/15/index.html.

216. IEEE 802.15 WPAN™ Task Group 4f (TG4f) Active RFID System, http://www.ieee802.org/15/pub/TG4f.html.

217. TG4f Merged Proposal: Decawave, Guard RFID, Time Domain, Ubisense, ZES, November 19, 2009, https://mentor.ieee.org/802.15/dcn/09/15-09-0804-01-004f-tg4f-merged-proposal-decawave-guard-rfid-time-domain-ubisense-zes.pptx.

218. H. Arslan, Z. N. Chen, M. G. Di Benedetto, *Ultra Wideband Wireless Communication*, John Wiley & Sons Inc., New Jersey, USA, 2006.

219. E. Elkhouly, A. Fathy, M. Kuhn, M. Mahfouz, "Investigation of challenges towards achieving sub-millimeter accuracy for UWB localization," in *IEEE AP-S Int. Symp.*, Spokane, WA, 2011, pp. 137-140.

220. M. Kuhn, M. Mahfouz, N. Rowe, E. Elkhouly, et al., "Ultra wideband 3-D tracking of multiple tags for indoor positioning in medical applications requiring millimeter accuracy," accepted in *IEEE Topical Conference on Biomedical Wireless Technologies, Networks, and Sensing Systems (BioWireleSS)*, Santa Clara, CA, 2012.

221. D. Lin, A. Trasser, H. Schumacher, "Si/SiGe HBT differential impulse generator for high-speed UWB applications," *Electronics Letters*, 46(24), 2010, pp. 1634 – 1635.

222. D. Lin, A, Trasser, H. Schumacher, "A fully differential IR-UWB front-end for noncoherent communication and localization," accepted *IEEE ICUWB*, Bologna, Italy, 2011.

223. B. Denis, N. Daniele, "NLOS ranging error mitigation in a distributed positioning algorithm for indoor UWB ad-hoc networks," *Int. Workshop on Wireless Ad-Hoc Networks*, Oulu, Finland, 2004, pp. 356-360.

224. Hittite HMC506LP4 Datasheet, Hittite Microwave Corp., Boston, MA, 2009, http://hittite.com/content/documents/data_sheet/hmc506lp4.pdf.

225. M. Mahfouz, M. Kuhn, G. To, *The Future of Ultra Wideband Systems in Medicine: Orthopedic Surgical Navigation* in Novel Applications of the UWB Technologies, InTech, August 2011.

226. M. Mahfouz, G. To, M. Kuhn, "No strings attached," IEEE Microwave Magazine, 12(7), Supplement, 2011, pp. S34-S48.

227. M. Mahfouz, G. To, M. Kuhn, "Smart Instruments: wireless technology invades the operating room," accepted in IEEE Topical Conference on Biomedical Radio and Wireless Technologies, Networks, and Sensing Systems, Jan. 2012.

228. E. Elkhouly, Q. Liu, M. Kuhn, M. Mahfouz, A. Fathy, "A study of the effect of jitter on UWB system positioning accuracy," accepted in IEEE Radio and Wireless Symposium, Jan. 2012.

229. M. Kuhn, M. Mahfouz, Y. Wang, J. Turnmire, A. Fathy, "Towards sub-millimeter accuracy in UWB positioning for indoor medical environments," in IEEE Topical Conference on Biomedical Radio and Wireless Technologies, Networks, and Sensing Systems, 2011, pp. 83-86.

230. M. Kuhn, M. Mahfouz, J. Turnmire, Y. Wang, A. Fathy, "A multi-tag access scheme for indoor UWB localization systems used in medical environments," in IEEE Topical Conference on Biomedical Radio and Wireless Technologies, Networks, and Sensing Systems, 2011, pp. 75-78.

231. M. Mahfouz, M. Kuhn, "UWB channel measurements and modeling for positioning and communications systems in the operating room," in IEEE Topical Conference on Biomedical Radio and Wireless Technologies, Networks, and Sensing Systems, 2011, pp. 47-50.

Appendices

Appendix A: UWB System-Level Simulation Framework User's Guide

Overview

The system simulation framework is outlined in Figure 1. This document discusses how to use the downloadable files to follow this sequence of steps in simulating the overall UWB indoor positioning system. This setup has only been tested in a Windows operating environment (including Windows XP Pro, Windows Server 2003, and Windows Vista). 64 bit architectures are not recommended since errors in running the ADS-Matlab cosimulation tools in ADS were encountered (e.g. unhandled memory exceptions) each time a 64x machine was used (contact Agilent for hopefully updated information regarding this issue). The Verilog co-simulation is not covered in this manual since the leading-edge detection has also been implemented in Matlab and can be used in testing the simulation framework without incorporating the Verilog co-simulator.

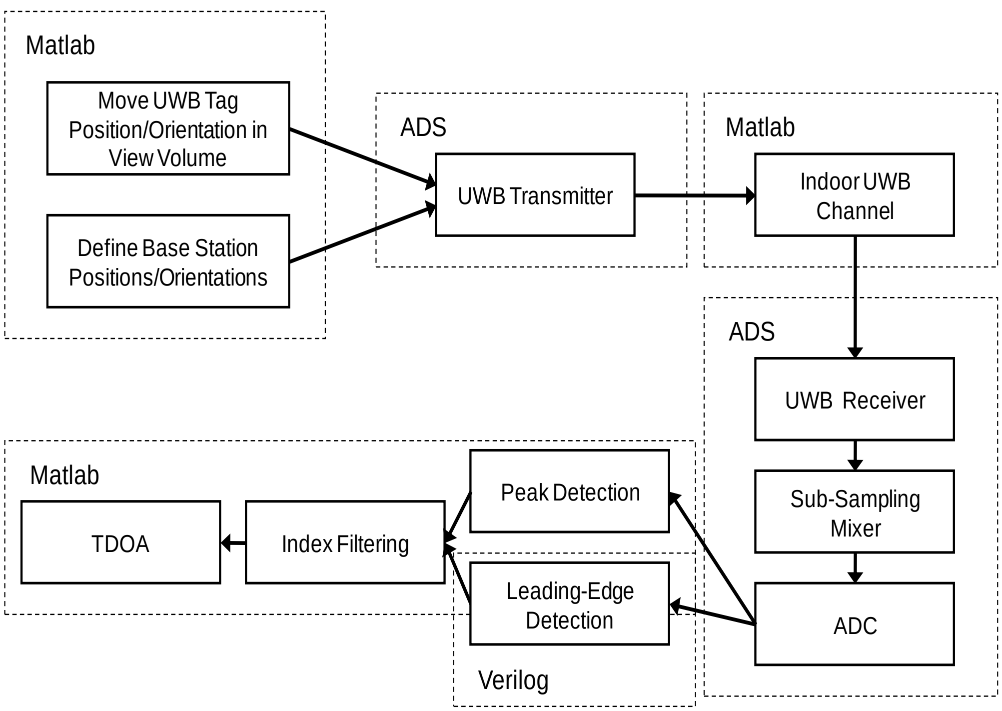

Fig. 1. Block diagram of overall system simulation framework outlining the various portions of the system simulated in Matlab, Agilent ADS, and Verilog.

Installation and Setup

1. Download UWB_System_Simulation_prj.zip from http://cmr.utk.edu.
2. Unzip and place in a path with no spaces (a requirement when running the ADS project).
3. Install Matlab 2006b. This is the only version of Matlab which has worked correctly with the ADS-Matlab cosimulation functions. Other versions of Matlab may work, but this is the only version which has been verified in running this framework. For example, Matlab 2006a, 2007a, 2007b, and 2008a were also tested and were unsuccessful in running the ADS-Matlab functions. Also, after contacting Agilent support in 2008, they stated that 2006b and potentially a couple earlier versions were the only ones supported for the ADS-Matlab cosimulation.
4. Verify that the bin folder for Matlab 2006b is included in the system path environment variable.
5. Install Agilent ADS 2006A or 2006C. Other versions of ADS may work, but these are the only ones which have been tested.
6. Go to Start->Programs->Advanced Design System->ADS Tools->License Preference Tool
    a. Add ALL licenses from the left side to the right side (Available to Selected). This is needed to ensure mdl_systemlib is enabled. The System Model Library (mdl_systemlib) is required for running the ADS-Matlab cosimulation tools.
7. Run ADS and open the project (the whole UWB_System_Simulation_prj folder).
8. Install the SRD design kit by going to the DesignKit menu on the main window and clicking "Install Design Kits…"
    a. Browse to the folder DesignKitSRD located in the main project folder and click OK.

UWB Transmitter via ADS

tx_iq.dsn

1. With the ADS project open, open a schematic window and open tx_iq.dsn
2. An overview of tx_iq is shown in Figures 2 and 3.
3. This is a transient simulation which includes the UWB pulse generator (in the form of a microwave circuit incorporating a step recovery diode on Rogers 4003C substrate of 20 mil thickness, epsilon_r = 3.55 for circuit design). Also included is LO_1 (modeled as the low phase noise source and amplifier as shown in Figure 2). Finally, the mixer and LNA (shown in Figure 2) are also included in tx_iq. Both I and Q channels are used to generate a complex signal (the Q signal is generated using a pi/4 time delay). This is done so that the complex signal from the UWB transmitter can be convolved with the complex impulse response generated from the IEEE 802.15.4a channel model. At the receiver side, only one channel (in the current setup Q) is used in the final time extended output signal to simulate the single channel noncoherent architecture of the positioning system.
4. The SRD design kit must be installed for this simulation to work. 100ns is used for the total simulation time (corresponds to PRF=10MHz). Max sample spacing of 10ps is used because this is the resolution of the subsampling mixer.
5. tx_rx_iq_testing.dds can be used after the simulation completes to analyze the UWB pulse.

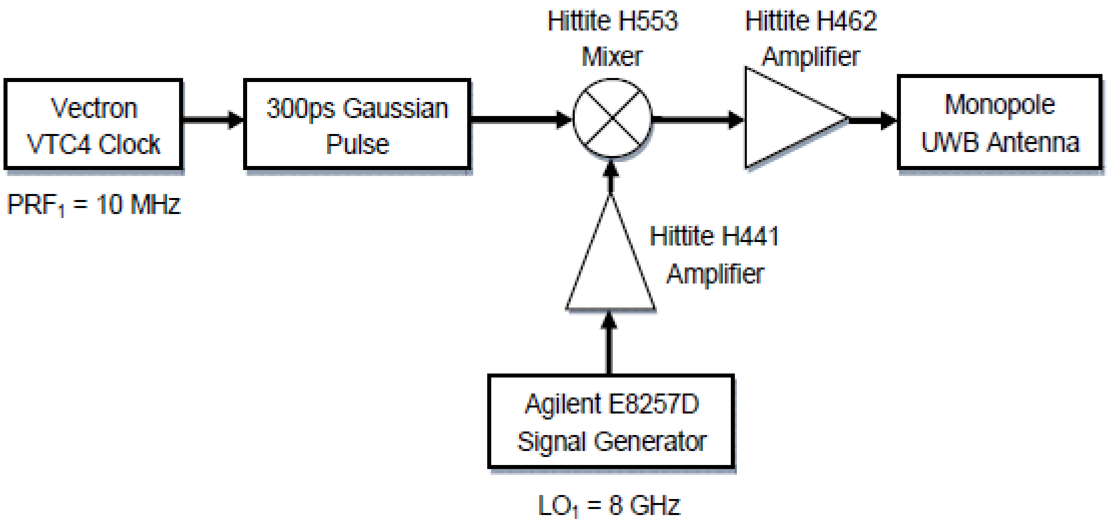

Fig. 2. Block diagram of the UWB transmitter where a 10 MHz clock triggers a step recovery diode pulse generator. The baseband pulse is then upconverted by a low phase noise LO (LO$_1$) and amplified by a low noise amplifier. The signal is transmitted via an omnidirectional monopole antenna.

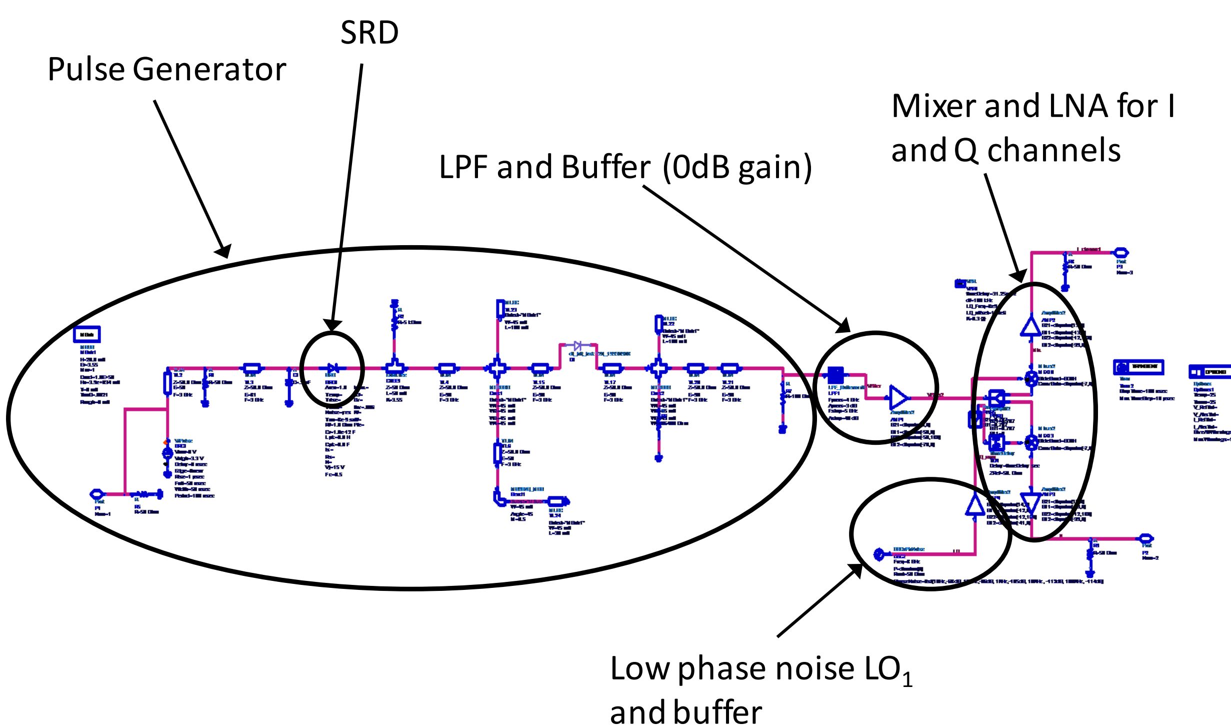

Fig. 3. Overview of tx_iq transient simulation which simulates the UWB transmitter including pulse generator, LO$_1$, mixer, and LNA.

transmitter_UWB_channel_RF_PG.dsn

1. With the ADS project open, open a schematic window and open transmitter_UWB_channel_RF_PG.dsn
2. An overview of transmitter_UWB_channel_RF_PG is shown in Figure 4. It is a discrete time simulation with 100ns total time and 10ps sample spacing (similar to tx_iq). tx_iq is embedded in this simulation (must be fed a timed signal). The I and Q signals output from tx_iq are combined into a complex waveform which is saved via a Matlab sink.
3. The ScriptDirectory for the Matlab sink should be set to the absolute path of the UWB_System_Simulation_prj/data directory. The MatlabWrapUp field defines where the MAT file containing the transmitted pulse is saved (currently set to TxChannelSignal_new.mat saved in the data directory). Figure 5 shows the UWB pulse after upconversion (real component).
4. This simulation only produces one pulse. Channel effects and a corresponding pulse train (needed for undergoing the subsampling/time extending process) are created via Matlab after completing this step. The Matlab Command Window and a figure of the frequency response of the pulse should popup as the simulation completes (ensures Matlab cosim is working).

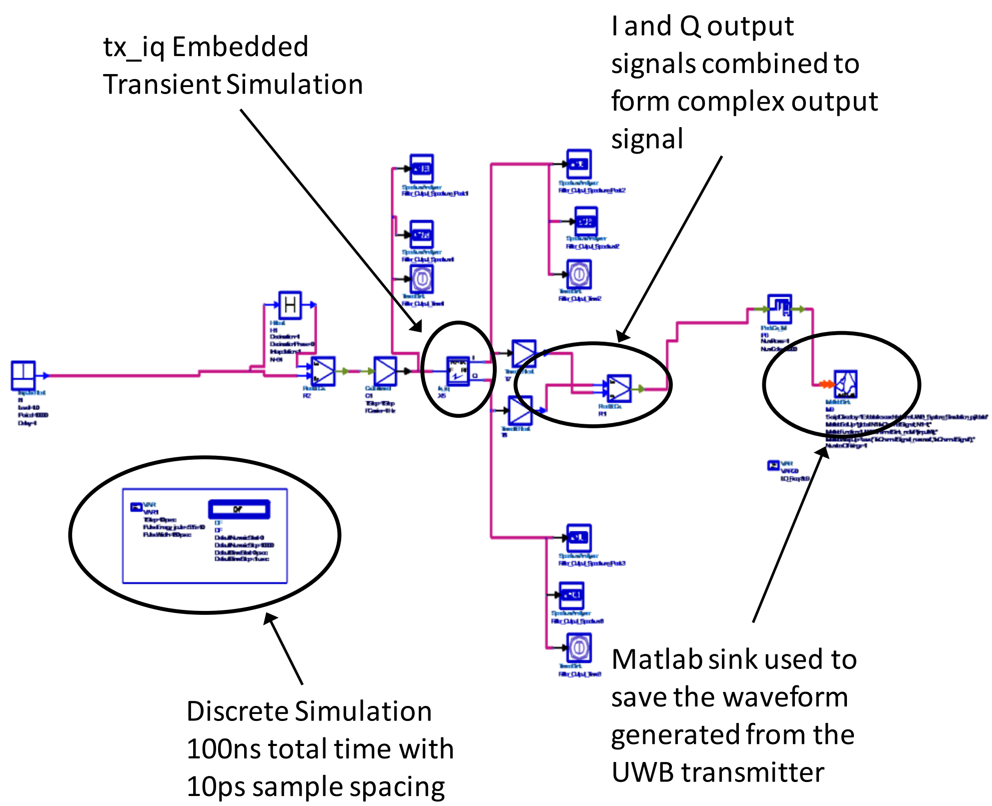

Fig. 4. Overview of transmitter_UWB_channel_RF_PG discrete time simulation which embeds the tx_iq transient simulation and formats the I and Q output signals into a complex waveform passed to a Matlab sink for processing and saving as a MAT file.

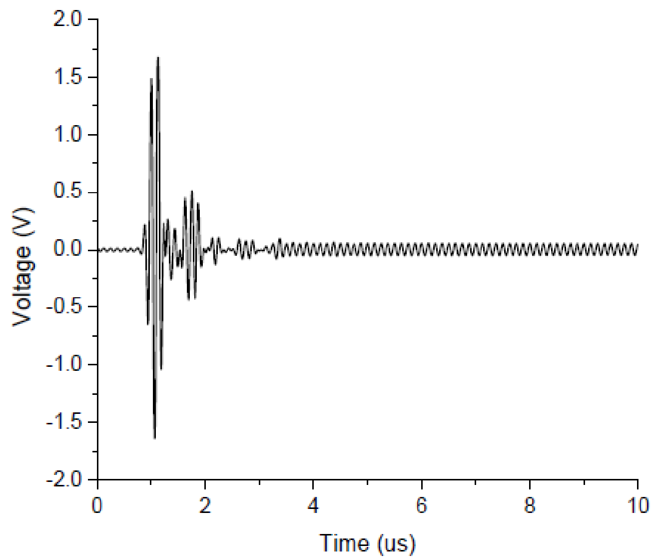

Fig. 5. Simulated UWB pulse after upconversion from LO_1 and amplification.

UWB Channel Effects via Matlab

Complex Impulse Responses

1. The Matlab file generate1000IRs.m (located in the data directory) is used to create the complex impulse responses.
2. The channel model number can be specified (1,2,3,4,7,8,10). The default parameters (including 10ps sample spacing) will work for CM 3,4,7,8,10 – Commercial LOS, Commercial NLOS, Industrial LOS, Industrial NLOS, Operating Room LOS (my own addition ☺)). Instead of generating 1000 IRs (time intensive), the default is 8. This is a more reasonable number for the receiver step since each receiver simulation (i.e. each impulse response through the receiver chain) takes 1-2 hours to run due to subsampling 1000-10,000 pulses (although you can have multiple ADS applications open at once to run in parallel as outlined in the ADS UWB Receiver section). The CM7 IRs take substantially longer to generate – be patient! It is running.

   10ps sample spacing will NOT work for generating IRs for CM 1,2 (Residential LOS and NLOS). This seems to be due to the larger values of γ_0 which occur in the residential LOS channel (power delay profile decay constant for each individual cluster) and must violate some sort of assumption in discretizing energy bins on the order of 10ps sample spacing. This problem is resolved by increasing the sample period to above 70ps (sampT). If the sample spacing is increased to generate IRs for CM 1,2, you MUST resample (see Matlab "resample" command) to get IRs back to 10ps sample spacing (or whatever sample spacing is set for the overall simulation).
3. Make sure to save the IRs into a MAT file to be loaded in the next step.

Add Channel Effects to transmitted UWB signal

1. The Matlab file createPTwithPL2.m (located in the data directory) is used to create the complex pulse train which will be input to the UWB receiver.
2. A typical call to this function would be:
   myOutputPulseTrain=createPTwithPL2('CM3_outputPTs.mat',3,1,50e6,1000,10e-12,8);

   a. 'CM3_outputPTs.mat' is the output MAT file to the current (data) directory
   b. 3 is the channel model
   c. 1 is the transmitter/receiver distance (1m)
   d. 50MHz is the pulse repetition frequency (could also be 10MHz, but 50MHz is only a 20ns period which significantly reduces simulation time of the UWB receiver with ADS).
   e. 1000 is the expansion factor (number of pulses in the pulse train)
   f. 10e-12 is the sample spacing (10ps)
   g. 8 is the number of impulse responses read in from the MAT file generated in the previous step. You MUST make sure this path is correct in the body of createPTwithPL2.m. You MUST also make sure the path to the transmitted signal from ADS (the UWB Transmitter) is correct.
3. The output of this function is an array which contains pulse trains for each impulse response generated in the previous step. These values are complex numbers. The transmitted pulse is convolved with the impulse response. Pathloss effects and Tx/Rx antenna gain/loss effects are also added in during this step. Figure 6 shows an example using Commercial LOS (CM3).

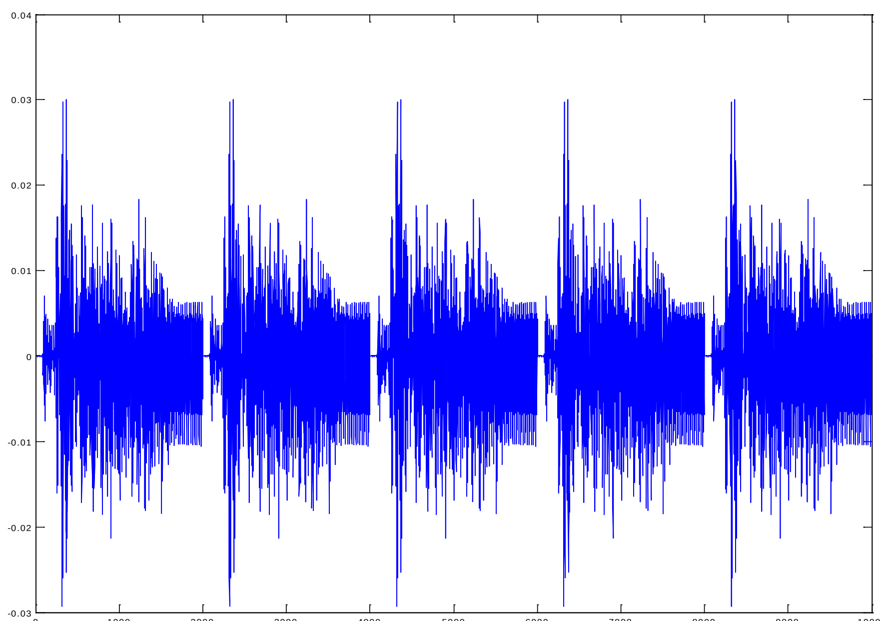

Fig. 6. Typical UWB pulse train. 2000 points per pulse at 10ps sample spacing for each 20ns period (50MHz pulse repetition frequency). This is for the CM3 (Commercial LOS) channel. The peak-to-peak amplitude is around 60mV. Multipath fading and pathloss can clearly be seen.

UWB Receiver via ADS

rx_sub_transient.dsn

1. With the ADS project open, open a schematic window and open rx_sub_transient.dsn
2. An overview of rx_sub_transient is shown in Figures 7 and 8.
    a. This is a transient simulation which starts at the low noise amplifier in the receiver chain (Fig. 7). Also included is the medium power amplifier and LO_2 (modeled as the low phase noise source shown in Fig. 7). The mixer downconverts the signal with LO_2. This is followed by two stages of low pass filtering (DC-5 GHz). Next comes the subsampling process which uses the ADS component Sampler. Only the Q channel is utilized, although the I channel is also output from rx_sub_transient. The variable LO_offset is added to LO_Freq to get the final LO_2 frequency. f0 is the pulse repetition frequency (should be the same as f0 used in tx_iq.dsn). df is the offset in pulse repetition frequency needed for subsampling. df depends on PRF and the expansion factor. For example, for PRF=100MHz and α=1000 (expansion factor), df=100kHz. For PRF=10MHz and α=10,000, df=1kHz. (1) solves for α while (2) solves for df.

$$\alpha = \frac{PRF_1}{|PRF_1 - PRF_2|} \tag{1}$$

$$df = |PRF_1 - PRF_2| = \frac{PRF_1}{\alpha} \tag{2}$$

3. rx_sub_transient cannot be run by itself, rather, it has to be embedded in receiverQ.dsn and run from there. This will ensure that the pulse train is input to rx_sub_transient.

receiverQ.dsn

1. With the ADS project open, open a schematic window and open receiverQ.dsn
2. An overview of receiverQ is shown in Figure 9. It is a discrete time simulation with $\frac{1}{PRF_1}\alpha$ total time (e.g. if PRF_1=100MHz and α=1000, Sim Time = 10us) and 10ps sample spacing. rx_sub_transient is embedded in this simulation (must be fed a timed signal). The input signal to the Matlab Source is the final pulse train created in the UWB Channel Effects via Matlab section. The signal output to the Matlab Sink is the time extended UWB pulse after subsampling and analog-to-digital conversion. An example of the final received signal is shown in Figure 10.
3. The ScriptDirectory for the Matlab Source should be set to the absolute path of the UWB_System_Simulation_prj/data directory (or another directory with the pulse train MAT file). In MatlabWrapUp, the proper MAT file with the pulse train should be loaded (make sure name is correct). In MatlabFunction, the proper variable name should be fed into output#1.
4. For the Matlab Sink, the ScriptDirectory should be set correctly. The data can either be processed in MatlabFunction (e.g. saveSig.m) or saved in a MAT file in MatlabWrapUp. The final signal is stored in the variable finalRxChainSigsQ (which must be initialized in MatlabSetUp).

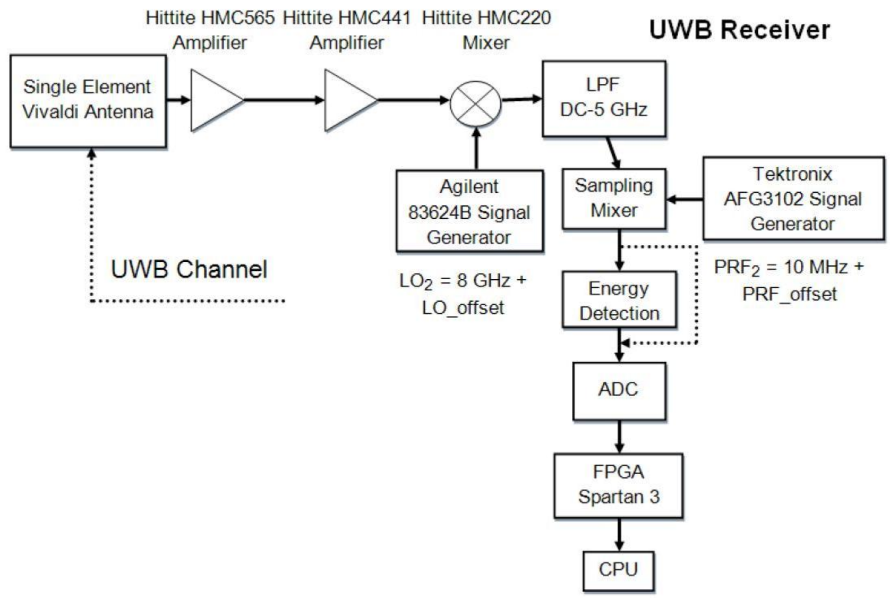

Fig. 7. Block diagram of UWB receiver where the signal, after passing through the UWB channel, is received by a single element Vivaldi antenna. It goes through a low noise amplifier and a medium power amplifier. It is then downconverted via a low phase noise source (LO_2) and low pass filtered. It undergoes a subsampling process to time expand the signal and lessen the ADC requirements. Energy detection can then be optionally employed. On the digital side, the signal goes through the ADC and then goes to an FPGA for peak or leading-edge detection. The final TDOA calculations and index filtering are done on a computer.

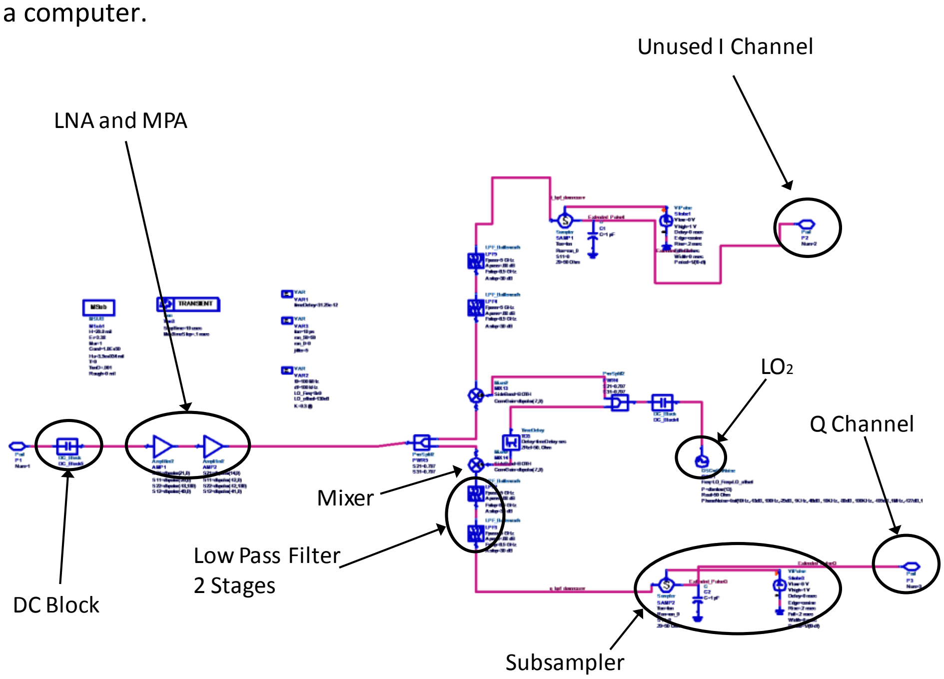

Fig. 8. Overview of rx_sub_transient transient simulation which simulates the UWB receiver including LNA, MPA, mixer (downconversion), LO_2, two stages of low pass filtering, and subsampling.

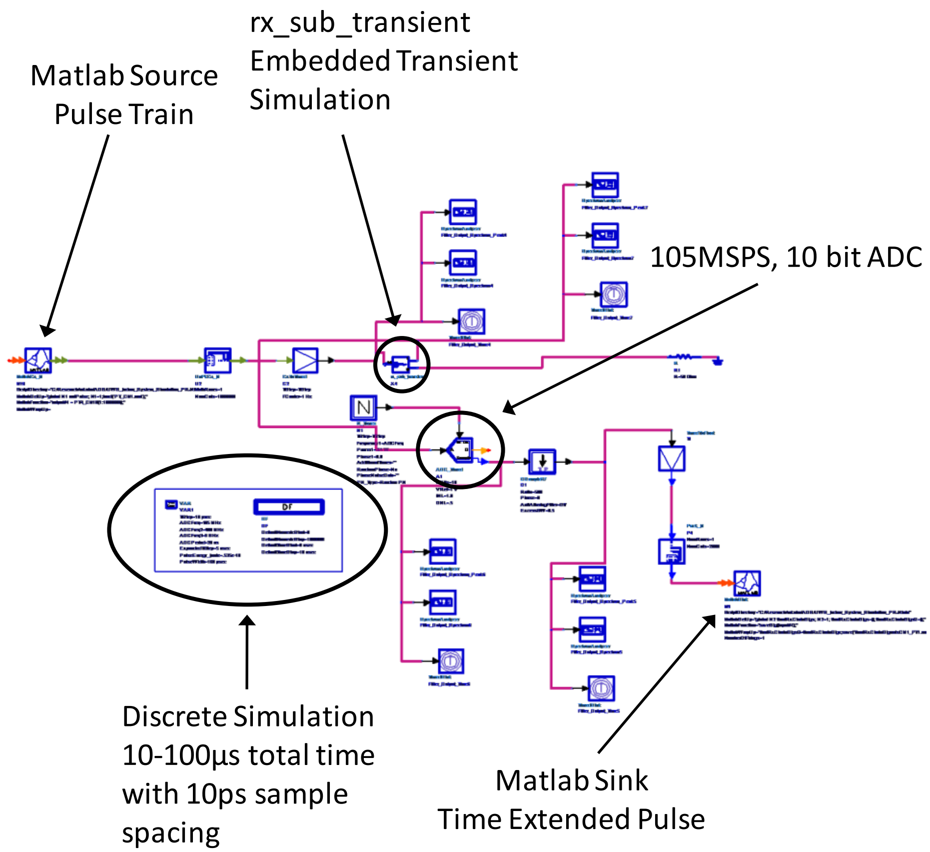

Fig. 9. Overview of receiverQ discrete time simulation which embeds the rx_sub_transient transient simulation. The UWB pulse train is read from the Matlab source. The subsampling takes place in the rx_sub_transient block. The pulse then goes through the ADC and finally the time extended, digital pulse is saved via the Matlab sink.

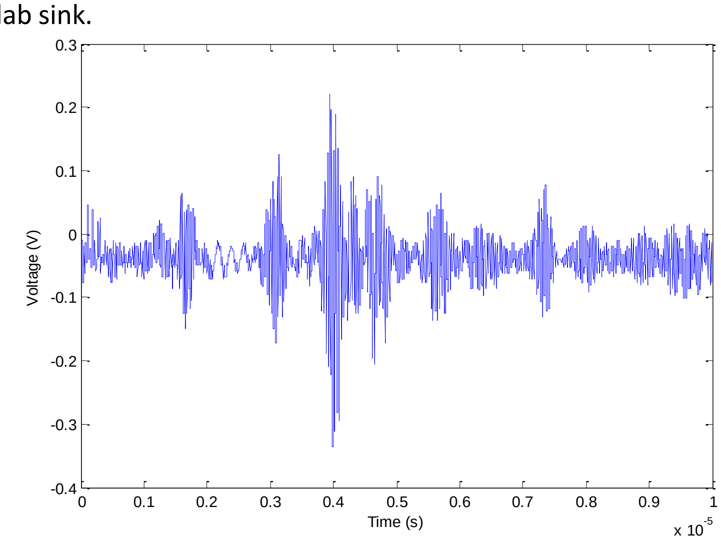

Fig. 10. Received CM3 Commercial LOS signal after passing through the receiver chain depicted in Figures 8 and 9.

Final Simulations of Experimental Setups via Matlab

The driver Matlab files for the two experimental setups outlined in the corresponding journal article (Kuhn et al., “A system level simulation framework for UWB localization,” IEEE Trans Microwave Theory Tech, Oct, 2010) are included in the data directory. Here is an overview of the five driver files:

postProcessRxDataTrack4BS_CM1_jitter.m – Runs final simulation of CM1 Residential LOS IEEE 802.15.4a channel model for optical rail experiment outlined in Section III of the paper.

postProcessRxDataTrack4BS_CM3_jitter.m – Runs final simulation of CM3 Commercial LOS IEEE 802.15.4a channel model for optical rail experiment outlined in Section III of the paper.

postProcessRxDataTrack4BS_CM7_jitter.m – Runs final simulation of CM7 Industrial LOS IEEE 802.15.4a channel model for optical rail experiment outlined in Section III of the paper.

postProcessRxDataTrack6BS_Exp_CM1_jitter.m - Runs final simulation of CM1 Residential LOS IEEE 802.15.4a channel model for multi-base station experiment outlined in Section IV of the paper.

postProcessRxDataTrack6BS_Exp_noMP_jitter.m - Runs final simulation of no multipath channel model for multi-base station experiment outlined in Section IV of the paper.

All of these files are meant to be opened and run directly. They are not functions but rather driver files which call all of the necessary functions. The final output is min error, RMS error, and max error of the TDOA obtained points for the five different algorithms (signal strength, first peak detection, iterative peak subtraction, matched filter, and leading-edge detection) obtained from all applicable points (975 points for the optical rail experiment and 9 points for the multi-base station experiment). This error is using the points obtained from the optical tracking system as the correct ground truth 3-D position of the UWB transmitter for each point in the experiment.

The final received signal after subsampling and analog-to-digital conversion must be input when running any of these Matlab drivers. It is easiest to save the signal as a MAT file in the data directory and manually change the name of the loaded MAT file. This line of code appears near the top of the driver files. Please note that the final received signal is the first parameter sent to the addJitterAWGNToTimeExtendedSig.m function. You MUST change this variable depending on what you input from your MAT file. Typically I name it finalRxChainSigsQ and have at least 4-6 signals stored from my ADS simulations. Each signal should be a separate instantiation of the applicable channel model. The function addJitterAWGNToTimeExtendedSig.m will create a new pulse train which adds random jitter between the pulses as well as AWGN and even time scaling (dependent on the expansion factor). The jitter and AWGN are based on experimental measurements. The jitter is dependent on isPRFCoherent and isLowPNLOs.

Due to the statistical nature of the channel model signals, the jitter, the time scaling, and the AWGN, simulation results will vary from run to run. It may be necessary to run a batch of simulations and average the results to get a better idea of how the system is performing. It is sometimes necessary to turn on and off energy detection to see how the various peak and leading edge detection algorithms perform. For example, when looking at the 6BS case in CM1, leading-edge detection performed correctly with energy detection enabled but gave poor results with energy detection disabled. Iterative peak subtraction, on the other hand, performed correctly without energy detection (and typically performs betters without it given the nature of the algorithm since energy detection averages out some of the multipath pulses). Here is a summary of the parameters which can be set/changed when running the final simulation:

```
N=4875; %actual number of data points needed to do 5x TDOA averaging
         given 975 transmitter points x 5
c=3e8; %speed of light
T=5e-9; %sample spacing for ADC
T_PRF=100e-9; %10 MHz
addTS=1; %add Time Scaling, yes(1) or no(0)
scalingFactor=100e-15; % per 10 MHz clock period for drift of system
                         clocks
alpha=2500; %expansion factor
useED=1; %energy detection
numAve=1; %how many pulses to average on the FPGA before peak/leading
           edge detection
isPRFCoherent=0; %are pulse repetition frequency clocks coherent
isLowPNLOs=1; %are low phase noise LOs used
useMIQR=1; %turn on/off MIQR filter
TDOA_ave=5; %number of samples to average at TDOA step
whichCM=1; %channel model number
N_Tx_P = 975; %number of distinct transmitter points
N_BS = 4; %number of base stations
sampT=10e-12; %analog sampling rate of ADS simulations and
               subsampler…default is 10ps
```

The main parameters to consider include usED (use energy detection). Energy detection effectively averages or takes the envelope of the signal before running the leading-edge or peak detection algorithms. For example, first peak detect and iterative peak subtraction typically work better without energy detection while leading-edge detection typically works better with energy detection enabled (at least in LOS conditions). isPRFCoherent defines how much jitter to add based on whether or not the PRF clocks at the transmitter and receiver are coherent (based on experimental measurements). isLowPNLOs specifies whether or not low phase LOs (i.e. Agilent sources with phase locked loops) are used at the

Tx/Rx or if high phase noise LOs (i.e. VCOs) are used at the Tx/Rx. whichCM defines the IEEE 802.15.4a channel model (CM1=Residential LOS, CM2=Residential NLOS, CM3=Commercial LOS, CM4=Commercial NLOS, CM7=Industrial LOS, CM8=Industrial NLOS, CM10=Operating Room LOS). useMIQR enables or disables MIQR filtering for the index values after peak/leading-edge detection (typically set to 1). TDOA_ave is the number of TDOA values to average for the final 3-D Tx position. Values of 1-5 are typically used. alpha is the expansion factor (depends on ADS simulations and effects jitter seen in final pulse train). T is the sample spacing from the ADC (5ns or 200MSPS is used since it is close to the 105MSPS ADC used in the experimental system). N_Tx_P is the number of transmitter points. These points are typically obtained with an optical tracking system used as ground truth for examining the UWB positioning system. N_BS is the number of base stations. The 3-D base station positions are also obtained with the optical tracking system.

Experimental Setup

`BS(x,:)` – 3-D base station position for base station x, must be defined for all N_BS base stations
`myTxPoints` – 3-D transmitter positions, must be defined for all N_Tx_P transmitter points

The experimental setup can be custom defined with a certain number of base stations and tag positions. In the optical rail experiment shown in Figure 11, the points for the 3-D base station positions (static) as well as the 975 points of the transmitter moving along the optical were input in the upper portion of the Matlab drivers (postProcessRxDataTrack4BS_CM1_jitter.m, postProcessRxDataTrack4BS_CM3_jitter.m, postProcessRxDataTrack4BS_CM7_jitter.m). Any experimental setup can be defined, although these values are used as ground truth so that the RMS error of the UWB positioning system can be calculated for the various peak and leading-edge detection algorithms.

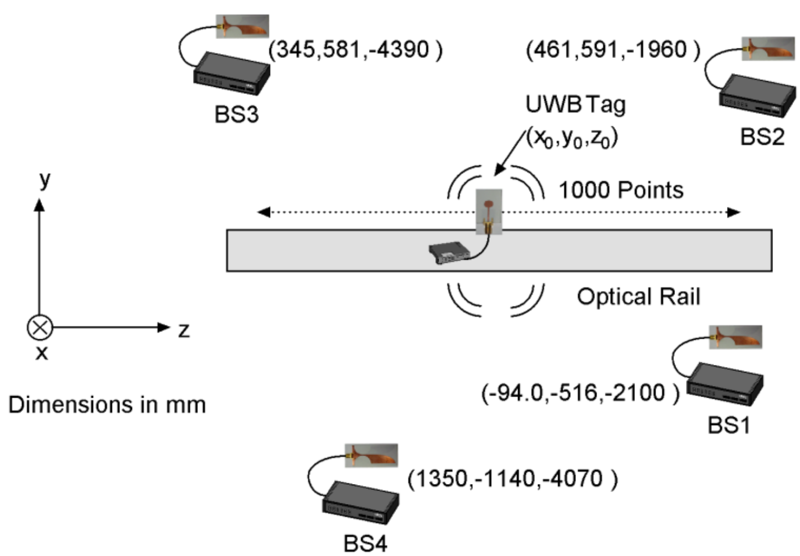

Fig. 11. Optical rail experimental setup where 1000 (or really 975) points are obtained as the tag is moved along the rail. For all 4BS Matlab driver files, this is the experimental setup used.

Overview of Function Calls

All functions should have some internal documentation on their purpose and the input and output variables needed for their operation.

addJitterAWGNToTimeExtendedSig.m – creates a pulse train with jitter, AWGN, and time scaling for each Tx-BS path using the overall simulation parameter settings. Must pass final sub-sampled received signal.

runLE_PD_AlgsPT.m – runs the peak and leading-edge detection algorithms on the created pulse trains. Need a call to this function for each Tx-BS path. The actual peak and leading-edge detection sample index values are returned for the entire pulse train.

The reference sample index values (e.g. FP_Ref, MF_Ref, SS_Ref, IPS_Ref, and LE_Ref) were obtained from simulating idealized received signals with no multipath, phase offset, jitter, AWGN, or time scaling. They are used to calculate the error between the correct peak or leading-edge detection sample index and the value which the algorithm returned for the non-idealized received signal.

MIQR_filter.m – applies the MIQR filter to the sample index arrays – default is 21 samples

Ranging errors for all algorithms are then calculated. This is followed by actual TDOA calculations using the non-ideal ranging values for all of the various algorithms. The min, max, and RMS error for the entire simulation is then output for all five algorithms (signal strength, iterative peak subtraction, leading-edge detection, first peak detect, and matched filter). An example output of the final error calculations would be (for the optical rail experiment with CM7 channel model with and without Energy Detection):

CM7 Industrial LOS without Energy Detection

RSS:	RMS 42.3889	MAX 60.525564	MIN 28.399577
Matched:	RMS 45.0582	MAX 67.008492	MIN 29.251802
First Peak:	RMS 48.8279	MAX 323.48309	MIN 6.955923
IPS:	RMS 44.7212	MAX 71.647588	MIN 24.658873
LE:	RMS 7.5755	MAX 21.627760	MIN 0.688366

CM7 Industrial LOS with Energy Detection

RSS:	RMS 108.7345	MAX 135.934548	MIN 85.052730
Matched:	RMS 107.5453	MAX 134.770702	MIN 82.740932
First Peak:	RMS 103.0297	MAX 1056.89475	MIN 26.897813
IPS:	RMS 107.5451	MAX 134.770702	MIN 82.740932
LE:	RMS 6.8458	MAX 21.576710	MIN 1.042849

All variables, including ranging errors, sample index values, etc., will be stored and available for display and analysis once the final Matlab simulation completes. This simulation (975 points) takes roughly 5-6 hours on an Intel Xeon 2.0 GHz, quad processor, 8 GB RAM, Dell Poweredge 6650 Server (utilizing only one core). The 6BS experiment (9 points) only takes 5 or so minutes to run on the same server.

Appendix B: Tag RF Board Layout and Bill of Materials

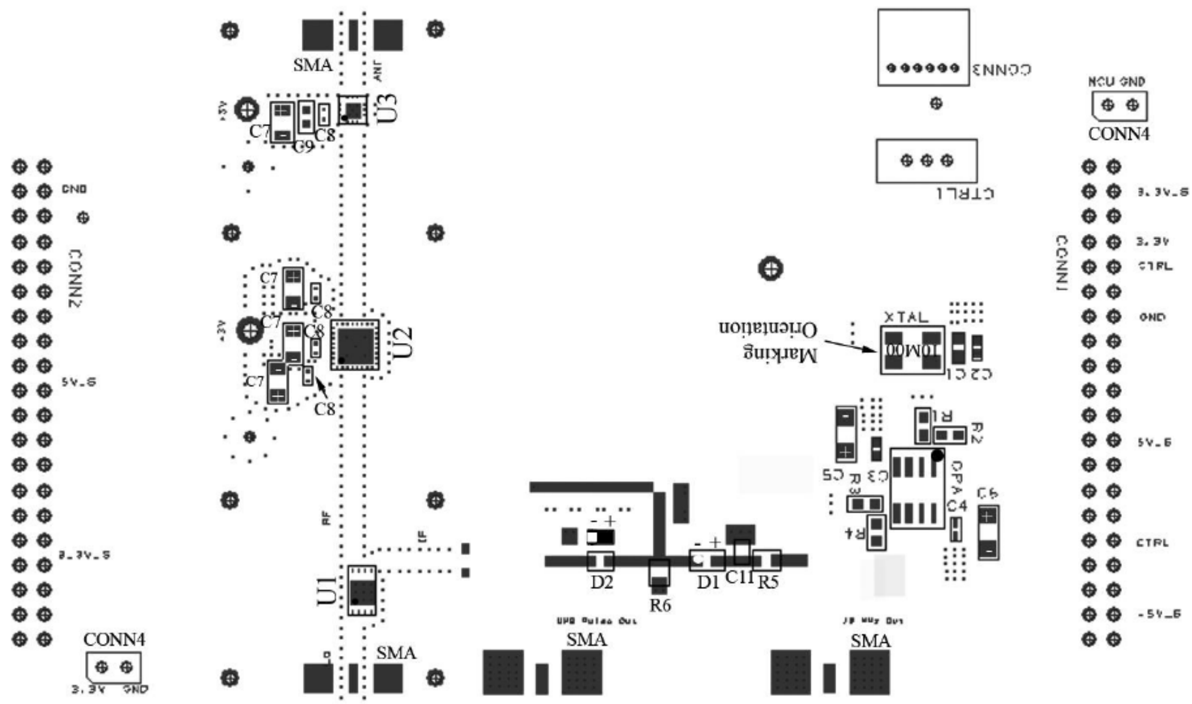

Top Layer Silk and Mask Layers

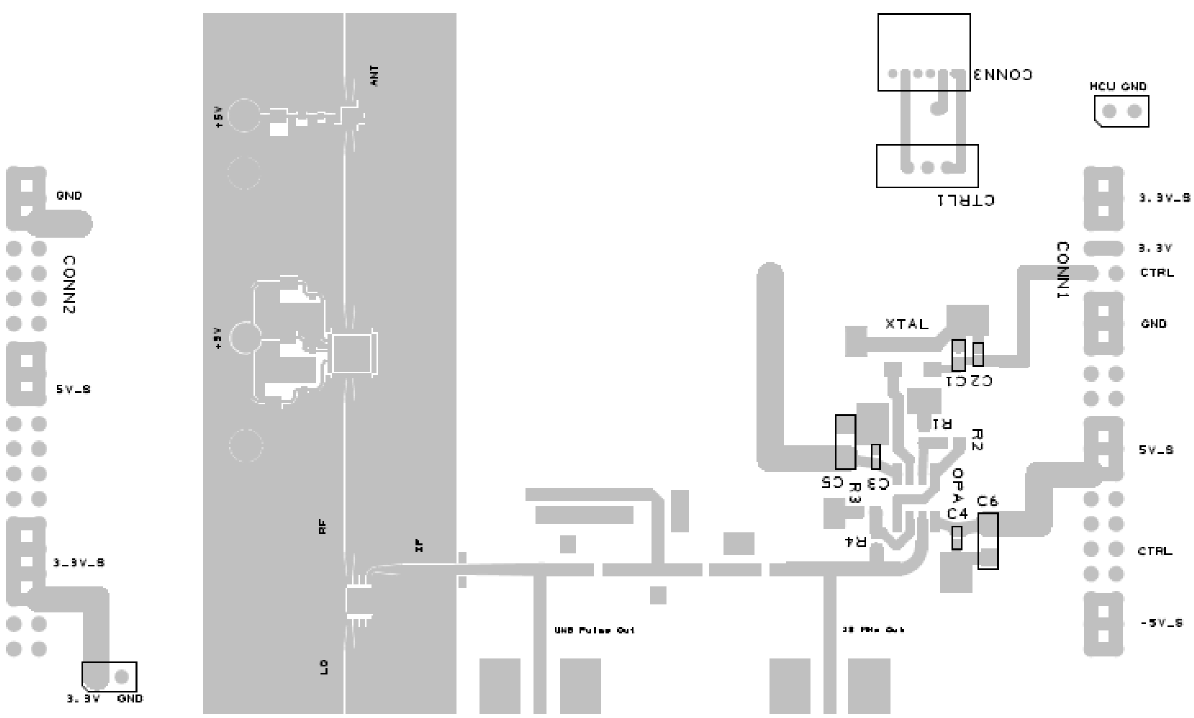

Top Layer Copper

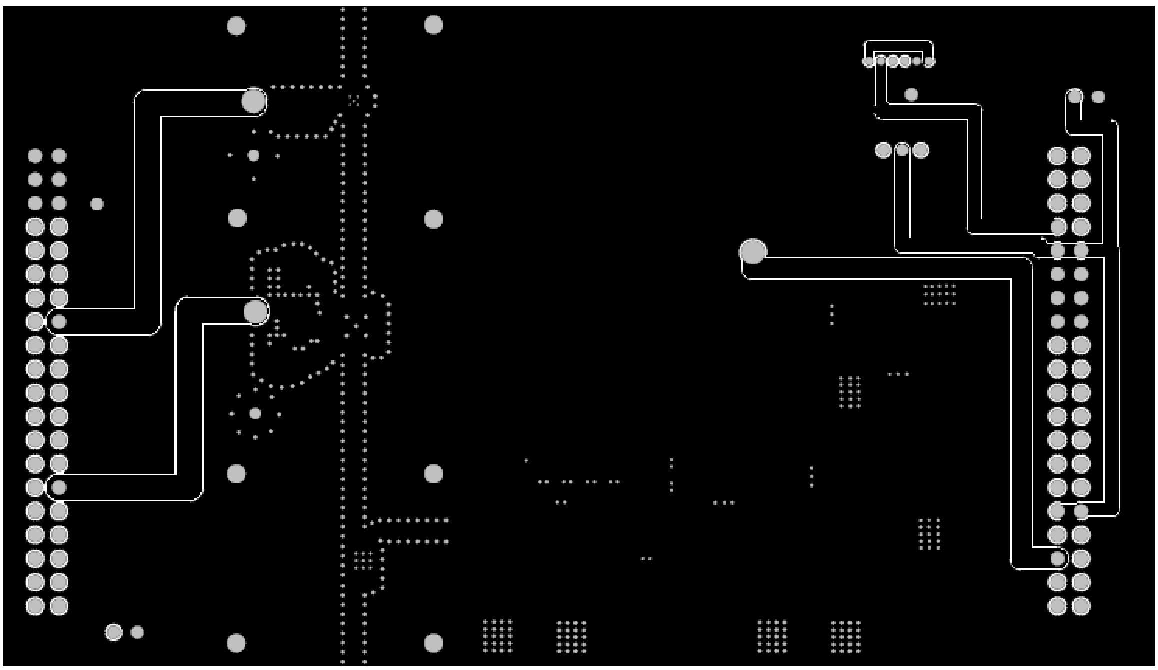

Bottom Layer

Bill of Materials

Board Annotation	Quantity	Part Number	Description
U1	1	HMC220MS8E	Mixer
U2	1	HMC565LC5	LNA
U3	1	HMC441LC3B	MPA
SMA	4	PSF-S01-000	SMA Connectors
C1	1	445-5100-1-ND	10000pF, 0603
C2,C3,C4	3	490-1318-1-ND	0.1uF, 0402
C5,C6,C7	6	478-1753-1-ND	2.2uF tantalum capacitor, 1206 SMT
C8	4	478-1082-1-ND	100pF 0402 capacitor
C9	1	PCC1772CT-ND	1000pF CAP, 50V, 0603
XTAL	1	VTC4	Vectron, 10MHz crystal
R1,R3	2	RMCF0603FT237RCT-ND	237 Ohm RES, 0603, OPA
R2,R4	2	RHM475HCT-ND	475 Ohm RES, 0603, OPA
OPA	1	296-15212-5-ND	Current limiting op amp, PG
R5	1	311-2.00HRCT-ND	2.0Ohm, 0.1W, 0603, PG
C11	1	478-1371-1-ND	1000pF CAP, 50V, 0805, PG
D1	1	MSD700	Micrometrics SRD, PG
R6	1	P51GCT-ND	50 Ohm Resistor, 0603, PG
D2	1	SMSD6004-SOD323	Metelics Schottkey Diode, PG
CTRL1	1	450-1634-ND	SWITCH SLIDE 2POS VERT BLACK SSJ
CONN1,CONN2 --> THESE CONNECTORS GO ON BOTTOM OF THE BOARD	2	IPS1-120-01-S-D-FL	Power Socket Strip SKT 40 POS 2.54mm Solder ST Thru-Hole, AVNET
CONN3	1	850-10-006-20-001000	6 pin header to interface
CONN4	2	609-3469-ND	2 pin header

Appendix C: Tag Power Board Layout and Bill of Materials

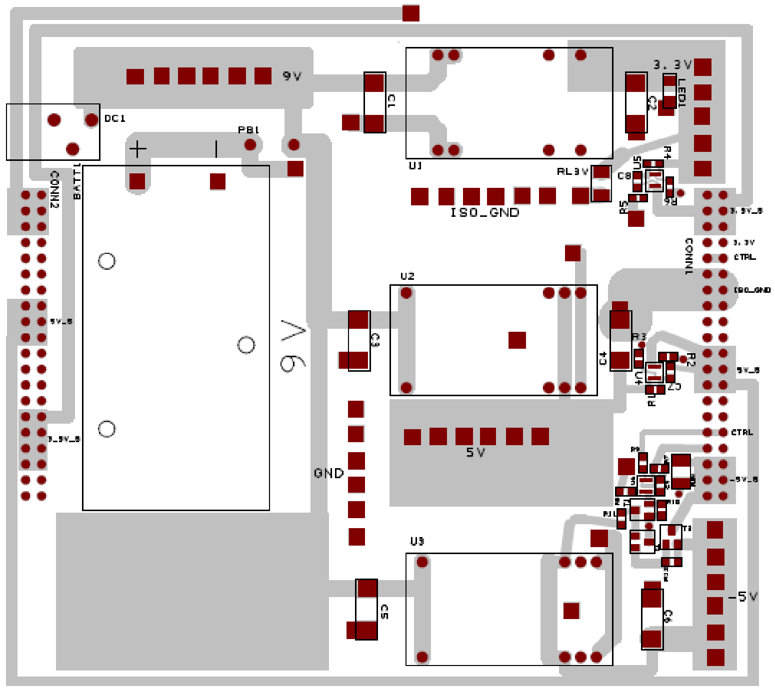

Top Layer

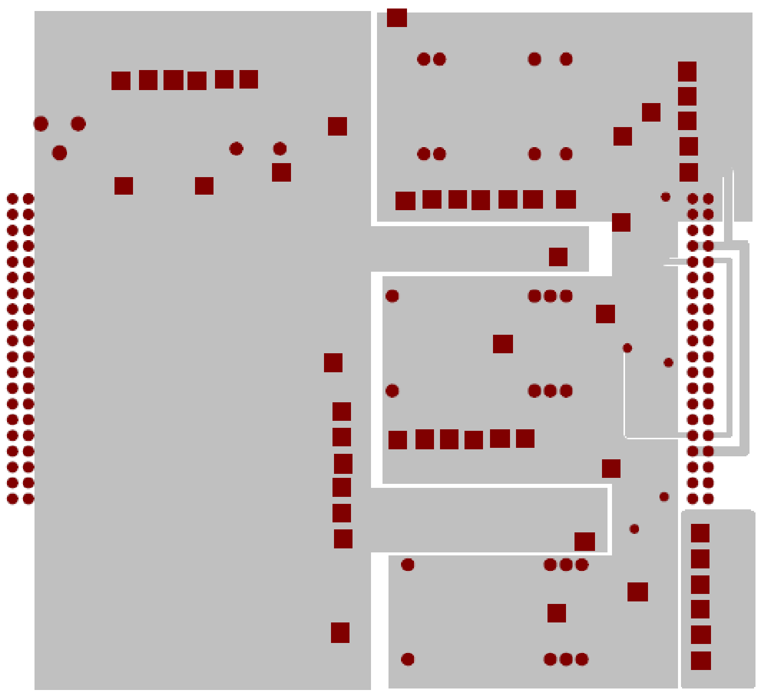

Bottom Layer

Bill of Materials

Board Annotation	Quantity	Part Number	Description
BATT1	1	BC9VPC-ND	9V PC Mountable Battery Case
C1,C3,C4,C5,C6	5	399-5202-1-ND	100uF, 25V, CAP, SMT, 0.15Ohm
U1	1	811-1383-5-ND	3.3V DC-DC Converter, Flyback, Isolated
C2	1	495-1552-1-ND	220uF, 16V, CAP, SMT, 0.10Ohm
U2,U3	2	811-1399-5-ND	5V, DC-DC Converter, Flyback, Isolated
LED1	1	P11539CT-ND	1206, Blue LED, 3.2-3.7 V, 5mA current consumption
CONN1, CONN2	2	IPT1-120-08-S-D	Strip HDR 40 POS 2.54mm Solder ST Thru-Hole, AVNET
PB1	1	518PB-ND	SPST Switch, 0.3A @ 12VDC, Pushbutton
DC1	1	CP-102A-ND	2.1mm connector jack
T3	1	FDN359BNCT-ND	N-Type MOSFET, Load Switch for -5V
U4,U5,U6	3	FDG6342LCT-ND	Integrated Load Switch for 5V, 3.3V
T1	1	NDS332PCT-ND	MOSFET P-CH 20V 1A SSOT3
T2	1	FDV301N	Trans MOSFET N-CH 25V 0.5A 3-Pin SOT-23 T/R
R3,R6,R9	3	P100KGCT-ND	RES 100K OHM 1/10W 5% 0603 SMD
R1,R4,R7	3	P1.0KGCT-ND	RES 1.0K OHM 1/10W 5% 0603 SMD
R2,R5,R8	3	P100GCT-ND	RES 100 OHM 1/10W 5% 0603 SMD
C7,C8,C9	3	490-1570-1-ND	CAP CER 1000PF 25V Y5V 0603
R10,R11,R12	3	P100GCT-ND	RES 100 OHM 1/10W 5% 0603 SMD

Schematic

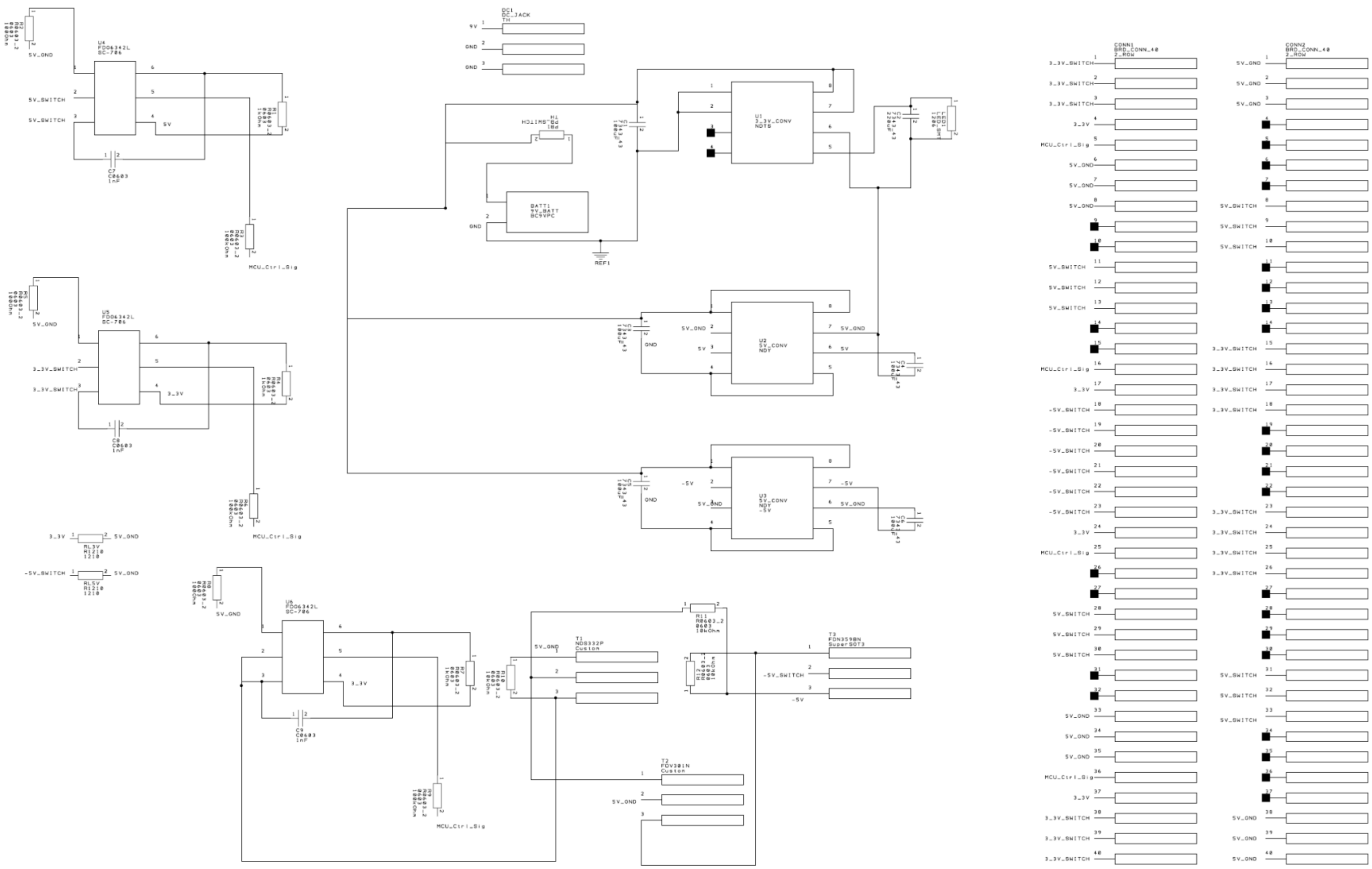

Appendix D: MCU Code for UWB Access Point

```
#include <string.h>
#include "bsp.h"
#include "mrfi.h"
#include "bsp_leds.h"
#include "bsp_buttons.h"
#include "nwk_types.h"
#include "nwk_api.h"
#include "nwk_frame.h"
#include "nwk.h"
#include "virtual_com_cmds.h"

void toggleLED(uint8_t);

/* reserve space for the maximum possible peer Link IDs */
static linkID_t sLID[NUM_CONNECTIONS] = {0};
static linkID_t sSleepingLID[NUM_CONNECTIONS] = {0}; // allow tags to come in and out of range
static uint8_t  sNumCurrentPeers = 0;
static uint8_t  sNumSleepingPeers = 0;
static uint16_t  tagTimedOutIter[NUM_CONNECTIONS];

/* callback handler */
static uint8_t sCB(linkID_t);

// TDMA state variables for UWB transmission
static uint8_t is_TDMA_Response;
static uint8_t is_UWB_Transmission_OK;
static uint8_t sProceedToNextTag;
static uint8_t current_TDMA_Index;

/* received message handler */
static void processMessage(linkID_t, uint8_t *, uint8_t);

/* work loop semaphores */
static volatile uint8_t sPeerFrameSem = 0;
static volatile uint8_t sJoinSem = 0;
static volatile uint8_t sSelfMeasureSem = 0;
static volatile uint8_t sCountTimerIter = 0;
static volatile uint8_t sProceedToNextTagIter = 0;
static volatile uint8_t sNumUWBTransmissions = 0;

/* How many times to try a Tx and miss an acknowledge before doing a scan */
#define MISSES_IN_A_ROW  2

//data for terminal output
const char splash[] = {"\r\n--------------------------------------------------\r\n     ****\r\n     ****          eZ430-RF2500\r\n
******o****     UWB Positioning System\r\n********_///_***\r\n--------------------------------------------------\r\n"};
volatile int * tempOffset = (int *)0x10F4;
```

```
__interrupt void ADC10_ISR(void);
__interrupt void Timer_A (void);

/*     ************** END interference detection support                    */

#define SPIN_ABOUT_A_QUARTER_SECOND   NWK_DELAY(250)

void main (void)
{
  bspIState_t intState;
  uint8_t msg_TDMA[2], msg_WhichTag[4];
  uint8_t      noAck;
  uint8_t     misses, done;
  int i;

  msg_TDMA[0] = 'O';
  msg_TDMA[1] = 'N';

  msg_WhichTag[2] = 'T';
  msg_WhichTag[3] = 'X';
  msg_WhichTag[0] = '\r';
  msg_WhichTag[1] = '\n';

  memset(sSample, 0x0, sizeof(sSample));
  sProceedToNextTag = 1;

  BSP_Init();

  BCSCTL3 |= LFXT1S_2;                    // LFXT1 = VLO
  TACCTL0 = CCIE;                          // TACCR0 interrupt enabled
  TACCR0 = 120;                          // ~1 second
  TACTL = TASSEL_1 + MC_1;                 // ACLK, upmode

  COM_Init();
  TXString( (char*)splash, sizeof splash);
  TXString( "\r\nInitializing Network....", 26 );

  SMPL_Init(sCB);

  // network initialized
  TXString( "Done\r\n", 6);
  SMPL_Ioctl( IOCTL_OBJ_RADIO, IOCTL_ACT_RADIO_RXON, 0);

  /* main work loop */
  current_TDMA_Index = 0;
  while (1)
  {
    /* Wait for the Join semaphore to be set by the receipt of a Join frame from a
     * device that supports an End Device.
```

```
 *
 * An external method could be used as well. A button press could be connected
 * to an ISR and the ISR could set a semaphore that is checked by a function
 * call here, or a command shell running in support of a serial connection
 * could set a semaphore that is checked by a function call.
 */
if (sJoinSem && (sNumCurrentPeers < NUM_CONNECTIONS))
{
  /* listen for a new connection */
  while (1)
  {
    if (SMPL_SUCCESS == SMPL_LinkListen(&sLID[sNumCurrentPeers]))
    {
      tagTimedOutIter[sNumCurrentPeers] = 0;
      break;
    }
    /* Implement fail-to-link policy here. otherwise, listen again. */
  }

  BSP_ENTER_CRITICAL_SECTION(intState);
  sJoinSem--;
  sNumCurrentPeers++;
  BSP_EXIT_CRITICAL_SECTION(intState);
}

// if it is time to measure our own temperature...
if(sSelfMeasureSem)
{
  char msg [6];
  char addr[] = {"HUB0"};
  char rssi[] = {"000"};
  int degC, volt;
  volatile long temp;
  int results[2];

  ADC10CTL1 = INCH_10 + ADC10DIV_4;     // Temp Sensor ADC10CLK/5
  ADC10CTL0 = SREF_1 + ADC10SHT_3 + REFON + ADC10ON + ADC10IE + ADC10SR;
  for( degC = 240; degC > 0; degC-- );  // delay to allow reference to settle
  ADC10CTL0 |= ENC + ADC10SC;           // Sampling and conversion start
  __bis_SR_register(CPUOFF + GIE);      // LPM0 with interrupts enabled
  results[0] = ADC10MEM;

  ADC10CTL0 &= ~ENC;

  ADC10CTL1 = INCH_11;                  // AVcc/2
  ADC10CTL0 = SREF_1 + ADC10SHT_2 + REFON + ADC10ON + ADC10IE + REF2_5V;
  for( degC = 240; degC > 0; degC-- );  // delay to allow reference to settle
  ADC10CTL0 |= ENC + ADC10SC;           // Sampling and conversion start
  __bis_SR_register(CPUOFF + GIE);      // LPM0 with interrupts enabled
  results[1] = ADC10MEM;
```

```
ADC10CTL0 &= ~ENC;
ADC10CTL0 &= ~(REFON + ADC10ON);      // turn off A/D to save power

// oC = ((A10/1024)*1500mV)-986mV)*1/3.55mV = A10*423/1024 - 278
// the temperature is transmitted as an integer where 32.1 = 321
// hence 4230 instead of 423
temp = results[0];
degC = (((temp - 673) * 4230) / 1024);
if( (*tempOffset) != 0xFFFF )
{
 degC += (*tempOffset);
}

temp = results[1];
volt = (temp*25)/512;

msg[0] = degC&0xFF;
msg[1] = (degC>>8)&0xFF;
msg[2] = volt;
msg[3] = sNumUWBTransmissions;
transmitDataString(1, addr, rssi, msg );
//BSP_TOGGLE_LED1();
sNumUWBTransmissions = 0;
sSelfMeasureSem = 0;

/* process all frames waiting */
for (i=0; i<sNumCurrentPeers; ++i)
{
 // check for any tags which may have timed out
 // currently they have a 5 second time out
 if (tagTimedOutIter[i] > 499)
 {
  // need to remove node i from current peers
  linkID_t tempLinkID;
  int j;
  tagTimedOutIter[i] = 0;
  sSleepingLID[sNumSleepingPeers] = sLID[i];
  sNumSleepingPeers++;

  if (sNumCurrentPeers>1)
  {
   for (j=i+1; j<sNumCurrentPeers; ++j)
   {
    sLID[j-1] = sLID[j];
   }
  }
  else
   sLID[i] = 0;

  sNumCurrentPeers--;
```

```
    }
  }
}

/* Have we received a frame on one of the ED connections?
 * No critical section -- it doesn't really matter much if we miss a poll
 */
if (sPeerFrameSem)
{
  uint8_t     msg[MAX_APP_PAYLOAD], len, i;

  /* process all frames waiting */
  for (i=0; i<sNumCurrentPeers; ++i)
  {
    if (SMPL_SUCCESS == SMPL_Receive(sLID[i], msg, &len))
    {
      ioctlRadioSiginfo_t sigInfo;
      tagTimedOutIter[i] = 0;
      sigInfo.lid = sLID[i];
      SMPL_Ioctl(IOCTL_OBJ_RADIO, IOCTL_ACT_RADIO_SIGINFO, (void *)&sigInfo);
      transmitData( i, sigInfo.sigInfo.rssi, (char*)msg );

      BSP_ENTER_CRITICAL_SECTION(intState);
      sPeerFrameSem--;
      BSP_EXIT_CRITICAL_SECTION(intState);
    }
  }
}
if (BSP_BUTTON1())
{
  SPIN_ABOUT_A_QUARTER_SECOND;  /* debounce */
  changeChannel();
}
else
{
  checkChangeChannel();
}
BSP_ENTER_CRITICAL_SECTION(intState);
if (sBlinky)
{
  if (++sBlinky >= 0xF)
  {
    sBlinky = 1;
  }
}
BSP_EXIT_CRITICAL_SECTION(intState);

// this section is added to implement the TDMA scheme
// for transmission of tag 3-D position via UWB system
// iterate through all tags currently present
```

```
if (sProceedToNextTag && sNumCurrentPeers > 0)
{
 BSP_ENTER_CRITICAL_SECTION(intState);
 sProceedToNextTag = 0;
 BSP_EXIT_CRITICAL_SECTION(intState);
 // need to get acknowledgement from tag
 done = 0;
 while (!done)
 {
  noAck = 0;
  smplStatus_t rc;
  uint8_t tempInt;

  // Try sending message MISSES_IN_A_ROW times looking for ack
  sNumUWBTransmissions++;
  for (misses=0; misses < MISSES_IN_A_ROW; ++misses)
  {
   if (SMPL_SUCCESS == (rc=SMPL_Send(sLID[current_TDMA_Index], msg_TDMA,
     sizeof(msg_TDMA))))
   {
    tempInt = current_TDMA_Index;
    msg_WhichTag[3] = '0'+((tempInt+1)%10);
    TXString(msg_WhichTag,4);
    break;
   }
   if (SMPL_NO_ACK == rc)
   {
    // Count ack failures. Could also fail becuase of CCA and
    // we don't want to scan in this case.
    //
    noAck++;
   }
  }
  if (MISSES_IN_A_ROW == noAck)
  {
   // Message not acked. Toggle LED 2.
   // transmission to awake current tag failed
   BSP_ENTER_CRITICAL_SECTION(intState);
   if (current_TDMA_Index + 1 < sNumCurrentPeers)
    current_TDMA_Index++;
   else
    current_TDMA_Index = 0;

   //sProceedToNextTag = 1;
   BSP_EXIT_CRITICAL_SECTION(intState);

   done = 1;
  }
  else
```

```
      {
        // Got the ack or we don't care. We're done.
        // acknowledgement received...have to wait for final response
        // from tag stating 'OK' or 'ER' for UWB transmission
        BSP_ENTER_CRITICAL_SECTION(intState);
        if (current_TDMA_Index + 1 < sNumCurrentPeers)
          current_TDMA_Index++;
        else
          current_TDMA_Index = 0;

        //sProceedToNextTag = 1;
        BSP_EXIT_CRITICAL_SECTION(intState);

        done = 1;
        //transmitDataTDMA(current_TDMA_Index,1);
      } //else
    } // while (!done)
  } // if (sProceedToNextTag)
 } // while (1)
}

/* Runs in ISR context. Reading the frame should be done in the */
/* application thread not in the ISR thread. */
static uint8_t sCB(linkID_t lid)
{
 uint8_t tagInList = 0, tagAsleep = 0;
 int i,j;
 // see if this tag is in the sleeping category
 // bring back into active, if so
 for (i=0; i<sNumSleepingPeers; ++i)
 {
  if (lid == sSleepingLID[i])
  {
   // add tag back to active list
   tagAsleep = 1;
   sLID[sNumCurrentPeers] = sSleepingLID[i];
   sNumCurrentPeers++;

   if (sNumSleepingPeers>1)
   {
    for (j=i+1; j<sNumSleepingPeers; ++j)
    {
     sSleepingLID[j-1] = sSleepingLID[j];
    }
   }
   else
    sSleepingLID[i] = 0;

   sNumSleepingPeers--;
   return 0;
```

```
    }
  }

  if (lid)
  {
    sPeerFrameSem++;
    sBlinky = 0;
  }
  else
  {
    sJoinSem++;
  }

  /* leave frame to be read by application. */
  return 0;
}

/*------------------------------------------------------------------------------
* Timer A0 interrupt service routine
------------------------------------------------------------------------------*/
#pragma vector=TIMERA0_VECTOR
__interrupt void Timer_A (void)
{
  int i;
  if (sCountTimerIter == 0)
  {
    sSelfMeasureSem = 1;
  }

  if (sProceedToNextTagIter == 0)
  {
    sProceedToNextTag = 1;
  }

  if (sProceedToNextTagIter < 10)
    sProceedToNextTagIter++;
  else
    sProceedToNextTagIter = 0;

  if (sCountTimerIter < 99)
    sCountTimerIter++;
  else
    sCountTimerIter = 0;

  // used to watch for tags timing out
  for (i=0; i<sNumCurrentPeers; ++i)
    tagTimedOutIter[i]++;
}
```

Vita

Michael Joseph Kuhn was born in Wheat Ridge, Colorado, USA, in 1982. He received the B.S. degree in electrical engineering and the B.S. degree in computer science from the Colorado School of Mines, Golden, CO, in 2004, and the M.S. degree in engineering science from the University of Tennessee, Knoxville, TN, in 2008. He received the Ph.D. degree in biomedical engineering from the University of Tennessee, Knoxville, TN, in 2012. He is currently Research and Development Staff in the Global Nuclear Safeguards and Security Technology group at Oak Ridge National Laboratory, Oak Ridge, TN and began working as a staff member at Oak Ridge National Laboratory in 2010. He has published and presented at many international conferences in the fields of biomedical engineering, microwave and antenna engineering, and nuclear safeguards. He is active within the IEEE both as a member of technical programming committees and assisting with conference organization. His current research interests include wireless tracking and tagging technologies and sensors with emphasis on ultra-wideband, medical applications of wireless technologies, numerical techniques in microwave engineering, and R&D in nuclear safeguards. Michael received the James A. Euler award for outstanding graduate student from the Mechanical, Aerospace, and Biomedical Engineering department at the University of Tennessee in 2010.